OPEN ACCESS LIBRARY

Scientific International Journal of the World Academy
of Materials and Manufacturing Engineering
publishing scientific monographs in Polish or in English only

Published since 1998 as Studies of the Institute of Engineering Materials and Biomaterials

Volume 1, 2011

Leszek A. DOBRZAŃSKI (ed.)

Effect of casting, plastic forming or surface technologies on the structure and properties of the selected engineering materials

OPEN ACCESS LIBRARY

Scientific International Journal of the World Academy of Materials and Manufacturing Engineering publishing scientific monographs in Polish or in English only

Published since 1998 as Studies of the Institute of Engineering Materials and Biomaterials

Volume 1, 2011

Publisher

International OCSCO World Press
Gliwice 44-100, Poland, ul. S. Konarskiego 1 8a/366
e-mail: info@openaccesslibrary.com

Bank account: Stowarzyszenie Komputerowj Nauki o Materiałach i Inżynierii Powierzchni
Bank name: ING Bank Śląski
Bank addres: ul. Zwycięstwa 28, 44-100 Gliwice Poland
Account number/ IBAN CODE: PL 76105012981000002300809767
Swift code: INGBPLPW
Gliwice

Leszek A. DOBRZAŃSKI (ed.)

Effect of casting, plastic forming or surface technologies on the structure and properties of the selected engineering materials

EFFECT OF CASTING, PLASTIC FORMING OR SURFACE TECHNOLOGIES ON THE STRUCTURE AND PROPERTIES OF THE SELECTED ENGINEERING MATERIALS

REVIEWERS:

Prof. L. Kosec (University of Ljubljana, Slovenia)
Prof. W. Kwaśny (Silesian University of Technology, Poland)
Prof. R. Nowosielski (Silesian University of Technology, Poland)
Prof. J. Pacyna (AGH University of Science and Technology, Poland)
Prof. Z. Rdzawski (Institute of Non-Ferrous Materials, Poland)
Prof. J. Sieniawski (Rzeszów University of Technology, Poland)
Prof. M. Sokovic (University of Ljubljana, Slovenia)
Prof. J. Stobrawa (Institute of Non-Ferrous Materials, Poland)
Dr K. Gołombek (Silesian University of Technology, Poland)

SOURCE OF FUNDING:

The papers have been realised in relation to the project POKL.04.01.01-00-003/09-00 entitled "Opening and development of engineering and PhD studies in the feld of nanotechnology and materials science" INFONANO, co-founded by the European Union from fnancial resources of European Social Fund and headed by Prof. L.A. Dobrzański.

HUMAN CAPITAL
NATIONAL COHESION STRATEGY

PROJEKT infonano

EUROPEAN UNION
EUROPEAN
SOCIAL FUND

ISSN 2083-5191
ISBN 83-89728-88-5
EAN 9788389728883

CONTENTS

Introduction on the importance of the materials structure and properties forming processes for contemporary industrial production

L.A. Dobrzański*
Institute of Engineering Materials and Biomaterials, Silesian University of Technology, ul. Konarskiego 18a, 44-100 Gliwice, Poland
* Corresponding author: E-mail address: leszek.dobrzanski@polsl.pl

Many new and contemporary science branches and disciplines, especially at the interdisciplinary areas of the traditional ones, have emerged since a positivist – Auguste Comte had categorised them. As a consequence of the development of physical metallurgy and many other fields of science and technology connected with a various group of materials useful in practice, materials science was created in the 1950s as the fundamental branch of science and also materials engineering as the engineering knowledge applied in the industrial practice. It is worth noting that just rendering accessible newer and newer technical materials, and with time also engineering ones within the compass of history, decided – as a rule – the significant, and quantum leap at times technical progress, determining improvement of the quality of life. Not unlike it is today. Therefore progress in the field of the advanced engineering materials is predicted and expected, including, among others, nanomaterials (with the particularly fine structure, ensuring the unexpected so far mechanical, as well as physical and chemical properties), biomaterials (as a group of the biomimetic materials and/or making it possible to substitute the natural human tissues and/or organs directly or designed into the purpose built devices), and infomaterials (as the most advanced group of smart- and self-organising materials), and also (functional or tool ones) gradient materials (in which properties change continuously or discretely with location because of the chemical composition, phase composition, and structure, or atomic orientation changing with the location), and light metals alloys (as materials of the particular importance, apart from the composite materials, in design and operation of the contemporary transport means), which issues decide development of materials engineering as one of the few areas of science and technology development most important nowadays in the contemporary World. Of course, the development of all other

groups of engineering materials and process technology materials, traditionally considered to be less avant-garde today is constantly noticeable and still awaited. The development of materials engineering and materials science features also one of the most essential elements of the scientific-, scientific and technical-, and innovative policy of Poland within the framework of the knowledge based economy, consisting in knowledge generation, treated as production, and in distribution and practical use of knowledge and information.

A typical subject matter of materials science and engineering includes the description of phenomena and transformations occurring in technical materials, especially in the engineering ones, that is those manufactured in the purpose designed technological processes from raw materials available in the nature, in technological processes of manufacturing, processing, as well as forming of their structure and properties, for satisfying more and more complex practical requirements formulated by participants of the design process of products indispensable to the contemporary humans, including – among others - machines and devices. Materials have to be manufactured on demand today, meeting the complex set of the specific demands. Manufacturing is expected of materials with properties ordered by products users. This changes substantially the materials design methodology in general and the products materials design, as materials have to be delivered on demand of products manufacturers with the appropriately formed structure, ensuring the required set of physical and chemical properties, and not as before when the manufacturers were forced to select material closest to their expectations from the delivered materials with the offered structure and properties, yet – by assumption – not meeting them fully, which is not permitted by this design methodology. Therefore, the actual trends force classification of engineering materials based on their functional characteristics. Therefore, the type, and the chemical composition in particular, of the materials used are of less importance (to which materials engineers were used for decades, and especially the metallurgists), while its functionality is more important. Currently, materials engineers participate (and have to do so) in the products design processes and materials manufacturers have to face the requirements, as the effect of the multicriteria optimisation of, e.g., structure, properties, mass, product manufacturing and service costs, as well as of their ecological compatibility with the natural environment. Therefore, a change in the engineering materials role assessment is important, as they cannot be perceived any more as goods in themselves, with their applications sought for, and the market of the new engineering materials cannot remain the manufacturer's market any more. There is no way to offer materials which, by chance, are offered by their manufacturers, regardless of the users' needs. The market of materials manufacturers is never to return. This is so since the new engineering materials and

manufacturing processes have been subordinated to customer needs and functional requirements of products. Manufacturing materials on demand fulfilling needs of market products manufacturers at the right time and place features a priority for new materials technologies and manufacturing processes, as the complementary base technologies (improvement of the existing solutions), alternative ones (taking advantage of synergy of various solutions), and original ones (new solutions being developed).

It was decided that the results of various works made in the Institute of Engineering Materials and Biomaterials of the Silesian University of Technology in Gliwice, Poland, concerning advanced engineering materials and materials processing technologies will be published in the form of monographs. First of them, concerning chosen aspects of the effect of casting, forming and surface technologies on the structure and properties of the selected engineering materials beginning the cycle of those studies will be prepared both in English and Polish. In the given issue five detailed studies were presented. First of them presents an influence of Al concentration and cooling rate on structure and mechanical properties of magnesium alloys. Also the work presents a methodology to predict crystallisation temperatures obtained during crystallisation process using UMSA platform, based on cooling rate and chemical composition and mechanical properties and grain size based on characteristic temperatures. The next study consists in investigation of newly elaborated high-manganese austenitic steels with Nb and Ti microadditions in variable conditions of hot-working. The hot-deformation resistance and microstructure evolution in various conditions of hot-working for the new-developed high-manganese austenitic steels were investigated. The main objective of the third presented work is to elaborate the fabrication technology of novel sintered tool gradient materials on the basis of hard tungsten carbide phase with cobalt binding phase, and to carry out research studies on the structure and properties of the newly elaborated sintered tool gradient materials. The main objective of the fourth work is to investigate the structure and properties of multilayer gradient coatings produced in PVD and CVD processes on sintered carbides and on sialon ceramics, and to define the influence of the properties of the coatings such as microhardness, adhesion, thickness and size of grains on the applicable properties of cutting edges covered by such coatings. In the fifth work the investigation of the structure and properties of sintered tool materials, including cemented carbides, cermets and oxide ceramics deposited with single-layer and gradient coatings (Ti,Al)N and Ti(C,N) are included and the determination of the dependence between the substrate type, coating material or linear variation of chemical composition and the structure and properties of the obtained tool material were also investigated.

The presented researches are a fragment of many-year works made in the Institute of Engineering Materials and Biomaterials of the Silesian University of Technology in Gliwice, Poland, enabling further works to improve many materials design methodology activities changed because of changes of expectations and contemporary requirements of manufacturing of materials having required structure and utility properties. At present modelling, simulation and prediction of both the technological processes of manufacturing, processing, and forming their structure and properties, and especially of the service and use properties of materials, including those after long time service in the complex conditions, the development of safe materials and products technologies, the standardisation of materials testing procedures, the development of the prediction methodology of the new materials behaviour in service is necessary. One should note that many classic calculation models developed to date, employed in materials science, e.g., Avrami equation used for processes being a function of time and temperature, Fick's laws for diffusion processes, Hall-Petch equation describing dependence of mechanical properties and grain size, Huber-von Mises yield criterion for determining the material loading condition in the complex strain state, equations of the classic mechanics of solids, equations of classic fracture mechanics, models developed using FEM and BEM as well as the related numerical methods, parametric equations and empirical equations, and others, do not fulfil the refined expectations of the designers, especially related to materials – in case of many contemporary material groups or structural phenomena occurring in them, because of the insufficient adequacy of models, and also often because of superposition or superimposition of processes – oftentimes opposing processes, and also due to difficulties in the simultaneous modelling of phenomena occurring at the same time in various scales – from nanometric to metric inclusive, lack of generality of the statistic and parametric equations because of the limited function domain (range) encompassing selectively only some material grades or types, so these factors decide the limited usability or simply impossibility to use those models to fulfil all expectations. Moreover, the trial-and-error method is often the ground of the classically used modelling methods and practical verification of the calculation of obtained is needed nearly each time, because of the significantly excessive mass of the employed materials (and, therefore, also of the products), and the need to employ the high values of the safety factors in product design, because of the insufficient dependability of the used models. Absence of the relevant analytical models is frequently the reason for stopping the progress of the products materials and technological design processes. This stops also the R&D projects in many materials engineering areas, forcing the classic trial-and-error method approach with the extensive experimental investigations plan, even if those experiments are statistically planned.

All this causes also the unjustified increase of costs of such investigations and essential extension of the lead time needed to solve the scientific problem of the significant importance for the implementation practice.

In general, methodology of carrying out each of those scientific tasks consists in completing the entire set of the contemporary materials science examinations using methods and state-of-the-art scientific and research equipment at the unrestricted disposal of the Institute of Engineering Materials and Biomaterials of the Silesian University of Technology, in Gliwice, Poland, including structure examinations also on the transmission and scanning electron microscopes, on the light microscope and the laser confocal one, quantitative and qualitative diffraction analyses with X-ray methods, but also using EBSD, spectral analyses, including also WDS, EDS, and GDOES, and also the required mechanical tests, also in the nanoscale, examinations of the physical and chemical properties, and other dedicated and specialist tests depending on the task topic, after various necessary fabrication processes of the investigated materials and their processing and forming of their structure and properties expected in products for which they are going to be used, to set up the relevant databases and knowledge bases containing results of these investigations related to various groups of the contemporary engineering materials for development and verification of the relevant models, including those for the inverse analysis (specifying at the beginning the material type and its chemical composition, as well as conditions of the technological processes ensuring obtaining properties required and assumed at the beginning by the product designer) and for prediction (assuming the properties used by the product designer in the design process, also including properties after the long time service for the analysed contemporary engineering material type and its chemical composition, as well as conditions of the technological processes).

Effect of cooling rate and aluminum contents on the Mg-Al-Zn alloys' structure and mechanical properties

L.A. Dobrzański*, M. Król, T. Tański
Institute of Engineering Materials and Biomaterials, Silesian University of Technology, ul. Konarskiego 18a, 44-100 Gliwice, Poland
* Corresponding author: E-mail address: leszek.dobrzanski@polsl.pl

Abstract

Purpose: *This work present an influence of Al concentration and cooling rate on structure and mechanical properties of magnesium alloys. Also the paper presents a methodology to predict crystallization temperatures obtained during crystallization process using an UMSA platform, based on cooling rate and chemical composition and mechanical properties and grain size based on characteristics temperatures.*

Design/methodology/approach: *The experimental magnesium alloy used for thermal analysis and training of neural network was prepared in cooperation with the Faculty of Metallurgy and Materials Engineering of the Technical University of Ostrava and the CKD Motory plant, Hradec Kralove in the Czech Republic. The alloy was cooled with three different cooling rates in UMSA Technology Platform. The following results concern scanning electron microscopy investigations in the SE observation mode, as well as using BSE modus for better phase contrast results, also quantitative microanalysis was applied for chemical composition investigations of the phases occurred. Compression test were conducted at room temperature using a Zwick universal testing machine. Compression specimens were tested corresponding to each of three cooling rates. Rockwell F-scale hardness tests were carried out using a Zwick HR hardness testing machine.*

Findings: *The research show that the thermal analysis carried out on UMSA Technology Platform is an efficient tool for collect and calculate thermal parameters. The formation temperatures of various thermal parameters, mechanical properties (hardness and ultimate compressive strength) and grain size are shifting with an increasing cooling rate.*

Practical implications: *The parameters described can be applied in metal casting industry for selecting magnesium ingot preheating temperature for semi solid processing to achieve*

requirements properties. The presented models can be applied in computer systems of Mg-Al-Zn casting alloys, selection and designing for Mg-Al-Zn casting parts.
Originality/value: *The paper contributes to better understanding and recognition an influence of different solidification condition on non-equilibrium thermal parameters of magnesium alloys.*
Keywords: *Thermal treatment; Mechanical properties; Magnesium alloys*

Reference to this paper should be given in the following way:
L.A. Dobrzański, M. Król, T. Tański, Effect of cooling rate and aluminum contents on the Mg-Al-Zn alloys' structure and mechanical properties, in L.A. Dobrzański (ed.) Effect of casting, plastic forming or surface technologies on the structure and properties of the selected engineering materials, Open Access Library, Volume 1, 2011, pp. 9-54.

1. Introduction

The application of thermal analysis in different fields of science and engineering is an extensive topic which has been the subject of significant interest particularly since the beginning of the modern era of thermal analysis in the early 1960s. With the continuous development of new techniques using modern computers, more and more applications are constantly being explored and reported. In the last several years, applications on the fields of cement chemistry, clays and minerals, polymeric materials, pharmaceuticals and other general applications have been discussed in detail. Thermal analysis techniques have also been used extensively in the field of metallurgy and a large number of publications (several thousands in the last four decades). On this subject have been identified in the literature. For obvious practical reasons, however, only a select number of publications, in which thermal analyses were used as primary techniques or important supplementary techniques, were chosen to address metallurgical topics that have received most attention in the recent past. From the many thermal analysis techniques that have been used in a wide variety of applications, thermogravimetry (TG), differential thermal analysis (DTA) and differential scanning calorimetry (DSC) were found to be the most commonly used in metallurgy [1-3].

Every thermal method studies and measure a property as a function of temperature. The properties studied may include almost every physical or chemical property of the sample, or its product. The more frequently used thermal analysis techniques are shown in Table 1 together with the names most usually employed for them [1].

Table 1. *Thermal methods [1]*

Technique	Abbreviation	Property	Uses
Thermogravimetry	TG	Mass	Decompositions
(Thermogravimetric analysis)	TGA		Oxidations
Differential thermal analysis	DTA	Temperature difference	Phase changes, reactions
Differential scanning calorimetry	DSC	Power difference of heat flow	Heat capacity, phase changes, reactions
Thermomechanical analysis	TMA	Deformations	Mechanical changes
Dynamic mechanical analysis	DMA	Dimensional change Moduli	Expansion Phase changes, glass transitions, polymer curve
Dielectric thermal analysis	DETA	Electrical	As DMA
Evolved gas analysis	EGA	Gases evolved or reacted	Decompositions
Thermiptometry		Optical	Phase changes, surface reactions, colour changes
Less frequently used methods Thermosonimetry	TS	Sound	Mechanical and chemical changes
Thermoluminescence	TL	Light emitted	Oxidation
Thermomagnetometry	TM	Magnetic	Magnetic changes

The modern instrumentation used for any experiment in thermal analysis or calorimetry is usually made up of four major parts [2, 4]:

- the sample and a container or holder;
- sensors to detect and measure a particular property of the sample and to measure temperature;
- an enclosure within the experimental parameters (e.g. temperature, pressure, gas atmosphere) may be controlled;
- a computer to control the experimental parameters, such as the temperature programme, to collect the data from the sensors and to process the data to produce meaningful results and records.

Sometimes in literature can be found an acronym SCRAM which mean sample-crucible-rate of heating-atmosphere-mass. It enable the analyst to obtain good, reproducible results for most thermal methods provided that the following details are recorded for each run:

The *sample*: A proper chemical description must be given together with the source and pre-treatments. The history of the sample, impurities and dilution with inert material can all affect results.

The *crucible.* The material and shape of the crucible or sample holder is important. Deep crucibles may restrict gas flow more than flat, wide ones, and platinum crucibles catalyse come reactions more than alumina ones. The type of holder or clamping used for Thermomechanical methods is equally important. The make and type of instrument used should also be recorded.

The *rate of heating:* this has most important effects. A very slow heating rate will allow the reactions to come closer to equilibrium and there will be less thermal lag in the apparatus. Conversely, high heating rate will give a faster experiment, deviate more from equilibrium and cause greater thermal lag. The parameters of special heating programmes, such as modulated temperature or sample control, must be noted.

The *atmosphere:* both the transfer of heat, the supply and removal of gaseous reactants and the nature of reactions which occur, or are prevented, depend on chemical nature of the reactions and its flow. Oxidations will occur well in oxygen, less so in air and not at all in argon. Product removal by a fairly rapid gas flow may prevent reverse reactions occurring.

The *mass of the sample:* A large mass of sample will require more energy, and heat transfer will be determined by sample mass and dimensions. These include the volume, packing, and particle size of the sample. Fine powders react rapidly, lumps more slowly. Large samples may allow the detection of small effects. Comparison of runs should preferably be made using similar sample masses, sizes and shapes.

Specific techniques require the recording of other parameters, for example the load on the sample in thermomechanical analysis. Calorimetric methods, too, require attention to the exact details of each experiment.

Thermal Analysis techniques are used in a wide range of disciplines, from pharmacy and foods to polymer science, materials and glasses; in fact any field where changes in sample behaviour are observed under controlled heating or controlled cooling conditions. The wide range of measurements possible provide fundamental information on the material properties of the system under test, so thermal analysis has found increasing use both in basic characterisation of materials and in a wide range of applications in research, development and quality control in industry and academia [1-4].

For the experimental determination of phase diagrams the use of different techniques can be beneficial. The role of thermal analysis has been of primary importance since the beginning of this research field, as has been pointed out by different authors [2, 4, 5].

Thermal analysis as a technique is used to evaluate the melt quality. By this method, some characteristic values are extracted from a cooling curve and/or its derivative, and then a regression relationship is built up between the characteristics and quality indexes as grain size, eutectic structure, silicon morphology, and so on [1].

In metal casting industry an improvement of component quality mainly depends on better control over the production parameters. Thus, computer-aided cooling curve thermal analysis of alloys is extensively used for the evaluation of several processing and material parameters. Thermal analysis of alloys can provide information about the composition of the alloy, the latent heat of solidification, the evolution of the fraction solid, the types of phases that solidify, and even dendrite coherency. There are also many other uses for thermal analysis, such as, determining dendrite arm spacing, degree of modification and grain refining in aluminium alloys, the liquidus and solidus temperature, and characteristic temperatures related to the eutectic regions and intermetallic phase formation [6, 7].

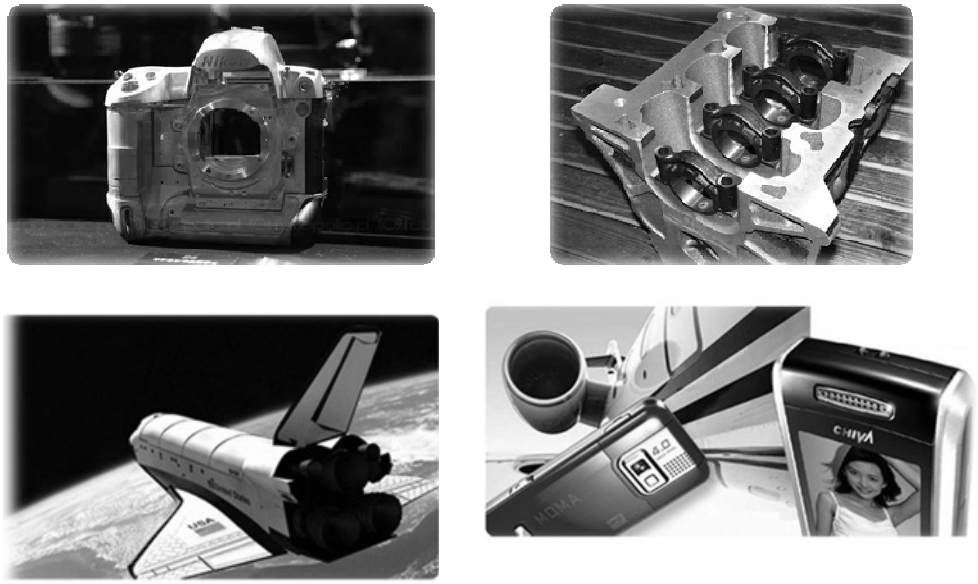

Figure 1. *Examples of application magnesium alloys*

As the lightest metal construction material, magnesium is extremely attractive for many lightweight construction applications (Fig. 1). Due to the high strength of magnesium in comparison to its weight, magnesium die casting is particularly suitable for many types of equipment housings. Magnesium is attractive for more than just its weight – due to the low viscosity of the melt, highly complex components can be manufactured with thinner walls and

larger surface areas than die cast aluminium. The good heat conductivity and electromagnetic screening of die cast magnesium make it attractive for many segments of machine construction and the electronics industry. The disadvantage of high corrosion from other metals or acids can be counted by high purity magnesium alloys, design measures and suitable surface protection such as passivation, anodizing or coatings [8-10].

In its pure form, magnesium is soft, mechanically weak, and hence not generally used for structural applications. By careful selection of alloying elements, alloys can be produced - both for general-purpose and for special applications. As with other metallic alloy systems, a combination of well-known hardening mechanisms (solid solution hardening, particle dispersion hardening, work hardening, and grain boundary hardening) determines the mechanical properties of magnesium alloys. Alloying additions influence other properties including reactivity of the melt, castability, and corrosion performance [9, 10].

The alloying elements used with magnesium can be grouped into two categories [11, 12]:

- elements that actively influence the melt. Examples are: beryllium (≤ 15 ppm), which lowers the rate of melt oxidation, and manganese (<= 0.6 wt%), which reduces the iron content and hence the corrosion rate of the alloys. These additions are active in relatively small amounts and do not require extensive solubility in the melt.
- elements that modify the microstructure of the alloy via the above-mentioned hardening mechanisms. This group includes elements that influence castability. Except for grain-refining additions (carbon inoculation), which can be active in small amounts, these elements must be relatively soluble in liquid magnesium. Commercially interesting alloying elements include aluminum, cerium, copper, lanthanum, lithium, manganese, neodymium, silver, thorium, yttrium, zinc, and zirconium.

Magnesium's physical properties are certainly influenced by the amount of added constituents. The effect of the constituent added is mostly directly pro rata to its amount. The processing and property effects of the individual alloying elements are more important in most structural applications than the physical properties. Here is a description of each alloying constituent's effect on the alloy quality.

Aluminum has the most favorable effect on magnesium of any of the alloying elements. It improves strength and hardness, and it widens the freezing range, and makes the alloy easier to cast. When exceeding 6 wt%, the alloy becomes heat treatable, but commercial alloys rarely exceed 10 wt% aluminum. An aluminum content of 6 wt% yields the optimum combination of strength and ductility [13].

Zinc is next to aluminum in effectiveness, as an alloying ingredient in magnesium. It is often used in combination with aluminum to produce improvement in room-temperature strength; however, it increases hot shortness when added in amounts greater than 1 wt% to magnesium alloys containing 7-10 wt% aluminum. Zinc is also used in combination with zirconium, rare earths, or thorium to produce precipitation-hardenable magnesium alloys having good strength. Zinc also helps overcome the harmful corrosive effect of iron and nickel impurities that might be present in the magnesium alloy.

Calcium is added in very small amounts, being a special alloying component. It has a dual purpose: when added to casting alloys immediately prior to pouring, it reduces oxidation in the molten condition as well as during subsequent heat treatment of the casting, and it improves the rollability of magnesium sheet. However, the addition of calcium must be controlled so that it is below about 0.3 wt% - or the sheet will be susceptible to cracking during welding.

Manganese does not affect tensile strength considerably, yet it slightly increases the yield strength. Its most important function is to improve saltwater resistance of Mg-Al and Mg-Al-Zn alloys by removing iron and other heavy-metal elements into relatively harmless intermetallic compounds, some of which separate out during melting. The amount of manganese that can be added is limited by its relatively low solubility in magnesium. Commercial alloys containing manganese rarely contain over 1.5 wt%, and in the presence of aluminum, the solid solubility of manganese is reduced to about 0.3 wt%.

Copper adversely affects the corrosion resistance of magnesium if present in amounts exceeding 0.05 wt%. However, it improves high-temperature strength.

Iron is one of the most harmful impurities in magnesium alloys due to considerable reduction of corrosion resistance even in present in small amounts. In ordinary commercial-grade alloys, the iron content can average as high as 0.01-0.03 wt%. However, for maximum corrosion resistance, 0.005% is specified as the upper limit for iron content.

Nickel , just like iron, is another harmful impurity in magnesium alloys because it also reduces the corrosion resistance if present, even in small amounts. In ordinary commercial-grade alloys, the nickel content can average as high as 0.01-0.03 wt%, but for maximum resistance to corrosion, 0.005% is specified as the upper limit for nickel content.

Lithium has relatively high solid solubility in magnesium (5.5 wt%, 17.0 at.%) and low relative density (0.54). It has attracted interest as an alloying element in magnesium alloys to lower the density to values even lower than that of unalloyed magnesium. Moreover, only some 11 wt% of lithium is needed to form the β phase, which has a body-centered cubic crystal structure, thereby improving formability of wrought products. The addition of lithium

decreases strength, but increases ductility. Mg-Li alloys are also amenable to age hardening, although they tend to overage at only slightly elevated temperatures. Nevertheless, the Mg-Li alloys have found only limited application [8-10, 25, 27].

Silicon increases fluidity of the metal in the molten state. However, it decreases corrosion resistance of magnesium alloys in case of iron presence in the alloy.

Silver additions improve the mechanical properties of magnesium alloys by increasing response to age hardening.

Thorium increases the creep strength of magnesium alloys at temperatures up to 370°C. The most common alloys contain 2-3 wt% thorium in combination with zinc, zirconium, or manganese. Thorium improves the weldability of zinc-containing alloys.

Tin is useful when alloyed with magnesium in combination with small amounts of aluminum. It increases the ductility of the alloy and makes it better for hammer forging, because it reduces the tendency for the alloy to crack while being hot-worked.

Yttrium has a relatively high solid solubility in magnesium (12.4 wt%) and is added with other rare earths to promote creep resistance at temperatures up to 300°C. About 4-5% Zr is added to magnesium to form commercial alloys such as WE54 and WE43, where it imparts good elevated-temperature properties up to about 250°C.

Zirconium has a powerful grain-refining effect on magnesium alloys. It is added to alloys containing zinc, rare earths, thorium, or a combination of these elements, where it serves as a grain refiner (up to its limit of solid solubility). However, it cannot be used in alloys containing aluminum or manganese because it forms stable compounds with these elements and is thus removed from solid solution. It also forms stable compounds with any iron, silicon, carbon, nitrogen, oxygen, and hydrogen present in the melt. Because only the portion of the zirconium content available for grain refining is that which is in solid solution, the soluble zirconium content, rather than the total zirconium content, is the value important to the alloy.

Rare earth metals are added to magnesium alloys either as mischmetal or as didymium. Mischmetal is a natural mixture of rare earths containing about 50 wt% cerium, the remainder being mainly lanthanum and neodymium; didymium is a natural mixture of approximately 85% neodymium and 15% praseodymium. Additions of rare earths increase the strength of magnesium alloys at elevated temperatures. They also reduce weld cracking and porosity in casting because they narrow the freezing range of the alloys.

A series of high-performance magnesium-based alloys was developed after discovery of the extremely efficient grain-refining action of zirconium. This effect results from the formation of high-density tiny zirconium particles in the melt, which act as potent grain nuclei.

Unfortunately, elements such as aluminum and manganese lower the solubility of zirconium in the melt, thus precluding exploitation of the grain-refining mechanism in common aluminum-containing alloys.

Mg-Zn-RE-Zr. Binary Mg-Zn alloys show inferior mechanical properties and castability, but the addition of zirconium for grain refinement and rare earth (RE) elements to reduce microporosity, led to the development of alloys such as EZ33 and ZE41. These alloys have been used widely as sand castings in the T5 condition (cooled and artificially aged) for applications involving exposure to moderately elevated temperature (up to ca. 200°C). The ZE63 alloy is a high-strength variant in which solution heat treatment in a hydrogen atmosphere is employed to remove some of the embrittling Mg-Zn-RE grain boundary phases. In extrusion, microporosity is of less concern and Mg-Zn-Zr alloys are used without RE additions [9-13, 27].

Mg-Ag-RE-Zr. Addition of silver and neodymium-rich misch metal, in addition to zirconium, promotes age hardening efficiently when the alloy is given a full T6 treatment (solution heat-treated and artificially aged). The precipitates formed are relatively stable; the alloy shows high mechanical strength and good creep properties at temperatures approaching 250°C [9, 26].

Mg-Y-RE-Zr. The most recently developed alloy system for high-temperature application is based upon additions of yttrium and neodymium-rich misch metal. This alloy system was developed to meet the ever-increasing high-temperature performance requirements of the aerospace industry and may replace the Mg-Ag-RE-Zr and thorium-containing alloys. The alloys must be melted in a special inert atmosphere (argon) and develop their properties by T6 heat treatment [10].

This work present an influence of Al concentration and cooling rate on structure and mechanical properties of magnesium alloys. Also the paper presents a methodology to predict crystallization temperatures obtained during crystallization process using an UMSA platform, based on cooling rate and chemical composition and mechanical properties and grain size based on characteristics temperatures.

2. Experimental procedure

2.1. Material

The investigations have been carried out on test pieces of MC MgAl12Zn1, MC MgAl9Zn, MC MgAl6Zn1, MC MgAl3Zn magnesium alloys in as-cast and after heat treatment states

made in cooperation with the Faculty of Metallurgy and Materials Engineering of the Technical University of Ostrava and the CKD Motory plant, Hradec Kralove in the Czech Republic. The chemical compositions of the investigated materials are given in Table 2. A casting cycle of alloys has been carried out in an induction crucible furnace using a protective salt bath *Flux 12* equipped with two ceramic filters at the melting temperature of 750±10ºC, suitable for the manufactured material. In order to maintain a metallurgical purity of the melting metal, a refining with a neutral gas with the industrial name of *Emgesalem Flux 12* has been carried out. To improve the quality of a metal surface a protective layer *Alkon M62* has been applied. The material has been cast in dies with betonite binder because of its excellent sorption properties and shaped into plates of 250x150x25. The cast alloys have been heated in an electrical vacuum furnace *Classic 0816 Vak* in a protective argon atmosphere.

Table 2. *Chemical composition of investigated magnesium alloys*

The mass concentration of main elements, %						
Al	Zn	Mn	Si	Fe	Mg	Rest
12.1	0.62	0.17	0.047	0.013	86.96	0.0985
9.09	0.77	0.21	0.037	0.011	89.79	0.0915
5.92	0.49	0.15	0.037	0.007	93.33	0.0613
2.96	0.23	0.09	0.029	0.006	96.65	0.0361

2.2. Test sample

The experiments were performed using a pre-machined cylindrical test sample with a diameter of ∅=18 mm and length of l=20 mm taken from the ingot (Fig. 2). In order to assure high repeatability and reproducibility of the thermal data, the test sample mass was ≈9.2 g. Each sample had a predrilled hole to accommodate a supersensitive K type thermocouple (with extra low thermal time constants) positioned at the centre of the test sample to collect the thermal data and control the processing temperatures.

2.3. Thermal analysis

The thermal analysis during melting and solidification cycles was carried out using the Universal Metallurgical Simulator and Analyzer (UMSA) (Fig. 3) [28, 29]. The melting and solidification experiments for the magnesium alloys were carried out using Argon as cover gas.

The data for Thermal Analysis (TA) was collected using a high-speed National Instruments data acquisition system linked to a personal computer. Each TA trial was repeated three times.

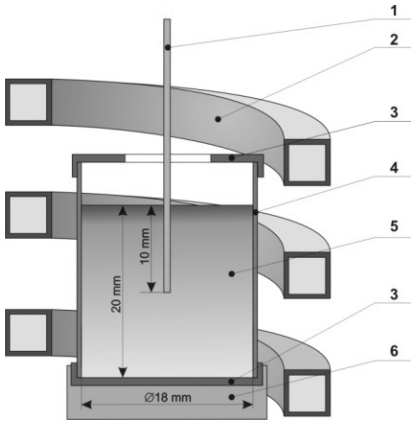

Figure 2. *Schematic of the UMSA Thermal Analysis Platform experimental set-up: 1 – low thermal mass thermocouple, 2 – heating and cooling coil, 3 – thermal insulation, 4 – steel foil, 5 – test sample, 6 – ceramic base*

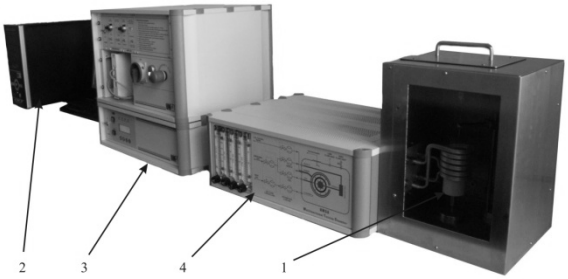

Figure 3. *UMSA apparatus – (1) sample chamber, (2) supervisory computer, (3) temperature control, (4) gas flow control*

The TA signal in the form of heating and cooling curves was recorded during the melting and solidification cycles. The temperature vs. time and first derivative vs. temperature were calculated and plotted. The cooling rates for these experiments were determined using the following formula [18]:

$$CR = \frac{T_{liq} - T_{sol}}{t_{sol} - t_{liq}} \quad \left[\frac{°C}{s}\right] \tag{1}$$

were T_{liq} and T_{sol} are the liquidus and solidus temperatures (°C), respectively, and t_{liq} and t_{sol} the times from the cooling curve that correspond to liquidus and solidus temperatures, respectively [16, 17].

The procedure comprised of the following steps. First, the test sample was heated to 700±2°C and isothermally kept at this temperature for a period of 90s in order to stabilize the melt conditions. Next, the test sample was solidified at cooling rate of approximately 0.6°C/s, that was equivalent to the solidification process under natural cooling conditions. To achieve an intentional cooling rate:

- 0.6°C/s sample was cooled without forces air
- 1.2°C/s sample was cooled in airflow 30 l/min,
- 2.4°C/s sample was cooled in airflow 125 l/min.

Fraction solid (FS) was determined by calculating the cumulative surface area between the first derivative of the cooling curve and the so-called base line (BL) [19, 20]. The BL represents the hypothetical first derivative of the cooling curve that does not exhibit phase transformation/metallurgical reactions during the solidification process. The area between the two derivative curves (calculated between the liquidus and solidus temperatures) is proportional to the latent heat of solidification of the given alloy. Therefore, the latent heat directly delivered to the test sample affected the fraction liquid evolution. Similar calculations were performed for the fraction solid except that fraction solid was proportional to the latent heat released during the solidification [14, 15].

The magnesium nucleation temperature T_N, T_{Dmin}, T_{DKP}, T_G, $T_{(Mg+Si+Al+Mn)}$, $T_{E(Mg+Al)N}$, $T_{E(Mg+Al)min}$, $T_{E(Mg+Al)G}$ and solidus temperatures T_{sol}, where calculated using the first derivative of the cooling curve [30].

The α-Mg Dendrite Nucleation Temperature, ($T^{\alpha DEN}{}_{NUC}$) represents the point at which primary stable dendrites start to solidify from the melt. This event is manifested by the change in the slope of the cooling curve and determined by the first derivative inflection point. The liquidus temperature signifies the beginning of the fraction solid that, at this point, is equal to zero.

The α-Mg Dendrite Minimum (Undercooling) Temperature, ($T^{\alpha DEN}{}_{MIN}$) represents a state where the nucleated dendrites have grown to such an extent that the liberated latent heat of fusion balances the heat extracted from the test sample. After passing this point, the melt

temperature increases to a steady state growth temperature ($T^{\alpha DEN}{}_{G}$). $T^{\alpha DEN}{}_{NUC}$ as the local minimum is determined by the point at which the first derivative intersects the zero line (dT/dt=0). The time period required for heating up of the test sample to the $T^{\alpha DEN}{}_{G}$ is called recalescence [30].

At the start of solidification of a melt, small equiaxed crystals are developing, separate from one another. The viscosity of the melt and hence torque is very small. As the dendrites grow in size and start to impinge upon one another, a continuous solid network builds up throughout the sample volume. There is a sudden increase in the torque force needed to shear the solid network. This point is called "coherency point".

The α-Mg Dendrite Growth Temperature, ($T^{\alpha DEN}{}_{G}$) represents the local maximum temperature of this reaction (and is also called the "steady state growth temperature). The $T^{\alpha DEN}{}_{G}$ corresponds to the second zero point on the first derivative curve (dT/dt=0) following the start of nucleation (dT/dt = 0). If the first derivative curve in this region does not intersect the zero line, $T^{\alpha DEN}{}_{MIN}$ the $T^{\alpha DEN}{}_{G}$ temperatures are identical and correspond to the maximum point on the first derivative curve (Figs. 4-6 and Table 3) [14, 15, 30].

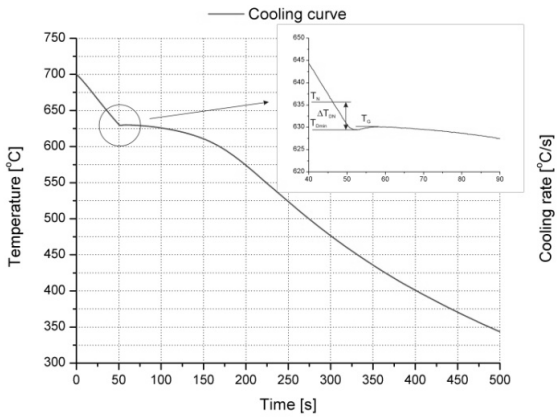

Figure 4. *Cooling curve of MC MgAl3Zn1 alloy obtained under non-equilibrium experimental condition: ΔT_{DN} nucleation undercooling*

The shape of the cooling curve is the result of the heat lost to the surroundings by the cooling metal and the heat evolved in the melt during phase transformation. At the beginning of solidification of any phase, the derivative increases in value, and decreases at the end of solidification [21-24].

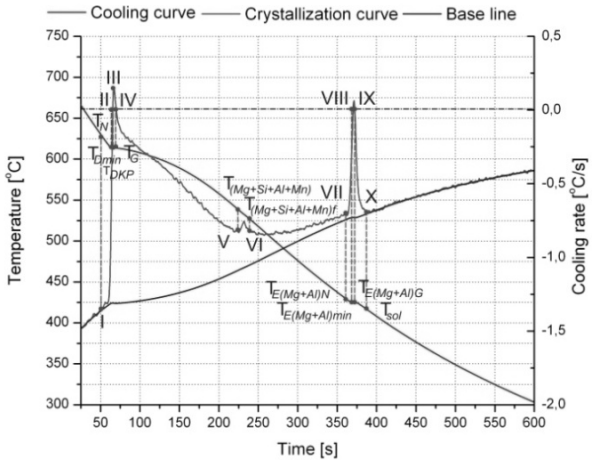

Figure 5. *Representative cooling, crystallization and calorimetric curves with characteristics points of crystallization process of MC MgAl6Zn1 alloy cooled at 0.6 ℃/s*

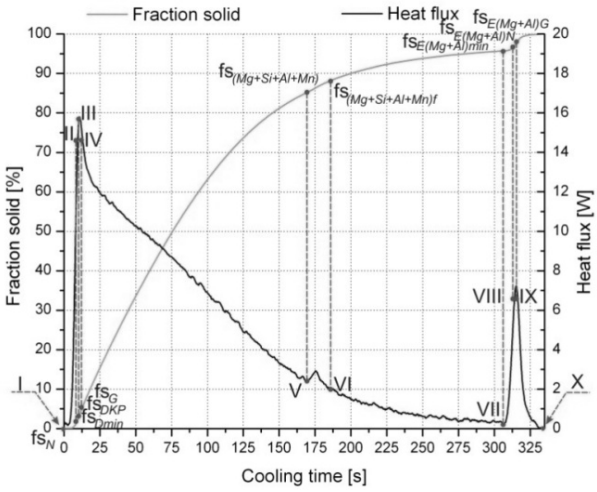

Figure 6. *Representative curves illustrate changes of heat flux and fraction solid of MC MgAl6Zn1 alloy cooled at 0.6 ℃/s*

Based on characteristics points from the thermal analysis, heat of phase transition individual phases was calculated. Temperatures and times of thermal processes were calculated as well. Heat capacity of the alloy was determined using the following formula [16, 17]:

$$c_p(t) = c_{psol} \cdot \int_{t_N}^{t} f_s(t)dt + c_{psol} \cdot (1 - \int_{t_N}^{t} f_s(t)dt) \quad (2)$$

where: fs – participation of fraction solid, considering that for fs ($t \leq t_N$)= 0 and fs($t \geq t_N$)= 1. Thermal-Calc Software was used to determine a specific heat capacity in liquid and solid state. Total heat of crystallization process of analyzed alloys was calculated based on:

$$Q = c_p \cdot m \cdot \int_{t_N}^{t_{sol}} \left[\frac{dT}{dt} - \left(\frac{dT}{dt} \right)_c \right] \quad (3)$$

Table 3. *Characteristic points obtained from thermal-derivative analysis*

Point	Temperature	Time	Description
I	T_N	t_N	Nucleation of α-phase (liquidus temperature)
II	T_{Dmin}	t_{Dmin}	The α-Mg dendrite minimum (undercooling) temperature
III	T_{DKP}	t_{DKP}	Coherency point
IV	T_G	t_G	The α-Mg dendrite growth temperature
V	$T_{(Mg+Si+Al+Mn)}$	$t_{(Mg+Si+Al+Mn)}$	Crystallization of α-Mg, Mg_2Si and phases contains Al and Mn
VI	$T_{(Mg+Si+Al+Mn)f}$	$t_{(Mg+Si+Al+Mn)f}$	End of crystallization of Mg_2Si and phases contains Al and Mn
VII	$T_{E(Mg+Al)N}$	$t_{E(Mg+Al)N}$	Beginning of nucleation of α(Mg)-γ ($Mg_{17}Al_{12}$) eutectic
VIII	$T_{E(Mg+Al)min}$	$t_{E(Mg+Al)min}$	The α(Mg)- γ ($Mg_{17}Al_{12}$) minimum (undercooling) temperature
IX	$T_{E(Mg+Al)G}$	$t_{E(Mg+Al)G}$	The α(Mg)- γ ($Mg_{17}Al_{12}$) eutectic growth temperature
X	T_{sol}	t_{sol}	End of solidification (solidus temperature)

2.4. Microstructure examinations

Metallographic samples were taken from a location close to the thermocouple tip. Samples were cold mounted and grounded on 240, 320, 400, 600 and 1200 grit SiC paper and then polished with 6 μm, 3 μm and 1 μm diamond paste. The polished surfaces were etched with a solution of 2 g oxalic acid, 100 ml water, with fresh alcohol blotted repeatedly onto the surface to prevent residue deposits. The observations of the investigated cast materials have been made on the light microscope LEICA MEF4A as well as on the electron scanning microscope Opton DSM-940.

The X-ray qualitative and quantitative microanalysis and the analysis of a surface distribution of cast elements in the examined magnesium cast alloys have been made on the Opton DSM-940

scanning microscope with the Oxford EDS LINK ISIS dispersive radiation spectrometer at the accelerating voltage of 15 kV. Phase composition and crystallographic structure were determined by the X-ray diffraction method using the XPert device with a copper lamp, with 40 kV voltage. The measurement was performed by angle range of 2θ: 30º - 120º.

Observations of thin foil structure were carried out in the JEM 3010UHR JEOL transmission electron microscope using an accelerating voltage of 300 kV.

2.5. Mechanical properties

Samples for compression testing were machined from a centre of the thermal analyses specimen ingots. The machined samples were polished with fine sandpaper to remove any machining marks from the surface. Compression tests were conducted at room temperature using a Zwick universal testing machine. Prior to testing, an extensometer was used to minimize frame bending strains. Compression specimens were tested corresponding to each of the three cooling rates.

Rockwell F–scale hardness tests were conducted at room temperature using a Zwick HR hardness testing machine.

2.6. Data collection and database construction

The performance of an ANN model depends upon the dataset used for its training. Therefore, for a reliable neural network model a significant amount of data as well as powerful computing resources are necessary [33-37].

Amounts of data on mechanical properties of magnesium alloys at different conditions are currently available in the literature [31, 32].

However, these data are rather disordered and confusing for the use of engineering practice. Moreover, in Mg-system, the experimental data in the literature are very sparse compared to Al-alloys and steels.

The gathered set of data designed for formation of a numerical model determining: UCS, HRF and GS in relation to the chemical composition and cooling rate were divided into two subsets: the learning set and the validation set. The data were divided in a proportion of 75% for the learning set and 25% for the validation set. For data analysis four neural networks models were used:

- multilayer perceptron MLP,

- linear neural networks,
- radial basis functions neural network RBF,
- generalized regression neural networks GRNN,

also the following learning methods:

- back propagation method,
- conjugate gradient,
- quasi-Newtona method,
- fast propagation.

3. Results and discussion

3.1. Thermal analysis

Representative thermal analysis of the magnesium alloys have been presented in Figure 4. Three visible temperature arrests were noted on the cooling curves. More detailed information pertaining to the alloy's thermal characteristics such as non-equilibrium liquidus, nucleation of the α(Mg)-γ($Mg_{17}Al_{12}$) eutectic, etc. were determined using the first derivative curves.

An example of the cooling and crystallization curve of the Mg-Al-Zn alloy cooled with different cooling rates are presented in Figures 7 and 8.

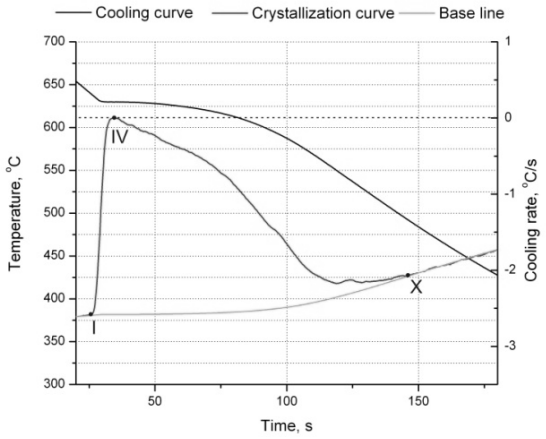

Figure 7. *Representative cooling and crystallization curves of MC MgAl3Zn1 magnesium alloys cooled at 1.2 ℃/s*

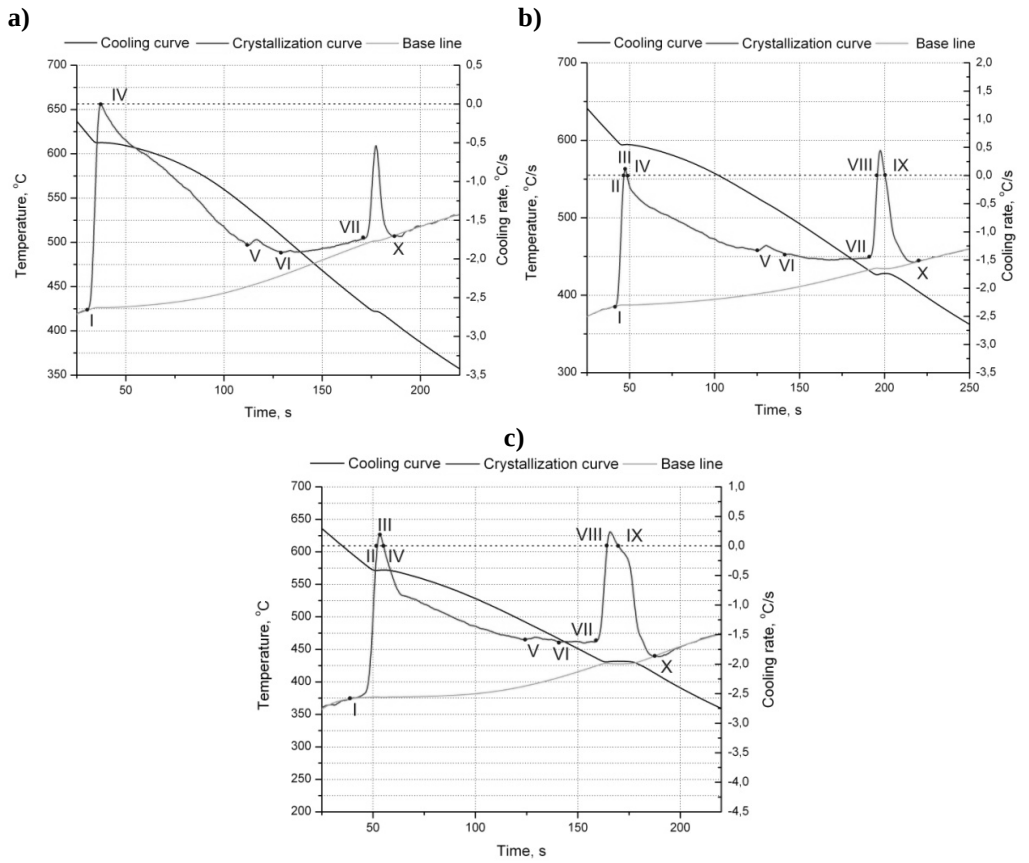

Figure 8. *Representative cooling and crystallization curves of magnesium alloys cooled at 1.2 ℃/s, a) MC MgAl6Zn1, b) MC MgAl9Zn1, c) MC MgAl12Zn1*

The performed crystallization process analysis on the basis of the achieved curves allows it to state, that the nucleation process of the α phase begins at the T_{DN} temperature. This effect is present on the curve in form of an inflexion in point I, as well in form of an instantaneous decrease of the cooling rate. Decrease of the crystallisation rate of the remaining liquid metal is caused by the heat provided from the α phase nuclei, which is smaller compared to the heat amount submit into the surrounding by the solidified metal. This process ends in point II, where the crystallization temperature achieves the minimal value - T_{Dmin}, where the α phase crystals begins to growth. In this point the derivative value achieves the zero value. The cooled alloy, resulting in crystallisation heat emission, reheats the remaining liquid until the T_{DKP} (point III) temperature. The further crystal growth causes an increase of the temperature of the remaining liquid to the maximal crystallisation temperature of the α phase – T_G (point IV).

Further alloy cooling causes the beginning of crystallisation of the silicon, aluminium and manganese- rich phases, which are emitting an additive heat amount present on the crystallisation curve in form of clear heat effect – described as $T_{(Mg+Si+Al+Mn)}$ and $T_{(Mg+Si+Al+Mn)f}$ (points V and VI). As a result of further alloy cooling after reaching the $T_{E(Mg+Al)N}$ temperature there occurs the nucleation of the α+γ eutectic (point VII). The cooled alloy reach the $T_{E(Mg+Al)min}$ (point VIII) temperature, as next the temperature increases until the maximum crystallisation temperature of the eutectic $T_{E(Mg+Al)G}$ (point IX). The alloy crystallisation ends in point X, where the T_{sol} value is reached. The temperatures of the metallurgical reactions are presented in Tables 4-7.

Table 4. *Non-equilibrium characteristics of the MC MgAl3Zn1 alloy*

Point	Cooling rate, °C/s		
	0.6	1.2	2.4
	Temperature, °C	Temperature, °C	Temperature, °C
I	633.16	635.39	640.32
II	630.44	Not observed	Not observed
III	630.64	Not observed	Not observed
IV	630.85	630.42	629.71
V	Not observed	Not observed	Not observed
VI	Not observed	Not observed	Not observed
VII	Not observed	Not observed	Not observed
VIII	Not observed	Not observed	Not observed
IX	Not observed	Not observed	Not observed
X	508.96	502.03	492.28

Table 5. *Non-equilibrium characteristics of the MC MgAl6Zn1 alloy*

Point	Cooling rate, °C/s		
	0.6	1.2	2.4
	Temperature, °C	Temperature, °C	Temperature, °C
I	615.88	615.74	619.77
II	611.51	Not observed	Not observed
III	611.75	Not observed	Not observed
IV	611.92	610.33	608.14
V	533.65	532.77	536.37
VI	520.18	509.72	511.99
VII	429.45	431.69	432.99
VIII	426.59	Not observed	Not observed
IX	427.17	Not observed	Not observed
X	419.47	415.44	401.66

Table 6. *Non-equilibrium characteristics of the MC MgAl9Zn1 alloy*

Point	Cooling rate, °C/s		
	0.6	1.2	2.4
	Temperature, °C	Temperature, °C	Temperature, °C
I	597.97	600.74	600.89
II	592.29	593.02	Not observed
III	592.65	593.27	Not observed
IV	592.91	592.79	592.01
V	515.8	524.28	524.43
VI	503.07	504.96	502.88
VII	428.78	429.5	433.71
VIII	425.76	424.76	Not observed
IX	427.25	425.83	Not observed
X	413.01	412.19	404.11

Table 7. *Non-equilibrium characteristics of the MC MgAl12Zn1 alloy*

Point	Cooling rate, °C/s		
	0.6	1.2	2.4
	Temperature, °C	Temperature, °C	Temperature, °C
I	580.76	583.51	586.2
II	572.92	572.09	Not observed
III	573.22	572.49	Not observed
IV	576.03	572.87	575.09
V	491.36	492.58	497.22
VI	481.74	476.63	476.44
VII	433.03	435.69	438.75
VIII	430.58	430.15	Not observed
IX	432.57	431.92	Not observed
X	420.86	416.11	417.04

In Figures 9 and 10 there are presented the solid state fraction change as well the heat flux generated by the crystallised phases. This information is used for determination of the crystallising heat emitted by the particular phases (Tables 8-11). In Figure 11 is presented the influence of the cooling rate as well the magnesium content on the temperature - T_{DN} of the α

phase nucleation. On the basis of the performed investigation it was found that the biggest influence on the nucleation temperature has the aluminium content (it decreases the nucleation temperature of the α phase according to the liquidus line) as well the cooling rate (it causes an increase of the α phase nucleation temperature). For example for the MC MgAl3Zn1 alloy an increase of the cooling rate from 0.6 to 1.2°C/s causes an increase of the α phase nucleation temperature from 633.16 to 635.39°C, further increase of the cooling rate until 2.4°C/s causes a temperature growth until 640.32°C.

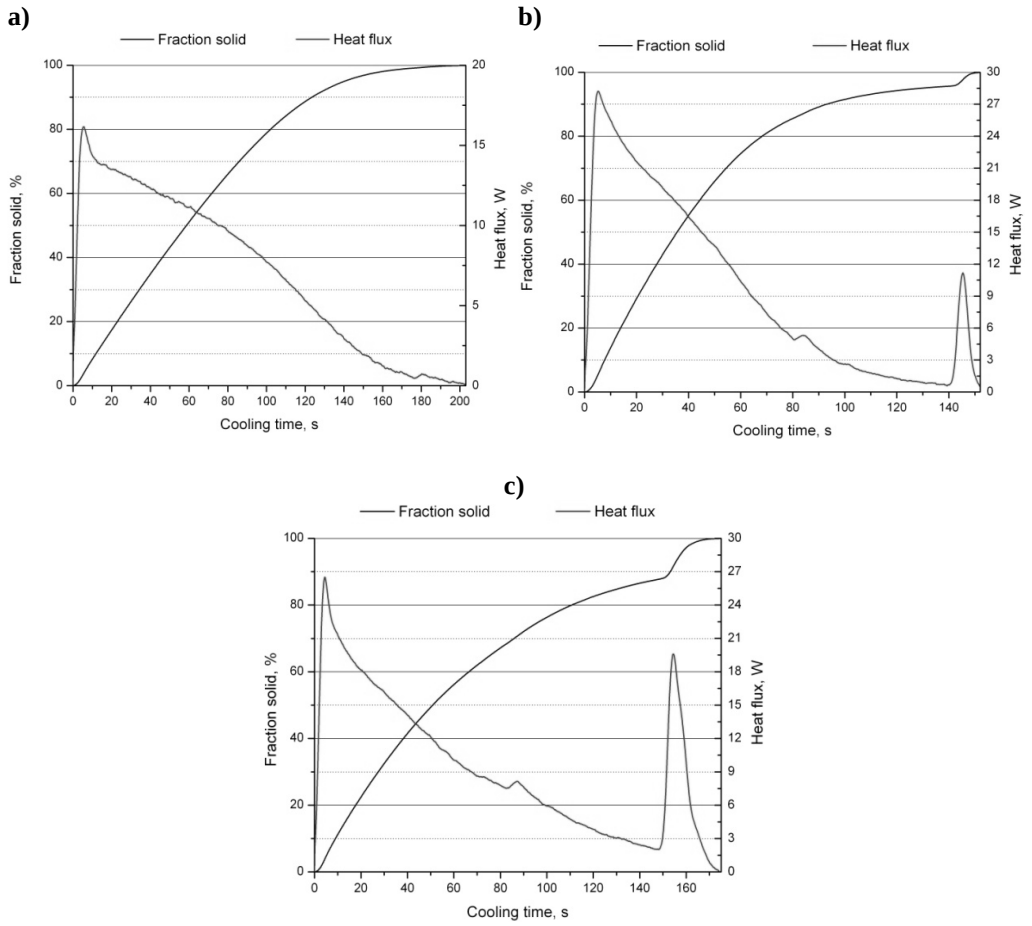

Figure 9. *Representative curves illustrate changes of heat flux and fraction solid of magnesium alloys cooled at 1.2 ℃/s, a) MC MgAl3Zn1, b) MC MgAl6Zn1, c) MC MgAl9Zn1*

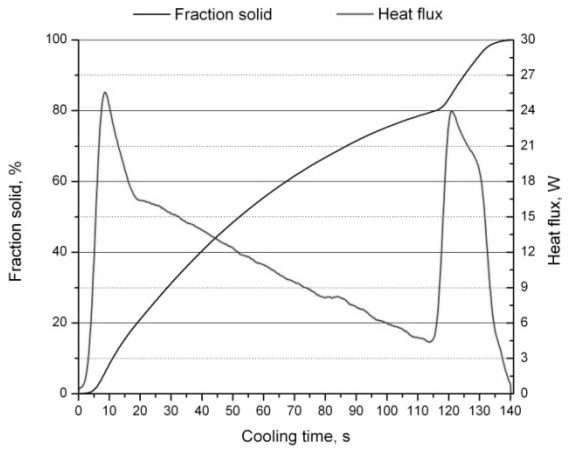

Figure 10. *Representative curves illustrate changes of heat flux and fraction solid of MC MgAl12Zn1 magnesium alloys cooled at 1.2℃/s*

Table 8. *Latent heat of crystallization process emitted during solidification of MC MgAl3Zn1*

	Cooling rate, °C/s		
Reaction	0.6	1.2	2.4
L→ α(Mg)	1400.96	1422.31	1392.02
L→ α(Mg)+ +Mg_2Si+(Al+Mn)	Not observed		
L→ α(Mg)+γ($Mg_{17}Al_{12}$)			
sum	1400.96	1422.31	1392.02

Table 9. *Latent heat of crystallization process emitted during solidification of MC MgAl6Zn1*

	Cooling rate, °C/s		
Reaction	0.6	1.2	2.4
L→ α(Mg)	1258.22	1255.55	1390
L→ α(Mg)+Mg_2Si+(Al+Mn)	143.63	131.32	161.17
L→ α(Mg)+γ($Mg_{17}Al_{12}$)	55.98	56.86	107.71
sum	1457.84	1443.74	1658.88

Table 10. *Latent heat of crystallization process emitted during solidification of MC MgAl9Zn1*

	Cooling rate, °C/s		
Reaction	0.6	1.2	2.4
L→ α(Mg)	1180.37	1153.43	1213.15
L→ α(Mg)+ +Mg_2Si+(Al+Mn)	273.84	302.22	289.91
L→ α(Mg)+γ($Mg_{17}Al_{12}$)	172.39	183.41	195.91
sum	1626.6	1639.09	1698.98

Table 11. *Latent heat of crystallization process emitted during solidification of MC MgAl12Zn1*

	Cooling rate, °C/s		
Reaction	0.6	1.2	2.4
L→ α(Mg)	985.47	1113.78	1029.97
L→ α(Mg)+Mg_2Si+(Al+Mn)	200.47	221.56	216.07
L→ α(Mg)+γ($Mg_{17}Al_{12}$)	246.05	349.35	270.17
sum	1432	1684.7	1516.21

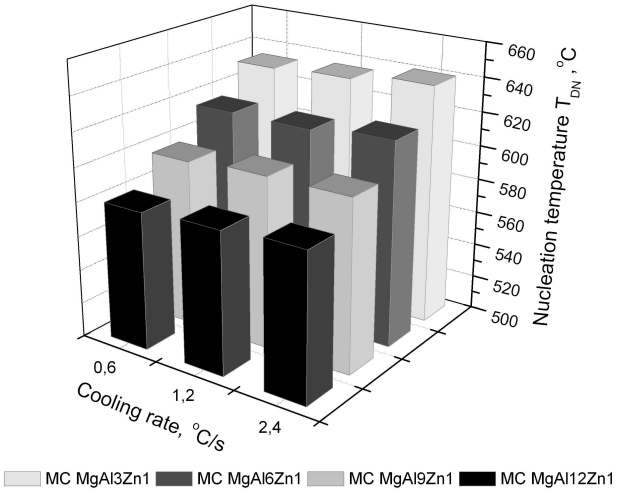

Figure 11. *Influence of cooling rate and aluminium concentration on nucleation temperature*

In Figure 12 there is presented the influence of the magnesium mass concentration as well the cooling rate on the maximal crystallization temperature (T_G) of the α phase. On the basis of the performed investigation it was found that the change of the cooling rate does not influence the maximal crystallization temperature (T_G) of the α phase. It was also found that the T_G temperature decreases together with the increase of the aluminium content. For example for the alloys cooled with a rate of 0.6°C/s, the increase of aluminium content from 3 to 6% causes a decrease of the maximal crystallization temperature of the α phase from 630.85 to 611.92°C, and a further increase of the aluminium content of 9% causes a decrease of the temperature value to 592.91°C. The lowest values of the maximal α phase crystallization temperature - equal 576.03°C, was observed for the alloy with 12% aluminium content.

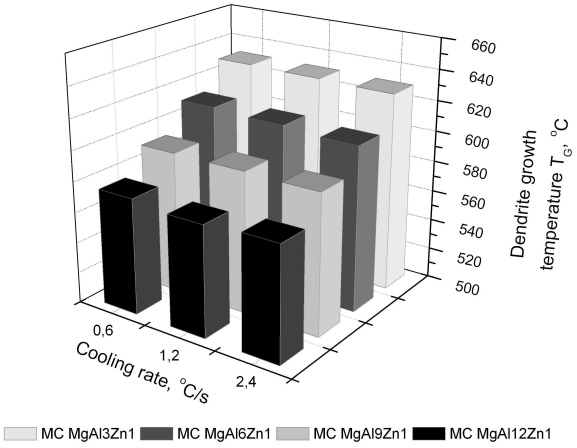

Figure 12. *Influence of cooling rate and aluminium concentration on dendrite growth temperature*

Figure 13 presents an influence of aluminium mass concentration and cooling rate on solidus temperature. On the basis of the performed investigation it was found that the biggest influence on the nucleation temperature has the aluminium content (it increases the solidus temperature) as well the cooling rate (it causes an decrease of the solidus temperature).

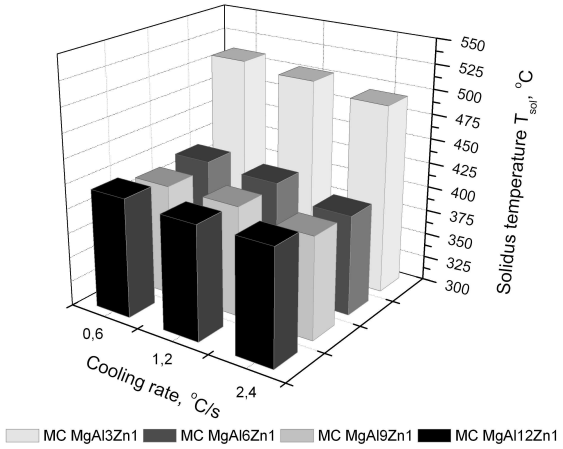

Figure 13. *Influence of cooling rate and aluminium concentration on dendrite growth temperature*

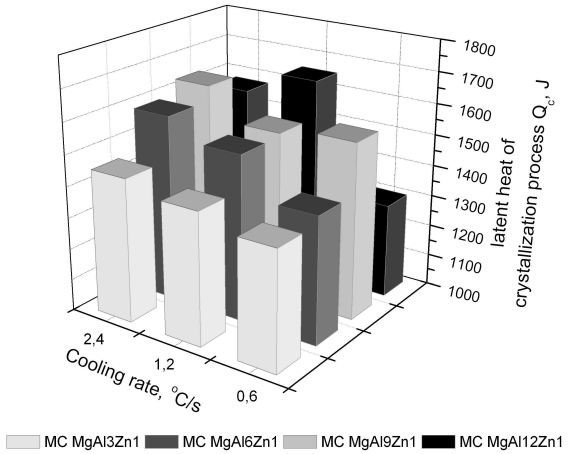

Figure 14. *Influence of cooling rate and aluminium concentration on latent heat of crystallization process*

In Figure 14 there is presented the influence of cooling rate as well the influence of aluminium mass content on the heat amount emitted during the alloy crystallisation. On the basis of the performed calculations it was found, that the biggest influence on the heat (Q_c) increase generating during alloy crystallization has the variable aluminium content. An increase of thee aluminium content in the investigated alloys causes an increase of the heat Q_c. In case of an increase of the cooling rate there was observed a small growth of the generating crystallization heat except the MC MgAl3Zn1 alloy.

3.2. Microstructure characterization

The analysis of thin foils (Figs. 15-17) after thermal analysis has validated the fact that the structure of the magnesium cast alloy consists of the solid solution α – Mg (matrix) and an intermetallic secondary phase γ – $Mg_{17}Al_{12}$ in the form of needle precipitations (Figs. 15, 17).

According to the X–ray phase analysis, the investigated magnesium alloys cooled with solidification rate: 0.6, 1.2 and 2.4. ºC/s is composed of two phases (Fig. 18): α–Mg solid solution as matrix and γ($Mg_{17}Al_{12}$). In the diffraction pattern of the matrix, the {011} Mg–diffraction line has very intensity. Based on the X–ray phase analysis was found, that change of solidification rate don't influence on the phases composition of investigated alloy. The X–ray phase analysis don't ravel occurring of Mg_2Si and phases contains Mn and Al, what suggested that the fraction volume of these phases is below 3%.

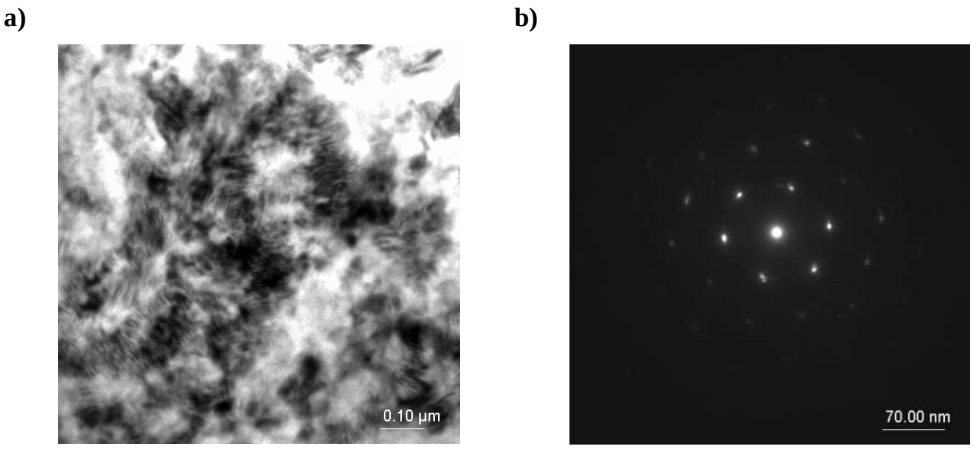

Figure 15. *TEM image of the MC MgAl6Zn1 alloy cooled at 0.6℃/s a) bright field; b) diffraction pattern of area shown in a)*

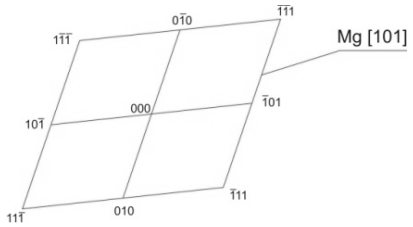

Figure 16. *Part of solution for diffraction pattern shown in Fig. 15b*

The general microstructure after thermal analysis revealed the presence of dendrite of solid solution of Al in Mg (α-phase) and divorced eutectic structure made of Al-rich Mg solid solution and $Mg_{17}Al_{12}$ (γ-phase). Moreover, angular particles of Mg_2Si and globular particles of phases contains Al and Mn mainly located at interdendritic spaces were observed (Figs. 19, 20). This observation was in agreement with thermal analysis experiments where three distinct metallurgical reactions were noted on the cooling curve, i.e., nucleation of the α(Mg), the Mg_2Si and the α(Mg)+γ($Mg_{17}Al_{12}$) eutectic.

a)

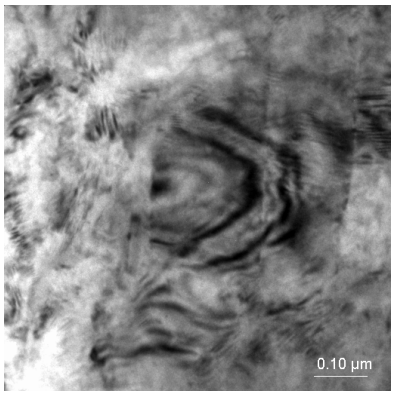

b)

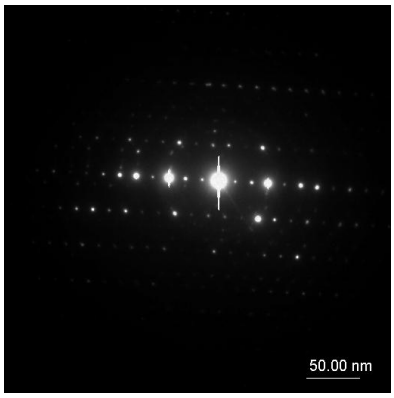

c)

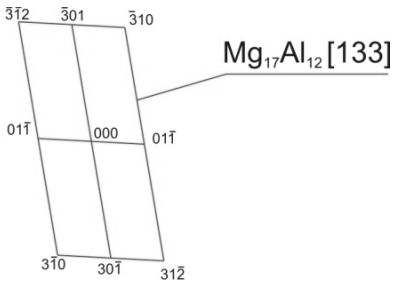

Figure 17. *TEM image of the MC MgAl9Zn1 alloy cooled at 0.6℃/s a) bright field; b) diffraction pattern of area shown in a), c) part of solution for diffraction pattern shown in b*

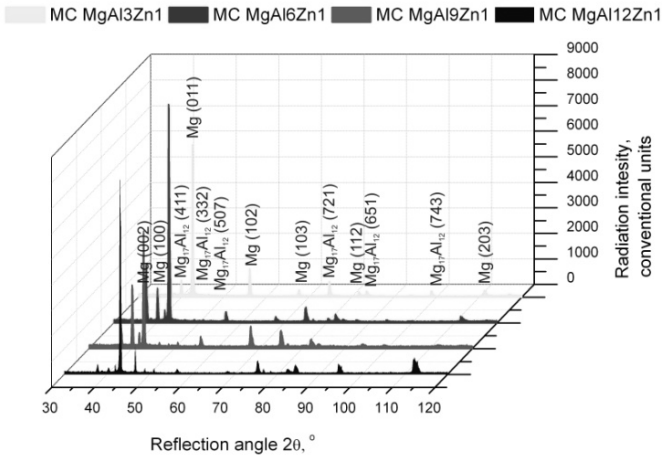

Figure 18. *XRD pattern of magnesium alloys at natural cooling*

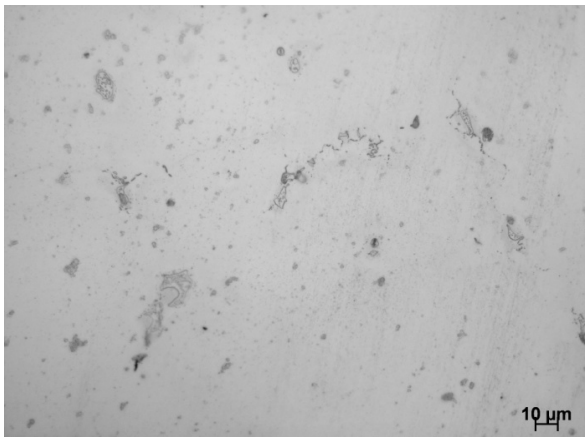

Figure 19. *Microstructure of MC MgAl3Zn1 magnesium alloy cooled at 1.2 ℃/s, mag. 500x*

The carried out investigations revealed, that the grain size decreases together with the cooling rate increase for each of the analysed alloys. On the basis of the performed investigations it was found that the largest grain size is characteristic for the MC MgAl6Zn1 alloy. A cooling rate change from 0.6 to 2.4°C/s causes a two times decrease of the grain size. A similar dependence was found also for other analysed alloys, which were studied in this investigation. An increase of the aluminium mass concentration causes a slightly decrease of the grain size (Fig. 21).

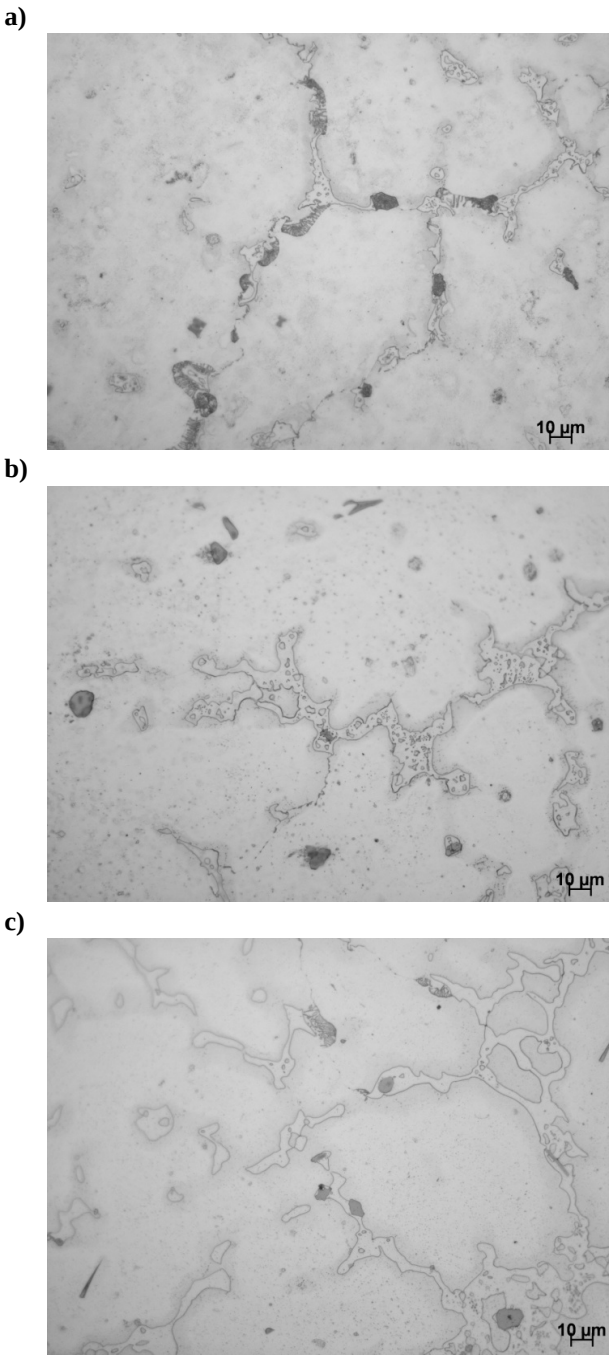

Figure 20. *Microstructure of magnesium alloys cooled at 1.2 ℃/s, a) MC MgAl6Zn1, b) MC MgAl9Zn1, c) MC MgAl12Zn1, mag. 500x*

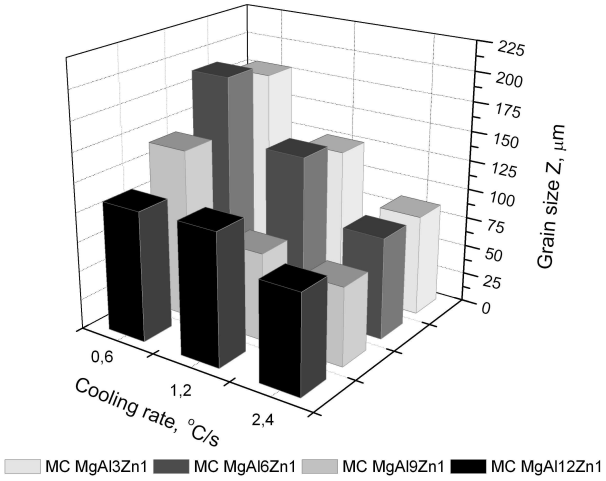

Figure 21. *Influence of cooling rate and aluminium concentration on grain size of analysed cast magnesium alloys*

Representative SEM micrographs of magnesium alloys cooled at 1.2°C/ are shown in Figures 22, 23. Results from EDS analysis are shown in Tables 12-15. EDS spectra for all samples confirms that, the matrix is α-Mg, and intermetallics phases mostly likely Mg_2Si, and Al-Mn (it could be a mixture of Al_8Mn_5 or $MnAl_4$). Because the size of particular elements of the structure is, in a prevailing measure, smaller than the diameter of the analysing beam, the obtained at the quantitative analysis chemical composition may be averaged as a result of which some values of element concentrations may be overestimated.

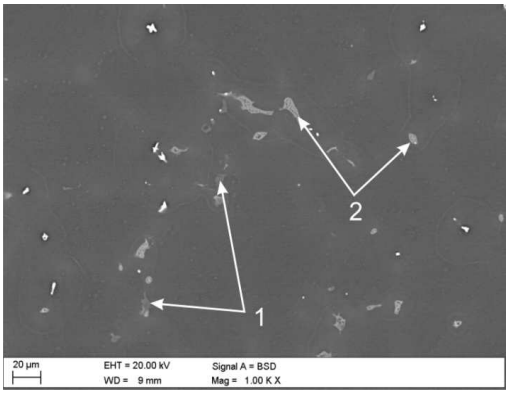

Figure 22. *Representative scanning electron microscope micrograph of MC MgAl3Zn1 magnesium alloy that solidified with cooling rate 1.2℃/s*

a)

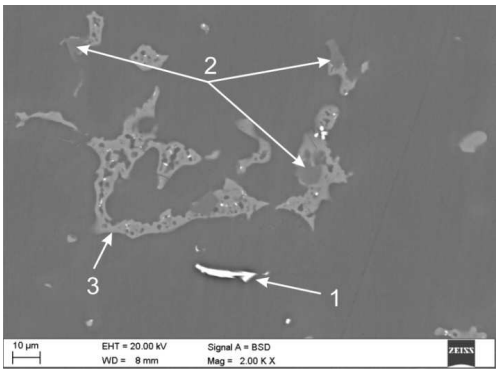

b)

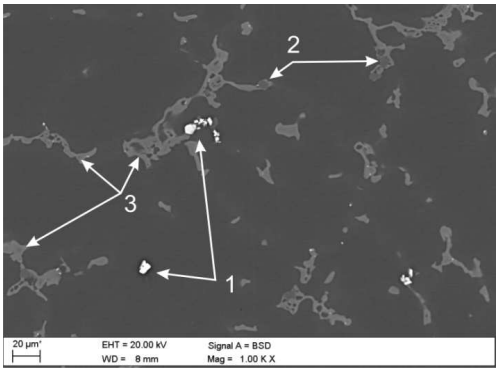

c)

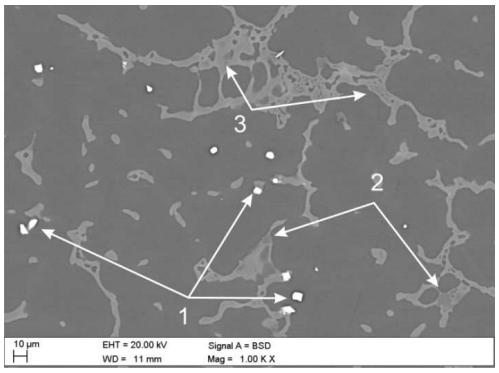

Figure 23. *Representative scanning electron microscope micrographs of magnesium alloy that solidified with cooling rate 1.2 ℃/s: a) MC MgAl6Zn1, b) MC MgAl9Zn1, c) MC MgAl12Zn1*

Table 12. *Pointwise chemical composition analysis from Fig. 22*

	Element	The mass concentration of main elements, %	
		weight %	atomic %
1	Mg	74.14	76.8
	Si	25.86	23.2
2	Zn	4.12	1.6
	Mg	78.63	82.16
	Al	17.25	16.24

Table 13. *Pointwise chemical composition analysis from Fig. 23a*

	Element	The mass concentration of main elements, %	
		weight %	atomic %
1	Mg	10.29	15.33
	Al	36.12	48.48
	Si	1.36	1.75
	Mn	52.23	34.43
2	Mg	66.6	69.73
	Si	33.4	30.27
3	Zn	6.03	2.41
	Mg	62.4	67.03
	Al	31.58	30.56

Table 14. *Pointwise chemical composition analysis from Fig. 23b*

	Element	The mass concentration of main elements, %	
		weight %	atomic %
1	Mg	12.41	17.27
	Al	45.05	56.51
	Mn	42.55	26.22
2	Zn	7.44	3.01
	Mg	66.16	72.08
	Si	26.4	24.9
3	Mg	66.42	70.15
	Al	29.81	28.37
	Zn	3.77	1.48

Table 15. *Pointwise chemical composition analysis from Fig. 23c*

	Element	The mass concentration of main elements, %	
		weight %	atomic %
1	Mg	1.57	2.38
	Al	45.17	61.82
	Mn	53.26	35.8
2	Mg	66.06	69.22
	Si	33.94	30.78
3	Zn	3.75	1.48
	Mg	61.58	65.36
	Al	34.68	33.16

Figure 24 presents a chemical analysis of the surface element decomposition.

3.3. Mechanical properties

Figure 25 shows the influence of aluminium mass concentration as well the cooling rate on hardness of the investigated alloys. On the basis of the performed investigations it was found a linear increase of the hardness compared to the increase of the aluminium content, and also an increase of the cooling rate for the MC MgAl6Zn1, MC MgAl9Zn1 and MC MgAl12Zn1 alloy. For the MC MgAl3Zn1 alloy it was found a hardness increase up to 26 HRF by a cooling rate of 1.2°C/s. A cooling rate increase up to 2.4°C/s causes a decrease of the hardness down to 19 HRF. The highest hardness value of 74 HRF was achieved for the MC MgAl12Zn1 alloy cooled with a rate of 2.4°C/s.

Figure 26 presents the influence of aluminium mass concentration as well the cooling rate on the ultimate compressive strength. On the basis of the performed investigations it was found that the highest value of the ultimate compressive strength of 296.7 MPa has the MC MgAl6Zn1 alloy, and the lowest value of 245.9 MPa the MC MgAl3Zn1 alloy (both alloys cooled with a rate of 0.6°C/s). A change of the cooling rate of the analysed alloys causes an increase of the ultimate compressive strength. The highest increase of the R_c value in comparison to the cooling rate increase was found in case of the MC MgAl3Zn1 and MC MgAl9Zn1 alloy. An increase of the cooling rate up to the maximum value causes an

increase of the ultimate compressive strength for the MCMgAl3Zn1 and MCMgAl9Zn1 alloy up to the value of 275.8 and 316 MPa adequately, as well is ca. 10-15 MPa higher in case of the MCMgAl6Zn1 and MCMgAl12Zn1 materials.

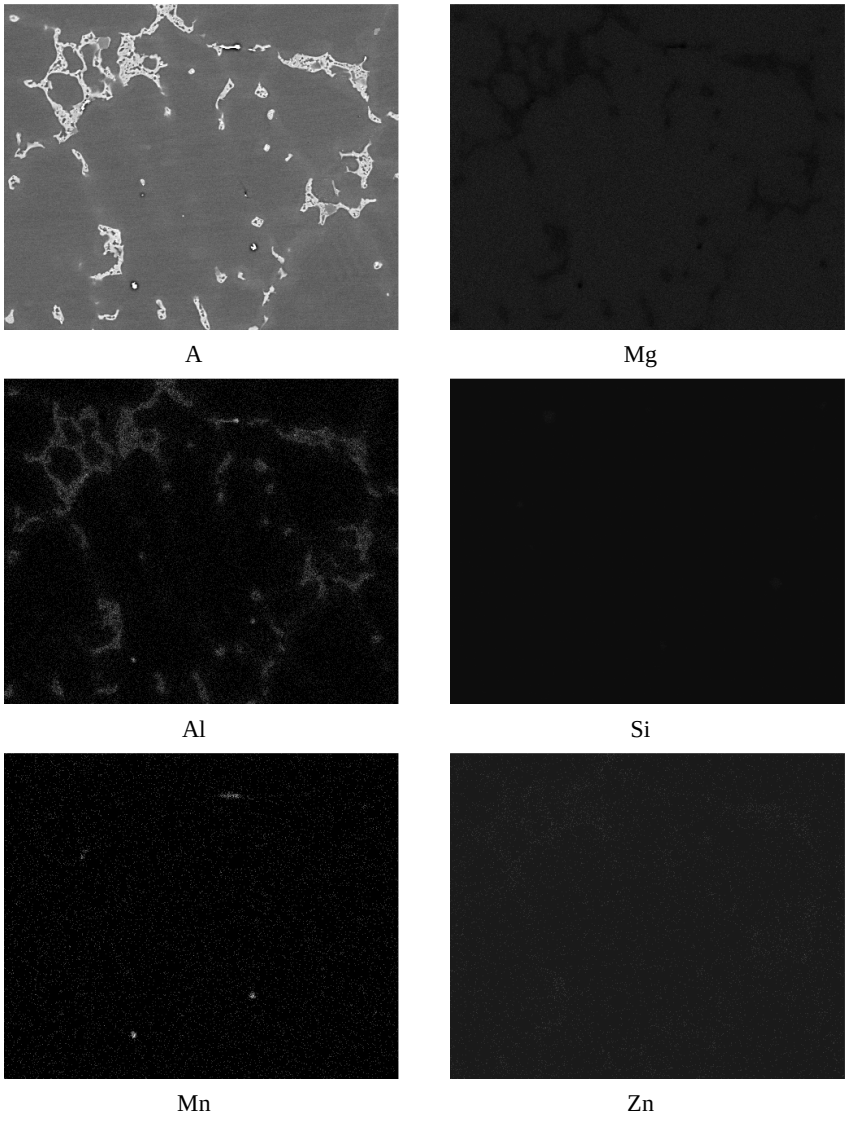

Figure 24. *The area analysis of chemical elements alloy MC MgAl6Zn1 cooled at 1.2 ℃/s cooling rate: image of secondary electrons (A) and maps of elements' distribution*

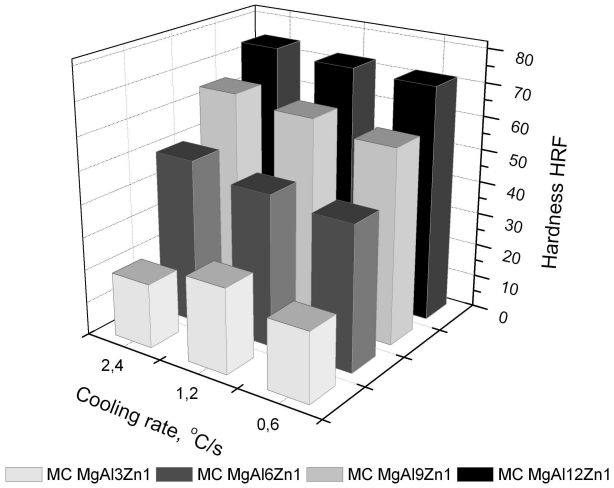

Figure 25. *Influence of cooling rate and aluminium concentration on hardness*

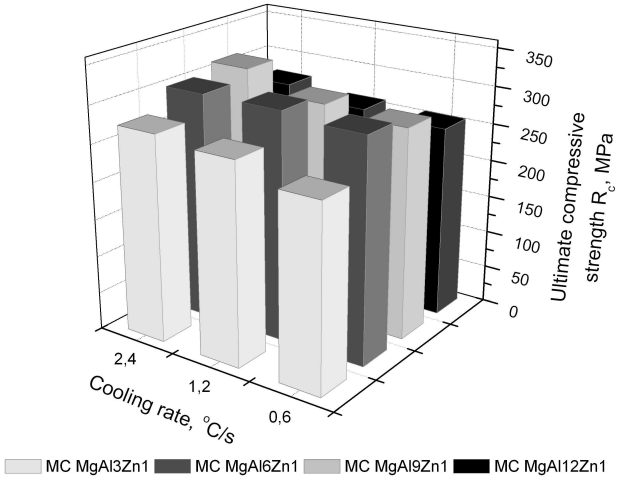

Figure 26. *Influence of cooling rate and aluminium concentration on ultimate compressive strength of cast magnesium alloys*

3.4. Database and the artificial neural network model

In this work two types of neural networks were used. First neural network were used to determine mechanical properties based on chemical composition and cooling rate. Model of

neural network was used to verify correctness of experimental mechanical properties including Rockwell hardness in F scale, ultimate compressive strength (UCS, MPa) and metallographic characterisation (grain size, μm). The feed forward neural networks have been applied for calculations – Multi Layers were applied for calculations – Multi Layerceptron (MLP). The number of nodes in input was defined as eight, which correspond to cooling rate (0.6, 1.2 and 2.4°C/s) and alloy compositions, including the commonly used alloying elements in magnesium alloys, namely Al, Zn, Mn, Si, Cu, Fe and Mg. Number of nodes in output layer was defined as three – hardness, ultimate compressive strength and grain size (Fig. 27). One-of-N conversion type was applied for nominal variable, and minimax conversion for other variables. One-of-N conversion type using neurons number answering one nominal variable is an equal number of values achieved by this variable. In order to represent selected variable, appropriate neuron is activated and the rest of them stays inactive.

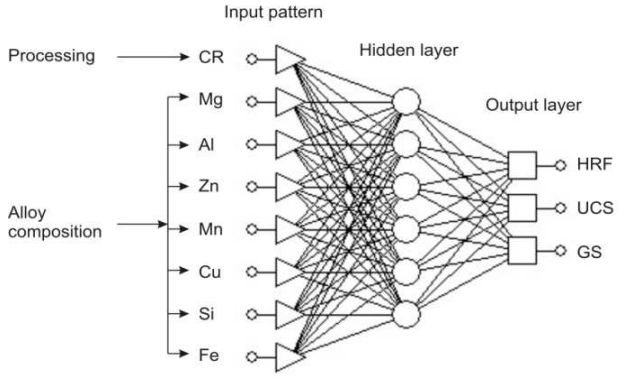

Figure 27. *Schematic diagram of the ANN model for prediction of properties of magnesium alloys*

Data set was divided into three subsets: training, validating and testing ones. The result of design and optimisation process is network, which is characterized by an error of value, standard deviation and Pearson's correlation coefficient.

The number of hidden layers, number of nodes in these layers and the number of training epochs were determined by observing the neural forecast error for the training and validating sets. Neural network training was carried with errors back propagation method and conjugate gradient algorithm.

The neural network with one hidden layer and numbers of neurons in this layer as 6 was assumed to be optimal. The highest value of Pearson's correlation coefficient and the lowest value of standard deviation were achieved for MLP neural network that was trained by error back propagation method in 50 epochs and conjugate gradient algorithm in 59 epochs.

Table 16. *Quality assessment coefficients for applied neural networks for calculate of mechanical properties for testing set*

Mechanical properties	Average of tested population	Absolute mean error	Standard error deviation	Standard deviation quotient	Pearson correlation coefficient
Hardness [HRF]	50.03	4.12	3.37	0.17	0.98
Ultimate compressive strength [MPa]	278.59	5.46	6.96	0.32	0.94
Grain size [μm]	118.36	6.43	7.59	1.85	0.91

The standard deviation ratio calculated for the training set is: 0.17 for hardness; 0.32 for ultimate compressive strength and 1.85 for grain size. Table 16 shows the values of errors, standard deviation ratios and Pearson correlation coefficients (R) for the calculated values of hardness ultimate compressive strength and grain size.

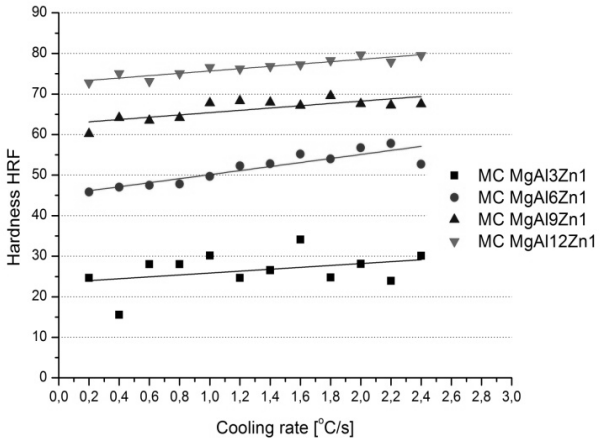

Figure 28. *Influence of cooling rate on the hardness of Mg-Al-Zn alloys*

Mechanical properties of the magnesium alloys are strongly depended on cooling rate and aluminium content (Fig. 28), the hardness grows with increment of aluminium content and slightly with increment of cooling rate. In the opposite way it is with ultimate compressive strength. UCS grows with increment of cooling rate and slightly with increment of aluminium content (Fig. 29). Measuring errors occurred during testing did not exceed 5%.

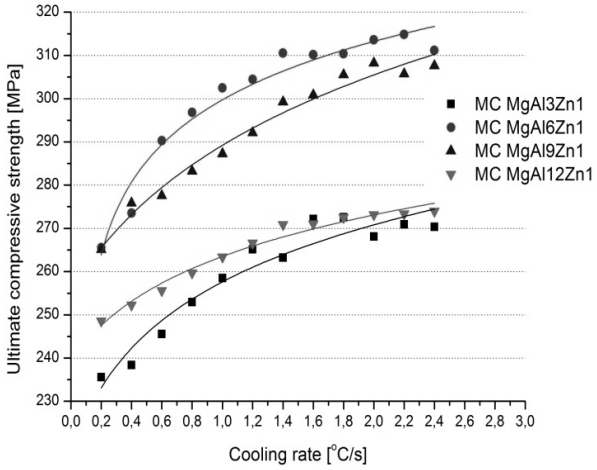

Figure 29. *The predicted influence of cooling rate on the ultimate compressive strength of Mg-Al-Zn alloys*

On the basis of the worked out models of neural networks, the diagrams of the influence of the cooling rate and aluminium content were done on the hardness, ultimate compressive strength and grain size of the analysed magnesium cast alloys (Figs. 30-32).

In second type of neural network data set was divided into three subsets: training, validating and testing ones. The data from the learning set has been used for the modification of the network weights, the data from the validating set, to evaluate the network during the learning process, while the remaining part of the values (the testing set) has been used for determining the network efficiency after ending completely the procedure of its creating.

The results used in the learning process and the network testing have been put to standardization. Scaling has been used in relation to the deviation from the minimal value, according to the mini-max function. The mini-max function transforms the variable domain to the range (0, 1). The type of the network, the number of neurons in the hidden layer (layers), the method and learning parameters have been determined observing the influence of these quantities onto the assumed network quality coefficients.

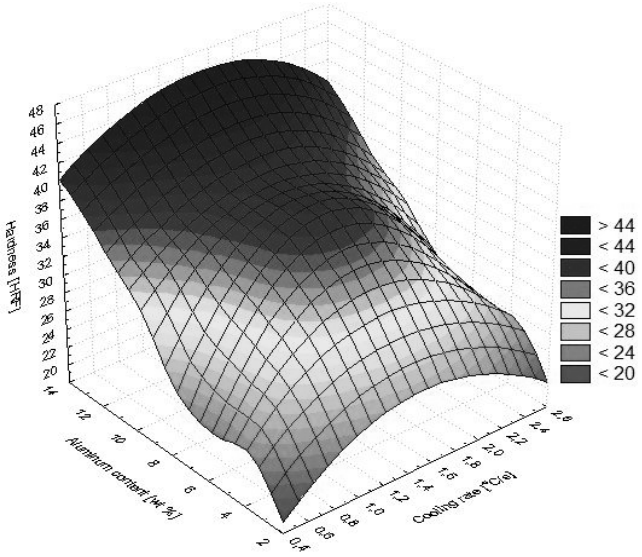

Figure 30. *Simulation of the cooling rate and aluminium content on hardness of the cast magnesium alloys*

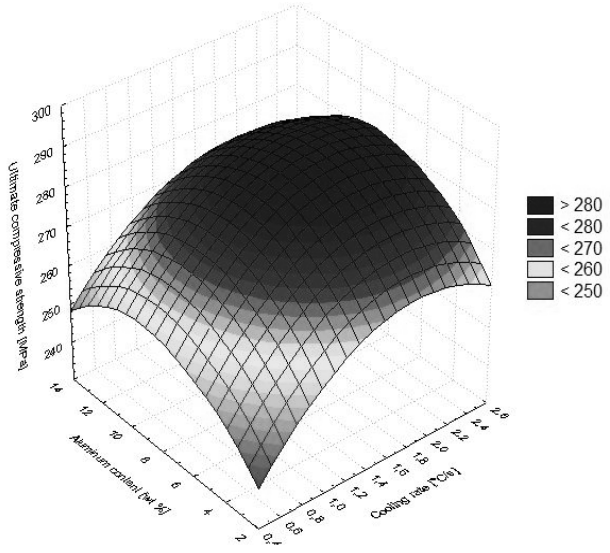

Figure 31. *Simulation of the cooling rate and aluminium content on ultimate compressive strength of the cast magnesium alloys*

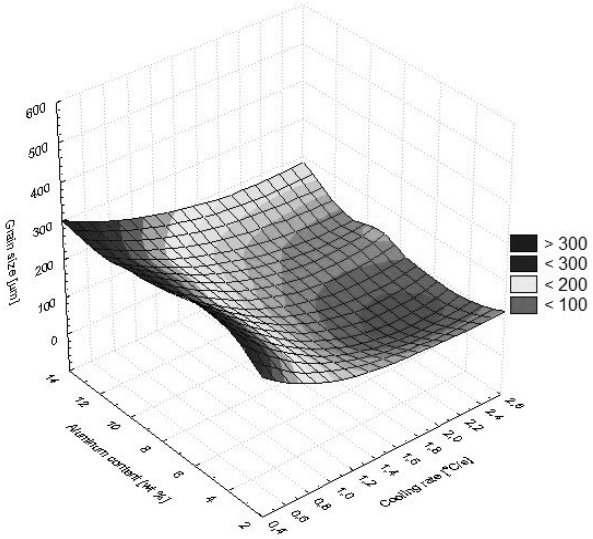

Figure 32. *Simulation of the cooling rate and aluminium content on grain size of the cast magnesium alloys*

The result of design and optimisation process is network, which is characterized by an error of value, standard deviation and Pearson's correlation coefficient. The quotient of standard deviations for errors and the data has been accepted, as the vital indicator of the model quality, made with the use of the neural network. The correctness of the network model may only be considered in case when the presented by networks forecasts are burdened with a smaller error than the simple estimation of the unknown output value.

Model of neural network was used to verify correctness of experimental crystallization temperatures including beginning of dendrite nucleation temperature T_{DN}, dendrite growth temperature T_G and solidus temperature T_{sol}. The feed forward neural networks have been applied for calculations – General Regression Neural Network (GRNN).

The number of nodes in input was defined as four, which correspond to cooling rate (0.6, 1.2 and 2.4°C/s) and alloy compositions, including the commonly used alloying elements in magnesium alloys, namely Al, Zn, Mn. Number of nodes in output layer was defined as three – dendrite nucleation temperature, dendrite growth temperature and solidus temperature (Fig. 33).

The number of hidden layers, number of nodes in these layers and the number of training epochs were determined by observing the neural forecast error for the training and validating

sets. The neural network with two hidden layers and numbers of neurons in this layers as 10 and 4 were assumed to be optimal.

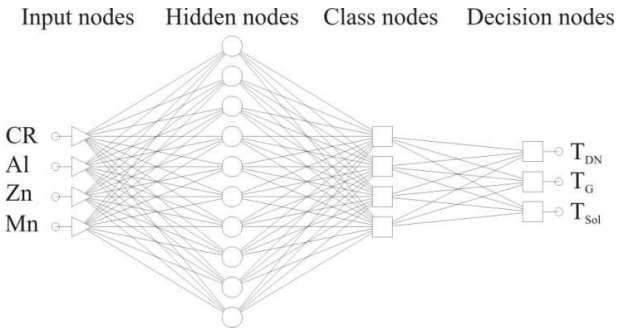

Figure 33. *Schematic diagram of the ANN model for prediction of properties of magnesium alloys*

The standard deviation ratio calculated for the training set is: 0.16 for T_{DN}; 0.3 for T_G and 0.25 for T_{sol}. Table 17 shows the values of errors, standard deviation ratios and Pearson correlation coefficients (R) for the calculated values of crystallization temperatures.

Table 17. *Quality assessment coefficients for applied neural networks for calculate of chemical composition and mechanical properties for testing set*

Mechanical properties	Average of tested population	Absolute mean error	Standard error deviation	Standard deviation quotient	Pearson correlation coefficient
T_{DN} [°C]	613.01	3.52	3.97	0.16	0.98
T_G [°C]	605.77	5.29	7.69	0.3	0.97
T_{SOL} [°C]	451.38	7.86	11.34	0.25	0.98

On the basis of the worked out models of neural networks, the diagrams of the influence of the cooling rate and aluminium concentration, zinc and manganese concentration as well were done on the dendrite nucleation temperature, dendrite growth temperature and solidus temperature of the analysed magnesium cast alloys (Figs. 34-39).

The presented, on the MC MgAl12Zn1, MC MgAl9Zn, MC MgAl6Zn, MC MgAl3Zn alloy example results, confirm the correlation between the results of the laboratory research of Mg alloys with the results obtained out of the neural networks.

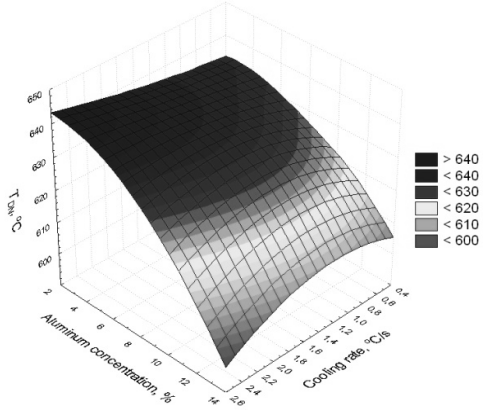

Figure 34. *Simulation of the cooling rate and aluminium concentration on beginnings of dendrite nucleation temperature*

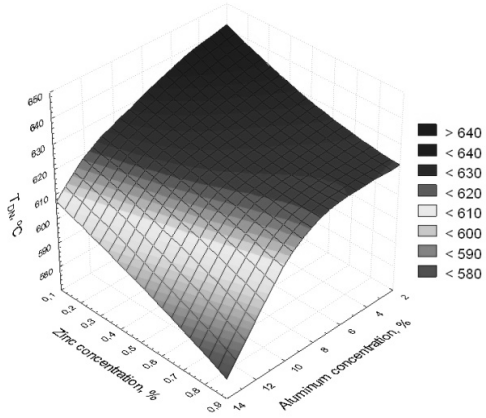

Figure 35. *Simulation of the aluminium and zinc concentration on beginnings of dendrite nucleation temperature*

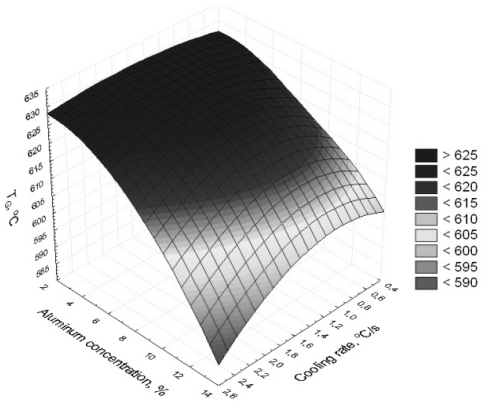

Figure 36. *Simulation of the cooling rate and aluminium concentration on dendrite growth temperature*

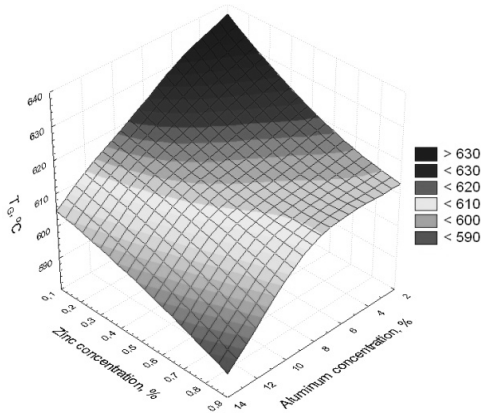

Figure 37. *Simulation of the aluminium and zinc concentration on dendrite growth temperature*

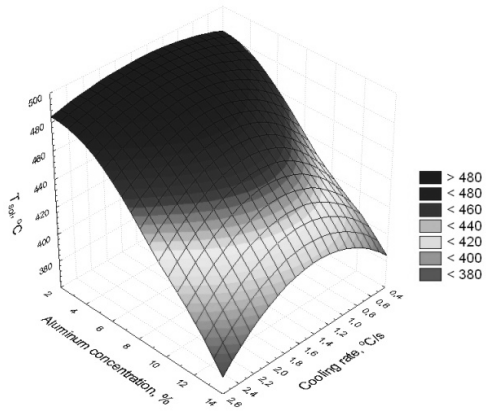

Figure 38. *Simulation of the cooling rate and aluminium concentration on solidus temperature*

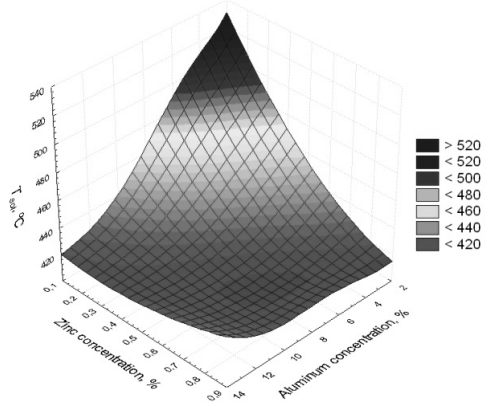

Figure 39. *Simulation of the aluminium and zinc concentration on solidus temperature*

4. Conclusions

The new developed experimental cast magnesium alloys MC MgAl3Zn1, MC MgAl6Zn1, MC MgAl9Zn1, MC MgAl3Zn1 are characterising an α solid solution microstructure, which is the matrix, intermetallic γ – $Mg_{17}Al_{12}$ phase in a shape of plates, placed manly at grain border regions, needle shaped eutectic (α+γ) as well Mg_2Si containing precipitations characterized by edged outlines, also steroidal or needle shaped phases with high Mn and Al concentration are present (can be Al_8Mn_5 or $MnAl_4$). This research shows that the thermal analysis carried out on UMSA Technology Platform is an efficient tool for collecting and calculations of data about temperature and time of liquidus and solidus temperatures as well. Derivative thermo-analysis performed allowed to achieve several representative cooling, crystallization and calorimetric curves with characteristics points of crystallisation process for magnesium alloys. Description of characteristics points obtained from thermal-derivative analysis made it possible to get better understanding of the thermal processes occurred during crystallization kinetics of the investigated Mg alloys.

Solidification parameters are affected by the cooling rate. The formation temperatures of various thermal parameters are shifting with an increasing cooling rate. Increasing the cooling rate increases significantly the Mg nucleate temperature and decreases the solidus temperature

simultaneously widens a solidification range. As expected, the results show that grain size reduces as the cooling rate increases. Increasing the cooling rate increases hardness and compressive ultimate strength of the examined magnesium alloys.

The artificial neural network model (ANN model) for predicting crystallization temperatures of crystallisable magnesium alloy was improved by refining pre-processing variables and using a more reasonable structure of hidden layers. The results show that the improved model could apparently decrease the prediction errors, and raise the accuracy of the prediction results. The improved ANN model was used to predict the crystallization temperatures of Mg-Al-Zn alloys. The predicted results were found to be in good agreement with the experimental data.

Acknowledgements

The paper has been realised in relation to the project POKL.04.01.01-00-003/09-00 entitled "Opening and development of engineering and PhD studies in the field of nanotechnology and materials science" INFONANO, co-founded by the European Union from financial resources of European Social Fund and headed by Prof. L.A. Dobrzański.

References

1. P.J. Haines, Principles of thermal analysis and calorimetry, The Royal Society of Chemistry, Cambridge, UK, 2002.
2. M.E. Brown, Introduction to thermal analysis. Techniques and application, Kluwer Academic Publisher, Netherlands, 2001.
3. R.F. Speyer, Thermal analysis of materials, Marcel Dekker, 1994.
4. P. Gabbott, Principles and applications of thermal analysis, Blackwell Publishing, UK, 2008.
5. G.W.H. Hohne, W.F. Hemminger, H.J. Flammersheim, Differential Scanning Calorimetry, Springer-Verlag Berlin Heidelberg, 2003.

6. P. Bassani, E. Gariboldi, A. Tuissi, Calorimetric analysis of AM60 magnesium alloy, Journal of Thermal Analysis and Calorimetry 80 (2005) 739-747.
7. A. Saccone, D. Macciò, S. Delfino, F. H. Hayes, R. Ferro, Mg-Ce alloys, Experimental investigation by Smith thermal analysis, Journal of Thermal Analysis and Calorimetry 66 (2001) 47-57.
8. B. Bronfin, N. Moscovitch, New magnesium alloys for transmission parts, Metal Science and Heat Treatment 48/11-12 (2006) 479-486.
9. D. Eliezer, E. Aghion, F.H. Froes, Magnesium science and technology, Advanced Materials Performance 5 (1998) 201-212.
10. ASM Specialty Handbook-Magnesium and Magnesium Alloys, ed. M.M. Avedesian, H. Baker, ASM International, USA, 1999, 3-84.
11. L.A. Dobrzański, T. Tański, L. Čížek, Influence of Al addition on structure of magnesium casting alloys, Journal of Achievements in Materials and Manufacturing Engineering 17 (2006) 221-224.
12. I.J. Polmear, Light Alloys, London, 1995.
13. K.U. Kainer, Magnesium – alloys and technologies, Wiley-VCH Verlag GmbH & Co. KG aA, Weinheim 2003, 33-341.
14. L. Backuerud, G. Chai, J Tamminen, Solidification characteristics of aluminum alloys Vol. 2 Foundry Alloys, AFS Skanaluminium, Stockholm, Sweden, 1990.
15. L. Backuerud, G. Chai, Solidification characteristics of aluminum alloys Vol. 3 Foundry Alloys, AFS Skanaluminium, Stockholm, Sweden, 1990.
16. L.A. Dobrzański, R. Maniara, J. Sokołowski, W. Kasprzak, Effect of cooling rate on the solidification behavior of AC AlSi7Cu2 alloy, Journal of Materials Processing Technology 191 (2007) 317-320.
17. L.A. Dobrzański, W. Borek, R. Maniara, Influence of the crystallization condition on Al–Si–Cu casting alloys structure, Journal of Achievements in Materials and Manufacturing Engineering 18 (2006) 211-214.
18. S. Jura, Z. Jura, Theory ATD method in studies of Al alloys, Solidification of Metals and Alloys 28 (1996) 57-87 (in Polish).
19. S. Jura, J. Sakwa, Application of thermal-derivative analysis to evaluate the mechanical properties of cast iron, Solidification of Metals and Alloys 5 (1982) 6-29 (in Polish).
20. M. Malekan, S.G. Shabestari, Computer-aided cooling curve thermal analysis used to predict the quality of aluminum alloys, Journal of Thermal Analysis DOI 10.1007/s10973-010-1023-2.
21. M. Kondracki, J. Gawroński, J. Szajnar, R. Grzelczak, K. Podsiadło, The study of the crystallization process MO95 brass based on ATD method, Archives of Foundry 2/4 (2002) 128-134 (in Polish).
22. J. Gawroński, Crystallization of alloys, Thermal and derivation method (ATD), Archives of Foundry 16 (2005) 256-261 (in Polish).
23. S. Jura, The essence of the ATD method. Modern methods for assessing the quality of alloys, PAN – Katowice, Institute of Foundry Silesian University, 1985 (in Polish).

24. J. Adamiec, A. Kiełbus, J. Cwajna, The procedure of quantitative description of the structure of cast magnesium alloys, Archives of Foundry 6/18 (2006) 209-214 (in Polish).
25. L.A. Dobrzański, T. Tański, Solid State Phenomena, Influence of aluminium content on behaviour of magnesium cast alloys in bentonite sand mould, Journal of Materials Processing Technology 147-149 (2009) 764-769.
26. L.A. Dobrzański, T. Tański, L. Cížek, Heat treatment impact on the structure of die-cast magnesium alloys, Journal of Achievements in Materials and Manufacturing Engineering 20 (2007) 431-434.
27. H. Baker, ASM Specialty Handbook. Magnesium and Magnesium Alloys, M.M. Avedesian (Ed.), ASM International, ISBN: 0871706571, (1999) USA.
28. http://uwindsor.ca/umsa
29. "Method and Apparatus for Universal Metallurgical Simulation and Analysis" – United States Patent, Patent No.: US 7,354,491 B2, Date of Patent: Apr. 8, 2008.
30. Universal Metallurgical Simulator and Analyzer (UMSA) Platform for the Advanced Simulation of Melting and Solidification Processes, Software Information, 2002.
31. E. Mares, J.H. Sokolowski, Artificial intelligence-based control system for the analysis of metal casting properties, Journal of Achievements in Materials and Manufacturing Engineering 40/2 (2010) 149-154.
32. L.A. Dobrzanski, T. Tanski, J. Trzaska, L. Čížek, Modelling of hardness prediction of magnesium alloys using artificial neural networks applications, Journal of Achievements in Materials and Manufacturing Engineering 26/2 (2008) 187-190.
33. L.A. Dobrzański, R. Honysz, Application of artificial neural networks in modelling of quenched and tempered structural steels mechanical properties, Journal of Achievements in Materials and Manufacturing Engineering 40/1 (2010) 50-57.
34. T. Masters, Neural networks in practice, PWN, Warsaw, 1996 (in Polish).
35. L.A. Dobrzański, S. Malara, J. Trzaska, Project of neural network for steel grade selection with the assumed CCT diagram, Journal of Achievements in Materials and Manufacturing Engineering 27/2 (2008) 155-158.
36. W. Sitek, J. Trzaska, L.A. Dobrzanski, Evaluation of chemical composition effect on materials properties using AI methods, Journal of Achievements in Materials and Manufacturing Engineering 20 (2007) 379-382.
37. J. Trzaska, L.A Dobrzański, A. Jagiełło, Computer programme for prediction steel parameters after heat treatment, Journal of Achievements in Materials and Manufacturing Engineering 24/2 (2007) 171-174.

The paper is published also in the Journal of Achievements in Materials and Manufacturing Engineering

Hot-working of advanced high-manganese austenitic steels

L.A. Dobrzański*, W. Borek
Institute of Engineering Materials and Biomaterials, Silesian University of Technology, ul. Konarskiego 18a, 44-100 Gliwice, Poland
* Corresponding author: E-mail address: leszek.dobrzanski@polsl.pl

Abstract

Purpose: *The work consisted in investigation of newly elaborated high-manganese austenitic steels with Nb and Ti microadditions in variable conditions of hot-working.*

Design/methodology/approach: *The force-energetic parameters of hot-working were determined in continuous and multi-stage compression test performed in temperature range of 850 to 1100°C using the Gleeble 3800 thermomechanical simulator. Evaluation of processes controlling work-hardening were identified by microstructure observations of the specimens compresses to the various amount of deformation (4x0.29, 4x0.23 and 4x0.19). The microstructure evolution in successive stages of deformation was determined in metallographic investigations using light, scanning and electron microscopy as well as X-ray diffraction.*

Findings: *The investigated steels are characterized by high values of flow stresses from 230 to 450 MPa. The flow stresses are much higher in comparison with austenitic Cr-Ni and Cr-Mn steels and slightly higher compared to Fe-(15-25)Mn alloys. Increase of flow stress along with decrease of compression temperature is accompanied by translation of ε_{max} strain in the direction of higher deformation. Results of the multi-stage compression proved that applying the true strain 4x0.29 gives the possibility to refine the austenite microstructure as a result of dynamic recrystallization. In case of applying the lower deformations 4x0.23 and 4x0.19, the process controlling work hardening is dynamic recovery and a deciding influence on a gradual microstructure refinement has statical recrystallization. The steel 27Mn-4Si-2Al-Nb-Ti has austenite microstructure with annealing twins and some fraction of ε martensite plates in the initial state. After the grain refinement due to recrystallization, the steel is characterized by uniform structure of γ phase without ε martensite plates.*

Research limitations/implications: *To determine in detail the microstructure evolution during industrial rolling, the hot-working schedule should take into account real number of passes and higher strain rates.*

Practical implications: *The obtained microstructure – hot-working relationships can be useful in the determination of power-force parameters of hot-rolling and to design a rolling schedule for high-manganese steel sheets with fine-grained austenitic structures.*

Originality/value: *The hot-deformation resistance and microstructure evolution in various conditions of hot-working for the new-developed high-manganese austenitic steels were investigated.*

Keywords: *High-manganese steel; Hot-working; TRIP/TWIP steels; Dynamic recrystallization; Static recrystallization; Grain refinement*

Reference to this paper should be given in the following way:

L.A. Dobrzański, W. Borek, Hot-working of advanced high-manganese austenitic steels, in L.A. Dobrzański (ed.) Effect of casting, plastic forming or surface technologies on the structure and properties of the selected engineering materials, Open Access Library, Volume 1, 2011, pp. 55-88.

1. Introduction

The beginning of XXI century has brought a development of new groups of steels to be applied for sheets in automotive industry. From the aspect of materials, this development has been accelerated by strong competition with non-metal aluminium and magnesium alloys as well as with composite polymers, which meaning is successively increasing. From the aspect of ecology, an essential factor it is to limit the amount of exhaust gas emitted into the environment. It's strictly connected to the fuel consumption, mainly dependant on car weight and its aerodynamics. Taking into consideration increased quantity of accessories used in modern cars, decreasing car's weight can be achieved solely by optimization of sections of sheets used for bearing and reinforcing elements as well as for body panelling parts of a car. Application of sheets with lower thickness preserving proper tautness requires using sheets with higher mechanical properties, however keeping adequate formability. Steels of IF and BH type with moderate mechanical properties and high susceptibility to deep drawing were elaborated for elements of body panelling [1]. The highest application possibilities belong to DP-type steels with ferritic – martensitic microstructure. Their mechanical properties can be formed in a wide range, controlling participation of martensite arranged in ferritic matrix. Sheets made of these steels are widely used for bearing and reinforcing elements [2].

In comparison to steels with ferritic microstructure they are characterized by high value of hardening exponent n, what decides about their strong strain hardening during sheet-metal forming [3].

Nowadays, apart from limiting fuel consumption, special pressure is placed on increasing safety of car's passengers. Constructional solutions and steels used in the frontal part of a vehicle are the most significant due to the possibility of accident occurrence. The goal of structural elements such as frontal frame side members, bumpers and the others is to take over the energy of an impact. Therefore, steels that are used for these parts should be characterized by high product of UTS and UEl, proving the ability of energy absorption. Among the wide variety of recently developed steels, high-manganese austenitic TRIP/TWIP steels with low stacking faulty energy (SFE) are particularly promising, especially when mechanical twinning occurs [3-6]. Beneficial combination of high strength and ductile properties of these steels depends on structural processes taking place during cold plastic deformation, which are a derivative of stacking fault energy (SFE) of austenite, dependent, in turn on the chemical composition of steel and deformation temperature [1-4, 7-10]. In case, when SFE is equal from 12 to 20 mJm^{-2}, partial transformation of austenite into martensite occurs, making use of TRIP effect (TRansformation Induced Plasticity) [1-4, 8]. Values of SFE from 20 to 60 mJm^{-2} determine intense mechanical twinning connected to TWIP effect (TWinning Induced Plasticity) [5-10]. The steels cover a very wide carbon concentration in a range from about 0.03 to 1 wt.%, 15-30% Mn, 0-4% Si, 0-8% Al.

The best conditions for obtaining the total elongation up to 80%, due to a gradual increase of mechanical twins, acting as obstacles for dislocation glide, occur when the carbon concentration is in the range of 0.4-0.8% and manganese from 17 to 22% [5, 11, 12]. However, high carbon content may lead to formation of M_3C and $M_{23}C_6$-type carbides, which precipitating on austenite grain boundaries negatively affect the strength and toughness of the steel [11]. Moreover, in the Fe-(17-22) Mn-(0.4-1) C steel grades, besides the formation of deformation twins during straining, a technologically undesirable jerky flow, which presents the features of dynamic strain aging and PLC (Portevin-LeChatelier) effect is observed [6]. Because of these reasons, Frommeyer et al. [1-4] proposed a group of high-manganese steels with carbon content, less than 0.1%. Lower hardening due to decreased carbon concentration was compensated by Si and Al additions, which together with Mn decide about SFE of the alloy and the main deformation mechanism. In a case of Mn $\geq$ 25%, the mechanical properties are mainly dependent on TWIP effect [1, 3, 13] and for Mn $\leq$ 20%, a process influencing a mechanical properties level is strain-induced martensitic transformation of austenite [2-4]. For

the latter the initial structure is consisted of γ phase as a matrix, some fraction of ε martensite and sometimes ferrite [2-4].

Results of our earlier investigations [14-17] indicate that ε martensite plates can appear in the initial structure of the (0.04-0.05) C-25Mn-4Si-2Al alloys as a result of Nb and Ti microadditions. The amount of C combined in precipitated carbonitrides reduces its content in the solid solution, thus decreasing the SFE of austenite and resulting in a presence of ε martensite despite high manganese concentration in the investigated steels. It was found [16-18] that the fraction of ε martensite plates is also dependent on a grain size of the γ phase and hot-working conditions. It was also observed that the fraction of mechanical twins within the austenite grains corresponds to the initial grain size, and at the same time affects the mechanical properties [5].

The hot-working behaviour of high-manganese steels is of primary importance for elaborating manufacturing methods consisted of hot rolling and successive cooling to room temperature. However, their hot work hardening and microstructural evolution controlled by thermally activated processes removing it, did not draw much attention compared to cold-working behaviour. Niewielski [19] compared the flow resistance of the 0.5C-17Mn-16Cr austenitic steel with conventional stainless steel of 18-8 type. He observed that the hardening intensity of Cr-Mn steel is much higher than in case of Cr-Ni steel. The difference in a course of work-hardening comes from a different ability of dislocations to splitting and association during straining.

High strain hardening rate is a result of the ability of manganese austenite for dislocation dissociation in the initial deformation stage [19, 20]. The reason for high hardening intensity of Cr-Mn steel are much higher flow stress values compared to Cr-Ni steel, however at lower deformation value of ε_{max} corresponding to maximal flow stress. For example, the yield stress of the Cr-Mn steel hot-twisted at a temperature of 1100°C with a strain rate of $1s^{-1}$ is equal to 134 MPa for the value $\varepsilon_{max} = 0.18$ and increases to 280 MPa for $\varepsilon_{max} = 0.23$ with decreasing the deformation temperature to 900°C [19]. Cabanas et al. [21] investigated the retarding effect of Mn content up to 20 wt.% on the grain boundary migration and dynamic recrystallization in binary Fe-Mn alloys. The influence of Al addition on the flow behaviour of 0.1C-25Mn-(0-8) Al alloys was the aim of investigations undertaken by Hamada et al. [22, 23]. They found that flow resistance is slightly higher for the 25Mn3Al than for the 25Mn steel. Moreover, they observed that the flow stress of the austenitic alloys containing Al up to 6% is much higher compared to the steel containing 8% Al with a duplex austenitic-ferritic structure [22].

Investigation results by Hamada et al. [22, 23], Sabet et al. [24] on 0.13C-29Mn-2.4Al steel and Kliber et al. [25] on (0.6-1)C-(17-20)Mn steels confirmed the high work hardening rate of high-manganese alloys in the deformation range lower than ε_{max}, likewise for Cr-Mn steels investigated by Niewielski [19].

For manufacturing methods elaborating, it is especially important that relatively low values of ε_{max} give the opportunities to refine austenitic structures in successive stages of hot-working. Unfortunately, the flow resistance of high-Mn steels is usually investigated under conditions of continuous compression or torsion [20-25]. To determine the softening kinetics, the double- or triple-deformation tests are rarely carried out [22, 25]. Hot-rolling of sheets consists of many passes characterized by the changing amount of deformation and strain rate from pass to pass. This means that the flow stresses should be determined during multi-stage straining testing and for various deformation values. In earlier investigations [14-16, 26, 27] we characterized the force-energetic parameters of hot-working of new-developed low-carbon high-Mn-Si-Al steels in continuous and four-stage compression tests. The aim of the paper is to describe in details the microstructure evolution and phase composition of 0.04C-27Mn-4Si-2Al-Nb-Ti steel subjected to four-stage compression with various amount of deformation.

2. Experimental procedure

Investigations were carried out on two high-manganese austenitic Mn-Si-Al steels containing Nb and Ti microadditions (Table 1). Melts were prepared in the Balzers VSG-50 vacuum induction furnace. After homogenization at 1200°C for 4 h to remove the segregation of Mn, ingots with a mass of 25 kg were submitted for open die forging on flats with a width of 220 mm and a thickness of 20 mm. Then, cylindrical machined samples ∅10x12 mm were made. In order to determine the influence of temperature on a steel grain growth, samples were solution heat-treated in water from the austenitizing temperature in a range from 900 to 1100°C (Fig. 1). Determination of processes controlling work hardening was carried out in continuous axisymetrical compression test using the DSI Gleeble 3800 thermomechanical simulator, used as laboratory equipment of the Institute for Ferrous Metallurgy in Gliwice [28, 29]. The stress – strain were defined in a temperature range from 850 to 1050°C with a strain rate of 10 s^{-1}.

In order to determine σ-ε curves, the four-stage compression tests were carried out. The temperatures of the successive deformations were 1100, 1050, 950 and 850°C. The details of

the hot-working are given in Table 2. To simulate various conditions of hot-rolling, the amount of true stain were 0.29, 0.23 and 0.19. The time of the isothermal holding of the specimens at a temperature of the last deformation was between 0 and 64 s. The specimens were inserted in a vacuum chamber, where they underwent resistance-heating. Tantalum foils were used to prevent from sticking and graphite foils used as a lubricant. The processes controlling the course of work-hardening were evaluated on a basis of the shape of σ-ε curves and structure observations of the specimens water-quenched on different stages of compression. To determine metallographically recrystallization progress at the interval between passes, a part of the specimen was water-cooled after isothermal holding of the specimens compressed at 900°C and 1000 °C with the amount of true strain of 0.29 and 0.5 and a strain rate of 10 s^{-1}.

Table 1. *Chemical composition of the investigated steels, mass fraction*

Designation	C	Mn	Si	Al	P	S	Nb	Ti	N
27Mn-4Si-2Al-Nb-Ti	0.040	27.5	4.18	1.96	0.002	0.017	0.033	0.009	0.0028
26Mn-3Si-3Al-Nb-Ti	0.065	26.0	3.08	2.87	0.004	0.013	0.034	0.009	0.0028

Table 2. *Parameters of the thermo-mechanical treatment carried out in the Gleeble simulator*

No	T_A, °C	Deformation I			Cooling I - II		Deformation II			Cooling II - III		Deformation III			Cooling III - IV		Deformation IV			$t_{isother}$ at 850°C, s	Final cooling
		T_1 °C	φ_1	$\dot{\varphi}_1$ s^{-1}	V_1 °C/s	t_1 s	T_2 °C	φ_2	$\dot{\varphi}_2$ s^{-1}	V_2 °C/s	t_2 s	T_3 °C	φ_3	$\dot{\varphi}_3$ s^{-1}	V_3 °C/s	t_3 s	T_4 °C	φ_4	$\dot{\varphi}_4$ s^{-1}		
1	1100	1100	0.29	7	5	10	1050	0.29	8	10	10	950	0.29	9	14	7	850	**0.29**	10	**0**	Water
2	1100	1100	0.29	7	5	10	1050	0.29	8	10	10	950	0.29	9	14	7	850	**0.29**	10	**4**	
3	1100	1100	0.29	7	5	10	1050	0.29	8	10	10	950	0.29	9	14	7	850	**0.29**	10	**16**	
4	1100	1100	0.29	7	5	10	1050	0.29	8	10	10	950	0.29	9	14	7	850	**0.29**	10	**32**	
5	1100	1100	0.29	7	5	10	1050	0.29	8	10	10	950	0.29	9	14	7	850	**0.29**	10	**64**	
6	1100	1100	0.29	7	5	10	1050	0.29	8	10	10	950	0.29	9	14	7	-	-	-	-	
7	1100	1100	0.23	7	5	10	1050	0.23	8	10	10	950	0.23	9	14	7	850	**0.23**	10	32	
8	1100	1100	0.19	7	5	10	1050	0.19	8	10	10	950	0.19	9	14	7	850	**0.19**	10	32	

T_A – austenitizing temperature, $T_{1...}$- T_4 – deformation temperatures, $\varphi_{1...}$- φ_4 – true strains, V_1…- V_4 – cooling rates between deformations, $t_{1...}$- t_3 – times between deformations, $t_{isother}$ – time of the isothermal holding of the specimens at a temperature of 850°C

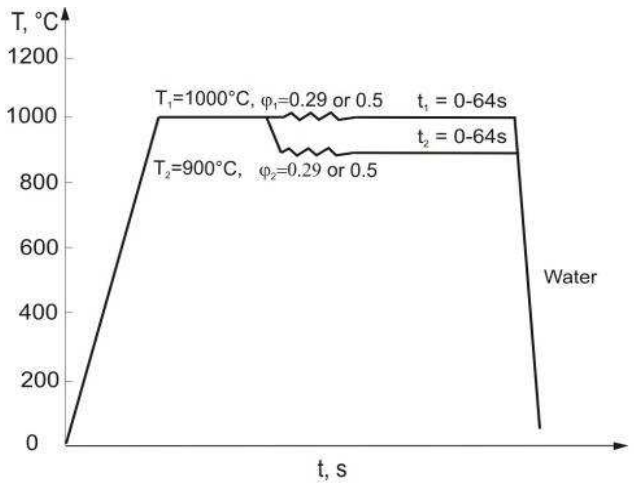

Figure 1. *Parameters of the preliminary hot upsetting tests*

Metallographic investigations were performed on LEICA MEF4A optical microscope. In order to reveal the austenitic structure, samples were etched in nitric and hydrochloric acids mixture in 2:1 proportion as well using a mixture of nitric acid, hydrochloric acid and water in 2:2:1 proportion. The structure of the investigated steel was also characterised using the SUPRA 25 scanning electron microscope and the JEOL JEM 3010 transmission electron microscope working at accelerating voltage of 300 kV. TEM observations were carried out on thin foils. The specimens were ground down to foils with a maximum thickness of 80 μm before 3 mm diameter discs were punched from the specimens. The disks were further thinned by ion milling method with the Precision Ion Polishing System (PIPS™), using the ion milling device (model 691) supplied by Gatan until one or more holes appeared. The ion milling was done with argon ions, accelerated by voltage of 15 kV.

3. Results and discussion

Melted steels possess diversified initial structure represented in Fig. 2 and Fig. 3. The new-developed 26Mn-3Si-3Al-Nb-Ti steel in the initial state is characterized by homogeneous microstructure of austenite with a grain size in range from 100 to 150 μm, in which numerous annealing twins can be identified (Fig. 2a). Single-phase microstructure of the steel is confirmed by X-ray diffraction pattern in Fig. 2b.

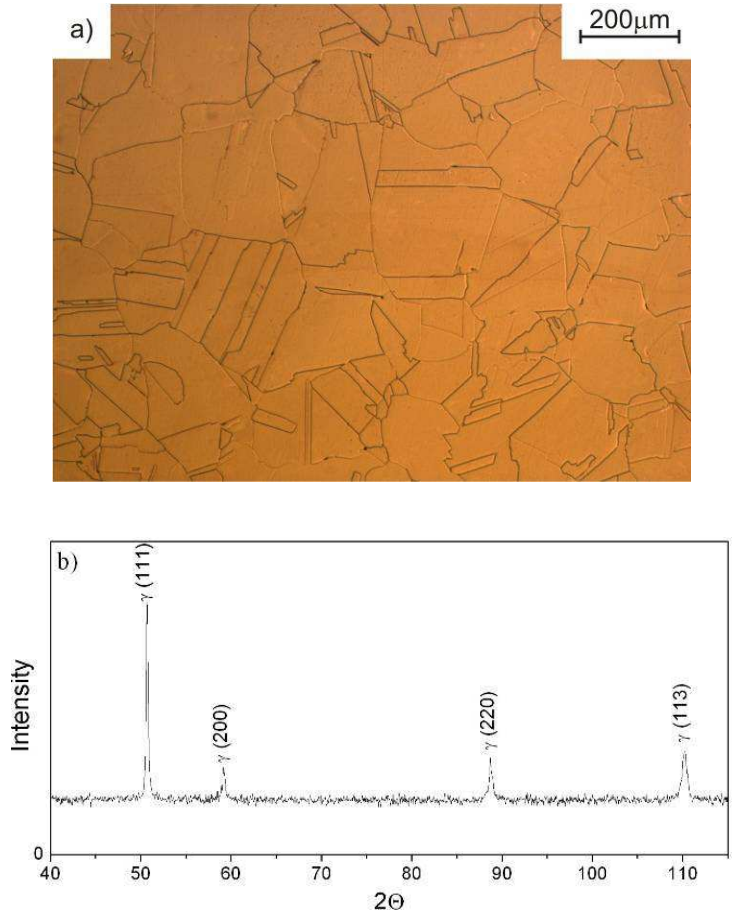

Figure 2. *Austenitic microstructure with numerous annealing twins of the 26Mn-3Si-3Al-Nb-Ti steel in the initial state (a) and X-ray diffraction pattern (b)*

The structure of the investigated 27Mn-4Si-2Al-Nb-Ti steel in the initial state after forging is shown in Fig. 3. Increased concentration of silicon up to 4% and its influence on the decreasing of the stacking fault energy of austenite result in the presence of some fraction of ε martensite in the austenite matrix containing many annealing twins. The ε martensite is present in a form of parallel plates inside austenite grains with a mean grain diameter of about 120 μm (Fig. 1b). The martensite plates are hampered by austenite grain or annealing twins boundaries. The presence of ε martensite is confirmed by X-ray diffraction pattern in Fig. 3b.

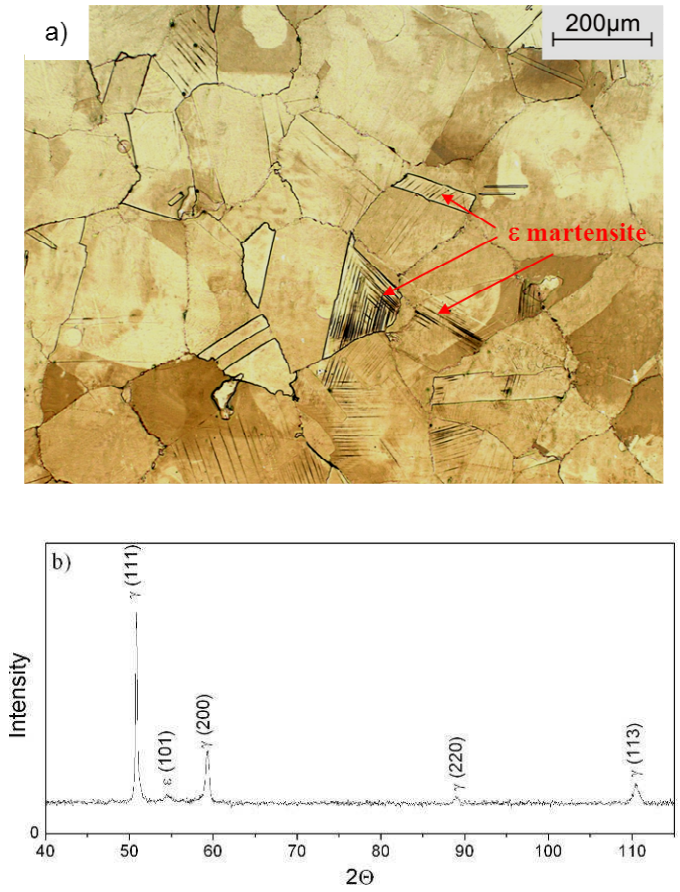

Figure 3. *X-ray diffraction pattern (b) and the austenite structure with many annealing twins and parallel ε martensite plates of the investigated steel 27Mn-4Si-2Al-Nb-Ti in the initial state (a)*

Starting point for microstructure analysis of specimens that were plastically hot-compressed in variable conditions are microstructures of steel subjected to solution heat treatment from a temperature range from 900 to 1100°C. The steel possesses fine-grained microstructure of austenite with grain sizes from 10 to about 17 μm up to temperature of 1000°C (Figs. 4a, b, c, Fig. 5). Further increase in solutioning temperature to 1100°C results in a rapid grain growth up to about 50 μm (Fig. 4c). This behaviour is connected with a total dissolution of NbC particles above 1000°C, what was investigated elsewhere [19]. Moreover, numerous annealing twins can be observed in the microstructure and some fraction of ε martensite plates (Fig. 4).

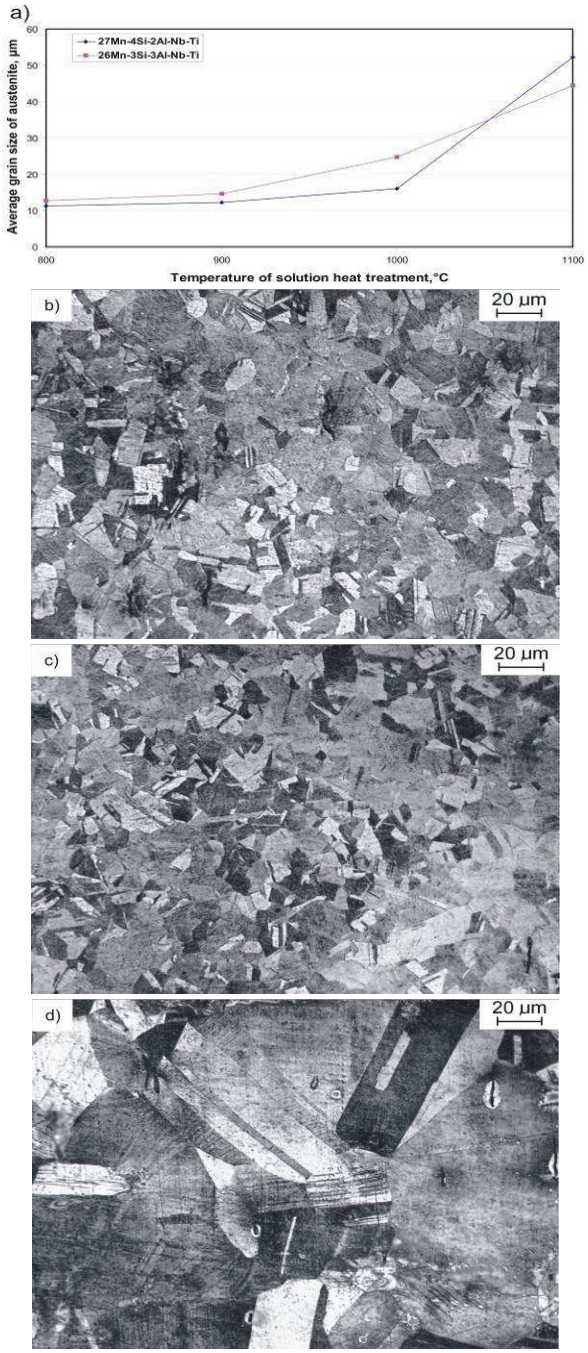

Figure 4. *Changes of austenite grain size in dependence on temperature (a) and structures obtained after solution heat treatment from a temperature: b) 900°C, c) 1000°C, d) 1100°C; 27Mn-4Si-2Al-Nb-Ti steel*

Figure 5. *Austenitic structure of the 26Mn-3Si-3Al-Nb-Ti steel after solution heat treatment from a temperature of 900°C*

Microstructure development of 27Mn-4Si-2Al-Nb-Ti steel, solution heat treated from temperature of 850 or 950°C, after application of specified reduction, as well as σ-ε curves obtained in continuous compression test are presented in Figs. 6a-h. It arises from Fig. 6a that the steel is characterized by values of yield stress equal from 240 to 450 MPa in investigated range of temperature. These values are considerably higher than they are for conventional C-Mn steels as well as for Cr-Ni and Cr-Mn austenitic steels [20].

It proves high strain hardening, which is probably caused by high Mn concentration in the steel. Additionally, the increase of flow stress is influenced by Si and Al additives as well as Nb and Ti microadditions. Decrease of strain temperature by around 100°C results in increase of flow stress by around 100 MPa. Along with strain temperature decreasing, the value of ε_{max} – corresponding to the maximum value of yield stress – is translating to a range of higher deformations. However, it's characteristic, that after strong strain hardening, peaks of ε_{max} are present for relatively low deformation values, i.e. from 0.23 to 0.48. It creates convenient conditions for using dynamic recrystallization for refinement of microstructure, what is confirmed by fine-grained microstructure of steel, solution heat treated from the temperature of 950°C after true strain of 0.5 (Fig. 6b). Decrease of true strain to 0.29, close to ε_{max} deformation in Fig. 6a, also leads to the initiation of dynamic recrystallization (Fig. 6c). Nevertheless, further decrease of reduction to 20% (true strain equal 0.23) is too low for initiating dynamic recrystallization (Fig. 6d). In such conditions, microstructure of steel is composed of dynamically recovered austenite grains elongated in the direction of plastic flow with size comparable to the sample solution heat treated from temperature of 900°C.

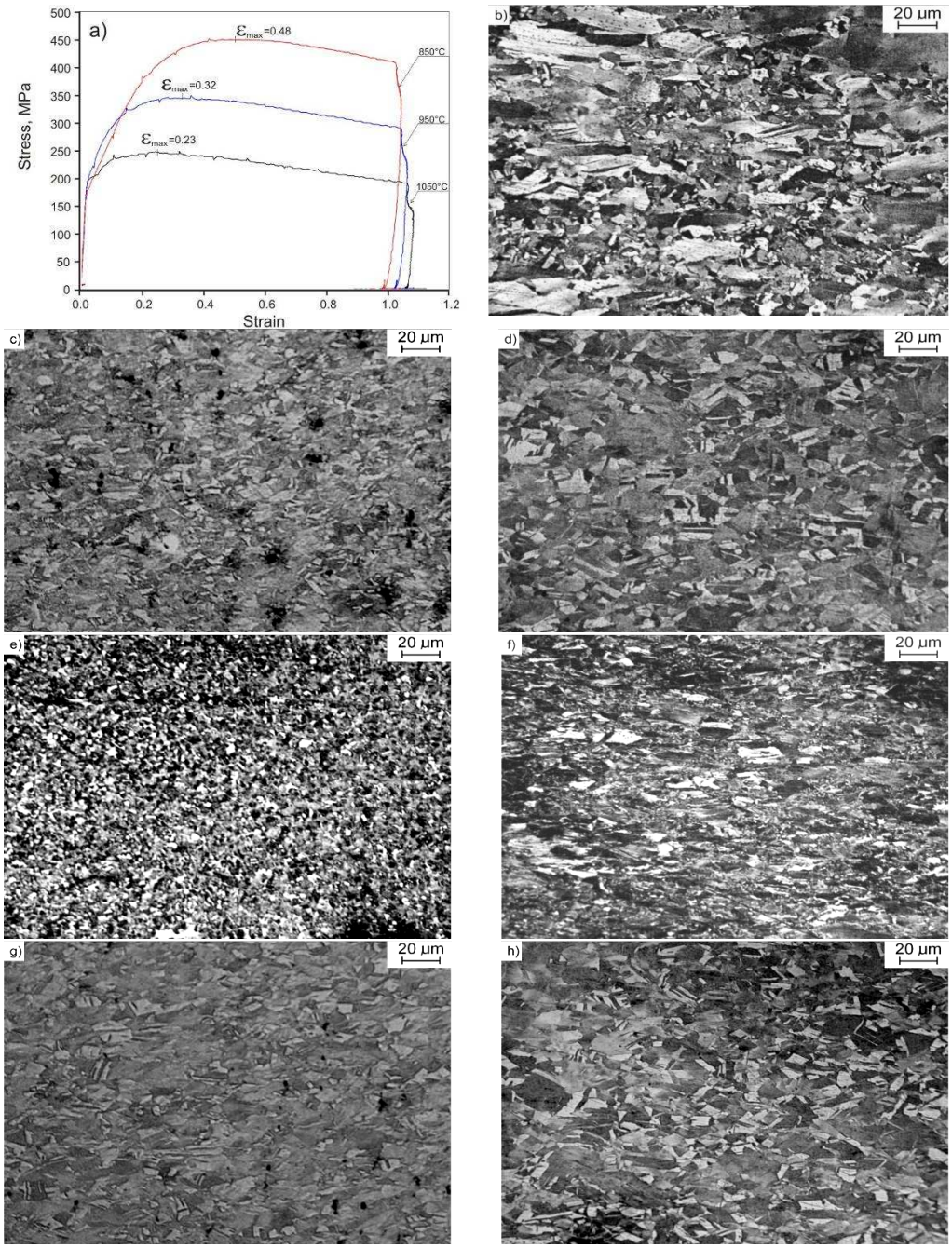

Figure 6. *Evolution of the microstructure of 27Mn-4Si-2Al-Nb-Ti steel compressed to a various strain: a) σ-ε curve; b) T = 950°C, ε = 0.5; c) T = 950°C, ε = 0.29; d) T = 950°C, ε = 0.23; e) T = 950°C, ε = 0.91; f) T = 850°C, ε = 0.5; g) T = 850°C, ε = 0.29; h) T = 850°C, ε = 0.23*

After decreasing compression temperature to 850°C, fully recrystallized microstructure of austenite with grain size of approximately 3 μm was achieved through application of true strain equal 0.9 (Fig. 6e). Decrease of reduction to 40% results in obtaining microstructure of recrystallized grains of austenite uniformly distributed in matrix of dynamically recovered grains with sizes slightly smaller than for the strain temperature of 950°C (Fig. 6f). Decrease of true strain to 0.29 is sufficient for initiation of dynamic recrystallization also for the deformation temperature of 850°C (Fig. 6g), although the value of ε_{max} is equal 0.48. It's in accordance with data presented in [16], in which it was stated that the initiation of dynamic recrystallization can occur at critical deformation value $\varepsilon_{cd}=(0.5\text{-}0.85)\varepsilon_m$. Solution heat treatment from temperature of 850°C after true strain of 0.23 doesn't cause grain refinement of microstructure as a result of dynamic recrystallization. Microstructure of steel is composed of slightly deformed grains of dynamically recovered austenite (Fig. 6h).

The σ-ε curves together with microstructures of 26Mn-3Si-3Al-Nb-Ti steel solution heat treated from the temperature of 850°C and specified reduction are presented in Figs. 7a-d. The course of σ-ε curves is almost identical as in case of steel discussed above (Fig. 7a). It refers both to the values of flow stresses and values of ε_{max} deformations. It can be observed in Fig. 7a that the only difference derives from slightly lower values of flow stress for the strain temperature of 850°C, what can be caused by lower solution hardening of aluminium when compared to silicon, which concentration is twice smaller than in 26Mn-3Si-3Al-Nb-Ti steel. Similarly as for the second steel, true strain equal 0.23 is too low for initiating dynamic recrystallization (Fig. 7b), which occurs after increasing true strain to 0.29 (Fig. 7c). Still, significant microstructure refinement requires application of deformation equal 0.5 (Fig. 7d).

Development of microstructure of steel 26Mn-3Si-3Al-Nb-Ti isothermally held in temperature of 900°C, after true strain equal 0.29 is presented in Fig. 8. After 4 s of holding, microstructure is slightly different in comparison with microstructure of steel solution heat treated directly after deformation (Fig. 8a). Increase of holding time to 16 s results in obtaining high participation of recrystallized grains at the cost of dynamically recovered grains (Fig. 8b). Fast progress of microstructure reconstruction confirms occurrence of metadynamic recrystallization, not requiring any period of incubation. Confirmation of this fact is large portion of dynamically recrystallized grains after deformation with reduction of 25% at temperature of 850°C (Fig. 7c). Increase of holding time to 64 s leads to achievement of highly fine-grained microstructure of metadynamically and statically recrystallized grains (Fig. 8c).

Successive stages of microstructure development of steel 27Mn-4Si-2Al-Nb-Ti in function of isothermal holding time are shown in Fig. 9a-c. The progress of recrystallization of this steel

is slightly slower, what proves higher contribution of static recrystallization to removal of strain hardening than in case of steel 26Mn-3Si-3Al-Nb-Ti.

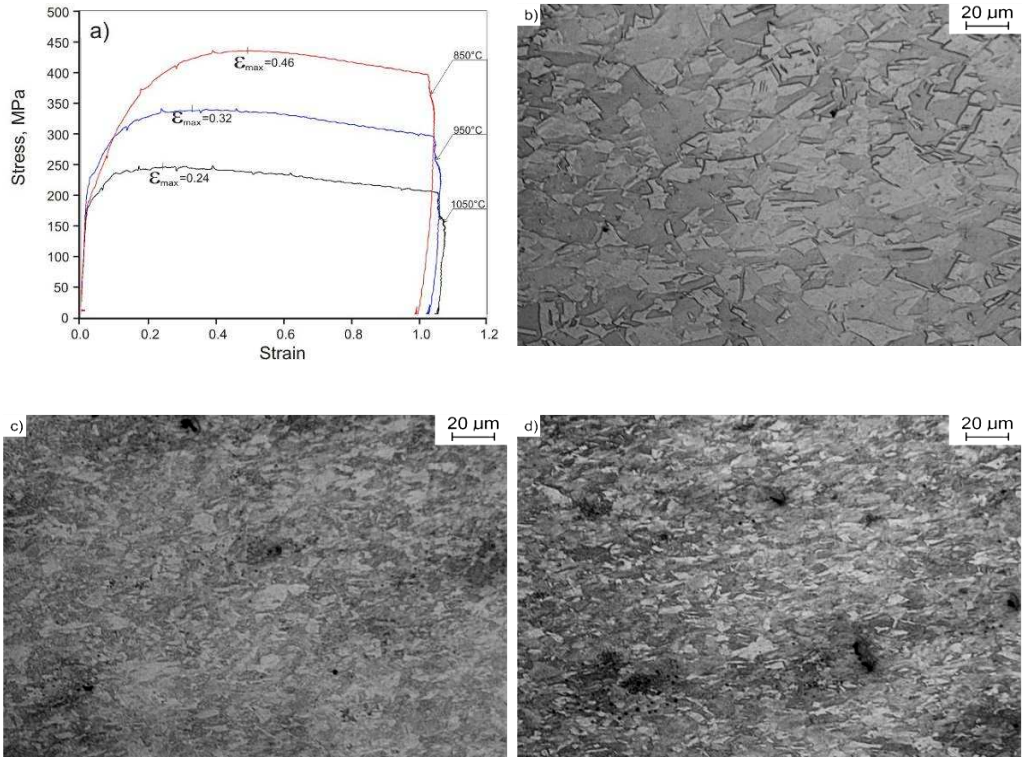

Figure 7. *Evolution of the microstructure of 26Mn-3Si-3Al-Nb-Ti steel compressed to a various strain: a) σ-ε curve; b) T = 850°C, ε = 0.23; c) T = 850°C, ε = 0.29; d) T = 850°C, ε = 0.5*

The conditions of hot-working additionally influence phase state of steel. Steel 26Mn-3Si-3Al-Nb-Ti with initial austenitic microstructure keeps its stability independently from conditions of plastic deformation. X-ray diffraction patterns for steel 27Mn-4Si-2Al-Nb-Ti indicate presence of peaks coming from ε martensite. However, their intensity connected with participation of this phase differs depending on applied variant of hot-working. The highest intensity from (101) planes belongs to the sample deformed with lowest reduction (Fig. 10a). Increase of reduction causes decrease of peaks intensity (Fig. 10b, 10c). Isothermal holding for 16 s after deformation at 900°C doesn't change phase composition of steel 27Mn-4Si-2Al-Nb-Ti. Still, slight peaks coming from ε martensite are present (Fig. 10d). Increase of holding time

to 64 s leads to substantial increase of (101) peak intensity of ε martensite (Fig. 10e). It means, that in spite of fine-grained microstructure of steel having impeding impact on growth of ε martensite laths [18], also state of internal stresses, effectively limited in process of metadynamic and static recrystallization, decides about tendency of formation of this phase in high-manganese steels.

The fraction of the recrystallized phase in intervals between successive passes can be evaluated from Figs. 11 and 12, showing a progress of recrystallization as a function of time for the specimens compressed in various deformation conditions. It arises from Fig. 11, that participation of recrystallized phase of 27Mn-4Si-2Al-Nb-Ti steel increases along with increasing deformation temperature and increase of reduction. Half-time of recrystallization at the temperature of 1000°C after deformation with 40% of reduction is equal 13 s and increases to 18 s after decreasing strain temperature to 900°C. Decrease of reduction to 25% results in elongation of $t_{0.5}$ time to 32 s, because of the change of prevailing participation of metadynamic recrystallization – in removing the effects of hardening – on behalf of static recrystallization. Half-times of recrystallization of 26Mn-3Si-3Al-Nb-Ti steel are shorter and are equal – 8, 12 and 17 s, respectively for analogical strain conditions (Fig. 12). It comes from higher participation of metadynamic recrystallization in removing effects of strain hardening, what arises directly from higher portion of dynamically recrystallized grains during plastic strain (Fig. 7c).

Stress-deformation curves of steels plastically deformed according to the parameters shown in Table 2 are presented in Figs. 13-15. Application of true strain equal 0.29 during cyclic compression creates possibility of the course of dynamic recrystallization, what is indicated by peaks that can be distinguished on σ-ε curves – especially for deformations realized at temperature of 1100 and 1050°C (Fig. 13). After decreasing plastic deformation temperature, maximum on σ-ε curves is present for maximum value of true strain (0.29). Initiation of dynamic recrystallization at this deformation value is additionally confirmed by microstructures of steels solution heat treated after deformation in analogical conditions of continuous compression (Figs. 6c, 6g, 7c). The values of yield stress in the range of strain temperature from 1100 to 950°C are comparable with values obtained in continuous compression test; however deformation of steel with lower concentration of Si and Mn requires slightly lower pressures. Significant decrease of flow stress is noted for the last deformation realized at the temperature of 850°C (Fig. 13). It's a result of partial removal of strain hardening through metadynamic recrystallization that occurs during the interval between third and fourth deformation. Additionally, cyclic deformation as well as the course of partial recrystallization result in much faster achievement of maximum on σ-ε curve for the fourth deformation when comparing to σ-ε curve of continuous compression at the temperature of 850°C.

a) 950°C-25%-4 s – water

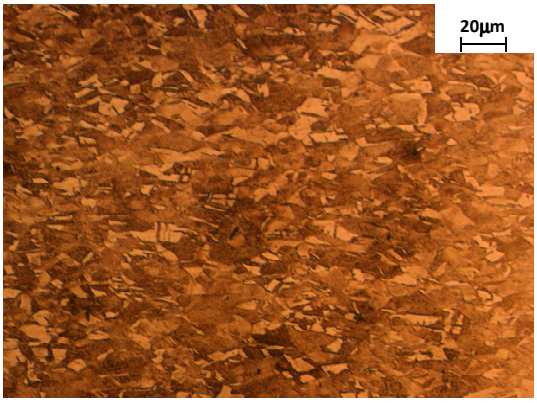

b) 950°C-25%-16 s – water

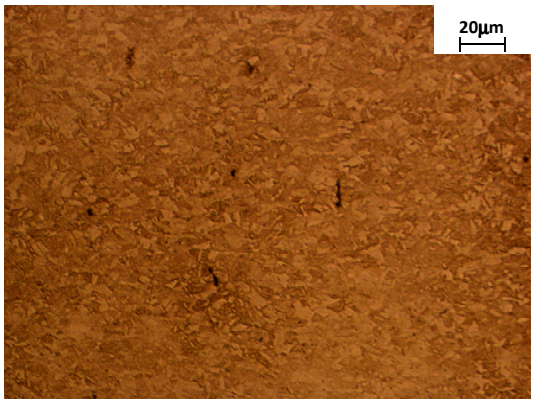

c) 950°C-25%-64 s – water

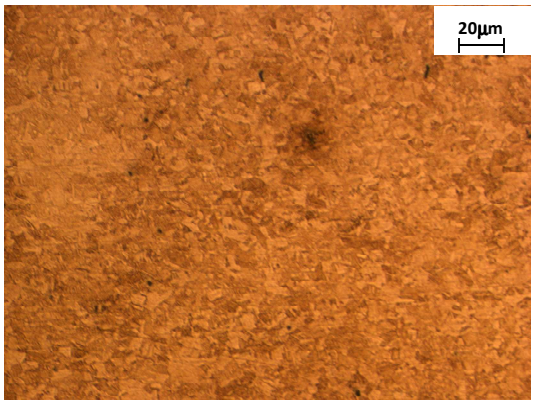

Figure 8. *Microstructure evolution of the 26Mn-3Si-3Al-Nb-Ti steel after isothermal holding for time: a) t = 4 s; b) t = 16 s; c) t = 64 s; for the specimens plastically deformed at 900°C,* $\varepsilon = 0.29$

a) 950°C-25%-4 s - water

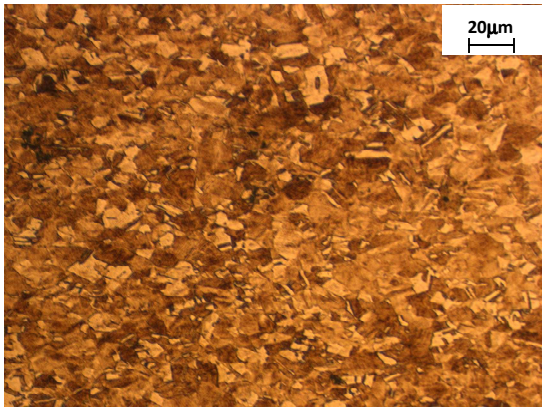

b) 950°C-25%-16 s - water

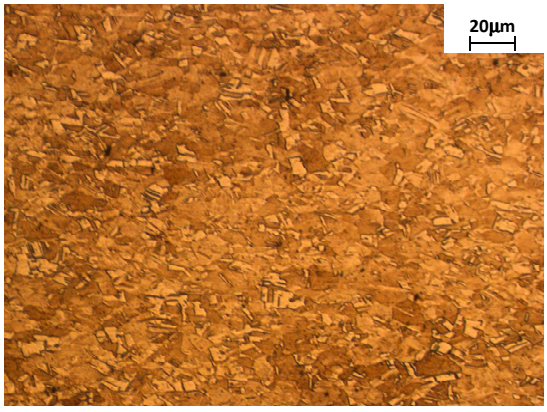

c) 950°C-25%-64 s - water

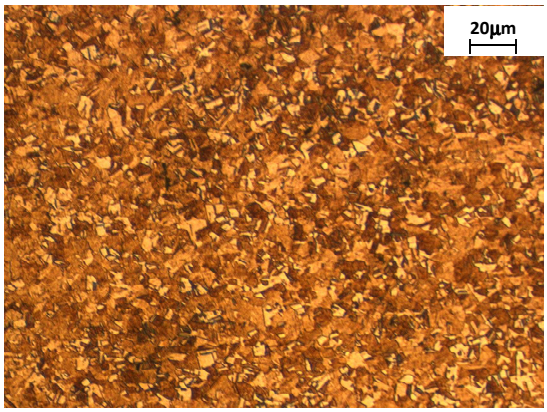

Figure 9. *Microstructure evolution of the 27Mn-4Si-2Al-Nb-Ti steel after isothermal holding for time: a) t = 4 s; b) t = 16 s; c) t = 64 s; for the specimens plastically deformed at 900°C, $\varepsilon = 0.29$*

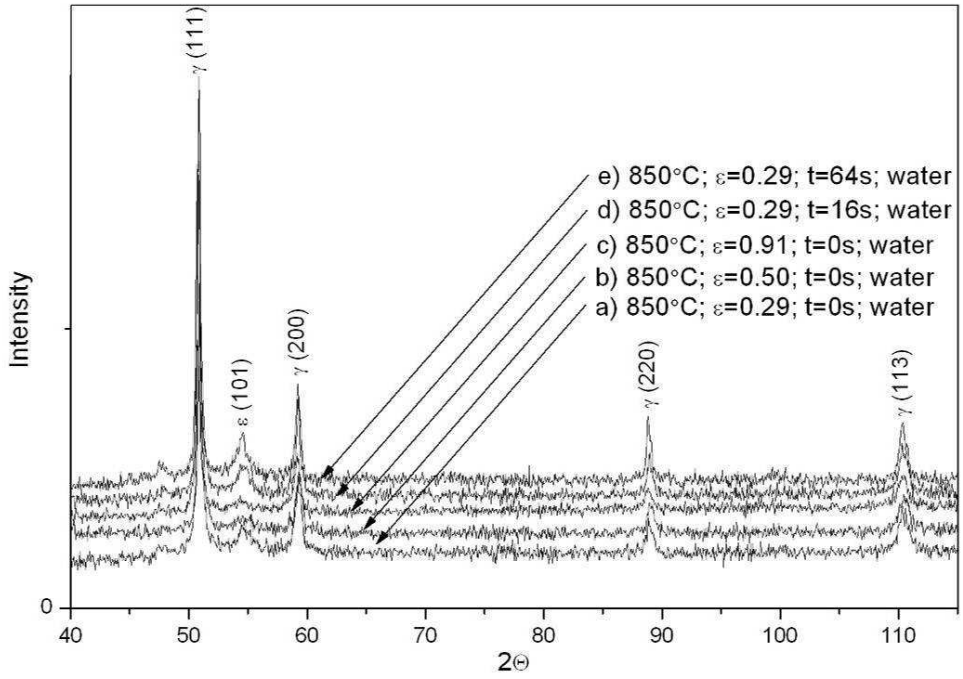

Figure 10. *X-ray diffraction patterns for 27Mn-4Si-2Al-Nb-Ti steel after various variants of the thermo-mechanical treatment; a) 850°C, ε=0.29, t=0 s, b) 850°C, ε=0.5, t=0 s, c) 850°C, ε=0.91, t=0 s, d) 850°C, ε=0.29, t=16 s, e) 850°C, ε=0.29, t=64 s*

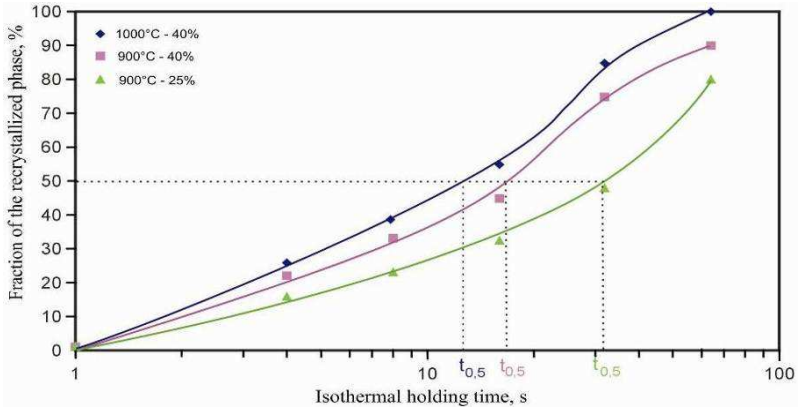

Figure 11. *Progress of recrystallization of the 27Mn-4Si-2Al-Nb-Ti steel isothermally held after plastic deformation in various conditions*

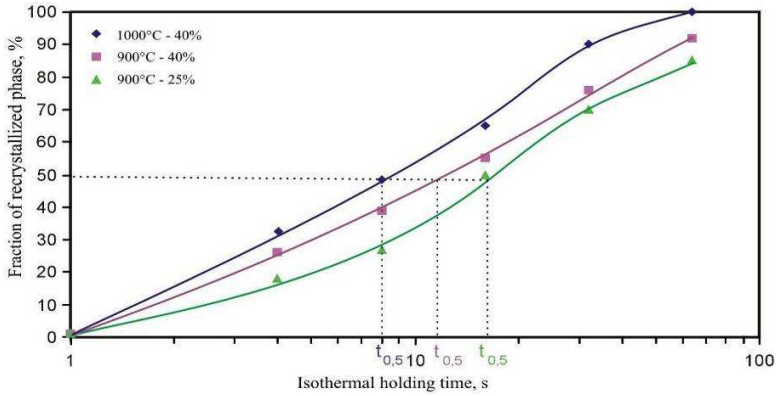

Figure 12. *Progress of recrystallization of the 26Mn-3Si-3Al-Nb-Ti steel isothermally held after plastic deformation in various conditions*

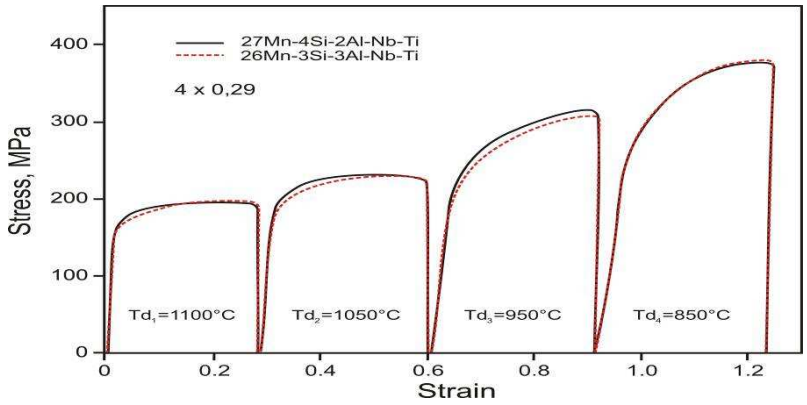

Figure 13. *Stress – strain curves for the specimens plastically deformed 4 x 0.29*

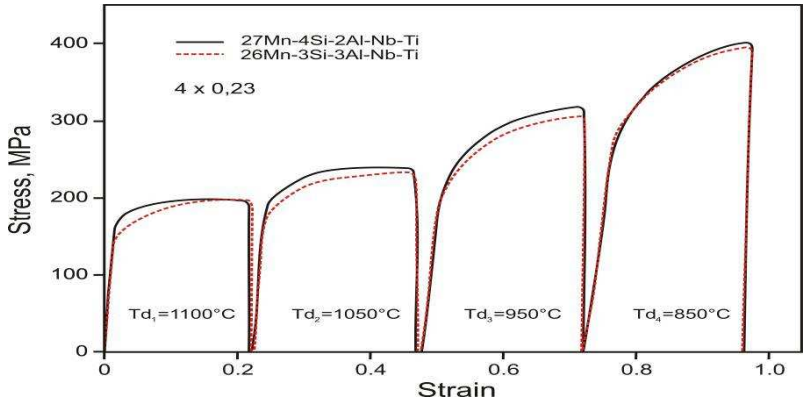

Figure 14. *Stress – strain curves for the specimens plastically deformed 4 x 0.23*

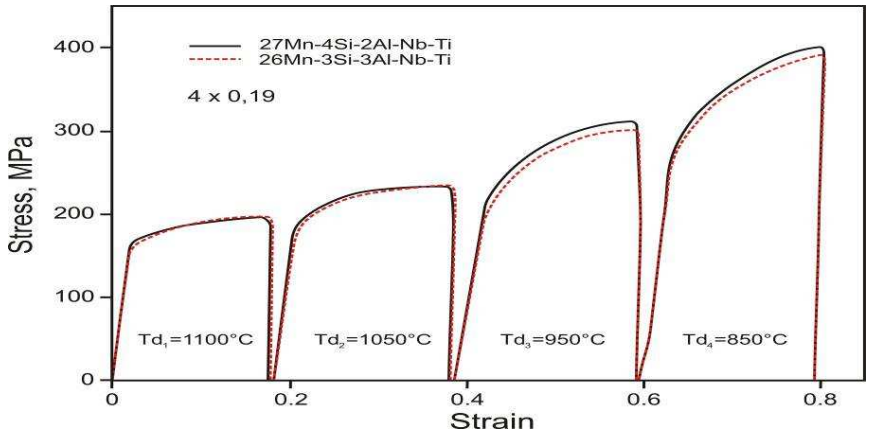

Figure 15. *Stress – strain curves for the specimens plastically deformed 4 x 0.19*

Decrease of true strain to 0.23 leads to a change of the course of σ-ε curves (Fig. 14). Shape of the curves after deformation at the temperature of 1100 and 1050°C indicate possibility of initiating dynamic recrystallization. However, decreasing the temperature causes that dynamic recovery is the process controlling strain hardening. Moreover, only partial course of static recrystallization during cooling of sample between third and fourth deformation results in increasing the value of yield stress during deformation at 850°C. Further decrease of true strain to 0.19 causes that dynamic recovery is the process controlling strain hardening in the whole temperature range of deformation (Fig. 15), at comparable values of yield stress.

The microstructure evolution of steel 27Mn-4Si-2Al-Nb-Ti in different stages of multi-stage compression is shown in Fig. 16. After deformation of the specimen at a temperature of 950°C and subsequent cooling for 7 s corresponding to the interpass time, the steel is characterised by uniform, metadynamically recrystallized austenite microstructure with a mean grain size of about 20 μm and many annealing twins (Fig. 16a). The initiation of dynamic recrystallization during the last deformation at the temperature of 850°C is confirmed by a micrograph in Fig. 16b, showing an initial state of dynamic recrystallization. The mean dynamically recovered austenite grain size decreased to about 12 μm and fine dynamically recrystallized grains are arranged along austenite grain boundaries as well as on twin boundaries. The similar role of twinning as a nucleation and growth mechanism of dynamic recrystallization was observed by Sabet et al. [24] in Fe-29Mn-2.4Al alloy. The repeated formation of twins during the whole temperature range of hot-working may be a reason of amplification of a number of dynamically recrystallized grains. The annealing twins are present both inside large dynamically recovered grains and fine recrystallized grains. A low tendency

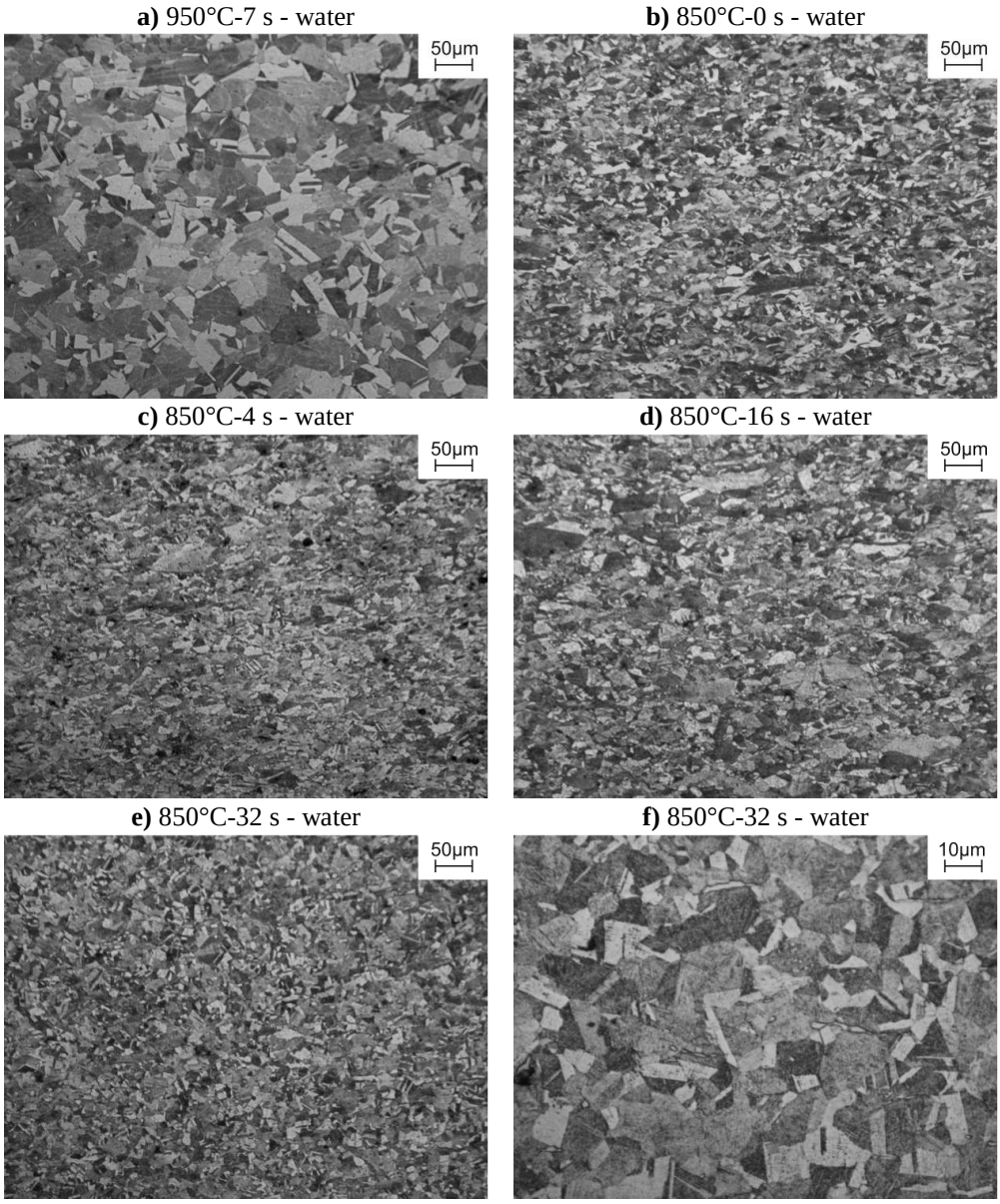

Figure 16. *Austenitic structures obtained after solutioning the steel 27Mn-4Si-2Al-Nb-Ti in successive stages of the hot-working for the specimens compressed to a true strain 4x0.29 and isothermally held for the time from 0 to 64s: a) metadynamically recrystallized grains during the interval between third and fourth deformation, b) initiation of dynamic recrystallization, c) grain refinement due to metadynamic recrystallization, d) grain refinement due to metadynamic and static recrystallization, e, f) fine statically recrystallized austenite grains*

of high-manganese austenite with a low SFE to dynamic recovery is confirmed by Fig. 17, revealing a weakly outlined cellular dislocation structure in a region still not subjected to dynamic recrystallization, despite the true strain of 0.29, slightly higher than corresponding to a maximal value of true stress.

The analysis of Fig. 17 allows to reveal the highly deformed austenite structure with a various density of crystal structure defects, where inside, it is possible to observe regions with a much lower dislocation density corresponding to a state directly before forming dynamic recrystallization nuclei. A lack of distinct cellular dislocation structure in metals with low SFE is due to the necessity of extended dislocations to recombine it to a perfect dislocation before the cross slip initiation, what requires providing activation energy, dependent on normalized stacking fault energy of γ phase.

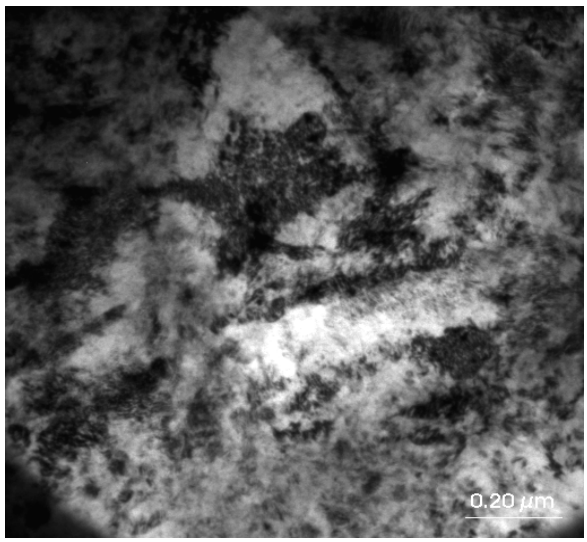

Figure 17. *Regions of dynamically recovered austenite with a various dislocation density of the steel 27Mn-4Si-2Al-Nb-Ti solution heat-treated from a temperature of 850°C directly after the true strain of 4x0.29*

Isothermal holding of the steel 27Mn-4Si-2Al-Nb-Ti after the deformation at 850°C for 4 s does not cause any essential modifications of microstructure. The microstructure consists of fine metadynamically recrystallized austenite grains and larger grains in which the process controlling the work hardening during deformation was just dynamic recovery (Fig. 16c).

Increase of isothermal holding of the specimen at a temperature of the last deformation for 16 s leads to growth of new grains as a result of metadynamic recrystallization and the initiation of static recrystallization on grain boundaries of large, flattened austenite grains whose fraction is still high (Fig. 16d). Further increase in the isothermal holding time to 32 s leads to obtain nearly 60% fraction of metadynamically and statically recrystallized microstructure with a mean austenite grain size of about 10 μm (Figs. 16e, f).

It is interesting that in Fig. 16 any ε martensite plates were observed, despite presence of this phase in the initial structure (Fig. 3). Confirmation of that fact is the X-ray diffraction patterns shown in Fig. 18 for different stages of thermo-mechanical treatment. A lack of ε martensite is connected with significant structure refinement compared to the initial state and hampering influence of grain boundaries on growth of ε martensite plates during cooling. Similar effects were reported in [18] for Fe-21Mn alloy and in [22] for Fe-25Mn alloy.

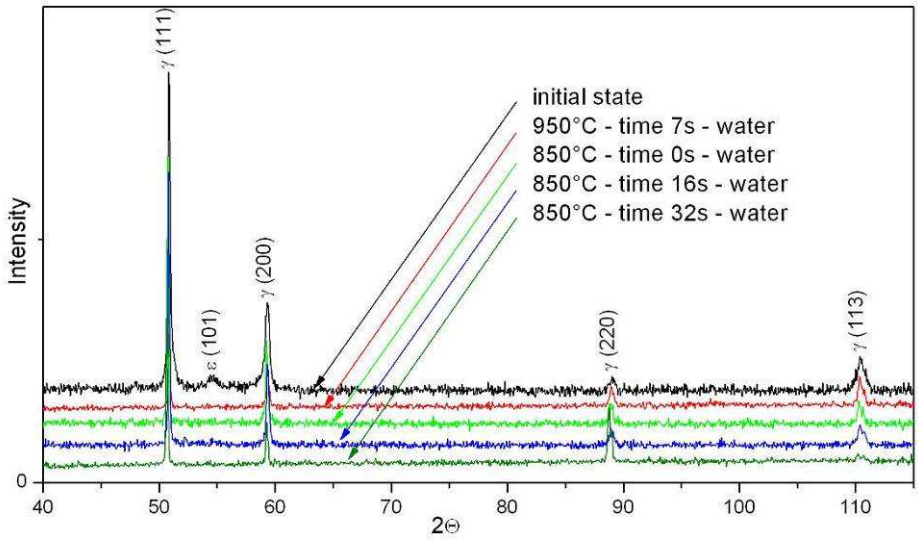

Figure 18. *X-ray diffraction patterns of the steel 27Mn-4Si-2Al-Nb-Ti in the initial state and after different stages of thermo-mechanical treatment*

Due to high rolling forces in final passes of sheet rolling, the amount of deformation is usually reduced. Because of this the four-stage compression with true strains of 4x0.23 and 4x0.19 were also carried out. Moreover, the applied strain is sufficient to initiate a course of dynamic recrystallization. However, decreasing the compression temperature to 950°C

causes that the flow stress is slightly higher and the applied strain value is too low to initiate dynamic recrystallization. Thus, process controlling a course of hot-working at 950°C is a dynamical recovery. Because of a lack of dynamic recrystallization in final passes, a refinement of microstructure requires the use of thermally activated, static processes removing work-hardening. For instance, the micrographs in Fig. 19 show the austenite microstructure of the steel isothermally held for 32 s at 850°C after compression with a true strain of 4x0.23. The fraction of statically recrystallized austenite equals approximately 60% (Fig. 19a). Numerous annealing twins can be observed in the microstructure (Fig. 19b) and a mean statically recrystallized austenite grain is higher compared to the specimen compressed 4x0.29, where a reconstruction of the microstructure was obtained both in static and metadynamic processes (Fig. 16f).

a) 850°C-32 s - water **b)** 850°C-32 s - water

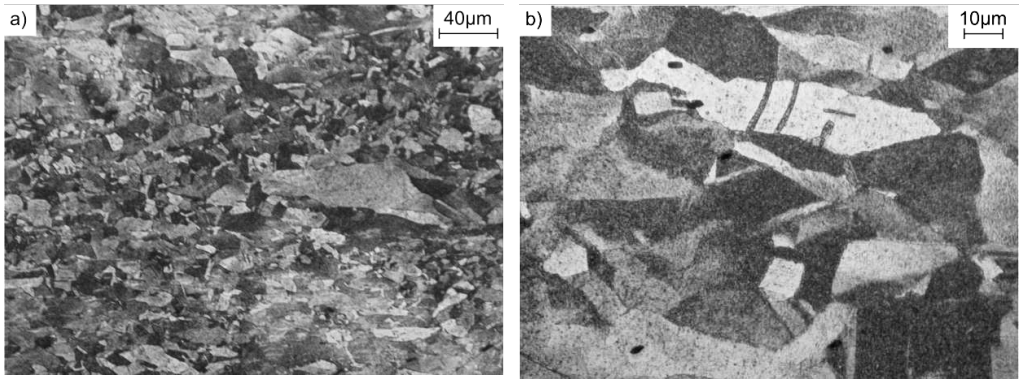

Figure 19. *Fine, statically recrystallized austenite grains and large statically recovered grains of the steel 27Mn-4Si-2Al-Nb-Ti solution heat-treated from a temperature of 850°C after isothermal holding for 32 s of the specimen compressed with the true strain of 4x0.23 (a, b)*

Relatively slow progress of static recrystallization is a result of impeding influence of high content of solutes on the migration of grain boundaries. The statically recovered, deformed austenite grains have low tendency to form a cellular dislocation structure, likewise dynamically recovered grains (Fig. 17). Inside these grains, regions characterized by various dislocation density can be observed (Fig. 20).

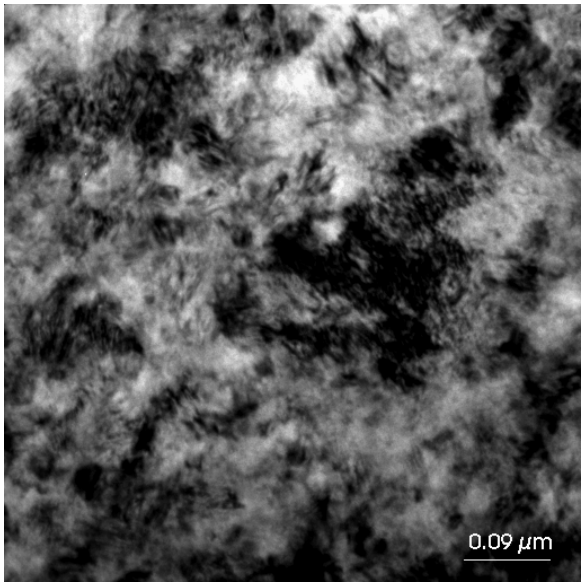

Figure 20. *Regions of statically recovered austenite with a various dislocation density of the steel 27Mn-4Si-2Al-Nb-Ti solution heat-treated from the temperature of 850°C after isothermal holding for 32 s of the specimen compressed with the true strain of 4x0.23*

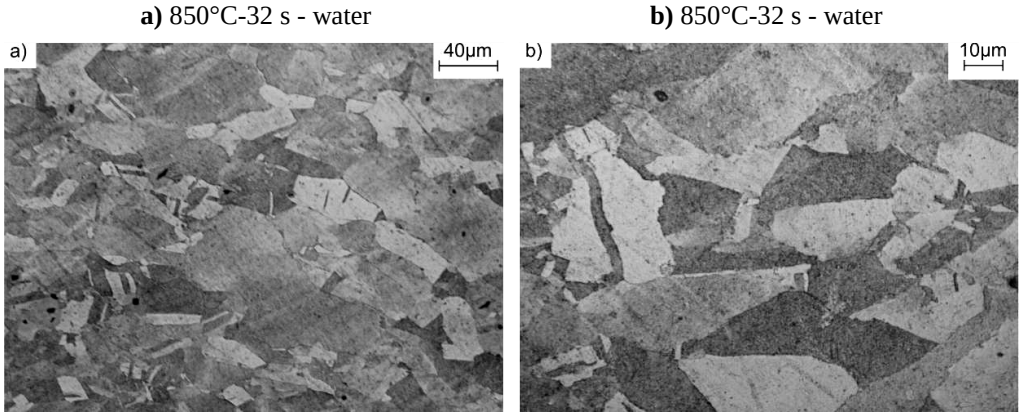

Figure 21. *Fine, statically recrystallized austenite grains and large statically recovered grains of the steel 27Mn-4Si-2Al-Nb-Ti solution heat-treated from the temperature of 850°C after isothermal holding for 32 s of the specimen compressed with the true strain of 4x0.19 (a, b)*

A decrease of true strain to 0.19 causes that dynamic recovery is the process controlling strain hardening in the whole temperature range of deformation (Fig. 15), at similar values of flow stress in comparison with the specimen deformed 4x0.23. However, the isothermal holding of the specimen for 32 s is too short to obtain a desired fraction of recrystallized phase, which equals approximately 15% (Fig. 21a). Fine, recrystallized grains are located mainly on grain boundaries of large, flattened statically recovered grains (Fig. 21b). Both recrystallized and recovered grains are bigger than those after applying the true strain being equal 0.23 (Fig. 19). Once again, numerous annealing twins can be observed in the microstructure (Fig. 21a, b). The microstructure in Fig. 22 clearly shows that new grains are located on grain boundaries of large, statically recovered austenite grains. Moreover, a jerky-like character of the boundaries of large grains can be observed. It is a characteristic feature of a state directly before forming a recrystallization nucleus [19].

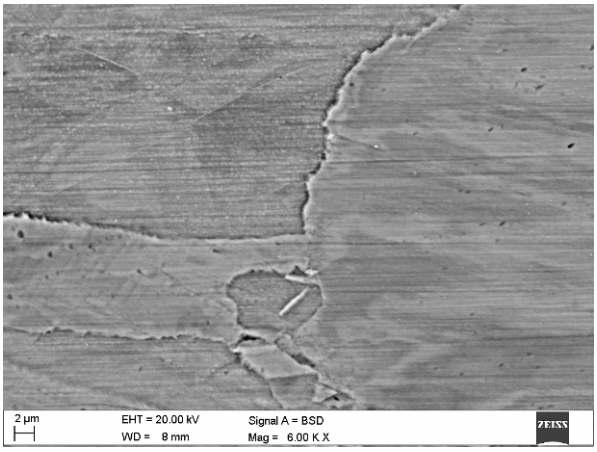

Figure 22. *The fine, statically recrystallized grain on jerky-like boundaries of three large, statically recovered grains of the steel 27Mn-4Si-2Al-Nb-Ti solution heat-treated from the temperature of 850°C after isothermal holding for 32 s of the specimen compressed with the true strain of 4x0.19*

Similarly microstructure evolution was observed for the specimens from 26Mn-3Si-3Al-Nb-Ti steel deformed in the multi-stage compression test. Microstructures of steel in the successive deformation stages and after its finish corresponding to σ-ε curves are put together in Fig. 23. After deformation of the specimen at a temperature of 1050°C and subsequent cooling for 10 s corresponding to the interpass time, the steel is characterized by uniform, metadynamically

recrystallized austenite microstructure with a grain size of about 40 μm (Fig. 23a). Lowering the deformation temperature to 950°C and the time of 7 s for cooling the specimen to 850°C results in much smaller fraction of metadynamically recrystallized grains located in a matrix of statically recovered grains (Fig. 23b). A partial removal of work-hardening through metadynamic recrystallization that occurs during the interval between third and fourth deformation is a result of significant decrease of flow stress noted for the last deformation realized at the temperature of 850°C (Fig. 13), compared to the curve obtained in the continuous compression test (Fig. 7a). Additionally, cyclic deformations as well as the course of partial recrystallization cause much faster achievement of maximum on σ-ε curve for the fourth deformation when comparing to continuous compression at the temperature of 850°C.

The initiation of dynamic recrystallization during the last deformation at a temperature of 850°C is confirmed by a micrograph in Fig. 23c, showing a partially recrystallized austenite with a grain size of about 20 μm. Isothermal holding of the specimen in a temperature of the last deformation for 16 s leads to a remarkably fine-grained metadynamically recrystallized austenite microstructure with a fraction of about 40%, located in the matrix of slightly elongated, statically recovered grains containing numerous annealing twins (Fig. 23d). Further extension of holding time to 32 s leads to obtaining almost fully recrystallized microstructure of steel (Fig. 23e) with a mean austenite grain size of about 10 μm. Holding of steel in the deformation temperature for 64 s causes gradual increase of recrystallized grains sizes (Fig. 23f).

Decrease of true strain to 0.23 during the multi-stage compression test leads to changes of the course of stress-strain curves (Fig. 14). A shape of the curves during deformation in a temperature range of 1100-1050°C and true stress values are comparable to that obtained after higher strain applying. Moreover, the applied strain is sufficient to initiate a course of dynamic recrystallization. However, decreasing the compression temperature to 950°C causes that the flow stress is slightly higher and the applied strain value is too low to initiate dynamic recrystallization. Thus, process controlling a course of hot-working at 950°C is a dynamical recovery.

Because of a lack of dynamic recrystallization in final passes, a refinement of microstructure requires the use of thermally activated, static processes removing work-hardening. For instance, the micrographs in Figs. 24a,b show the austenite microstructure of the steel isothermally held for 32 s at 850°C after compression with a true strain of 4x0.23. The fraction of statically recrystallized austenite equals approximately 50% (Fig. 24a). Numerous annealing twins can be observed in the microstructure (Fig. 24b) and a mean statically recrystallized austenite grain is higher compared to the specimen compressed 4x0.29, where a reconstruction of the microstructure was obtained both in static and metadynamic processes (Fig. 23e).

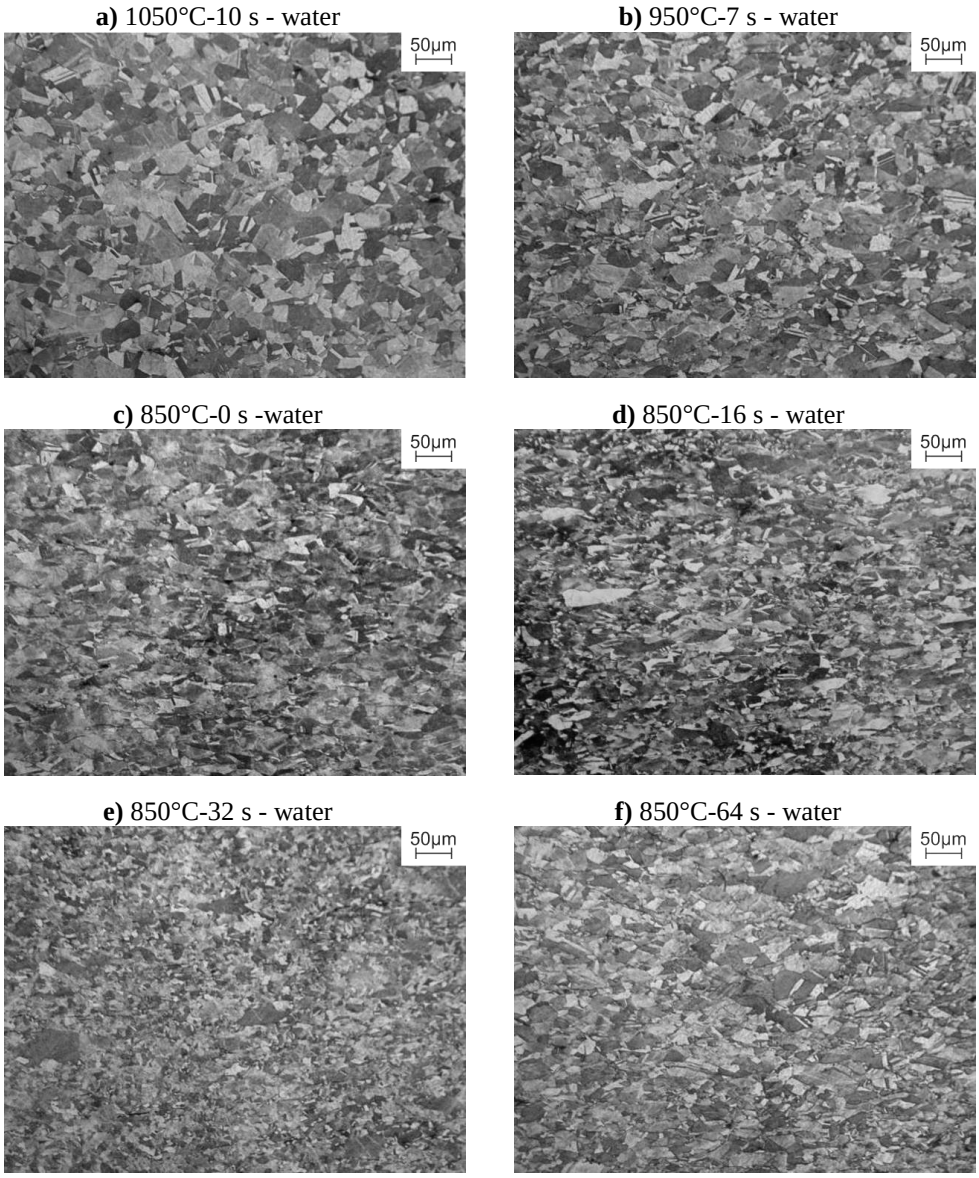

Figure 23. *Austenitic structures obtained after solutioning the 26Mn-3Si-3Al-Nb-Ti steel in successive stages of the hot-working for the specimens compressed to a true strain 4x0.29 and isothermally held for the time from 0 to 64s: a) metadynamically recrystallized grains during the interval between second and third deformation, b) metadynamically recrystallized grains during the interval between third and fourth deformation, c) initiation of dynamic recrystallization, d) grain refinement due to metadynamic and static recrystallization, e) fine statically recrystallized austenite grains, f) grain growth as a result of metadynamic recrystallization*

a) 850°C-32 s - water **b)** 850°C-32 s - water

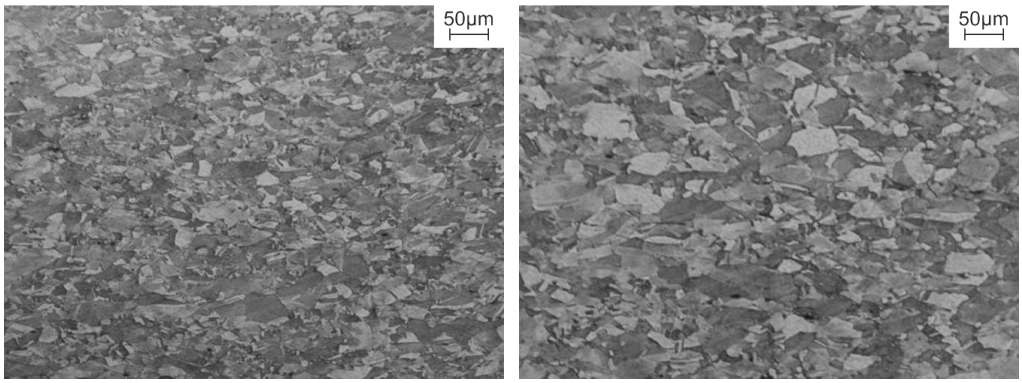

Figure 24. *Fine, statically recrystallized austenite grains and large statically recovered grains of the 26Mn-3Si-3Al-Nb-Ti steel solution heat-treated from a temperature of 850°C after isothermal holding for 32 s of the specimen compressed with the true strain of 4x0.23 (a, b)*

a) 850°C-32 s - water **b)** 850°C-32 s - water

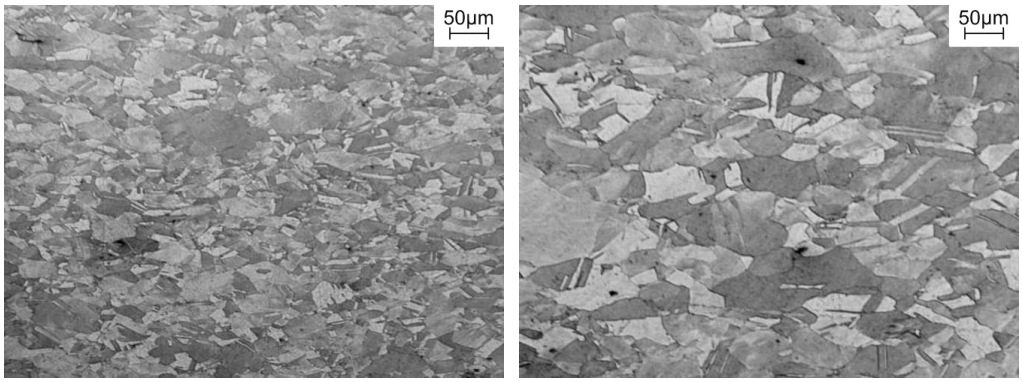

Figure 25. *Fine, statically recrystallized austenite grains and large statically recovered grains of the 26Mn-3Si-3Al-Nb-Ti steel solution heat-treated from the temperature of 850°C after isothermal holding for 32 s of the specimen compressed with the true strain of 4x0.19 (a, b)*

Further decrease of true strain to 0.19 causes that dynamic recovery is the process controlling work hardening in the whole temperature range of deformation (Fig. 15), at similar values of flow stress in comparison with the specimen deformed 4x0.23. However, the isothermal holding of the specimen for 32 s is to short to obtain a desired fraction of

recrystallized phase, which equals approximately 20% (Fig. 24a). Once again, numerous annealing twins can be observed in microstructure and fine statically recrystallized grains of γ phase are located mainly on boundaries of elongated statically recovered austenite grains (Fig. 24b).

4. Conclusions

Despite slight difference in chemical composition, brought mainly to concentration of Si and Al, elaborated steels show different microstructure in the initial state. Steel with higher Al concentration has stable microstructure of austenite with annealing twins, while steel with higher Si concentration consists of certain portion of ε martensite in form of plates. The differences in chemical composition don't have meaningful influence on behaviour of these steels in conditions of hot-working. Solutioning the steels do not change its phase composition but has essential effect on a grain size of austenite, which is fine-grained up to a temperature of about 1000°C.

Elaborated steels are characterized by relatively high values of flow stress, equal from 240 to 450 MPa, and values of ε_{max} deformation come from a range from 0.23 to 0.48, corresponding to maximum value of yield stress. Despite high value of ε_{max} at temperature of 850°C, initiation of dynamic recrystallization occurs already after true strain equal approximately 0.29, what creates possibility of refinement of microstructure. Dynamic recrystallization occurs more intensively in the steel containing 3%Al and 3%Si. It also results in faster course of removing the effects of hardening in the consequence of metadynamic recrystallization during isothermal holding of this steel in temperature of 900°C. Removal of strain hardening effects in steel 27Mn-4Si-2Al-Nb-Ti takes place mainly with participation of static recrystallization. The conditions of hot-working additionally influence phase state of investigated steels. Steel 26Mn-3Si-3Al-Nb-Ti keeps stable austenite microstructure independently from conditions of plastic deformation. Steel with initial bi-phase microstructure keeps a certain portion of martensite, yet dependant on conditions of hot-working. Grain size of γ phase as well as the state of internal stresses dependent on thermally activated mechanisms removing effects of strain hardening, have decisive influence on precipitation of the phase.

Determined half-times of recrystallization of austenite indicate that in the time of intervals between individual roll passes, partial recrystallization of γ phase should occur, contributing to achievement of fine-grained microstructure of steel. Faster course of metadynamic

recrystallization in 26Mn-3Si-3Al-Nb-Ti steel is probably caused by lower total concentration of Si and Mn, when comparing to 27Mn-4Si-2Al-Nb-Ti steel.

Taking advantage of dynamic recrystallization are confirmed by multi-stage compression results, in which lowering the flow stress in a range from 20 to 80 MPa dependent on a deformation temperature was observed and decreasing the critical strain ε_{max} to lower values. In case of applying the true strain 4x0.29, the refinement of the austenite microstructure during intervals between successive stages of deformation is caused by metadynamic recrystallization, whereas the fine-grained structure of the steel after the last deformation at a temperature of 850°C is a result of dynamic recrystallization. Further refinement of the microstructure can be obtained by isothermal holding of the steelss in a finishing hot-working temperature for about 16s. In case of applying the lower deformations 4x0.23 and 4x0.19 often used in finishing stages of hot-working, the process controlling work hardening is dynamic recovery and a deciding influence on a gradual grain refinement of microstructure has statical recrystallization occurring during intervals between successive stages of deformation and after its finish as well.

High-manganese austenite with a low SFE has a low tendency to dynamic recovery and forming a distinct cellular dislocation structure. Repeated recrystallization and corresponding grain refinement causes that the thermo-mechanically processed steel is characterized by uniform structure of γ phase without ε martensite plates. The fine-grained structure has influence on a phase composition of steel and should increase mechanical properties during subsequent cold plastic deformations.

Acknowledgements

Scientific work was partially financed from the science funds in the framework of project No. N N507 287936 headed by Prof. L.A. Dobrzański.

The authors would like to express their gratitude to Prof. R. Kuziak from Institute for Ferrous Metallurgy in Gliwice for carrying out the experiments using the Gleeble 3800 simulator.

References

1. G. Frommeyer, U. Brüx, K. Brokmeier, R. Rablbauer, Development, microstructure and properties of advanced high-strength and supraductile light-weight steels based on Fe-Mn-Al-Si-(C),

Proceedings of the 6th International Conference on Processing and Manufacturing of Advanced Materials, Thermec'2009, Berlin, 2009, 162.

2. G. Frommeyer, O. Grässel, High strength TRIP/TWIP and superplastic steels: development, properties, application, La Revue de Metallurgie-CIT 10 (1998) 1299-1310.
3. G. Frommeyer, U. Brüx, P. Neumann, Supra-ductile and high-strength manganese-TRIP/TWIP steels for high energy absorption purposes, ISIJ International 43 (2003) 438-446.
4. O. Grässel, L. Krüger, G. Frommeyer, L.W. Meyer, High strength Fe-Mn-(Al, Si) TRIP/TWIP steels development – properties – application, International Journal of Plasticity 16 (2000) 1391-1409.
5. A. Saeed-Akbari, W. Bleck, U. Prahl, The study of grain size effect on the microstructure development and mechanical properties of a high-Mn austenitic steel, Proceedings of the 6th International Conference on Processing and Manufacturing of Advanced Materials, Thermec'2009, Berlin, 2009, 194.
6. K. Renard, H. Idrissi, S. Ryelandt, F. Delannay, D. Schryvers, P.J. Jacques, Strain-hardening mechanisms in Fe-Mn-C austenitic TWIP steels: Mechanical and micromechanical characterisation, Proceedings of the 6th International Conference on Processing and Manufacturing of Advanced Materials, Thermec'2009, Berlin, 2009, 72.
7. Y.G. Kim, J.M Han, J.S. Lee, Composition and temperature dependence of tensile properties of austenitic Fe-Mn-Al-C alloys, Materials Science and Engineering A 114 (1989) 51-59.
8. S. Allain, J.P. Chateau, O. Bouaziz, S. Migot, N. Guelton, Correlations between the calculated stacking fault energy and the plasticity mechanisms in Fe-Mn-C alloys, Materials Science and Engineering A 387-389 (2004) 158-162.
9. T. Bator, Z. Muskalski, S. Wiewiórkowska, J.W. Pilarczyk, Influence of the heat treatment on the mechanical properties and structure of TWIP steel in wires, Archives of Materials Science and Engineering 28 (2007) 337-340.
10. E. Mazancova, I. Schindler, K. Mazanec, Stacking fault energy analysis of the high manganese TWIP and TRIPLEX alloys, Hutnicke Listy 3 (2009) 55-58.
11. J. Kliber, T. Kursa, I. Schindler, The influence of hot rolling on mechanical properties of high-Mn TWIP steels, 3rd International Conference on Thermomechanical Processing of Steels, TMP'2008, (CD-ROM), Padua, 2008, s.1-12.
12. J. Kliber, T. Kursa, I. Schindler, Hot rolling of steel with TWIP effect, Metallurgist – Metallurgical News 8 (2008) 481-483.
13. S. Vercammen, B. Blanpain, B.C. De Cooman, P. Wollants, Mechanical behaviour of an austenitic Fe-30Mn-3Al-3Si and the importance of deformation twinning, Acta Materialia 52 (2004) 2005-2012.
14. A. Grajcar, W. Borek, The thermo-mechanical processing of high-manganese austenitic TWIP-type steels, Archives of Civil and Mechanical Engineering 8/4 (2008) 29-38.

15. L.A. Dobrzański, A. Grajcar, W. Borek, Influence of hot-working conditions on a structure of high-manganese austenitic steels, Journal of Achievements in Materials and Manufacturing Engineering 29/2 (2008) 139-142.
16. L.A. Dobrzański, A. Grajcar, W. Borek, Microstructure evolution and phase composition of high-manganese austenitic steels, Journal of Achievements in Materials and Manufacturing Engineering 31/2 (2008) 218-225.
17. A. Grajcar, M. Opiela, G. Fojt-Dymara, The influence of hot-working conditions on a structure of high-manganese steel, Archives of Civil and Mechanical Engineering 9/3 (2009) 49-58.
18. K.K. Jee, J.H. Han, W.Y. Jang, Measurement of volume fraction of ε martensite in Fe-Mn based alloys, Materials Science and Engineering A 378 (2004) 319-322.
19. G. Niewielski, Changes of structure and properties of austenitic steel caused by hot deformation, Scientific Books of the Silesian University of Technology 58, The Silesian University of Technology Publishers, Gliwice, 2000 (in Polish).
20. G. Niewielski, M. Hetmańczyk, D. Kuc, Influence of the initial grain size and deformation parameters on the mechanical properties during hot plastic deformation of austenitic steels, Materials Engineering 24/6 (2003) 795-798 (in Polish).
21. N. Cabanas, N. Akdut, J. Penning, B.C. De Cooman, High-temperature deformation properties of austenitic Fe-Mn alloys, Metallurgical and Materials Transactions A 37 (2006) 3305-3315.
22. A.S. Hamada, L.P. Karjalainen, M.C. Somani, The influence of aluminium on hot deformation behaviour and tensile properties of high-Mn TWIP steels, Materials Science and Engineering A 467 (2007) 114-124.
23. A.S. Hamada, L.P. Karjalainen, M.C. Somani, R.M. Ramadan, Deformation mechanisms in high-Al bearing high-Mn TWIP steels in hot compression and in tension at low temperatures, Materials Science Forum 550 (2007) 217-222.
24. M. Sabet, A. Zarei-Hanzaki, S. Khoddam, An investigation to the hot deformation behaviour of high-Mn TWIP steels, 3rd International Conference on Thermomechanical Processing of Steels, TMP'2008, (CD-ROM), Padua, 2008, s.1-7.
25. J. Kliber, K. Drozd, Stress-strain behaviour and softening in manganese TWIP steel tested in thermal-mechanical simulator, Hutnicke Listy 3 (2009) 31-36.
26. L.A. Dobrzański, A. Grajcar, W. Borek, Hot-working behaviour of high-manganese austenitic steels, Journal of Achievements in Materials and Manufacturing Engineering 31/1 (2008) 7-14.
27. L.A. Dobrzański, A. Grajcar, W. Borek, Microstructure evolution of high-manganese steel during the thermo-mechanical processing, Archives of Materials Science and Engineering 37 (2009) 69-76.
28. R. Kuziak, Modelling of structure changes and phase transformations occurring in thermo-mechanical processes of steel, Institute for Ferrous Metallurgy, Gliwice, 2005 (in Polish).
29. R. Kuziak, R. Kawalla, S. Waengler, Advanced high strength steels for automotive industry, Archives of Civil and Mechanical Engineering 8/2 (2008) 103-117.

30. H. Takechi, Application of IF based sheet steels in Japan, Proceedings of the International Conference on the Processing, Microstructure and Properties of IF Steels, Pittsburgh, 2000, 1-12.
31. J. Adamczyk, A. Grajcar, Heat treatment and mechanical properties of low-carbon steel with dual-phase microstructure, Journal of Achievements in Materials and Manufacturing Engineering 22/1 (2007) 13-20.
32. A.K. Lis, B. Gajda, Modelling of the DP and TRIP microstructure in the CMnAlSi automotive steel, Journal of Achievements in Materials and Manufacturing Engineering 15 (2006) 127-134.
33. A. Grajcar, Hot-working in the $\gamma+\alpha$ region of TRIP-aided microalloyed steel, Archives of Materials Science and Engineering 28/12 (2007) 743-750.
34. B. Gajda, A.K. Lis, Thermal processing of CMnAlSi steel at ($\alpha+\gamma$) temperature range, Journal of Achievements in Materials and Manufacturing Engineering 18 (2006) 355-358.
35. E. Doege, S. Kulp, Ch. Sunderkötter, Properties and application of TRIP-steel in sheet metal forming, Steel Research 73 (2002) 303-308.
36. S. Ganesh, S. Raman, K.A. Padmanabhan, Tensil deformation-induced martensitic transformation in AISI 304LN austenitic stainless steel, Journal of Materials Science Letters 13 (1994) 389-392.
37. S. Allain, J.P. Chateau, O. Bouaziz, S. Migot, N. Guelton, Correlations between the calculated stacking fault energy and the plasticity mechanisms in Fe-Mn-C alloys", Materials Science and Engineering A 387-389 (2004) 158-162.
38. J. Adamczyk, Theoretical Physical Metallurgy, The Silesian University of Technology Publishers, Gliwice, 2002, (in Polish).
39. A.D. Paepe, J.C. Herman, Improved deep drawability of IF-steels by the ferrite rolling practice, Proceedings of the 37th Mechanical Working and Steel Processing Conference, Baltimore, 1999, 951-962.

The paper is published also in the Journal of Achievements in Materials and Manufacturing Engineering

Structure and properties of sintered tool gradient materials

L.A. Dobrzański, B. Dołżańska*
Institute of Engineering Materials and Biomaterials, Silesian University of Technology, ul. Konarskiego 18a, 44-100 Gliwice, Poland
* Corresponding author: E-mail address: barbara.dolzanska@polsl.pl

Abstract

Purpose: *The main objective of the presented is to elaborate the fabrication technology of novel sintered tool gradient materials on the basis of hard wolfram carbide phase with cobalt binding phase, and to carry out research studies on the structure and properties of the newly elaborated sintered tool gradient materials.*

Design/methodology/approach: *The following research studies have been carried out to elaborate a new group of sintered tool gradient materials, wolfram carbide with cobalt matrix, to elaborate their fabrication technology and to determine their structure and properties: a fabrication technology of mixtures and the formation technology of wolfram carbide gradient materials with cobalt matrix WC-Co was applied and elaborated; sintering conditions were selected experimentally: time, temperature and sintering atmosphere as well as isostatic condensation, ensuring the best structure and properties; phase and chemical composition of the sintered gradient WC-Co materials was determined using EDX, EBSD methods and qualitative X-ray analysis; the structure of sintered gradient WC-Co materials was investigated using scanning microscopy and transmission electron microscopy; mechanical and physical properties of sintered gradient WC-Co materials was determined: porosity, density, hardness, resistance to abrasive wear, resistance to brittle cracking.*

Findings: *The presented research results confirm that the newly elaborated technology of powder metallurgy, which consists in sequential coating of the moulding with layers having the increasing content of carbides and decreasing concentration of cobalt, and then sintering such a compact, ensures the acquisition of the required structure and properties, including the resistance to cracking and abrasive wear of tool gradient materials, due to earned high hardness and resistance to abrasive wear on the surface as well as high resistance to cracking in the core of the materials fabricated in such a way.*

Practical implications: *The material presented in this paper is characterized by very high hardness of the surface and relative ductility of the core. TGM with smooth changes of the cobalt phase in the material.*

Originality/value: *The obtained results show the possibility to manufacture TGMs on the basis of different portions of cobalt reinforced with hard ceramics particles in order to improve the abrasive resistance and ductility of tool cutting materials.*

Keywords: *Cemented carbides; Mechanical alloying; Powder Metallurgy*

Reference to this paper should be given in the following way:

L.A. Dobrzański, B. Dołżańska, Structure and properties of sintered tool gradient materials, in L.A. Dobrzański (ed.) Effect of casting, plastic forming or surface technologies on the structure and properties of the selected engineering materials, Open Access Library, Volume 1, 2011, pp. 89-132.

1. Introduction

A rapid development of the industry, technology and know-how induces the introduction of higher standards to meet the requirements which the cemented tool materials have to satisfy with respect to mechanical properties and resistance to wear. The functional properties of many products and of their components depend not only on the ability to transfer mechanical load through the whole active section of the component, on its physicochemical properties but also on the structure and properties of the material. The common fault of the operating tools is their tendency to crack, which in most cases eliminate the tool from further service, and the wear gradually and progressively diminishes its operating efficiency. Hence the resistance to cracking is a basic property, since the occurrence of minute microstructural defects results in the formation and propagation of cracks, whereas the resistance to wear stays unchanged [9,21, 39,49,58].

A considerable share of cobalt matrix results in high ductility of the core, since the propagation of a crack through cobalt is connected with the dissipation of relatively high energy. In contrast, transcrystalline cracks through carbide grains have the character of low energy brittle cracks. The combination of high hardness and resistance to abrasive wear with high resistance to brittle cracking is unobtainable in one homogeneous material. The acquisition of tool materials (Tool Gradient Materials (TGMs)) fabricated with the use of

powder metallurgy method, in effect of the gradient change of binding cobalt phase and the reinforcing phase of wolfram carbide, aims to solve the problem involving the combination of high hardness and resistance to abrasive wear with high resistance to brittle cracking, and consequently, to ensure their optimal synergy with operating conditions. The cutting edges of drill bits should combine in themselves these two contradictory properties where the surface layer is resistant to abrasive wear and the base is characterized by raised resistance to brittle cracking (Fig. 1) [1-10,17,23,33,60].

Figure 1. *Diagram of the cemented tool gradient material [49]*

One of numerous methods facilitating the fabrication of tool gradient materials is the technology of powder metallurgy. Through the application of the powder metallurgy technology for the fabrication of tool gradient materials we can closely control the chemical and phase composition as well as the structure of particular material layers [34-36,60]. In the Institute of Engineering Materials, at the Division of Materials Processing Technology, Management and Computer Techniques in Materials Science, research studies have been carried out for several years yielding the elaboration of a fabrication method of tool gradient materials with the application of powder metallurgy technology [23,34-49,50,53-56,59]. The desired material structure was obtained by the preparation of appropriate mixtures from the powder of wolfram carbide and cobalt, selection of suitable pressing pressure and technological conditions of cementing.

The objective of the presented here is to elaborate a fabrication technology of the newly developed cemented tool gradient materials on the basis of hard phase of wolfram carbide with the cobalt binding phase, and to carry out research studies on the structure and properties of the newly elaborated cemented tool gradient materials.

2. Experimental

2.1. Material and preparation of specimens for analysis

The analysis was carried out on specimens produced with the conventional method of powder metallurgy which consists in compacting in a closed moulding the successive, added layers having a gradually changing volumetric share of cobalt and wolfram carbide. In the research studies, we applied the powders of wolfram carbide (Fig. 2) and of cobalt (Fig. 3), having the chemical properties presented in Table 1. When selecting the material, we accepted the requirements involving its application in agreement with the Standard PN-ISO 513:1999.

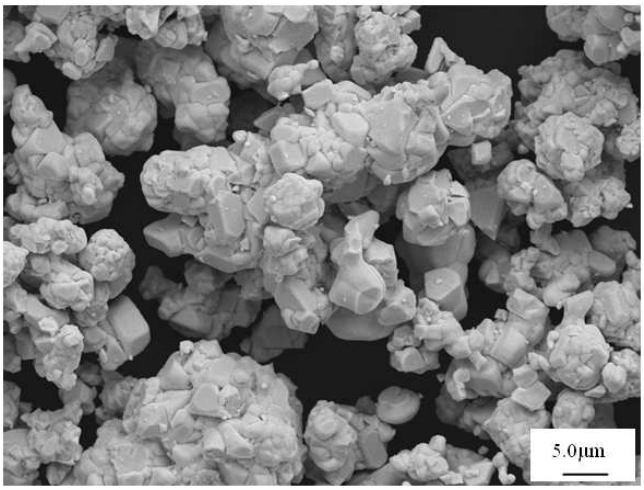

Figure 2. *Wolfram carbide powder*

The material for analysis was being prepared in two stages. In the first stage of the studies a set of mixtures of different chemical composition was elaborated, and then the compacts from wolfram carbide with cobalt matrix were formed, coating the moulding with successive layers of variable phase composition (Table 2). The selection of chemical composition of the materials was made experimentally through the change of cobalt concentration as the binding phase within the range from 3 to 15% and the share of wolfram carbide from 97 to 85%. The formation of the wolfram carbide and cobalt powder mixtures consisted in the preparation of appropriate portions of the said powders, adding each time paraffin as a sliding agent of the volumetric share of 2%. The powders prepared in this way were ground within the time

interval from 1 to 20 hours in a high-energy mill with ceramic balls (Fig. 4) and in a planetary ball mill with the balls from cemented carbides in order to make the powders homogeneous/uniform (Fig. 5). It was determined after the preliminary analyses that the time of 8 hours is long enough to ensure the homogeneity of the mixture and to coat the carbide grains with a cobalt layer.

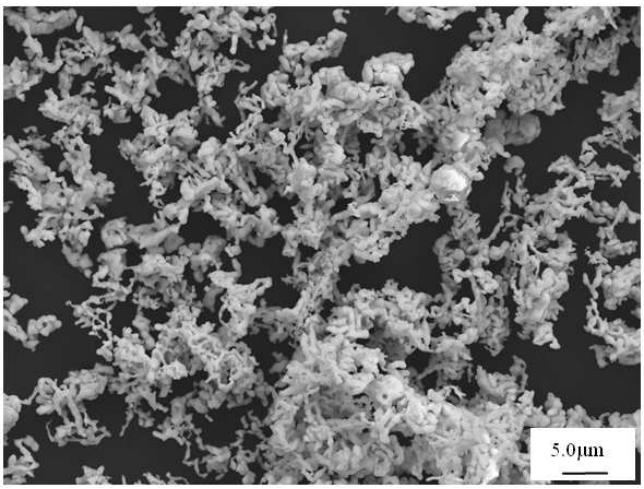

Figure 3. *Cobalt powder*

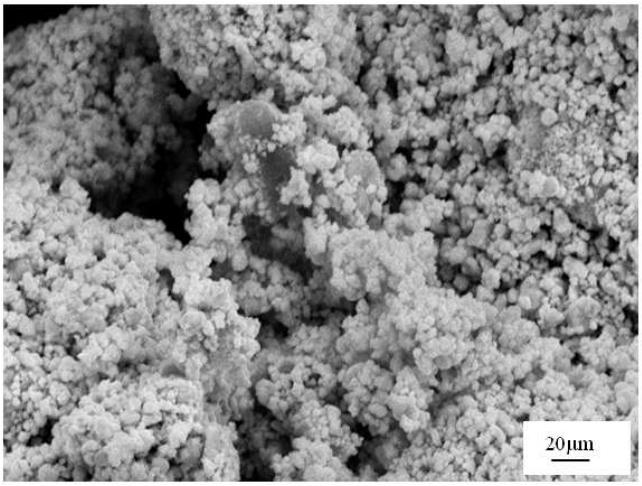

Figure 4. *Mixture of WC powder (97%), Co powder (3%) after 8 hours of milling in the high-energy mill of the spex type*

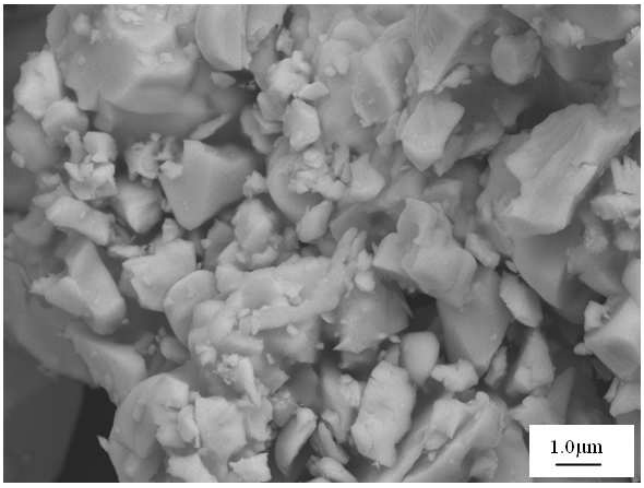

Figure 5. *Mixture of WC powder (97%), Co powder (3%) after 8 hours of milling in the ball mill*

Table 1*. Chemical composition of powders from wolfram carbide and cobalt*

Element	Mass concentration of particular elements in the powder	
	WC	Co
Mn	< 0.001	< 0.001
Ca	< 0.001	< 0.001
Zn	< 0.001	< 0.001
Si	< 0.002	< 0.002
Pb	< 0.002	< 0.002
Ni	< 0.002	< 0.002
S	< 0.002	< 0.002
Cu	< 0.002	< 0.002
O	0.45	0.45
Co	0.09	-
C	0.02	0.02

Using the obtained mixtures, WC-Co compacts were prepared for analysis in which, from the surface side of the layer, successive transit layers were formed with progressively lower share of wolfram carbide down to the base. The pressure during the pressing was being selected experimentally, pressing the powders in a closed moulding on a uniaxial hydraulic press under the pressure changing within the range from 300 to 450 MPa. The pressing

pressure was being selected by testing the densification of the powder mixture and observing the metallographic compacts. Ultimately, the pressure of 340 MPa was selected for further analyses.

a) **b)**

Figure. 6. *a) Compact pressed under the pressure of 340MPa from the 3-7%Co/97-73%WC_5 material, b) cemented tool material 3-7%Co/97-93%WC_5*

The compacts prepared in this way were characterized by smooth surface and had no signs of cracking, delamination or chipping (Fig. 6). The denotation of specimens and the volumetric share of the particular components in the mixture is presented in Table.2.

The cementing of the produced compacts was carried out in a vacuum furnace at the temperature Tsp=1450°C (Fig. 6b). Then, basing on the preliminary macroscopic observations of the sinters and on the porosity and density tests, assuming low porosity and high density as a selection criterion, a four-layer material containing from 3 to 9% of Co and from 97 to 91% of Co was selected for further research. During the selection process we were also taking into account the structure demonstrating uniform distribution of particular components in a given layer and the lack of surface deformation of the sinter. It was found, basing on preliminary metallographic observations and on the analyses of gradient porosity and density of tool materials having different number of layers and different phase composition of particular layers, that an excessive rise of the phase share difference between successive layers of the material has a negative influence on the structure and properties of the material.

Table 2*. Denotation of WC-Co tool gradient material specimens*

Denotation	3-15Co/97-85WC_3	3-9Co/97-91WC_4	3-7Co/97-93WC_5	3-15Co/97-85WC_5
Material type	3%Co+97%WC	3%Co+97%WC	3%Co+97%WC	3%Co+97%WC
	9%Co+91%WC	5%Co+95%WC	4%Co+96%WC	6%Co+94%WC
	15%Co+85%WC	7%Co+93%WC	5%Co+95%WC	9%Co+91%WC
		9%Co+91%WC	6%Co+94%WC	12%Co+88%WC
			7%Co+93%WC	15%Co+85%WC

a)

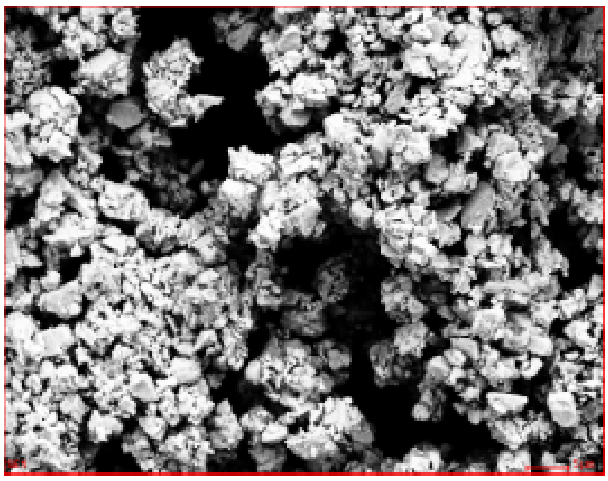

b)

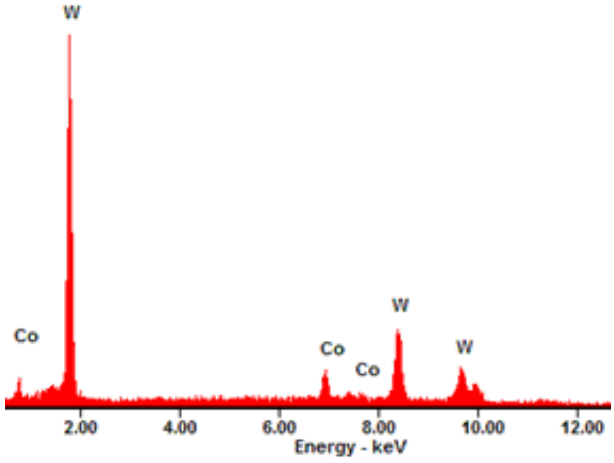

Figure 7. *a) Mixture of WC powder (97%), Co powder (3%) after 8 hours of milling in a ball mill, b) Intensity graph as the function of the energy dispersion intensity of X-ray radiation for the WC powder (97%), Co powder (3%) after 8 hours of milling in a ball mill*

The second stage of research involving the applied material fabrication technology consisted in milling the selected mixtures of wolfram carbide and cobalt in a ball mill with carbide balls for 8 hours (Fig. 7). The produced powder mixtures were then scattered down into the moulding, which yielded layers of gradually changing volumetric concentration of cobalt

and wolfram carbide share. In the material of the volumetric concentration of 3% Co and 97%WC in the surface layer, four further transit layers were formed with the 2% rise of cobalt concentration, down to the base layer containing 9% of Co and 91% of WC. Hence the denotation of the specimen being 3-9Co/97-91WC_4 (Table 2). The compacts were obtained in effect of the pressing at the already determined pressure of 340 MPa.

Then, basing on literature analysis [12-19, 28-32, 41-49, 53, 59], cementing conditions were selected experimentally. The specimens were cemented in a vacuum furnace in the conditions presented in the Table 3. In order to obtain better densification level, after the ultimate cementing, the condensation of sinters through hot isostatic pressing – HIP) was applied at the temperature of 1425°C and under the pressure of 200 MPa, as well as the sintering technology under pressure (Sinter-HIP) at the temperature of 1420°C and under the pressure of 6 MPa (Table 3).

Table 3. *Cementing conditions for the newly elaborated tool gradient material 3-9%Co/97-91%WC*

Cementing type	Cementing conditions		
	t_{sp} [min]	T_{sp}	
Unbound	30	1400˚C 1430˚C 1460˚C	
With isostatic condensation	90	1400˚C 1430˚C 1460˚C	1425˚C
Under pressure	60	1420˚C	

In one apparatus and in one cycle the processes of deparaffination, cementing and hot isostatic condensation in argon atmosphere under the pressure of 6 MPa were carried out. Then, for the obtained tool gradient materials, metallographic tests were carried out, physical and mechanical properties of the sinters were determined and the distribution of eigen-stresses in the material after sintering and during the operation were analyzed.

2.2. Methodology

The density of the cemented tool gradient materials was determined in congruence with the Standard PN-EN ISO 3369:2010. The density of the sinters was measured using the methods of underwater weighing and air weighing. The results were subjected to statistical analysis.

The measurement of open and total porosity was carried out using the following equations:

$$P_o = \frac{m_n - m_s}{m_n - m_w} \times 100\% \tag{2.1}$$

where:
Po – open porosity [%],
m_s – mass of dry specimen [g],
m_w – mass of underwater weighed specimen [g],
m_n – mass of water saturated specimen [g].

$$P_c = \frac{d - d_p}{d} \times 100\% \tag{2.2}$$

where:
P_c – total porosity [%],
d – true density of the material [g/cm^3],
d_p – apparent density [g/cm^3].

The metallographic tests were carried out on polished sections of the cemented specimens. The specimens were sectioned along the plane perpendicular to the formed layers on the cut-off machine "Minitom" (Struers), using water cooling. Then they were hot mounted in thermohardening resin, ground on diamond shields of the grain size from 220 to 1200 µm/mm^2 at the speed of 300 rev/min and polished on diamond pastes of the granulation from 9 to 1 µm at the velocity of 150 rev/min.

The structure of the fabricated WC-Co tool gradient materials was observed in the scanning electron microscope Supra 35 (Zeiss Company). To obtain the images of the investigated specimens, we applied the detection of secondary electrons (SE) and of backscattered electrons (BSE) with the accelerating voltage from 5 to 20 kV and with the maximum magnification of 20000 times. The quantitative and qualitative X-ray analysis and the analysis of surface distribution of elements was carried out on the ground and polished sections in the scanning electron microscope (SEM) Supra 35 of Zeiss Company furnished with the X-ray energy-dispersive detector EDS.

The texture, grain size and their orientation distribution along the cross-section of WC-Co tool gradient materials was determined using the Electron Backscatter Diffraction method (EBSD) in the scanning electron microscope Supra 35 of Zeiss Company (Fig. 8). Before the testing the specimens were subjected to long-lasting grinding and then polishing with small thrusts using the SiO_2 suspension of the granulation of 0.04 µm. The analysis was carried out with the magnification of 4000x, scanning range of 40 µm x 40 µm, step of 100 nm in four measurement points of the material. In order to improve the image of Kikuchi diffraction lines, the image and background were subjected to averaging. The detachment of background is aimed to eliminate all intensity gradients present on the image and to improve the contrast of diffraction lines, since the algorithms identifying the qualities are more efficient in the case of images having uniform, averaged intensity [29, 40, 44]. The pattern of Kikuchi lines is defining the orientation set-up of each of the investigated microareas dependent on the crystallographic orientation. The diffractions were solved using a program with the application of algorithms allowing for the diversification of Kikuchi lines properties such as width, length, contrast against the surroundings and brightness.

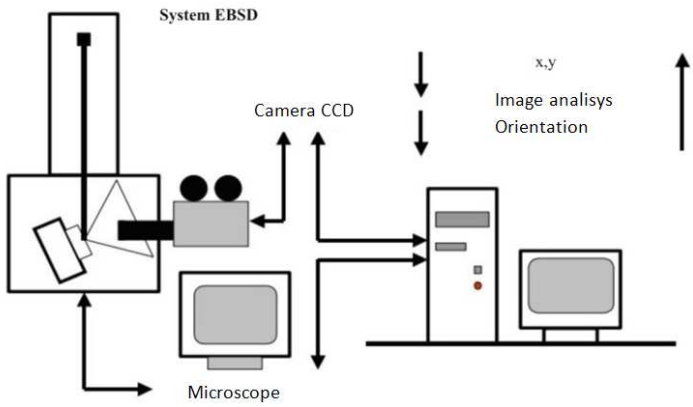

Figure 8. *Flow-chart of EBSD system*

The analyses of phase composition of cobalt or carbide powders and of cemented gradient materials were carried out with the application of the X-ray diffractometer X'Pert PRO of PANalytical Company in the Bragg-Brentano system, using Kα ray filtering of the cobalt tube with the voltage of 40 kV and filament current of 30 mA. The measurement of the secondary radiation intensity was carried out within the angle range 2Θ from 30 to 120 with the step of

0.05° and calculation time of 10 s using the strip detector Xcelerator in the geometry of grazing incident X-ray diffraction technique with the application of a parallel-beam collimator before the proportional detector.

The diffraction tests and the analyses of the structure of thin foils from the selected places on the specimens from cemented tool gradient materials were carried out in the transmission electron microscope (TEM) JEM 3010UHR of JEOL Company, with the accelerating voltage of 300 kV. Thin foils were prepared from 1mm thick sinters cut off on the MINITOM precision cut-off machine from the cross section of the tool gradient material. The sinters were subjected to semi-mechanical decrement of the thickness of 80 μm on the diamond shield of the gradation of 220 μm/mm^2, and then to final decrement on an ion polisher using the apparatus of the Gatan Company. The thin foils prepared in this way were investigated in the transmission electron microscope, carrying out the observations in light field and dark field and making the diffraction analyses. The diffractograms from the transmission electron microscope were solved with the Diphra computer program.

The hardness of the materials was determined using the Vickers method with the indenter load of 10 and 300 N respectively. The operating time of the total loading force applied on the indenter was 15 seconds. The measurement was carried out along the whole cross-section width of the cemented specimens, starting the measurement 0.22 mm away from the external surface of the surface layer and finishing the measurement around the base area.

The testing on abrasive wear was carried out with the application of apparatus designed in the Institute of Engineering Materials and Biomaterials of the Silesian University of Technology (Fig. 9). The preparation of specimens for analysis consisted in grinding the surface on a diamond shield of the grain size of 1200 μm/mm^2 to ensure flat and even surface. On the specimens produced in this way the tests were carried out using a counter-specimen made up by a ceramic ball Al_2O_3 of the diameter of 5.556 mm. The tests were carried out with a diversified number of cycles 1000 and 5000, which translates itself respectively into 4 and 20 m, and with different loading 2.5 and 10 N. Due to the combination of the assumed in this way testing conditions, four results were obtained for the surface layers of each investigated specimen, whereby the abrasive wear could be determined. The same set of tests was carried out for the particular materials of the base, and then the respective measurement results were compared to verify the influence of the structure gradient on the functionality properties. The extent of wear was determined basing on geometric measurement of the wear and calculating its volume. The decrease of volume as the indication of absolute wear is applied when the decay of mass is too small and difficult to estimate [48]. The observation of wear was also

carried out on the confocal microscope LMS 5 Exciter and in the scanning electron microscope (SEM).

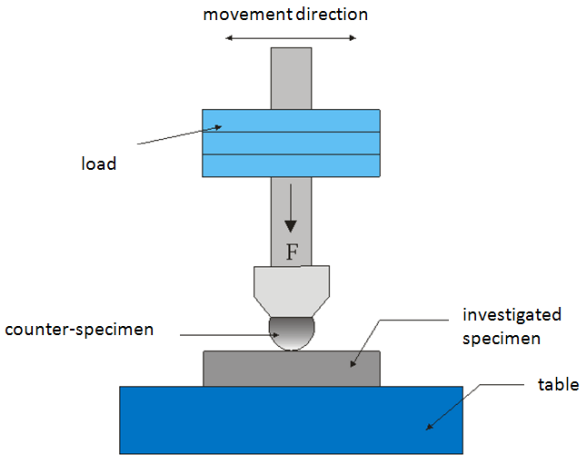

Figure 9. *Diagram of the apparatus for testing the resistance to abrasive wear*

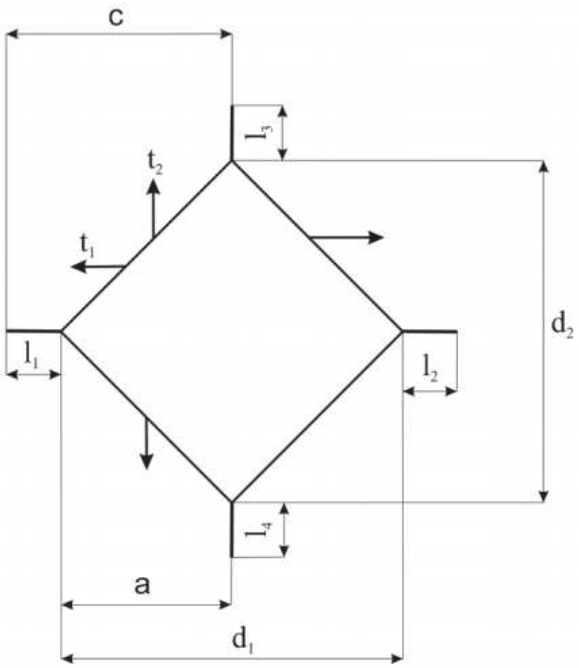

Figure 10. *Diagram of the cracking system obtained with Vickers method – Palmqvist method*

The tests involving the resistance to brittle cracking (K_{IC}) were performed in congruence with the Standard ISO 28079:2009, making use of the Palmqvist method (Fig. 10). The tests were carried out on the appropriately prepared specimens, polished to eliminate surface stresses which had been introduced to the hard surface layer through the gradation of chemical composition of the material, and then etched in the Murakami reagent of the composition ($[K_3Fe(CN)_6 + KOH + H_2O]$) to ensure a precise read-out of the cracking length.

The following equations were applied to determine the K_{IC} coefficient:

$$H = \frac{1.854 \times P}{[(d_1 + d_2) \times \frac{1}{2})]^2} \quad [\mathrm{N/mm^2}] \tag{2.3}$$

where:

P – applied load [N],

d_1, d_2 – length of the imprint diameter [mm].

$$T = l_1 + l_2 + l_3 + l_4 \tag{2.4}$$

where:

T – the total of cracking lengths [mm].

$$K_{IC} = A\sqrt{H} \times \sqrt{\frac{P}{T}} \quad [\mathrm{MNm^{-3/2}}] \tag{2.5}$$

where:

A – constant 0.0028.

The results of the investigation studies involving the density, porosity, hardness, abrasive wear and brittle cracking were subjected to statistical workout, calculating for each of the measurement series the arithmetic average, standard deviation and the confidence interval of the average value at the significance level $\alpha = 0.05$. For the measurement results of hardness and brittle cracking of the cemented tool gradient materials, the linear correlation factor was calculated and its significance test was carried out. The said characteristics were determined using the module ‘Data analysis’ available in Microsoft Excel.

Also the regression function was determined which is approximating the dependence of the

investigated output variable Y (e.g. material hardness or microhardness) on the input variables Xi (e.g. volumetric share of cobalt or temperature).

In the tests on the tool gradient materials of carbide, the finite elements method was applied for the computer simulation of eigen-stresses and strains of material operation [13, 18, 31-35, 53-56]. The true model of the tool gradient material was designed in the program Inventor 11, and the strength analysis was carried out using the program ANSYS 12.0. On account of the predicted simulation range, parametric input files were elaborated which allow to carry out the analysis comprehensively.

In order to carry out the simulation of eigen-stresses of the tool gradient material, the following boundary conditions were accepted:

- the change of cementing temperature is reflected by the cooling process of the specimen from 1400, 1420, 1460°C to the ambient temperature of 22°C,
- for the fabricated material, the material properties were accepted basing on the characteristics cards of MatWeb catalogue which were presented in Table 4.

Table 4. *List of mechanical and physical properties accepted in the computer simulation of eigen-stresses occurring in the fabricated material consisting of four layers of a difference share of wolfram carbide and of different cobalt concentration [48, 61]*

Properties	Phase composition of the layers of tool gradient material			
	3%Co+97%WC	5%Co+95%WC	7%Co+93%WC	9%Co+91%WC
Young modulus [Pa]10^9	665	640	615	590
Poisson factor	0.2809	0.2815	0.4774	0.5338
Density [kg/m^3]10^3	15.4	15.1	14.8	14.5
Thermal expansion [1/C] 10^{-6}	4.1	4.3	4.5	4.7
Thermal conductivity [W/ Mc]	98	90	82	76
Specific heat [J/kgC]	138.7	144.5	150.3	156.1
Resistivity (specific resistance) [Ωm]	5.4252	5.442	5.4588	5.4756
Tensile strength [Pa]10^6	1670.75	1641.25	1611.75	1580.25

The model whereof the objective is to determine eigen-stresses of tool operation was worked out using the finite elements method, assuming the true dimensions of the specimen (Fig. 11), where: the first layer – 3%Co+97%WC, the second layer – 5%Co+95%WC, the third layer – 7%Co+93%WC, the fourth layer – 9%Co+91%WC.

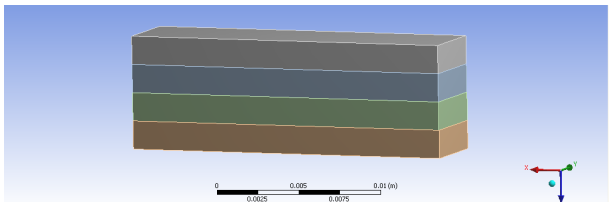

Figure 11. *True model of the fabricated material consisting of four layers of different share of wolfram carbide and of different cobalt concentration*

The true model was subjected to digitization (Fig. 12). The calculation model consists of 4968 nodes and 760 elements.

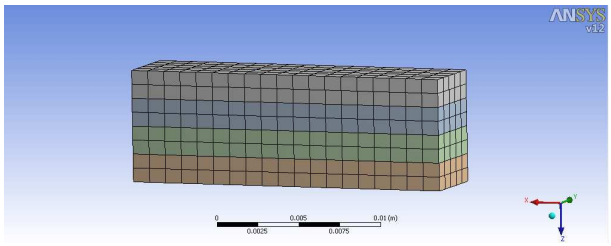

Figure 12. *True model of the fabricated material consisting of four layers of different share of wolfram carbide and different cobalt concentration after digitization*

For further simulation the same model was applied with the addition of the following boundary conditions:

- the sinter was fixed on one of the sides of the fabricated material by depriving the nodes lying on this plane of all degrees of freedom (Fig. 13),
- the force of 26000 N was applied which was reflecting the operation of the tool (Fig. 13).

The computer simulation was carried out in three stages:

- the first stage involved the simulation of eigen-stresses of the sinter consisting of four layers of different share of wolfram carbide and cobalt depending on the cementing temperature,

- the second stage included the comparative analysis of the computer simulation of the eigen-stresses of the tool gradient material with the experimental results,
- the third stage involved the computer simulation of operation strains of the fabricated tool gradient material applied for example in mining machinery.

The model whereof main objective is to determine eigen-stresses of the fabricated material was made using the finite elements method, assuming the true dimensions of the specimen (Fig. 13).

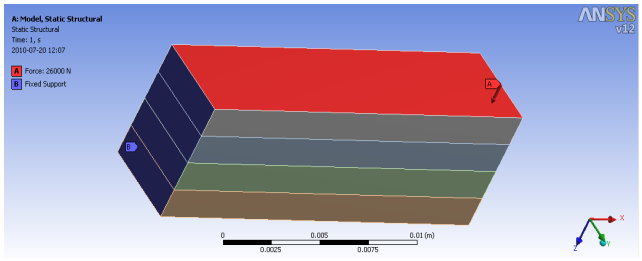

Figure 13. *True model of the fabricated material consisting of four layers of different share of wolfram carbide and of different cobalt concentration with the applied boundary conditions*

In order to verify the obtained results experimentally through the modeling with the finite elements method on the basis of measurements carried out by means of X-ray spectrometry, the true eigen-stresses in the investigated materials were calculated. The calculations were carried out with the use of $\sin^2\psi$ method, basing on the brand-name program X'Pert Stress Plus. The program has a data base with data indispensible to calculate the values of material constants. Then, the comparative analysis of computer simulation with experimental results was carried out.

3. Results

3.1. Structure, phase and chemical composition of the elaborated gradient materials

Irrespective of the type of cemented materials, their good properties depend on the fabrication and preparation of powders, forming and cementing conditions. In the cementing

process we cannot eliminate potential faults which can be brought about during the preparation of powders or during their formation, and therefore each of the fabrication stages has a considerable influence on the properties of the final product. An appropriate preparation of powder mixtures of homogeneous distribution of WC carbide in cobalt matrix is relevant in view of further pressing and cementing of tool materials. The experimental research demonstrated that the grinding in a high-energy mill yields exceptionally good results as early as after 8 hours. The mixture of powders is forming numerous conglomerates but it is homogeneous, and the cobalt grains surround the WC carbides. The mixture of WC-Co powders after grinding in a ball mill over the same time period is also homogeneous with locally occurring large carbides of the size of about 6 μm which were not fully powdered during the grinding process (Figs. 14, 15).

Irrespective of the applied mill, the rise of grinding time to 20 hours has only slight influence on grain comminution of WC carbide, and hence the grinding time of 8 hours was accepted as optimal.

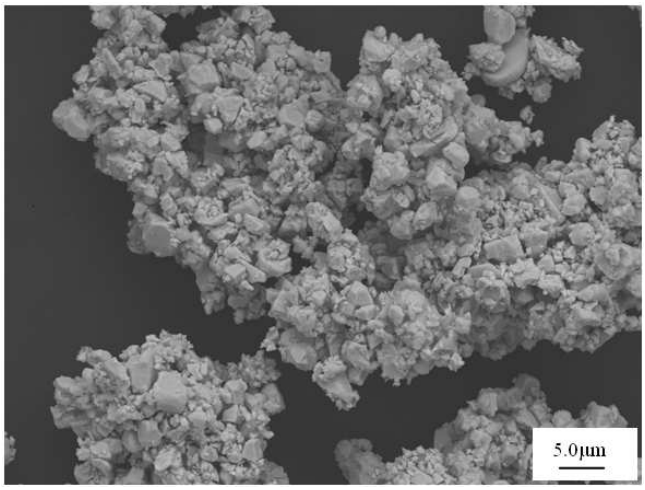

Figure 14. *Powder mixture WC (95%), Co (5%) after 8 hours of grinding in a ball mill*

For the formation of powders we applied a moulding enabling the pressing of specimens designated to three-point bending after cementing. The prepared powder mixtures of the changing share of WC carbide and appropriate concentration of cobalt matrix were being ground adding paraffin of the 2% volumetric share to reduce the friction between powder

grains and between powder and moulding during the pressing process. Due to small grain size of cobalt and WC carbide, having the average size of maximum 6 µm and connected with it poor flow rate of powder, the formation of further layers of powders mixture of the changing phase share is technologically difficult, and therefore it was agreed that maximum four layers would be formed. Commercial mixtures of WC-Co powders are prepared in the form of granulate of the granulate size of about 0.1 mm, and they are characterized by flow rate of about 30 s. The tests on the flow rate of the produced mixture was not successful since the powders did not pass through the designed for such tests Hall funnel. In spite of poor flow rate and low bulk density of the powders mixture, the compacts were characterized by sharp edges and did not exhibit cracks or chipping. Fig. 16, which presents the compact, illustrates the borders between successive layers. The pressing was carried out within the pressure range applied in the industry from 300 to 450 MPa, and experimentally the pressure for pressing was determined at 340 MPa.

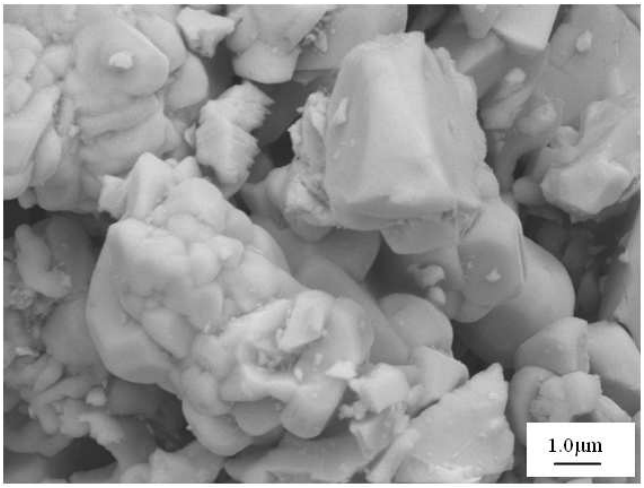

Figure 15. *Powder mixture WC (91%), Co(9%)*

In order to consolidate the powders we applied unbound sintering, sintering with isostatic condensation or hot isostatic pressing. For the unbound sintering and for the sintering with isostatic condensation we applied the temperature of 1400, 1430 and 1460°C. The hot isostatic sintering was carried out at the temperature of 1420°C.

a)

b)

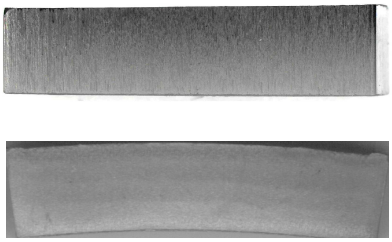

3-9%Co/97-91%WC_4

Figure 16. *a) Compact pressed under the pressure of 340 MPa, b) sintered tool material*

The sintering methods were selected basing on the results described in works [12,20-23, 28,30,43,60] in which, very frequently, for economical reasons or to simplify or accelerate the technological process of the fabricated tool materials, pressing and sintering is combined into one operation. It involves pressing in raised temperature or sintering under pressure. The material obtained in this way is not much porous and its physical and strength properties are considerably better as compared to separate operations of pressing and sintering [18-20,28,35,52,61]. Irrespective of the phase composition of the specimens it can be observed that all materials were deformed after sintering. Undoubtedly, one of the reasons of this deformation is non-homogeneous density of the compact. Numerous pores in lower layers of the compact get condensed during the sintering and hence there is a great contraction in this area. We can observe that the deformation of the specimen in which the phase share of WC powder is changing from 97% in the external layer to 85% in the layer around the core is higher (Fig. 17) as compared to the specimen in which the phase share of WC is changing from 97 to 91% (Fig. 16).

Figure 17. *Sintered tool material 3-5%Co/97-85%WC_5*

Therefore, in the further studies, we were using specimens in which the share of WC carbide was changing from 97% in the external layer to 91% in the layer around the core. The

appropriateness of the phase composition selected in this way has been confirmed by the research results involving the tests on hardness, density and porosity. Basing on the measurements of density and porosity of the sinters, it was demonstrated that the sintered tool gradient materials based on the powders of wolfram carbide and cobalt are characterized by higher density and lower porosity after sintering with isostatic condensation as compared to the materials after unbound sintering. Analyzing the influence of technological conditions of sintering on density and porosity, it has been demonstrated that the rise of density with the simultaneous decrease of porosity is dependent on temperature, time and technological conditions of sintering (Table 3).

Figures 18-19 present X-ray diffractograms from the investigated tool gradient materials of WC-Co type. The research studies confirmed the presence of phases corresponding to each material type. The X-ray diffractogram contains the reflexes from WC phases and reflexes from Co of the hexagonal structure.

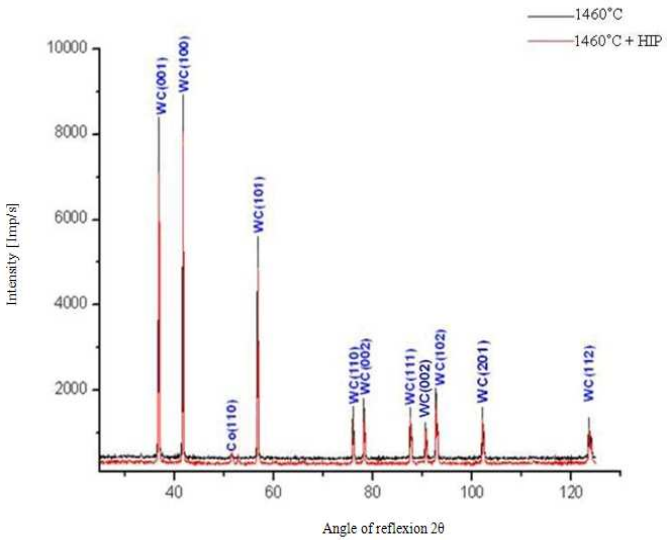

Figure 18. *Results of X-ray qualitative phase analysis of tool gradient materials 3-9%Co/97-91WC_4, sintered in a vacuum furnace at temperature T_{sp}=1460°C and subjected to isostatic condensation at T_{sp}=1425°C*

Basing on the density measurements of the sinters of the newly elaborated tool gradient materials with cobalt matrix, it was found that the highest density is exhibited by the sintered

material with the use of hot isostatic condensation and sintering under pressure. The density of materials obtained in effect of sintering with the use of hot isostatic condensation at the temperature of 1460, 1430 and 1400°C is respectively 14.60, 14.19, 14.16 g/cm^3, and the density of materials subjected to unbound sintering at the temperature of 1460, 1430 and 1400°C is respectfully 12.96, 13.79 and 14.42 g/cm^3. Analyzing the influence of technological parameters of sintering on density, it was found that the density is increasing with a simultaneous decrease of porosity with the rise of time and temperature of the process.

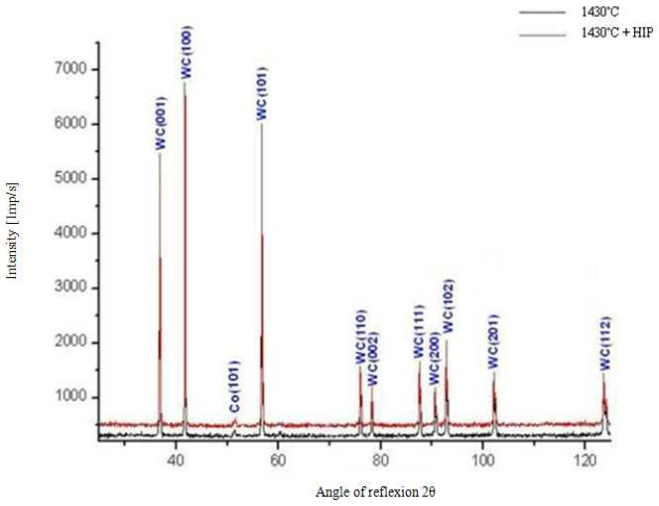

Figure 19. *Results of X-ray qualitative phase analysis of tool gradient materials 3-9%Co/97-91WC_4, sintered in the vacuum furnace at temperature T_{sp}=1430°C and isostatically condensed at T_{sp}=1425°C*

The presence of cobalt in the material results in the formation of liquid phase which during the sintering brings about the formation of low-melting eutectic phase. In this process it is most difficult to maintain the gradient which has a tendency to fade due to the oriented mass transport. In order to avoid such a phenomenon, a high-temperature synthesis with short sintering time is applied [4,15,19,20,53,55,61].

Since most of the infusible grains in the material have the size from 2.5 to 3 micrometers and the dissolution process involves only a small portion of their volume, therefore the final product consists of great oval grains of the basic phase bound by the unified liquid phase (Fig. 20).

In spite of low volumetric share of cobalt, at high sintering temperature this phase is

melting and is partially dissolving the surface of WC carbides. Hence the rise of the volumetric share of liquid phase i.e. low-melting eutectics during the sintering process, which moistens the WC solid phase (Fig. 20). In effect of the above, the capillary forces occurring around grain borders decrease the volume of the pore, increasing in this way the density of the material. The liquid phase during cooling and crystallization assumes the form of small layers separating solid grains (Fig. 20).

a)

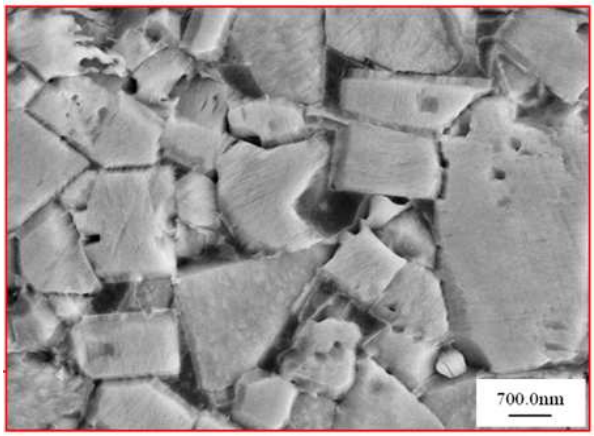

b)

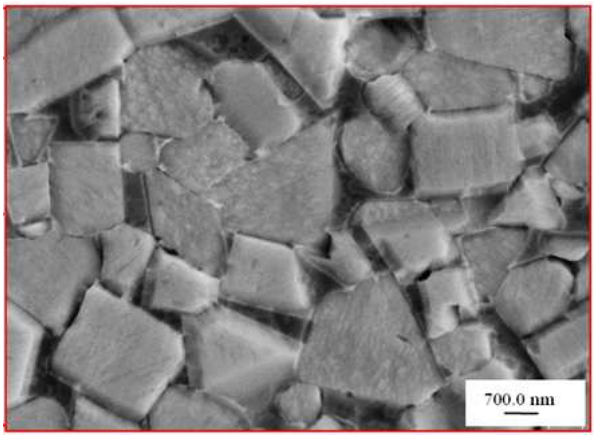

Figure 20. *Layer structure a) surface layer b) bottom layer of gradient the material 3-9%Co/97-91%WC_4 sintered in a vacuum furnace at temperature T_{sp}=1430°C and subjected to hot isostatic condensation at the temperature T_{sp}=1425°C*

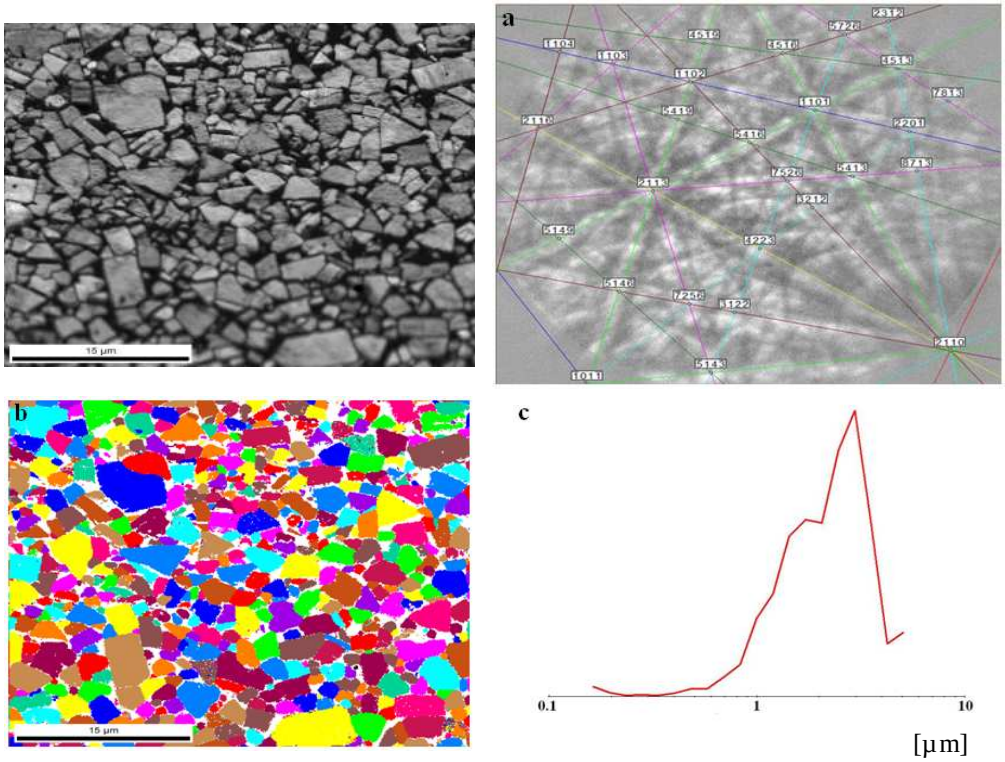

Figure 21. *Structure of gradient material 3-9%Co/97-91%WC_4, sintered in the vacuum furnace at temp. T_{sp}=1400°C and subjected to hot isostatic condensation at temp. T_{sp}=1425°C, the first layer: a) indexation of the diffraction of the Kikuchi line, b) map of grain size distribution, c) diagram of grain size distribution*

The research studies carried out with the use of EBSD method confirmed that the newly elaborated gradient material consists of basic grains of the components of WC and Co powders in which, along the interphase border, there are no microcracks or other discontinuities (Fig. 21). The colored topography maps present the crystallographic orientation of the grains of WC sintered carbides where the particular coloring of the WC grains denotes the normal direction to the surface plane of each grain. The measurements of grain size show that the average size of the grain ranges from 2.5 to 3 µm (Fig. 21c). A considerable decrease of grain size as compared to the input material (6 µm) is connected with the long-lasting milling of the powders of wolfram carbide.

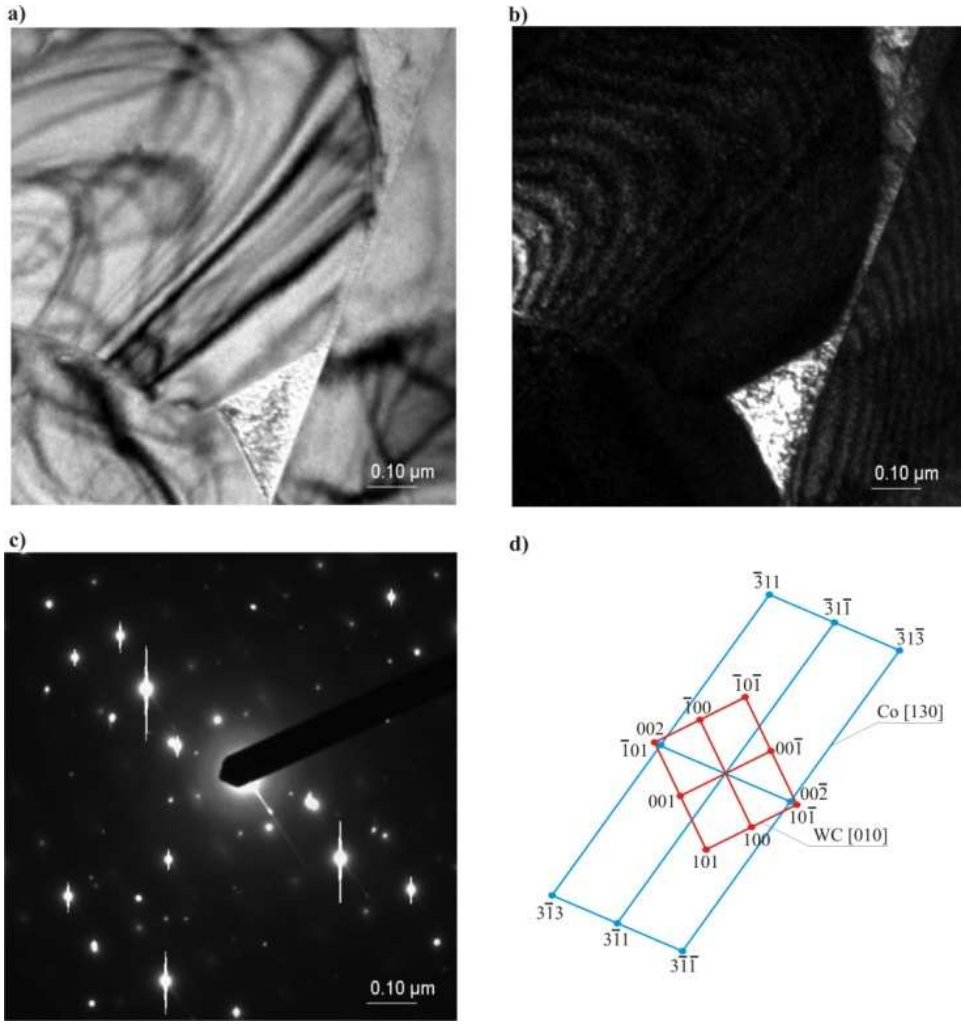

Figure 22. *Thin foil structure from WC-Co sintered carbide after sintering at temp. 1460°C; a) image in light field, b) image in dark field from the reflexes (002)Co and (101)WC, c) diffractogram from the area as in Fig. a, d) solution of the diffractogram from the Figure c*

The method of X-ray quantitative analysis carried out with the use of X-ray energy-dispersive spectrometer EDS confirms the occurrence of the element W, C and Co respectively in the solid phase of wolfram carbide and in the binding phase of cobalt in the particular layers of the tool gradient material. The newly elaborated tool gradient material is characterized by compact structure due to the uniformly distributed share of binding phase between the solid

phase of carbide. It was also found that the preparation time of mixtures is sufficient enough to ensure that the wolfram carbide grains are coated with cobalt matrix.

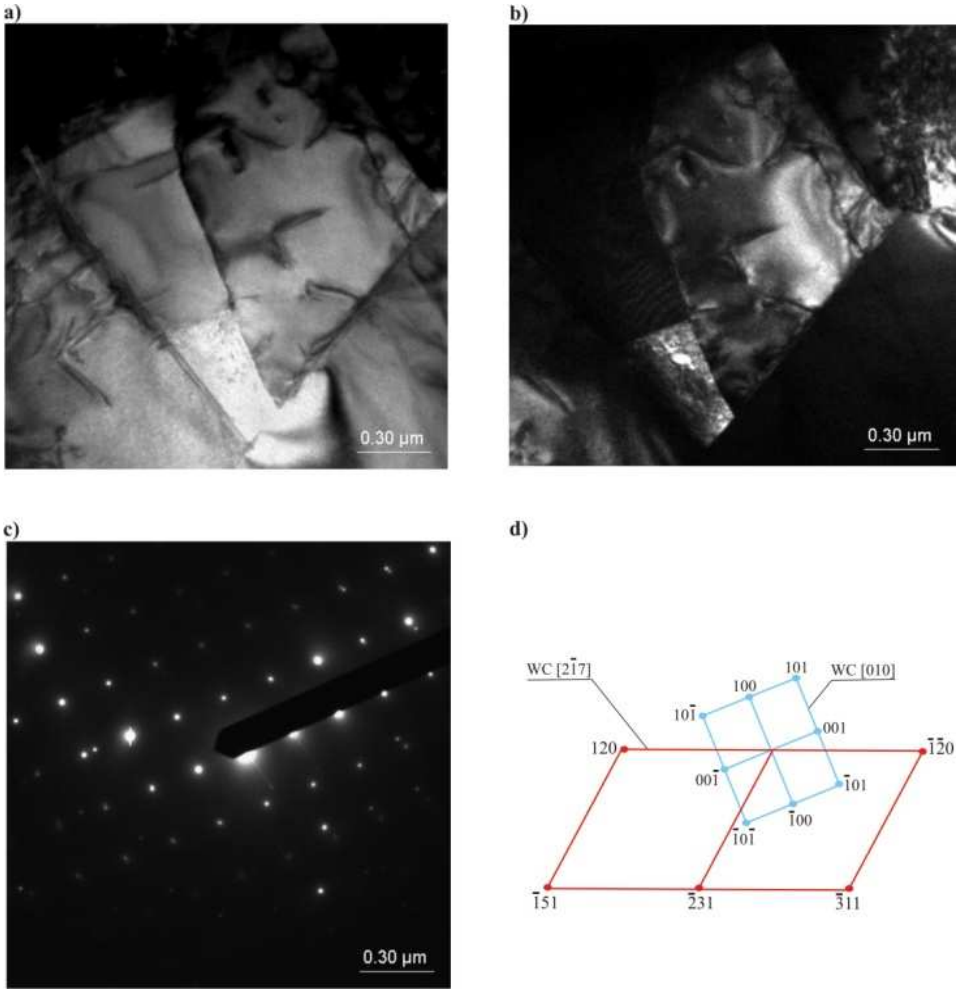

Figure 23. *Thin foil structure from WC-Co sintered carbide after sintering at temp. 1460°C; a) image in light field, b) image in dark field from the WC reflexes, c) diffractogram from the area as in Fig. a, d) solution of the diffractogram from Fig. c*

In effect of the research on thin foils fabricated in the transmission electron microscope (Figs. 22-24), it was confirmed that the sintered tool gradient materials contain the grains of wolfram carbide and cobalt of the hexagonal network (in the JCPDS file respectively no. 25-

1047 and 05-0727). Cobalt as a binding phase fills up the space between WC grains, frequently in the form of a thin layer between the neighboring carbide grains (Figs. 22-24).

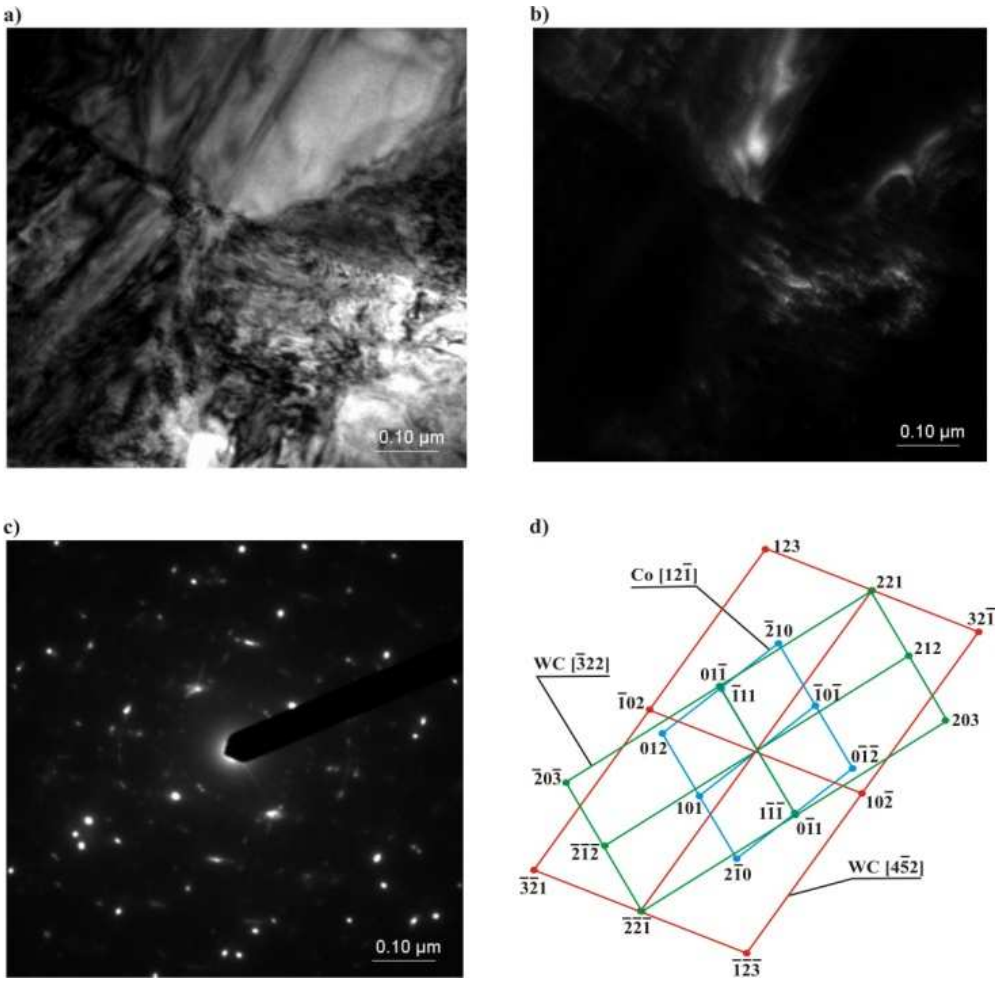

Figure 24. *Thin foil structure from WC-Co sintered carbide after sintering at temp. 1400°C; a) image in light field, b) image in dark field from the reflex (101)Co, c) diffractogram from the area as in Fig. a, d) solution of the diffractogram from the Figure c*

The observations involving the structure of thin foils (Figs. 23, 24) show that in the wolfram carbide grains there are many network flaws, in particular dislocation. A part of dislocations and other network flaws can be brought about during the long-lasting milling of

the powder, in effect of which crumbling and fracture of WC grains is taking place. In some WC grains there are subgrains whose disorientation angle is from several to around a dozen degrees. After the sintering process at the temperature of 1400°C we found that in many WC carbide grains there are thin sinters, most probably twins, of the thickness from several to several dozen nm These sinters are parallel to the WC planes {010} and {110} – as in the four-index Miller-Bravais denotation.

3.2. Mechanical properties and resistance to abrasive wear of the elaborated gradient materials.

The measurement results involving HV hardness (Figs. 26-28) of the fabricated tool materials of the growing share of WC carbide with respect to cobalt matrix in the direction towards tool surface are indicative of a gradual rise of hardness. The hardness of the 3-9%Co/97-91WC_4 material sintered in vacuum, depending on the sintering temperature, can be placed within the range of 1390-1460 HV in the surface layer and is decreasing, with the rise of the distance between the measurement point and the external surface of the surface layer, to 1290-1330 HV in the base (Fig. 26).

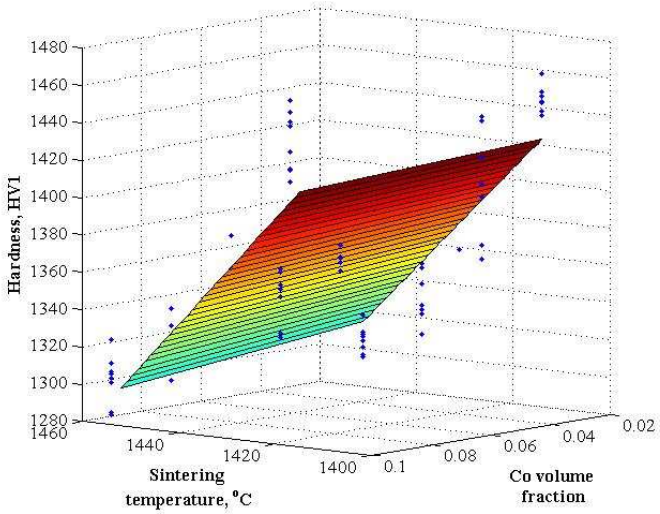

Figure 26. *Diagram of regression function describing the relation of HV1 hardness, volumetric share and sintering temperature for the material 3-9%Co/97-91%WC_4*

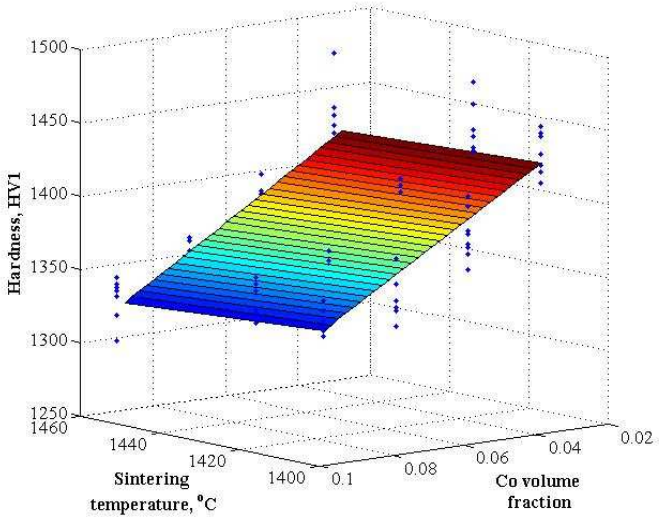

Figure 27. *Diagram of regression function describing the dependence of hardness on the volumetric share of cobalt and sintering temperature, for the 3-9%Co/97-91%WC_4 material subjected to sintering and hot isostatic condensation at the temperature of 1425°C in a vacuum furnace*

The hardness of the 3-9%Co/97-91WC_4 material sintered and subjected to isostatic condensation at the temperature of 1425°C is within the range of 1430-1470 HV in the surface layer and is decreasing to 1300-1360 HV in the base (Fig. 28). The hardness of the 3-9%Co/97-91WC_4 material sintered with isostatic condensation at the temperature of 1420°C is within the range of 1340-1400 HV in the surface layer and is decreasing, with the rise of the distance between the measurement point and the external surface of the surface layer, to 1310 HV in the base (Fig. 27). In effect of the carried out hardness tests we did not find any considerable difference in hardness of the investigated materials subjected to unbound sintering and those with isostatic condensation.

The relation involving the changes of HV hardness of materials with the changing share of Co phase, volumetric share and sintering conditions was described with the use of a regression function. The value of the multidimensional correlation factor and that of its significance level confirm the correct dependence of hardness on sintering conditions and on cobalt present in particular layers of the material.

Figures 26-28 present the diagrams of regression functions describing the dependence of

hardness on the volumetric share and sintering temperature (T_{sp}) and on the function in the planes defined by the values of input variables, together with confidence intervals at the significance level of α=0.05. The carried out measurements demonstrated the influence of sintering technological conditions and volumetric share of WC-Co phases on the hardness of the sintered tool gradient materials.

The research results involving the resistance to brittle cracking K_{IC} of the sintered tool gradient materials of different volumetric share of WC and Co phases in each material layer are presented in Figs. 29-30. The results involving the K_{IC} factor are indicative of a considerable dependence between sintering parameters and the resistance to cracking of particular tool materials. The material 3-9%Co/97-91%WC_4 sintered at the temperature of 1460°C (Figs. 31-35) and the material sintered under pressure at the temperature of 1420°C is characterized by high resistance to brittle cracking. The average value of K_{IC} factor of the surface layer of the material is 15 [$MNm^{-3/2}$] and of the base 18 [$MNm^{-3/2}$].

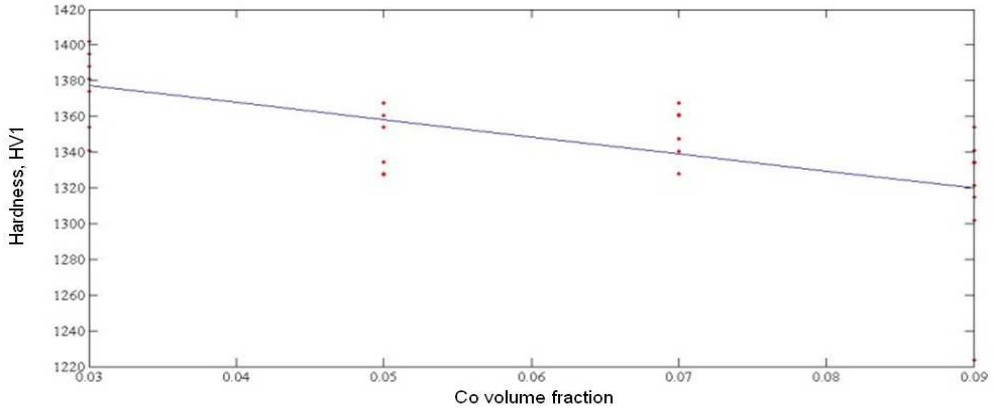

Figure 28. *Diagram of regression function describing the dependence of hardness on the volumetric share of cobalt for the 3-9%Co/97-91%WC_4 material subjected to sintering with hot isostatic condensation at the temperature T_{sp}=1420°C*

The average values of the K_{IC} factor of the material sintered at the temperature of 1420°C are respectively 17 [$MNm^{-3/2}$] for the surface layer and 19 [$MNm^{-3/2}$] for the base. The dependence of K_{IC} factor for the investigated materials of different Co concentration on the volumetric share and sintering conditions is presented by means of a regressive function. The value of multidimensional correlation factor and that of its significance level confirm the

dependence of K_{IC} factor on sintering conditions and volumetric concentration of cobalt in the particular layers of the material. Figs. 29-30 present the diagrams of regression functions describing the dependence of K_{IC} factor of the materials on the volumetric share, sintering temperature (T_{sp}) as well as their sections in the planes defined by the selected values of input variables, together with confidence intervals at the significance level of α=0.05.

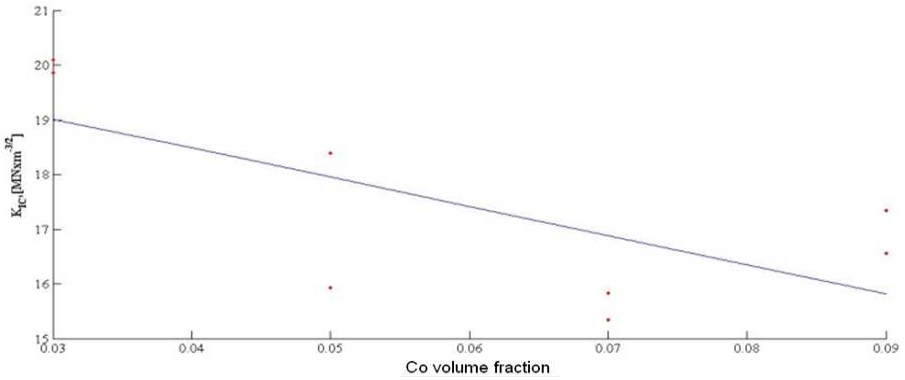

Figure 31. *Diagram of the regression function describing the dependence of brittle cracking on the volumetric share of cobalt for the 3-9%Co/97-91%WC_4 material sintered under the pressure in a vacuum furnace at the temperature T_{sp}=1420°C*

The lack of distinguished difference of the K_{IC} factor in the surface layer and in the base of materials sintered with isostatic condensation can be explained by too long sintering time, resulting in partial or total decay of gradient structure.

The carried out microscopic observations of specimen fractures (Fig. 31) are characterized by hollow systems and convexities, which displays a flaky character of the fracture typical for brittle materials.

The research results involving the resistance of the materials to cracking show that the areas rich in cobalt matrix are characterized by higher K_{IC} factor as compared to the areas rich in WC (Fig. 32).

In order to compare the tribological properties of the fabricated gradient materials, the test on the resistance to abrasive wear was carried out in the system 'investigated specimen and Al_2O_3 ball' as a counter-specimen. The results of the carried out abrasive trial (Table 4) show that the materials sintered with isostatic concentration are characterized by much lower abrasive wear than the materials obtained as a result of unbound sintering. The wear of gradient

materials subjected to unbound sintering, depending on the share of binding phase, temperature, load and number of cycles is presented in Table 4.

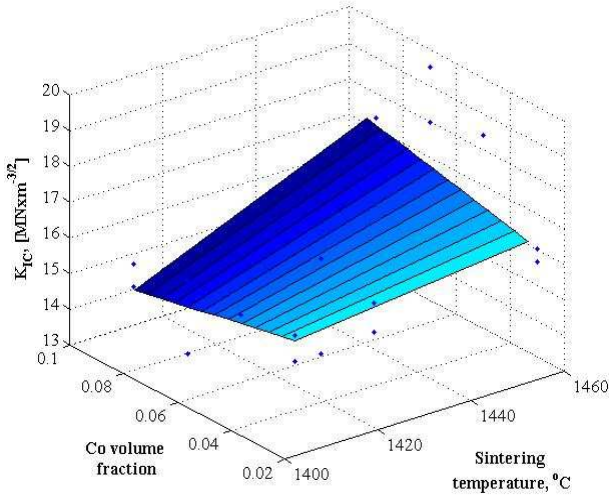

Figure 29. *Diagram of the regression function describing the dependence of brittle cracking on temperature and Co volumetric share for the 3-9%Co/97-91%WC_4 material sintered in a vacuum furnace*

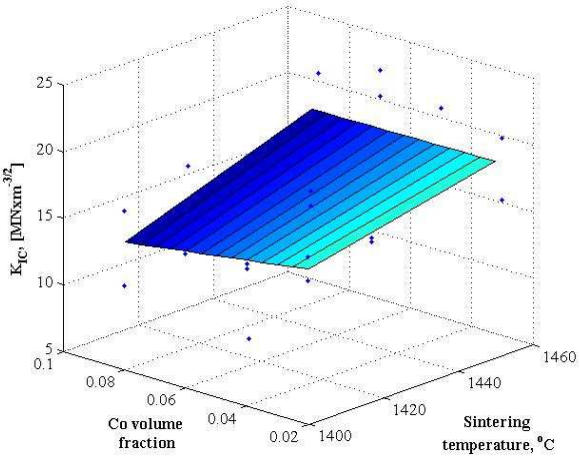

Figure 30. *Diagram of the regression function describing the dependence of brittle cracking on temperature, and on cobalt share for the 3-9%Co/97-91%WC_4 material sintered and subjected to hot isostatic condensation at the temperature of 1425°C in a vacuum furnace*

The decrement of material is effected by the separation of particles due to micromachining or scratching around the friction areas counter-specimen –material as a result of loose or fixed particles of the abrasive material or sticking out particles of the uneven, hard carbide phase (Fig. 33) [11, 39, 42, 44].

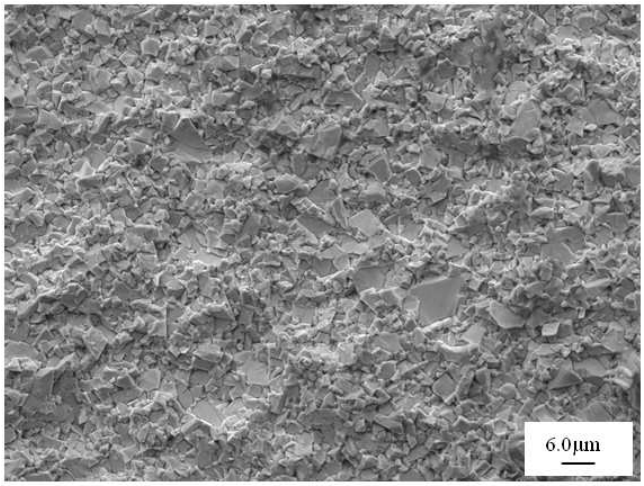

Figure 32. *Structure of the fracture of the surface layer of the 3-9%Co/97-91%WC_4 material sintered in a vacuum furnace at the temperature T_{sp}=1460°C and subjected to hot isostatic concentration at the temperature T_{sp}=1425°C in a vacuum furnace*

Non-uniform width of the wear bespeaks of the occurrence of wear which consists in sticking of the waste material to the counter pecimen which then breaks off in other places causing local unevenness in the place where the wear is lower (Fig. 33). Using the X-ray quantitative microanalysis carried out with the X-ray energy-dispersive spectrometer EDS along the wear path of the material the presence of aluminum and oxygen was confirmed, most probably released by aluminum oxide Al_2O_3 (Fig. 33), due to sticking of waste material to the counter-specimen which then breaks off in other places causing local unevenness around which the wear is lower [9, 10, 17, 30, 44, 51, 55, 56, 58].

The measurement results involving the abrasive wear of the sintered tool gradient materials of wolfram carbide with cobalt matrix are indicative of a gradient change of the properties of the investigated materials, depending on the share of binding phase. Therefore,

the wear of gradient materials is conditioned by many factors: the share of binding phase, loading value of counter-specimen and also the friction path (number of cycles).

3.3. Computer simulation of stresses, strains and displacements of the fabricated gradient material depending on the sintering temperature

Figure 35 presents the results of numerical analysis using the finite elements method gathered in the form of maps of stress distribution in the tool material consisting of four layers of different concentration of wolfram carbide and cobalt for the sintering temperature of 1400, 1420 and 1460°C. The elaborated model of the tool allows to simulate the influence of sintering temperature on stresses (Fig. 35).

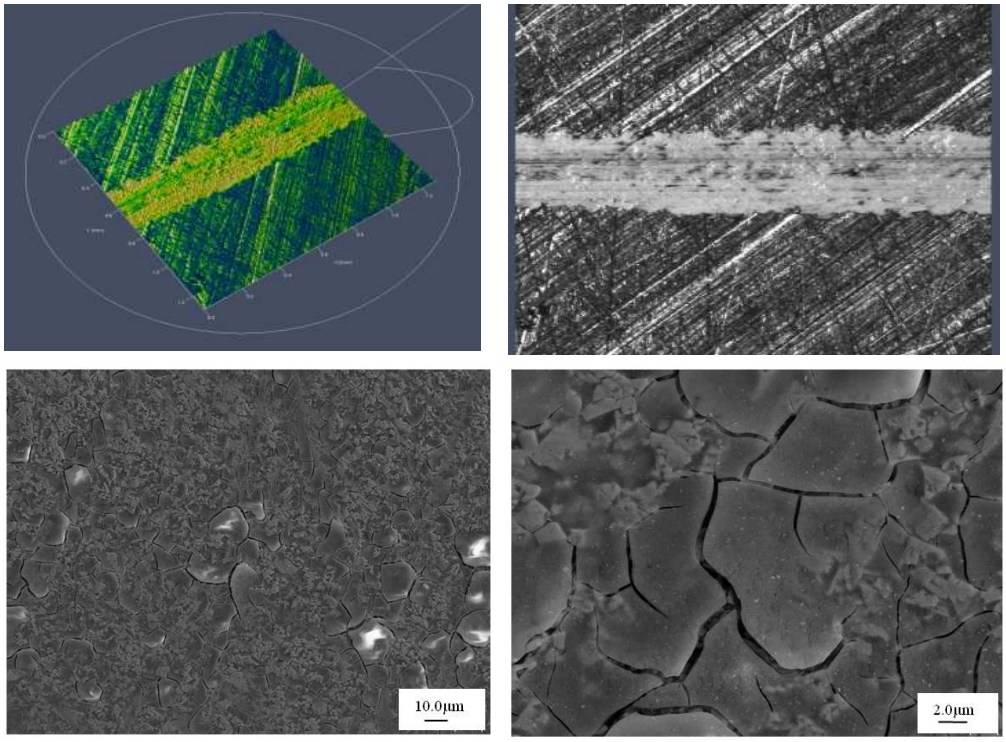

Figure 33. *Wear mark of the 3-9%Co/97-91%WC_4 material sintered in vacuum at the temperature of 1400°C and subjected to isostatic condensation at the temperature of 1425°C after 1000 cycles with the load of 10 N in the base*

Table 4. *Tribological wear of gradient material 3-9%Co/97-91%WC_4*

Layer denotation	T_{sp} [˚C]	Load [N]	Number of cycles	Statistical quantities	
				Arithmetic average	Standard deviation
97%WC - 3%Co	1460	2.5	5000	4.05×10^{-4}	0.36×10^{-4}
		10	5000	11.63×10^{-4}	0.62×10^{-4}
91%WC - 9%Co		2.5	5000	13.25×10^{-4}	1.22×10^{-4}
		10	5000	23.41×10^{-4}	1.58×10^{-4}
97%WC - 3%Co	1430+1425	2.5	5000	5.43×10^{-4}	0.29×10^{-4}
		10	5000	21.49×10^{-4}	1.71×10^{-4}
91%WC - 9%Co		2.5	5000	6.49×10^{-4}	0.40×10^{-4}
		10	5000	26.60×10^{-4}	2.80×10^{-4}

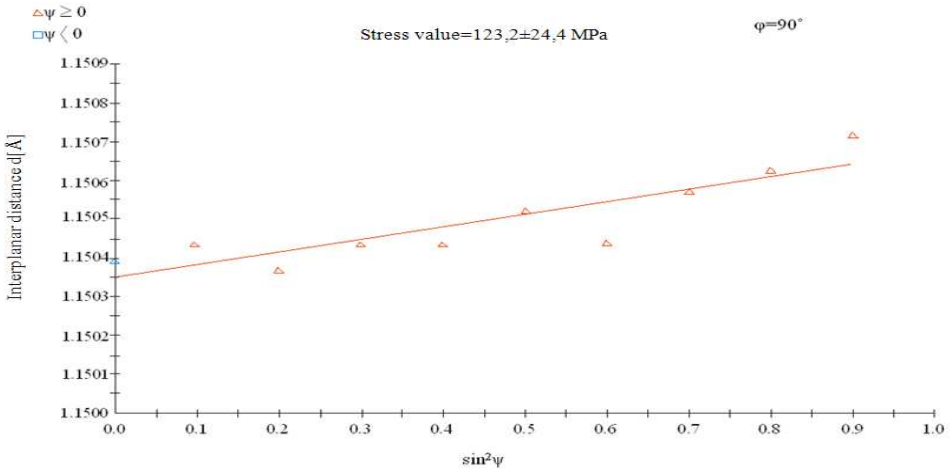

Figure 34. *Changes of interplanar distance d of the reflex (201) in the function of $sin^2\psi$, sintering temperature of 1400°C, 3%Co+97%WC*

The calculation results of eigen-stresses in the investigated materials obtained on the basis of reflex shift analysis (201) using the $\sin^2\psi$ method carried out to verify the modeling results are presented in Fig. 34 and in Table 5.

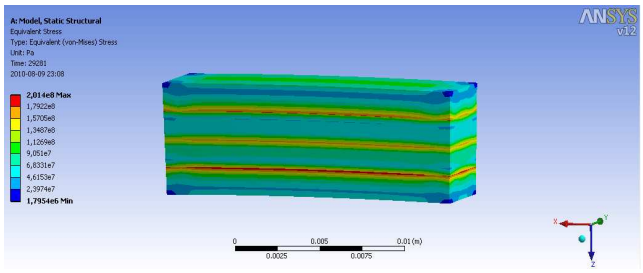

Figure 35. *The distribution of simulated eigen-stresses occurring in the cutting edge of a tool consisting of four layers of different share of wolfram carbide and cobalt for the sintering temperature of 1400°C*

Basing on the carried out investigation studies it was demonstrated that the highest stress values are characteristic of the material sintered at the temperature of 1460°C. They occur in the surface layer and equal 162 ± 24 MPa, and the simulated stresses equal 170 MPa. The base is characterized by lower stresses as compared to the upper layer. The stresses determined experimentally equal 91±22 MPa and the simulated stresses 80 MPa. The lowest stresses determined experimentally and with the use of computer simulation occur in the tool gradient material sintered at the temperature of 1400°C. The value of these stresses determined experimentally in the upper layer is 123±24 MPa, and the value of simulated stresses equals 116 MPa. The calculated values of stresses in the base are 41±9 and 36 for the simulated stresses.

Table 5. *Comparison of stresses obtained experimentally with the results of computer simulation*

	Sintering temperature, [°C]	Stresses determined experimentally, [MPa]	Simulated stresses, [MPa]
Upper layer 3%Co+97%WC	1400	123 ± 24	116
	1420	141 ± 7	140
	1460	162 ± 24	170
Bottom layer 9%Co+91%WC	1400	41 ± 9	36
	1420	87 ± 10	80
	1460	91 ± 22	80

The results of eigen-stresses obtained with the computer simulation using the finite elements method are in agreement with the results of stress measurements obtained with the use of $\sin^2\psi$ method (Table 5).

Figures 36-38 present the results of the computer simulation of the fabricated material, allowing for the mechanical loads simulating operating conditions (in mining or drilling machines), gathered as the maps of shifts, strains and stresses distribution.

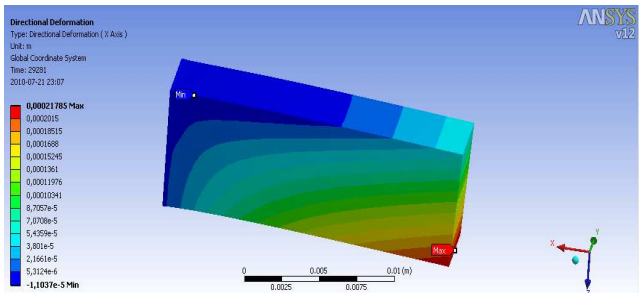

***Figure 36**. Distribution of the simulated shifts occurring in the cutting edge of a tool consisting of four layers of different share of wolfram carbide and cobalt for the sintering temperature T_{sp}=1400°C*

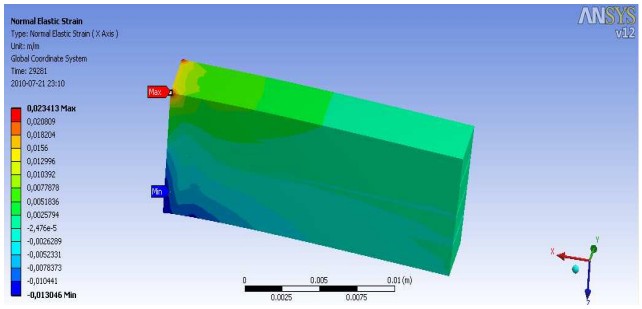

***Figure 37.** Distribution of the simulated strains occurring in the cutting edge of a tool consisting of four layers of different share of wolfram carbide and cobalt for the sintering temperature T_{sp}=1400°C*

It was demonstrated, basing on the elaborated model, that through appropriately applied technological procedures, it is possible to evoke tensile stresses in the surface layer of the material, which will increase the resistance of this material to the formation and propagation of

cracks. The difference in the value of heat expansion coefficient in the material is introducing tensile eigen-stresses on the surface of the material after its cooling from the sintering temperature to the ambient temperature.

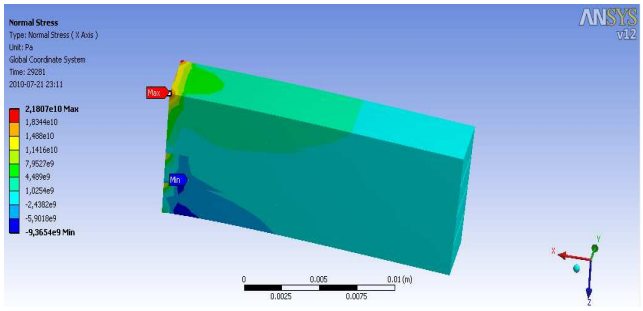

Figure 38. *Distribution of the simulated stresses occurring in the cutting edge of a tool consisting of four layers of different share of wolfram carbide and cobalt for the sintering temperature* T_{sp}*=1400°C*

Basing on the analysis of the obtained results: among others such as hardness, brittle cracking and abrasive wear it has been demonstrated that this novel method makes it possible to fabricate tool gradient materials resistant to abrasive wear with high resistance to brittle cracking.

4. Conclusions

Basing on the analysis of the obtained results involving sintered tool gradient WC-Co materials, the following conclusions have been formulated:

1. In effect of the carried out investigation studies on the newly elaborated gradient WC-Co tool materials fabricated with a novel technology consisting in sequential coating of the moulding with the layers of WC-Co powder mixtures of the decreasing share of WC carbides from 97 to 91% in the direction from the surface to the core and then pressing and sintering the compacts, the thesis put forward in the PhD dissertation has been proved, and it has been demonstrated that the application of the elaborated fabrication method for the production of tool materials is fully grounded, due to combining non-complementary properties of these materials i.e. resistance to abrasive wear and brittle cracking, due to

gradient structure of the fabricated material which is changing in the continuous way and which is characterized by the rise of the share of hard carbide phase in the direction from the core to the sinter surface and rising share of cobalt matrix concentration in the opposite direction.

2. The applied fabrication method of sintered tool gradient materials necessitates the preparation of WC-Co powder mixtures through their long-lasting milling during which hard and brittle WC carbides of the average equivalent diameter of the grain of 6 μm undergo fragmentation in effect of which their size after sintering does not exceed 3 μm, which has a positive influence on the resistance rise to brittle cracking in the sintered state of the fabricated tool materials to 19 $MNm^{-3/2}$ as compared to 15 $MN^{-3/2}$ characteristic of the sintered WC-Co materials containing 3% Co produced without gradient.
3. In effect of diffusion processes running during the sintering process, local unification of phase composition in the joint areas is taking place despite the laminar output structure of the compacts fabricated by coating the moulding with successive powder mixtures of a step-wise changing share of WC and Co concentration and then pressing, the gradient of changes of the final structure of the sinter is continuous and not step-wise as in the compact, yet too long heating over 90 min at high sintering temperature of 1460°C, in particular during hot isostatic sintering, results in a decay of gradient structure of the sinter due to the unification of the phase composition within the whole volume of the sinter.
4. Hardness, resistance to abrasive wear and brittle cracking of the sintered tool gradient materials are dependent respectively on the WC share and Co concentration as a binding phase and on the conditions of technological process applied for the fabrication of these materials, i.e. milling of powder mixtures, formation of the compact and sintering, yet the surface of the material is characterized by high hardness of 1460 HV, due to high WC share of 97%, and the core is characterized by higher resistance to brittle cracking 19 $MNm^{-3/2}$ as compared to the surface because of higher Co concentration of 9%, with the difference of 4 $MNm^{-3/2}$ between the K_{IC} values on the surface 15 $MNm^{-3/2}$ and in the core 19 $MNm^{-3/2}$.
5. Through the application of finite elements method we can model eigen-stresses generated in the newly elaborated tool gradient materials in effect of sintering, having the influence on the properties of these materials, and because the stress values determined through computer simulation are close to those determined experimentally, it is well-founded to apply calculation methods to estimate stresses and to draw conclusions about the trends involving the changes of the properties of the investigated tool gradient material, which necessitates further research.

Acknowledgements

The paper has been realised in relation to the project POIG.01.01.01-00-023/08 entitled "Foresight of surface properties formation leading technologies of engineering materials and biomaterials" FORSURF, co-founded by the European Union from financial resources of European Regional Development Found and headed by Prof. L.A. Dobrzański.

References

1. H.O. Andrén, Microstructure development during sintering and heat-treatment of cemented carbides and cermets, Materials Chemistry and Physics 67 (2001) 209-213.
2. Z.G. Ban, L.L. Shaw, Synthesis and processing of nanostructured WC-Co materials, Journal of Materials Science 37 (2002) 3397-3403.
3. U. Baste, S. Jacobson, A new view of the deterioration and wear of WC/Co cemented carbide rock drill buttons, Wear 264 (2008) 1129-1141.
4. K. Bonny, P. De Baets, J. Quintelier, J. Vleugels, D. Jiang, O. Van der Biest, B. Lauwers, W. Liu, Surface finishing: Impact on tribological characteristics of WC-Co hardmetals, International Journal of Reinfractory Metals and Hard Materials 43 (2010) 40-54.
5. A. Carpinteri, N. Puno, S. Puzzli, Strength vs. toughness optimization of microstructured composites, Chaos, Solitons and Fractals 39/3 (2009) 1210-1223.
6. S.I. Cha, K.H. Lee, H.J. Ryu, S.H. Hong, Analytical modeling to calculate the hardness of ultra-fine WC–Co cemented carbides, Materials Science and Engineering A 489 (2008) 234-244.
7. J.R. Cho, Optimum material composition design for thermal stress reduction in FGM lathe bit, Composites: Part A 37.
8. L.A. Dobrzański, B. Dołżańska, G. Matula, Influence of carbide (W, Ti)C on the structure and properties of tool gradient materials, Archives of Materials Science and Engineering 28/10 (2007) 617-620.
9. L.A. Dobrzański, B. Dołżańska, G. Matula, Influence of hard ceramic particles on structure and properties of TGM, Journal of Achievements in Materials and Manufacturing 24/2 (2007) 95-98.
10. L.A. Dobrzański, B. Dołżańska, G. Matula, Structure and properties of gradient cermets reinforcer with the (W, Ti)C carbides, ВісніИК 4/2 (2007) 15-20.
11. L.A. Dobrzański, B. Dołżańska, G. Matula, Structure and properties of tool gradient materials reinforced with the WC carbides, Journal of Achievements in Materials and Manufacturing Engineering 28/1 (2008) 35-38.

12. L.A. Dobrzański, K. Gołombek, Structure and properties of the cutting tools made from cemented carbides and cermets with the TiN + mono-, gradient – or multi (Ti,Al,Si)N+TiN nanocrystalline coatings, Journal of Materials Processing Technology 164-165 (2005) 805-815.
13. L.A. Dobrzański, J. Hajduczek, A. Kloc-Ptaszna, Effect of sintering parameters on structure of the gradient tool materials, Journal of Achievements in Materials and Manufacturing Engineering 36/1 (2009) 33-40.
14. L.A. Dobrzański, A. Kloc, G. Matula, J.M. Contreras, J.M. Torralba, Effect of manufacturing methods on structure and properties of the gradient tool materials with the non-alloy matrix reinforced with the HS6-5-2 type high-speed steel, Proceedings of the 11th International Scientific Conference on the Contemporary Achievements in Mechanics, Manufacturing and Materials Science CAM3S'2005, Gliwice-Zakopane, 2005, 223-228.
15. L.A. Dobrzański, A. Kloc, G. Matula, J. Domagała, J.M. Torralba, Effect of carbon concentration on structure and properties of the gradient tool materials, Journal of Achievements in Materials and Manufacturing Engineering 17 (2006) 45-48.
16. L.A. Dobrzański, A. Kloc-Ptaszna, G. Matula, J.M. Torralba, Structure and properties of a gradient tool materials manufactured using the conventional powder metallurgy method, Materials Science Forum (2009) (in print).
17. L.A. Dobrzański, A. Kloc-Ptaszna, G. Matula, J.M. Torralba, Structure and properties of gradient tool materials with the high-speed steel matrix, Journal of Achievements in Materials and Manufacturing Engineering 24/2 (2007) 47-50.
18. L.A. Dobrzański, A. Kloc-Ptaszna, G. Matula, J.M. Torralba, Structure and properties of the gradient tool materials of unalloyed steel matrix reinforced with HS6-5-2 high-speed steel, Archives of Materials Science and Engineering 28/4 (2007) 197-202.
19. L.A. Dobrzański, A. Kloc-Ptaszna, G. Matula, J.M. Torralba, Structure and Properties of Gradient Tool Materials with HS6-5-2 High-Speed Steel, Proceedings of the 7th Asia Pacific Conference on Materials Processing, Singapore, 2006, 128-133.
20. L.A. Dobrzański, A. Kloc-Ptaszna, G. Matula, Properties of sintered gradient tool WC/HS6-5-2 materials, Proceedings of the 2th International Conference on Modern Achievements in Science and Education, Netanua, Israel, 2008, 71-76.
21. L.A. Dobrzański, G. Matula, G. Herranz, A. Várez, B. Levenfeld, J.M. Torralba, Metal injection moulding of HS12-1-5-5 high-speed steel using a PW-HDPE based binder, Journal of Materials Processing Technology 175 (2006) 173-178.
22. L.A. Dobrzański, G. Matula, A. Várez, B. Levenfeld, J.M. Torralba, Structure and mechanical properties of HSS HS6-5-2 and HS12-1-5-5-type steel produced by modified powder injection moulding process, Journal of Materials Processing Technology 157-158 (2004) 658-668.
23. L.A. Dobrzański, G. Matula, A. Várez, B. Levenfeld, J.M. Torralba, Fabrication methods and heat treatment conditions effect on tribological properties of high speed steels, Journal of Materials Processing Technology 157-158 (2004) 324-330.

24. L.A. Dobrzański, A. Śliwa, W. Kwaśny, W. Sitek, The computer simulation of stresses in the Ti+TiC coatings obtained in the PVD process, Journal of Achievements in Materials and Manufacturing Engineering 17 (2006) 241-244.
25. L.A. Dobrzański, A. Śliwa, W. Sitek, W. Kwaśny, The computer simulation of critical compressive stresses on the PVD coatings, International Journal of Computational Materials Science and Surface Engineering 1/1 (2007) 28-39.
26. L.A. Dobrzański, A. Śliwa, W. Sitek, Finite Element Method application for modeling of PVD coatings properties, Proceedings of the 5th International Surface Engineering Congress, Washington, USA, 2006, 26-29.
27. L.A. Dobrzański, A. Śliwa, T. Tański, Numerical simulation model for the determination of hardness for casting the magnesium alloys McMgL16Zn1, Archives of Materials Science 29/3 (2008) 118-124.
28. M.H. Enayati, G.R. Aryanpour, A. Ebnonnasir, Production of nanostructured WC–Co powder by ball milling, International Journal of Refractory Metals and Hard Materials 27/1 (2009) 159-163.
29. P. Fan, J. Guo, Z.Z. Fang, P. Prichard, Design of cobalt gradient via controlling carbon content and WC grain size in liquid-phase-sintered WC–Co composite, International Journal of Refractory Metals and Hard Materials 27 (2009) 256-260.
30. P. Fan, J. Guo, Z.Z. Fang, P. Prichard, Effects of Liquid-Phase Composition on Its Migration during Liquid-Phase Sintering of Cemented Carbide, Metallurgical and Materials Transactions A 40/8 (2009) 1995-2006.
31. Z. Fang, G. Lockwood, A. Griffo, A dual composite of WC-Co, Metallurgical and Materials Transactions A 30 (1999) 3231-3238.
32. Z.Z. Fang, Correlation of transverse rupture strength of WC–Co with hardness, International Journal of Refractory Metals and Hard Materials 23 (2005) 119-127.
33. Z.Z. Fang, O.O. Eso, Liquid phase sintering of functionally graded WC-Co composities, Scripta Materialia 52 (2005) 785-791.
34. J.A.M. Ferreira, M.A. Pina Amaral, F.V. Antunes, J.D.M. Costa, A study on the mechanical behaviour of WC/Co hardmetals, International Journal of Refractory Metals and Hard Materials 27/1 (2009) 1-8.
35. R. Frykholm, H.O. Andre, Development of the microstructure during gradient sintering of a cementem carbide, Materials Chemistry and Physics 67 (2001) 203-208.
36. R. Frykholm, B. Jansson, H.O. Andrén, Methods for atom probe analysis of microgradients in functionally graded cemented carbides, Micron 33 (2002) 639-646.
37. R.M. German, A. Eugene, A. Olevsky, Modeling grain growth dependence on the liquid content in liquid-phase-sintered materials, Metallurgical and Materials Transactions A 29 (1998) 3057-3067.
38. V.T. Golovchan, N.V. Litoshenko, The stress–strain behavior of WC-Co hardmetals, Computational Materials Science 49/3 (2010) 593-597.

39. H.S. Kim, On the rule of mixtures for the hardness of particle reinforced composites, Materials Science and Engineering A 289 (2000) 30-33.
40. H.Ch. Kim, I.J. Shon, J.K. Yoon, J.M. Doh, Consolidation of ultra fine WC and WC–Co hard materials by pulsed current activated sintering and its mechanical properties, International Journal of Refractory Metals and Hard Materials 25/1 (2007) 46-52.
41. A. Kloc, L.A. Dobrzański, G. Matula, J.M. Torralba, Effect of manufacturing methods on structure and properties of the gradient tool materials with the non-alloy steel matrix reinforced with the HS6-5-2 type high-speed steel, Materials Science Forum 539-543 (2007) 2749-2754.
42. I. Konyashin, S. Hlawatschek, B. Ries, F. Lachmann, A. Sologubenko, T. Weirich, A new approach to fabrication of gradient WC–Co hardmetals, International Journal of Refractory Metals and Hard Materials 28/2 (2010) 228-237.
43. M.T. Laugier, Palmqvist toughness in WC-Co composites viewed as a ductile/brittle transition, Journal of Materials Science Letters 6 (1987) 768-770.
44. A. Lawley, T.F. Murphy, Metallography of powder metallurgy materials, Materials Characterization 51 (2003) 315-327.
45. G.H. Lee, S. Kang, Sintering of nano-sized WC-Co powders produced by a gas reduction-carburization process, Journal of Alloy and Compounds 419 (2006) 281-289.
46. W. Lengauer, K. Dreyer, Functionally gradient hardmetals, Journal of Alloys and Compounds 338 (2002) 194-212.
47. W. Lengauer, K. Dreyer, Tailoring hardness and toughness gradients in functional gradient hardmetals (FGHMs), International Journal of Refractory Metals and Hard Materials 24 (2006) 155-161.
48. K. Liu, X.P. Li, Ductile cutting of tungsten carbide, Journal of Materials Processing Technology 113 (2001) 348-354.
49. W. Liu, X. Song, J. Zhang, F. Yin, G. Zhang, A novel route to prepare ultrafine-grained WC-Co cemented carbides, Journal of Alloys and Compounds 458/1-2 (2008) 366-371.
50. G. Matula, L.A. Dobrzański, B. Dołżańska, Influence of cobalt portion on structure and properties of FGHM, International Journal of Materials and Product Technology 33/3 (2008) 280-290.
51. G. Matula, L.A. Dobrzański, B. Dołżańska, Structure and properties of TGM manufactured on the basis of cobalt, Journal of Achievements in Materials and Manufacturing 20 (2007) 151-154.
52. G. Matula, L.A. Dobrzański, G. Herranz, A. Várez, B. Levenfeld, J.M. Torralba, Influence of Binders on the Structure and Properties of High Speed-Steel HS6-5-2 Type Fabricated Using Pressureless Forming and PIM Methods, Materials Science Forum 534-536 (2007) 693-696.
53. A. Śliwa, L.A. Dobrzański, W. Kwaśny, W. Sitek, The computer simulation of internal stresses on the PVD coatings, Archives of Computational Materials Science and Surface Engineering 1/3 (2009) 183-188.
54. A. Śliwa, W. Kwaśny, L.A. Dobrzański, Computer simulation of stresses in coatings obtainted the PVD process, Engineering Materials 31/3 (2010) 732-734.

55. G.S. Upadhyaya, Cemented tungsten carbides, Production, Properties and Testing, Westwood, New Jersey, U.S.A., 1998.
56. G.S. Upadhyaya, Materials science of cemented carbides – an overview, Materials and Design 22 (2001) 483-489.
57. X. Wang, Z.Z. Fang, H.Y. Sohn, Grain growth during the early stage of sintering of nanosized WC-Co powder, International Journal of Refractory Metals and Hard Materials 26 (2008) 232-241.
58. X. Wu, J. Guo, Electric-discharge compaction of graded WC-Co composities, International Journal of Refractory Metals and Hard Materials 27/1 (2009) 90-94.
59. H. Zhang, Q. Lu, L. Zhang, Z. Zak Fang, Dependence of microcrack number density on microstructural parameters during plastic deformation of WC-Co composite, International Journal of Refractory Metals and Hard Materials 28 (2010) 434-440.
60. H. Zhang, Z. Zak Fang, Q. Lu, Characterization of a bilayer WC–Co hardmetal using Hertzian indentation technique, International Journal of Refractory Metals and Hard Materials 27 (2009) 317-322.
61. www.webelements.com

The paper is published also in the Journal of Achievements in Materials and Manufacturing Engineering

PVD and CVD gradient coatings on sintered carbides and sialon tool ceramics

L.A. Dobrzański, M. Staszuk*
Institute of Engineering Materials and Biomaterials, Silesian University of Technology, ul. Konarskiego 18a, 44-100 Gliwice, Poland
* Corresponding author: E-mail address: marcin.staszuk@polsl.pl

Abstract

Purpose: *The main objective of the work is to investigate the structure and properties of multilayer gradient coatings produced in PVD and CVD processes on sintered carbides and on sialon ceramics, and to define the influence of the properties of the coatings such as microhardness, adhesion, thickness and size of grains on the applicable properties of cutting edges covered by such coatings.*

Design/methodology/approach: *The investigation studies pertaining to the following have been carried out: the structures of the substrates and coatings with the application of transmission electron microscopy; the structure and topography of coating surfaces with the use of electron scanning microscopy; chemical composition of the coatings using the GDOES and EDS methods; phase composition of the coatings using X-ray diffraction and grazing incident X-ray diffraction technique (GIXRD); grain size of the investigated coatings using Scherrer's method; properties of the coatings including thickness, microhardness, adhesion and roughness; properties of the operating coatings in cutting trials. The models of artificial neural networks have been worked out which involve the dependencies between the durability of the cutting edge and properties of the coatings.*

Findings: *Good adhesion of the coatings to the substrate from sintered carbides is connected with the diffusive mixing of the components of the coating and substrate. In the case of PVD coatings obtained on sialon ceramics, the highest adhesion to the substrate (Lc=53-112 N) has been demonstrated by the coatings containing the AlN phase of the hexagonal lattice having the same type of atomic (covalence) bond in the coating as in the ceramic substrate. The damage mechanism of the investigated coatings depends to a high degree on their adhesion to the substrate. The durability of cutting edges covered by the investigated coatings depends principally on the adhesion of the coatings to the substrate, and to a lesser degree on the other properties.*

Practical implications: *While selecting a proper coating material on ceramic cutting edges, it is advisable to remember that the coatings having the same type of atomic bond as the ceramic substrate have higher adhesion to the substrate. Another relevant aspect of the research presented in the paper is the fact that the adhesion of the coatings contributes significantly to the durability of the cutting edge, whereas the microhardness of the coatings, their thickness and grain size have a slightly lower influence on the durability of the tool being coated.*

Originality/value: *The paper presents the research involving the PVD and CVD coatings obtained on an unconventional substrate such as sialon ceramics. Furthermore, to define the influence of coating properties on the durability of cutting edges, artificial neural networks have been applied.*

Keywords: *Working properties of materials and products, Mechanical properties, PVD and CVD coatings*

Reference to this paper should be given in the following way:

L.A. Dobrzański, M. Staszuk, PVD and CVD gradient coatings on sintered carbides and sialon tool ceramics, in L.A. Dobrzański (ed.) Effect of casting, plastic forming or surface technologies on the structure and properties of the selected engineering materials, Open Access Library, Volume 1, 2011, pp. 133-186.

1. Introduction

The process of machining at the beginning of the 21st century is still one of the most important production technologies applied in the industry of mechanical engineering. Even if we apply plastic hot or cold working or casting technologies, still the final working is most frequently done by machining [9,16,46,54,57,96].

The constantly improving properties of constructional materials, which are obtained through machining, are determining a demand for a high standard quality of produced tools which must satisfy such aspects as service life, hardness of the cutting edge as well as working conditions such as speed, depth and feed rate. It is the economic conditions which principally enforce the necessity to increase the efficiency of machining, which is being realized by raising the thickness of the material removed in a single pass and by reducing its time [10,42,49,70,73,84]. To meet such requirements, the tools should have high hardness and should be considerably resistant to abrasive, adhesive, diffusive and chemical wear [33,79].

Among a variety of tool making materials, sintered carbides are still a dominant group in view of machining technologies. Advantageous usability properties and hardness higher than that of high speed steel, and also a relatively low price involving their production costs make them popular and commonly applied. Furthermore, modern sintering methods make it possible to produce cutting edges from sintered carbides having very fine grains and properties better as compared to the carbides produced with standard methods [7,43,64,81]. On the other hand, the scientific and industrial environments are getting more and more interested in tool making ceramics, including also the β-sialon ceramics elaborated at the end of the 20th century. The mechanical properties of this alloy ceramics have been inherited from the isomorphic β-Si_3N_4, and the chemical properties correspond to aluminum oxide Al_2O_3 [56].

The hard coatings PVD and CVD used for cutting edges are an efficient means to increase the durability of tools made from high speed steel and sintered carbides, being already applied from the 1960s of the 20th century [4,63]. Recently, also the opinion stating that coating deposition on ceramic tools is aimless due to their hardness being high enough has been verified. There are ceramic tools offered recently on the market covered with coatings resistant to abrasion. The coatings resistant to wear based on nitrides, carbides, oxides and borides, principally of transition metals, make it possible to apply higher machining parameters of tools covered by them, and also enable working processes without the application of cutting-tool lubricants [11,12,22,23,25,72,85].

In spite of the fact that the coatings on machining cutting edges have been used for many years, their dynamic development can be observed during the last decade [4,16,18,23,25,28,29, 35,72]. At present, the modified PVD and CVD methods can be applied to produce coatings having extreme tribological properties of elements they are covered with. However, there is no universal coating which can have unlimited applicability. A wide range of coating applicability necessitates a proper selection of a coating depending on the actual application, deposition method and substrate type [68,78,88,96]. Presently we can distinguish two parallel research trends in the area of thin coatings. The first research trend is aiming to elaborate new coating types, possible search for new applicability for the already known coatings. The second research trend is connected with the development of deposition technologies of hard coatings resistant to wear, the search for new deposition methods and the modernization of the existing techniques [19,76].

The coatings resistant to wear are applied nowadays in all tool making materials, even the hardest ones [23,72]. The application of protective coatings has a considerable influence on the improvement of durability and efficiency of machining tools, due to the following factors [9]:

- high hardness of the operating surface of the tool covered with the coating; hardness is one of the basic qualities of surface layers; in most cases the rise of hardness results in the rise of the qualities of other coating systems [5,6].
- possibly low friction factor within the contact area between the tool and a machined object. This factor has a considerable influence on the machining process, among others through the reduction of machining forces, lowering the temperature; it also enables to do the machining without cutting tool lubricants, and it finally speeds up the machining process itself.
- creation of thermal barrier for the heat generated during the operation of the tool; lower temperature of the tool translates itself into lower thermal deformation, which contributes considerably to better durability of the tool [68].
- reduction in the diffusion of atoms in both directions along the path tool – machined object.

Thin coatings deposited with the PVD and CVD techniques on the cutting edges of machining tools are principally made up by nitrides, carbides, oxides, borides of transition metals (most frequently Ti, Zr, V, Cr, Mo, W, Nb, Hf) or their combinations. The interest aroused by these phases is connected with the fact that these hard-melting phases are usually very hard and brittle, and are usually resistant to corrosion and tribological wear [4,56,61,87].

The protective coatings can be divided into groups depending on the type of atomic bond dominating in a given type of coating. Having considered all types of coating materials, the most numerous group is made up by materials with the predominant number of metallic bonds. Here we can name such as nitrides and carbides of transition metals, but also some borides and silicides. In a great majority of these phases there are metallic-covalence bonds, whereby the said materials are combining in themselves high hardness and abrasive resistance with the resistance to brittle cracking, which is higher as compared to the phases of covalence and ionic bonds. Another group of coating materials is made up by materials with the prevalence of ionic groups. This group includes mainly oxides. And the third group is composed of materials with the prevalence of covalence bonds where we can place diamond coatings and those made from boron nitride. This group of materials has the highest hardness. Table 1 presents the examples of coatings from all three material groups [4,56].

The coatings from titanium nitride have been used since the 1960s of the 20th century and they are still widely applied in the industry [4,63], although we can observe a declining interest in this material in favor of other phases [3]. The titanium nitride crystallizes in a cubic lattice of NaCl type, and it is a typical interstitial phase of a very wide homogeneity range from 30 to 50% at. of nitrogen. The microhardness of this phase is growing proportionally with the

concentration of nitrogen (Table 1) [87]. The TiN layers have high resistance to abrasion [25,34,35,36], but they oxidize in the atmospheric air at the temperature of 670-870 K [3].

Table 1. *Selected properties of coating material about metallic, ionic and covalence bonds [4,56,66,96]*

Kind of bonding	Coating material	Microhardness, HV	Young's modulus, GPa	Density, g/cm^3	Coefficient of thermal expansion α, 10^{-6}·K
Metalic	TiN	2100-2400	256-590	5.40	9.35-10.1
	ZrN	1600-1900	510	7.32	7.9
	TiC	2800-3800	460-470	4.93	7.61-8.6
	ZrC	2600	355-400	6.63	6.93-7.4
	TiB_2	≥3000	560	4.50	7.8
Ionic	Al_2O_3	1800-2500	400	3.98	8.4-8.6
	TiO_2	1100	205	4.25	9.0
	ZrO_2	1200-1550	190	5.76	7.6-11.1
Covalent	C (diamond)	≥8000	910	3.52	1.0
	BN (cubic)	3000-5000	660	2.52	-
	BN (face centered)	4700	-	-	-
	AlN	1200	350	3.26	5.7

The admixture of other elements to the TiN phase such as zirconium, aluminum, carbon or boron results in the formation of isomorphic phases with titanium nitride [1,13,36,41,51,58,59,67, 77,82,90]. Multicomponent coatings Ti(C,N) are characterized by high hardness (2500-3500 HV0.05) [58] and by resistance to abrasion so they are applied for covering cutting tools from high speed steel and from sintered carbides [15,71,74,94]. In the coatings of (Ti,Al)N type, every second titanium atom is substituted with aluminum [59,77,82]. The presence of aluminum in such coatings results in the fact that the temperature of service durability of such coatings exceeds 970 K, and in working conditions with raised temperature a layer of Al_2O_3 is formed on the surface which generates a diffusion barrier for atmospheric oxygen [3,5,44,83]. By increasing the concentration of aluminum (Ti:Al 33:67) in (Al,Ti)N coatings we are raising the protective influence of this element [39]. The change of lattice parameters brought about by the dissolution of Al atoms in the TiN lattice is in congruence with the Vegard's law (Fig.1) [2,8]. We must note here that the metastable coatings (TiAl)N and (Al,Ti)N combine in themselves diverse properties of metallic-covalence materials (TiN) and of covalence ones (AlN) which can not be obtained as solid materials due to a different structure and a different type of bonds [96]. The coatings with the admixture of zirconium (Ti,Zr)N show better physical properties than TiN coatings, in particular hardness, resistance to

abrasion, wear and corrosion [90]. Such coatings can consist of single three-component phases and they can demonstrate two-component structure of TiN and ZrN [13,36,90]. In the case of Ti(B,N) coatings, their phase composition depends on the concentration of boron. Such coatings consist of single- or two-component phases, yet there are no three-component phases [41,47,48,60,66,67,95]. The microhardness of these coatings is within the range of 3000-5000 HV depending on phase composition. The highest hardness is demonstrated by Ti(B,N) coatings containing boron nitride [41,50]. Through the introduction of aluminum to the CrN coating, used as protective layers against corrosion and having good antiadhesive properties principally on plastic working tools, the nitride (Al,Cr)N was formed [37,40,61]. The admixture of aluminum of the concentration of 65-75% is stabilizing the AlN phase of the cubic lattice. Such coatings have high hardness and resistance to abrasion, higher than the conventional TiN coatings, whereby they can be applied to cover cutting edges. We should add here that such coatings exhibit high thermal stability, and their maximum operating temperature is 1100ºC [38,80].

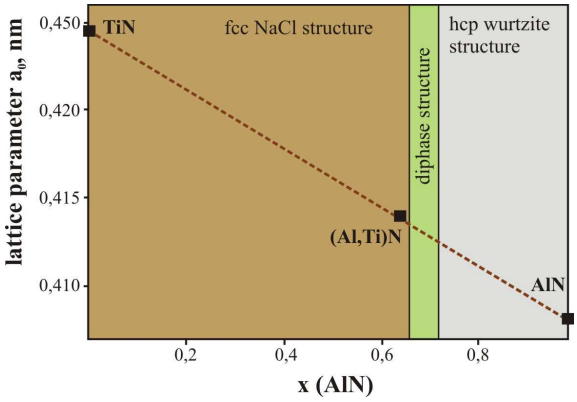

Figure 1. *Lattice parameters of the TiN, (Al,Ti)N films as a function of the AlN content and comparision with Vegard's law [2]*

Material designing is currently one of the most important issues of material engineering. A synergy obtained in the field of new material technologies involving the formation of structure and properties of surface layers of engineering materials has been brought about by the integration of many branches of science, engineering and technology. New materials and the technology of their manufacture is a challenge and great potential to be taken advantage of by the EU countries in view of hard competition with the developing countries of relatively cheap

workforce. The current approach to material designing is focused on the manufacture of materials having a structure ensuring that the materials have preset physicochemical properties meeting the specific requirements [30].

2. Materials

The research has been carried out on multi-point inserts from sintered carbides of the WC-Co type and from sialon tooling ceramics deposited and non-deposited with multilayer and gradient coatings resistant to abrasion in PVD and CVD processes. The inserts were being covered in the cathode arc evaporation process CAE-PVD with the coatings Ti(B,N), (Ti,Zr)N, Ti(C,N), Ti(C,N)+(Ti,Al)N, (Al,Ti)N, (Ti,Al)N and (Al,Cr)N, and in the high-temperature CVD process with multilayer coatings Ti(C,N)+Al_2O_3+TiN and Ti(C,N)+TiN.

3. Methodology

The surface topography and the structure of the produced coatings along the transverse fractures was observed on the scanning electron microscope Supra 35 of Zeiss Company. To obtain the images of the investigated samples, the detection of secondary electrons (SE) and backscattered electrons (BSE) was applied, with the accelerating voltage within the range of 5-20 kV.

The qualitative and quantitative analysis of the chemical composition in the microareas of the investigated coatings was carried out using the X-ray energy dispersive spectroscopy (EDS) with the application of the spectrometer EDS LINK ISIS of the Oxford Company being a component of the electron scanning microscope Zeiss Supra 35. The research was carried out with the accelerating voltage of 20 kV.

The orientation and grain size in the coating from sintered carbides was determined using the technique of Electron Backscatter Diffraction (EBSD) in the scanning electron microscope Supra 35 of Zeiss Company.

The changes of chemical concentration of the coating components along the direction perpendicular to its surface, and the concentration changes in the transit zone between the coating and the substrate material were determined basing on the tests in the glow discharge optical spectrometer GDOS-750 QDP of the Leco Instruments Company. The following operating conditions of the Grimm tube of the spectrometer were applied: internal diameter of the tube 4 mm, voltage feed to the tube 700 V, tube current 20 mA, operating pressure 100 Pa.

The observation of the structure of thin foils and the diffraction research was carried out in the transmission electron microscope JEM 3010 UHL of the JEOL Company, with the accelerating voltage of 300 kV and maximum magnification of 25000 times. The diffractograms from the transmission electron microscope were solved with the use of the computer program "Eldyf".

The analysis of phase composition of the substrates and of the obtained coatings was carried out using the X-ray diffraction method (XRD) on the X-ray apparatus X'Pert of the Panalytical Company using the filtered radiation of a cobalt lamp. Due to the superposition of reflexes of the substrate material and coating and due to their intensity hindering the analysis of the obtained results, in order to obtain more accurate information from the surface layer of the investigated materials, we applied in our further investigation studies the grazing incident X-ray diffraction technique (SKP).

The assessment of grain size in the investigated coatings was carried out using the diffractograms obtained with the application of the grazing incident X-ray diffraction technique (SKP) using the Scherrer's method.

The measurement of roughness of the surface of the polished samples from sintered carbides of the WC-Co type and of sialon ceramics without coating and covered with the investigated coatings were carried out on the profilographometer Surtronic 3+ of Taylor Hobson Company, whereas the roughness measurement of the surface of gray cast iron after the technological machining trial with cutting edges without coatings and with the investigated coatings was carried out on the profilographometer Diavite Compact of Asmeo Ag Company. We assumed the measurement length of Lc=0.8 mm and measurement accuracy of ±0.02 μm. The parameter Ra acc. the Standard PN-EN ISO 4287:1999 was assumed as the quantity describing the roughness. We carried out 6 measurements on each of the investigated samples and we determined the average, standard deviation and confidence interval, assuming the confidence factor at $1-\alpha=0.95$.

The hardness of the investigated materials was determined using the Vickers method. The hardness of the covered substrates from sintered carbides and sialon tooling ceramics was determined making use of the classical Vickers method, using the loading equal to 3 N according to the Standard PN-EN ISO 6507-1:2007. The hardness measurement of the produced coatings was carried out using the dynamic method of Vickers, in the mode 'load-unload'.

Using the variance analysis for a single classification we assessed the statistical significance between many averages for hardness measurements. The following hypotheses were formulated:

H0: m1=m2=…=mt

versus an alternative hypothesis:

H1: the averages differ significantly.

The statistical significance between the particular averages was assessed basing on the variance relation between the averages in the separated groups and the overall variance of the investigated variable.

The adhesion of the coatings to the substrate was determined basing on the Scratch Test analysis on the apparatus Revetest of the CSEM Company. The critical load Lc at which the adhesion of the coating fails was determined basing on the value of acoustic emission recorded during the measurement and on the observation of scratches formed during the scratch test. The said observations were made on the light microscope being a component of the apparatus. Detailed observations of the formed damage were carried out on the scanning electron microscope DSM-940 of the Opton Company, with the accelerating voltage of 20 kV.

In order to categorize the investigated machining inserts according to their usability properties, technological machining trials were carried out. The tests involving the cutting ability of inserts from sintered carbides and sialon ceramics covered and non-covered with PVD and CVD coatings were carried out basing on cutting trials without cutting tool lubricants on the lathe TUR 630M. The machining at room temperature was applied on gray cast iron EN-GJL-250 of the hardness of about 215 HB. The durability of the investigated inserts was determined basing on the measurements of the width of wear band on the tool flank. The measurement of the average width of flank wear VB and of the maximum width of wear band VB_{max} was carried out using the light microscope Carl Zeiss Jena. The machining trials were being stopped when the assumed wear criterion for after-machining of VB=0.2 mm was exceeded. The observation of the wear of tool flank and attack surface of the machining inserts was carried out using the scanning electron microscope Zeiss Supra 35. The analysis of chemical composition in the microareas was carried out using the EDS method. The obtained results were presented in a graphical form as the relation of wear band on the tool flank VB in the function of cutting trial time. The durability of the cutting edge is defined as the time T [min] after which the value of the assumed criterion VB=0.2 mm is exceeded.

Basing on the set of experimental results, a model of artificial neural networks (SSN) was elaborated, which made it possible to determine if there is a dependency between the properties of the coatings such as microhardness, adhesion to substrate, grain size or coating thickness and the durability of cutting edges covered with the investigated coatings. We investigated the possibility to apply networks of different architecture such as: linear networks, radial base

functions (RBF), regressive networks (GRNN) and multilayer perceptron (MLP). From among the tested networks the best quality factors were obtained for the network of multilayer perceptron (MLP) with one hidden layer (Fig. 2).

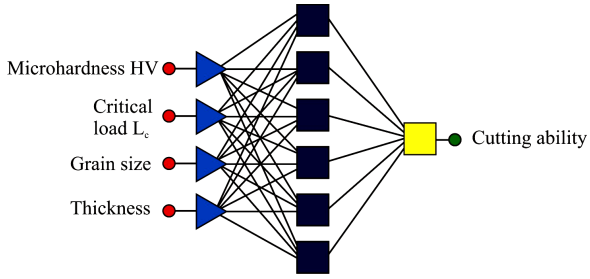

Figure 2. *Artificial neural network architecture of multilayer perceptron with one hidden layer*

The network was trained out using the algorithms of backward error propagation and coupled gradients. To verify the usefulness of the network we applied the average absolute error, standard deviation quotient and Pearson correlation factor.

4. Investigations results

Multi-point inserts from sintered carbides and from sialon tooling ceramics are characterized by well concentrated structure without pores or discontinuity (Fig. 3). The tests of thin foils in the electron transmission microscope have confirmed that the sintered carbides contain the grains of wolfram carbides WC of the hexagonal lattice (Fig. 4), and the sialons demonstrate isomorphic structure with silicon nitride Si_3N_4 of the hexagonal lattice. The phase composition of the investigated substrates was confirmed by the tests with the application of X-ray diffraction methods (Fig. 5).

In effect of the materialographic tests carried out on the scanning electron microscope it was found that the surface morphology of coatings produced with the PVD technique on sintered carbides of the WC-Co type and on tooling sialon ceramics is characterized by high non-homogeneity connected with the presence of numerous droplet-shaped microparticles (Figs. 6-9). The presence of these morphological defects is connected with the nature of cathode arc evaporation. The droplets observed in SEM are noticeably different in terms of size and shape. The size of these particles is within the range from the tenths of a micrometer to

around a dozen micrometers. Some particles have a regular shape, slightly flat, which can bespeak of high kinetic energy of the droplets colliding with a relatively cold substrate (Figs. 7, 9). We also observed solidified droplets of irregular shapes as well as agglomerates formed from several combined microparticles (Fig. 8). There were also some hollows formed probably when the solidified droplets break off after the PVD process has been completed (Figs. 7, 8). It was found that the hollows bespeaking of the breaking off of some microparticles frequently do not reach down to the substrate.

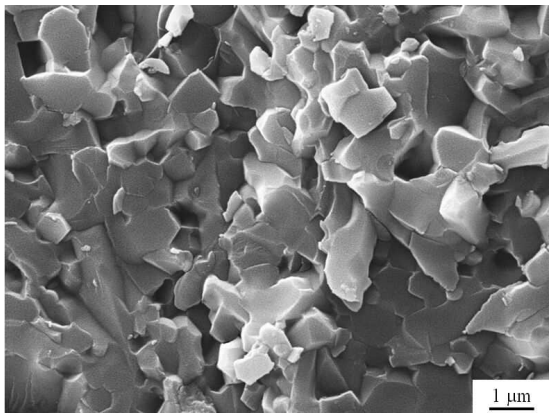

Figure 3. *Fracture of sialon tool ceramics*

The chemical analysis of particles present on the surface of PVD coatings (Fig. 9) shows that in these microareas there are predominantly metal elements from the evaporated shield pertaining to a given coating, i.e., titanium, zirconium and aluminum, which suggests that these are droplets of liquid metal broken off from the shield during the deposition of coatings and solidified on the substrate. In some cases the chemical analysis from the microarea of the droplet shows the presence of nitrogen, which can mean that a solidified metal droplet has been covered by a thin layer of coating material.

The analysis of surface morphology of coatings produced with the CVD technique on the substrate from sintered carbides and sialon ceramics shows that there occur networks of microcracks characteristic for this deposition method of thin coatings (Fig. 10). The surface of the coatings Ti(C,N)+Al_2O_3+TiN demonstrates a topography characteristic for the subsurface layer of Al_2O_3 consisting of numerous polyhedrons (Fig. 10). And the surfaces of the coating Ti(C,N)+TiN deposited on both substrates are different from each other. This coating deposited on sintered carbides has a slightly wavy surface of unsharpened shapes, and the coating Ti(C,N)+TiN on sialon consists of grains of spherical shapes and size of about 2 µm.

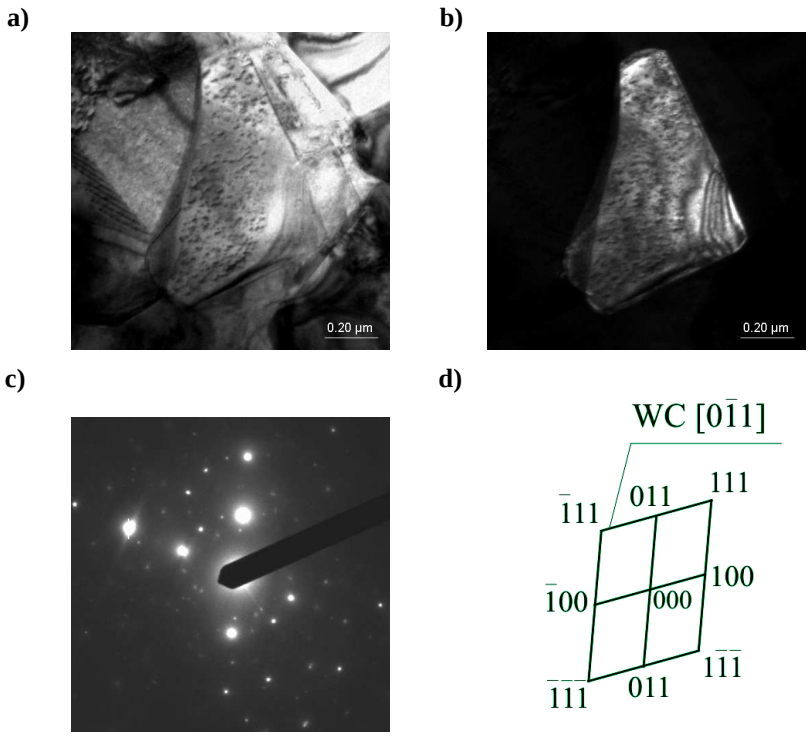

Figure 4. *Structure of sintered carbides substrate: a) bright field; b) dark field from 100 reflex; c) diffraction pattern from area b and d) solution of the diffraction pattern*

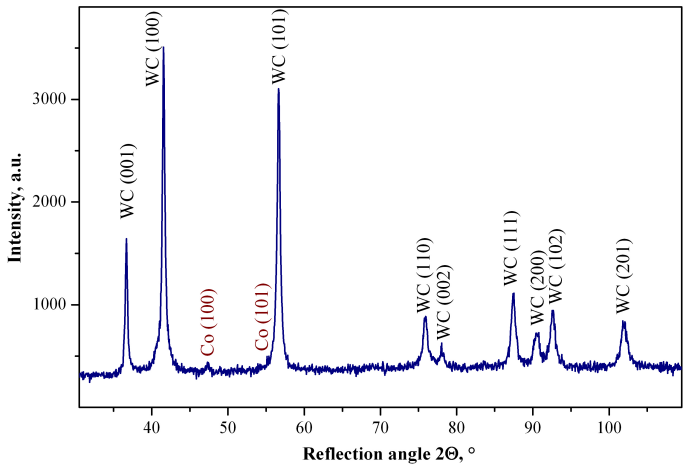

Figure 5. *X-ray diffraction pattern of sintered carbides substrate*

The morphology of coating surfaces has an influence on the rise of roughness Ra of the surfaces of inserts from sintered carbides and sialon ceramics covered by the investigated coatings (Table 2). The roughness of the multi-point inserts in both cases is the same and equals Ra=0.06 µm. The lowest rise of roughness of the surface is caused by the coating (Al,Ti) for which the averages Ra are 0.18 and 0.15 µm on the substrates respectively from sintered carbides and sialon ceramics. The highest roughness is demonstrated by the surfaces of samples covered by the CVD coating of the type Ti(C,N)+Al_2O_3+TiN, for which Ra is 0.63 µm in the case of sintered carbides and 0.82 µm in the case of sialons covered by the same coating. The roughness Ra of the surface of multi-point inserts covered by the PVD coatings is within the range from 0.15 to 0.50 µm, and the surface roughness with CVD coatings is within the range from 0.20 to 0.83 µm. However, there is no relation found between the durability of cutting edges and roughness of the coatings.

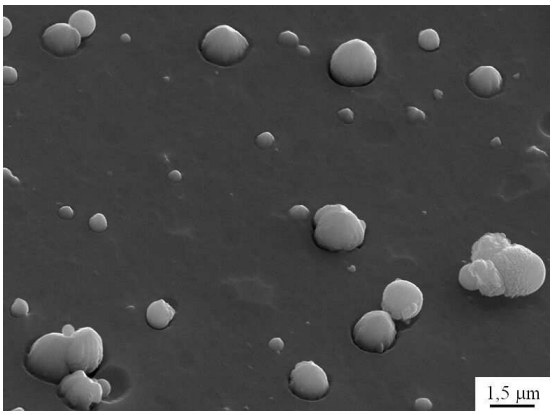

Figure 6. *Surface topography of the (Ti,Zr)N coating deposited onto the sintered carbides substrate*

Basing on the fractographic tests carried out in the scanning electron microscope, it was demonstrated that the PVD and CVD coatings are uniformly deposited and closely adhere to the substrate (Figs. 11-13). Furthermore, the particular layers of multilayer coatings Ti(C,N)+(Ti,Al)N, Ti(C,N)+Al_2O_3+TiN and Ti(C,N)+TiN are characterized by compact structure without delamination or defects and they closely adhere to one another (Fig. 13). It can be observed from the fractures of (Al,Cr)N coatings that this coating is also multilayer (Fig. 12), typical for multi-component coatings obtained through the application of separate sources of metal pairs Cr and Al. It was found that multilayer coatings of the type

Ti(C,N)+Al_2O_3+TiN and Ti(C,N)+TiN obtained by CVD method have a thin layer of fine-grained phase TiC in the interphase zone coating-substrate (Fig. 13), which was confirmed by X-ray diffraction methods and described in the further part of the paper. In addition, the Ti(C,N) layer in both CVD coatings is characterized by the structure which is changing in the gradient way from fine-grain close to the substrate and then turning gradually into column structure (Fig. 13). And the Al_2O_3 layer has the structure similar to the column one (Fig. 13).

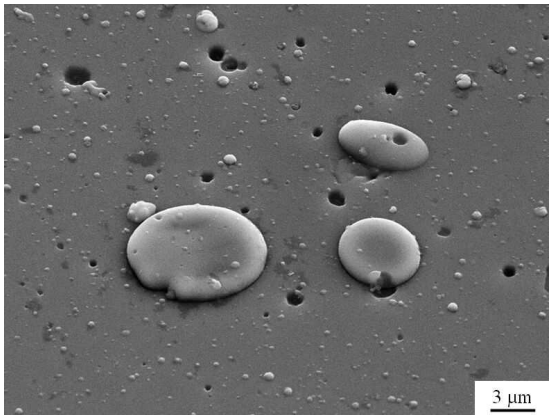

Figure 7. *Surface topography of the Ti(B,N) coating deposited onto the sialon ceramics substrate*

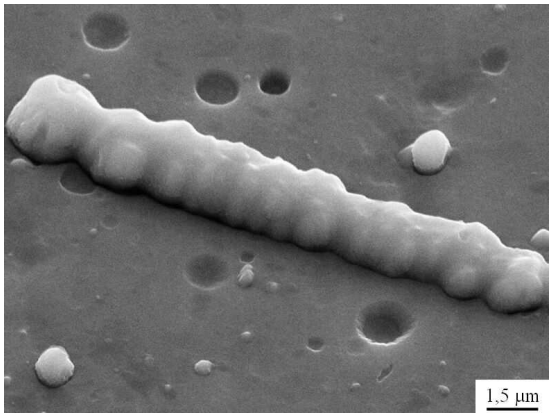

Figure 8. *Surface topography of the Ti(C,N) (2) coating deposited onto the sialon ceramics substrate*

The research on thin foils from Ti(B,N) coating deposited on the substrate from sintered carbides and sialon tooling ceramics confirms that in congruence with the assumptions the produced coatings contain phases of TiN type of the cubic lattice belonging to the spatial group Fm3m (Fig. 14). We must note here that due to the isomorphism of phases TiN and Ti(B,N) their diffractive differentiation is impossible. Also basing on the research on thin foils from the (Al,Ti)N coating it was demonstrated that this coating does not contain the AlN phase of the hexagonal lattice (spatial group $P6_3mc$) (Fig. 15) and TiN. All the observed structures of the coatings have high fine-grained character.

Table 2. *Roughness of investigated samples*

Coating	Roughness R_a, µm	
	Sintered carbides substrate	Sialon ceramics substrate
uncoated	0.06	0.06
Ti(B,N)	0.29	0.25
(Ti,Zr)N	0.30	0.40
Ti(C,N) (1)	0.22	0.23
Ti(C,N)+(Ti,Al)N	0.31	0.30
Ti(C,N) (2)	0.50	0.38
(Al,Ti)N	0.18	0.15
(Ti,Al)N	0.39	0.28
(Al,Cr)N	0.28	0.31
Ti(C,N)+Al_2O_3+TiN	0.63	0.82
Ti(C,N)+TiN	0.40	0.20

Table 3. *The results of quantitative chemical analysis from both X1 and X2 areas of coating Ti(C,N)+Al_2O_3+TiN deposited onto substrate from sintered carbides*

Element	Element of concentration, wt.%
C	15.20
N	10.93
Ti	73.87
O	41.50
Al	58.50

Also titanium droplets were found inside the investigated coatings whose presence is effected by the character of cathode arc evaporation. We also found the phases produced as a result of the solidification a droplet of the evaporated shield, which, due to the isomorphism of phases ε-TiN of the tetragonal latice and TiB of the rhombus lattice could not be explicitly identified (Fig. 16).

In effect of the qualitative X-ray microanalysis we obtained information about the elements present in the selected microareas of the investigated coatings (Figs. 9, 17), and in effect of the

quantitative analysis we obtained information about mass and atomic concentration of particular elements (Table 3). The qualitative and quantitative analysis EDS from the microareas of the coating demonstrates that the investigated layers contain elements appropriate for a given coating, and their quantitative composition is close to equilibrium. Additionally, in some cases the EDS spectrum shows the reflexes of the elements present in the substrate, and in the case of thin multilayer coatings the recorded result is an average of several layers whereof a given coating is composed. In the case of CVD coating of the type Ti(C,N)+Al_2O_3+TiN the analysis of chemical composition along the cross-section shows that the chemical composition of particular layers is close to equilibrium (Fig. 17, Table 3).

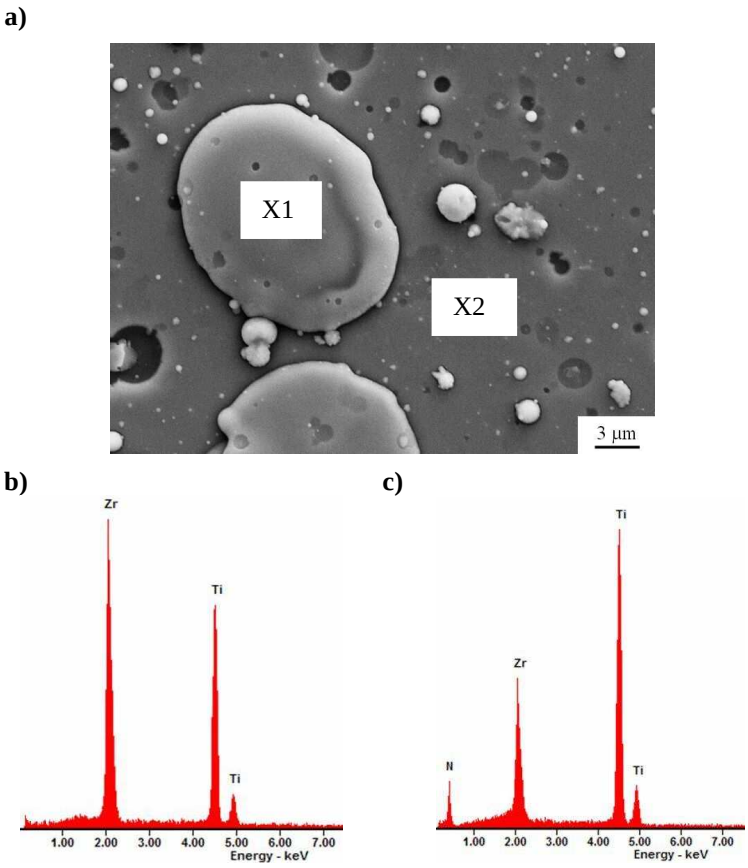

Figure 9. *Surface topography of the (Ti,Zr)N coating deposited onto the sialon ceramics substrate, b) X-ray energy dispersive plot the area X1 as in a figure a, c) X-ray energy dispersive plot the area X2 as in a figure a*

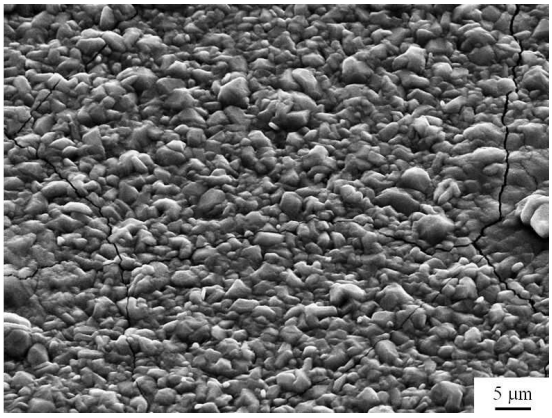

Figure 10. *Surface topography of the Ti(C,N)+Al_2O_3+TiN coating deposited onto the sialon ceramics substrate*

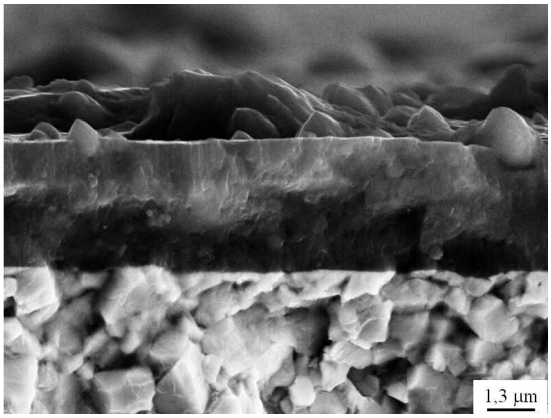

Figure 11. *Fracture of the Ti(C,N)+(Ti,Al)N coating deposited onto the sintered carbides substrate*

The research on chemical composition carried out on the glow discharge optical spectrometer GDOES confirms the presence of appropriate elements in gradient layers Ti(B,N), (Ti,Zr)N, Ti(C,N) (1), Ti(C,N) (2), (Al,Ti)N and in multilayer coatings Ti(C,N)+(Ti,Al)N, Ti(C,N)+TiN. Figures 18 and 19 present the changes of atomic concentration of the components of the coatings and of substrate material. The character of the changes of the concentration of elements which form the coatings bespeaks of their gradient structure. The character involving the concentration changes of the components in multilayer coatings of the type Ti(C,N)+(Ti,Al)N and Ti(V,N)+TiN is indicative of their multilayer

structure. In both cases, in the internal layer there occurs titanium, nitrogen and carbon, and in the external layer, respectively titanium, aluminum and nitrogen. In effect of the GDOES analysis it was demonstrated that in the contact zone from the surface of the coatings there is a concentration rise of elements that are components of the substrate with simultaneous decrease of the concentration of elements which are components of the coating. This fact can be caused by the presence of a transit zone of diffusive character between the substrate material and the coating, as it was suggested by the authors of earlier works [1,42,73,75], although we can not rule out the possibility of simultaneous non-homogeneous evaporation of the material from the surface of the samples during the tests on the glow discharge spectrometer.

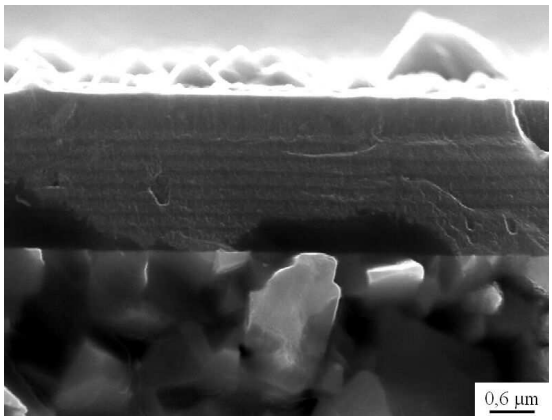

Figure 12. *Fracture of the (Al,Cr)N coating deposited onto the sintered carbides substrate*

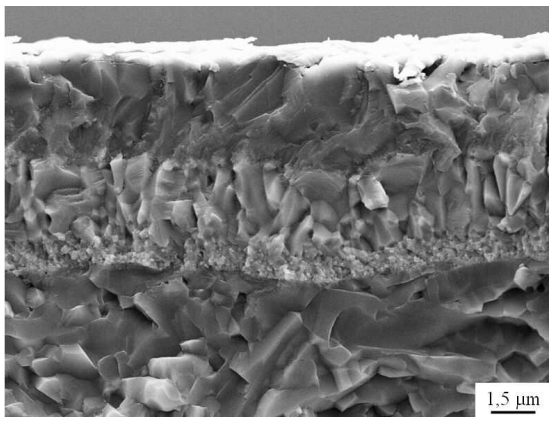

Figure 13. *Fracture of the Ti(C,N)+Al_2O_3+TiN coating deposited onto the sialon ceramics substrate*

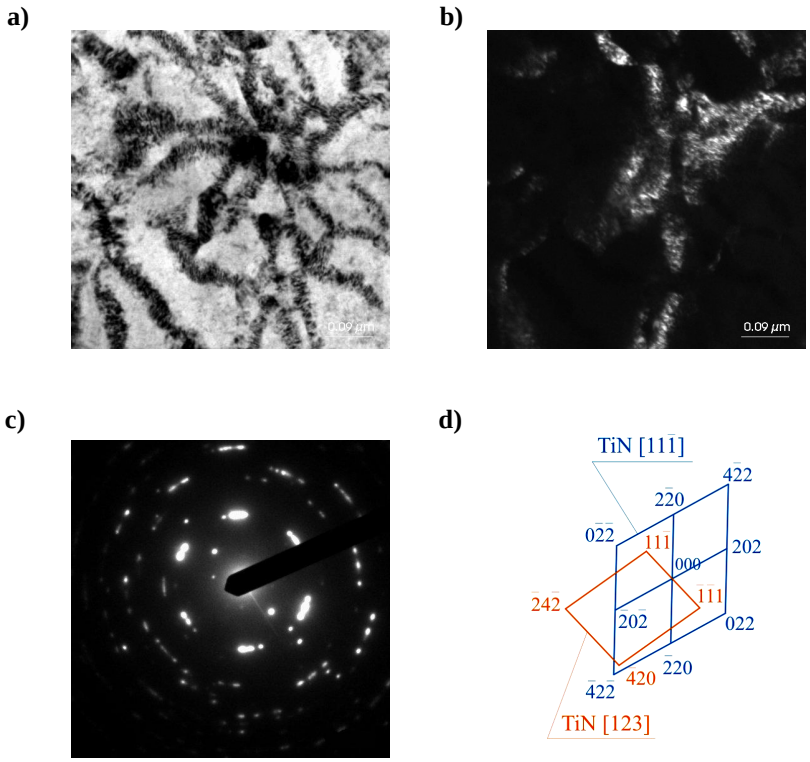

Figure 14. *Structure of Ti(B,N) coating: a) bright field; b) dark field from 0-2-2 reflex; c) diffraction pattern from area b and d) solution of the diffraction pattern*

The qualitative analysis of phase composition carried out with the X-ray diffraction method confirms that on the substrates from sintered carbides and sialon tooling ceramics, the coatings containing phases TiN, Ti(C,N), AlN and CrN were generated in congruence with the assumptions, and in the case of CVD coating - the phase Al_2O_3 (Figs. 20-23). On the X-ray diffractograms obtained with the use of Bragg-Brentano technique also the presence of the reflexes from phases WC and Si_3N_4 present in the substrate materials was demonstrated. The presence of reflexes from the substrate was found on all diffractograms from PVD coatings as well as on the diffractogram from the CVD coating of the type Ti(C,N)+TiN obtained on sialon ceramics, which is caused by the thickness of the obtained coatings 1.3-5.0µm, lower than the penetration depth of X-rays into the material. In effect of the tests with the application of grazing incident X-ray diffraction technique, at low incidence angles of the prime X-ray beam, we recorded the reflexes only from thin surface layers (Figs. 20b, 21b, 22b, 23a-c).

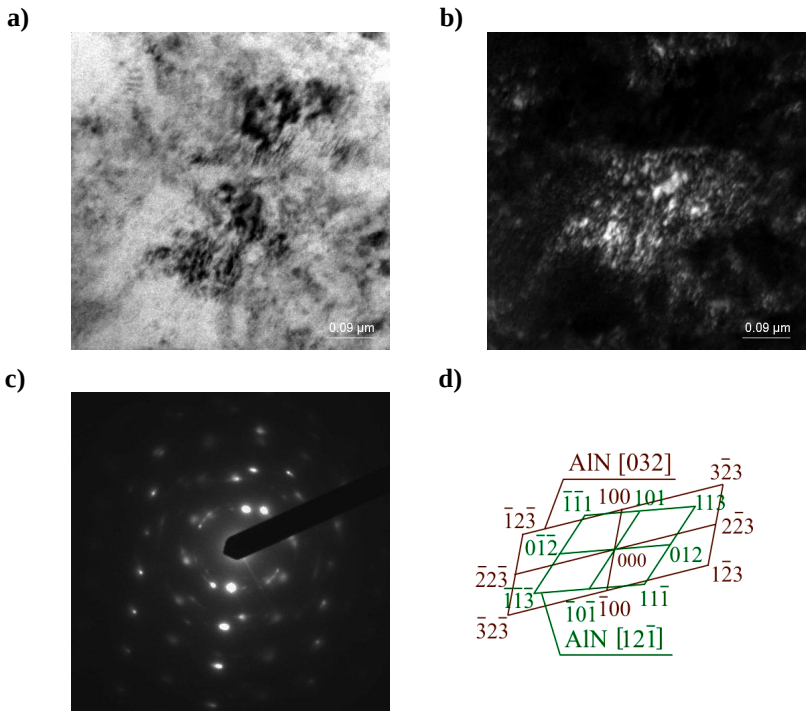

Figure 15*. Structure of (Al,Ti)N coating: a) bright field; b) dark field from -100 reflex; c) diffraction pattern from area b and d) solution of the diffraction pattern*

The lack of reflexes from the phases present in the substrates on the X-ray diffraction pattern obtained with the GIXRD technique bespeaks of the fact that the X-ray beam penetrating the investigated coatings did not get deep enough into the substrate. Table 4 presents the data involving the absorption depth of X-ray radiation depending on the incidence angle of the prime beam and on the type of chemical elements forming the coating material. Basing on the estimated absorption depths of X-rays and on the obtained diffraction patterns (Fig. 23a-c) we defined the structural models of multilayer coatings (Fig. 23d). It was demonstrated that the multilayer coatings Ti(C,N)+(Ti,Al)N, Ti(C,N)+Al_2O_3+TiN and Ti(C,N)+TiN contain appropriate phases for each of coating types in agreement with the assumed arrangement order of these phases. On the X-ray diffraction pattern obtained from the coatings Ti(B,N), (Ti,Zr)N, Ti(C,N)+(Ti,Al)N and (Ti,Al)N we found isomorphic phases from TiN, since these phases are a secondary solid solution on the basis of TiN. With respect to the coatings Ti(C,N) (1) and Ti(C,N) (2) the presence of titanium carbonitride was confirmed, and with respect to the coatings (Al,Ti)N and (Al,Cr)N the diffraction analysis confirmed the

presence of AlN phase of the hexagonal lattice in both coatings and of phases TiN and CrN respectively.

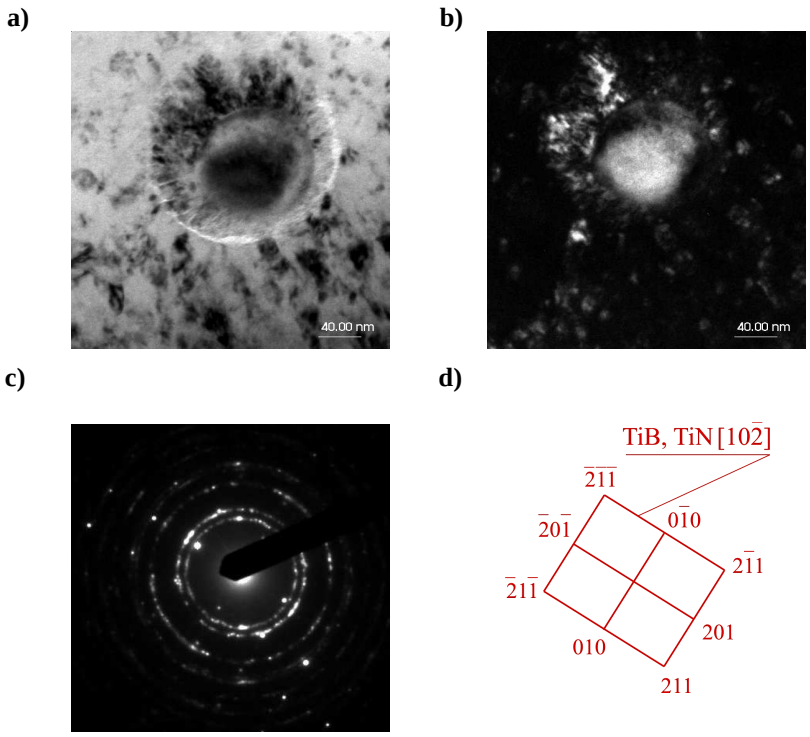

Figure 16. *Structure of Ti(B,N) coating: a) bright field; b) dark field from -20-1 reflex; c) diffraction pattern from area b and d) solution of the diffraction pattern*

Figures 24 and 25 present the assessment results of grain size from the coatings PVD and CVD obtained on the substrates from sintered carbides and sialon tooling ceramics. The data involving the grain size for the coatings obtained with PVD and CVD techniques is presented on separate diagrams due to considerably high differences of grain size for the coatings produced with these two techniques whereas the overall results of the carried out studies are presented in Table 5. The results show that the smallest grains are characteristic of the coating (Al,Ti)N in which the grain size values are 9.8 and 8.2 nm respectively for the coating obtained on the substrates from sintered carbides and sialon ceramics. The grain size of PVD coatings is within the range of 8.2-57 nm, and the grain size of the coatings obtained with the CVD technique is within the range of 112-421 nm. The measurement of the grain size shows that the coatings Ti(B,N), Ti(C,N) (1), Ti(C,N) (2), Ti(C,N)+(Ti,Al)N and (Ti,Al)N obtained on the

substrate from sintered carbides are characterized by smaller grains than the coatings of the same type obtained on sialon ceramics. In the case of coatings (Ti,Zr)N, (Al,Ti)N and (Al,Cr)N smaller grains are characteristic of the coatings obtained on sialon tooling ceramics. In general, the grain size range for the PVD coatings obtained on sialon ceramics is from 8.2 to 57 nm and is higher than the grain size range of the coatings obtained on the substrate from sintered carbides from 9.8 to 27 nm. A higher range is more advantageous for the analysis involving the influence of coating properties on cutting edge durability described in the further part of the work.

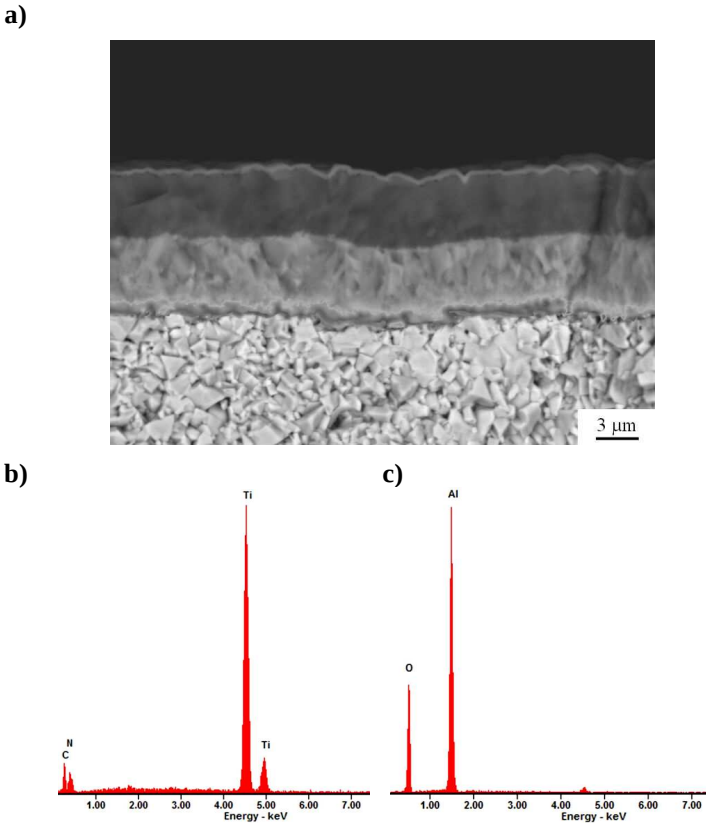

Figure 17. *Surface topography of the Ti(C,N)+Al_2O_3+TiN coating deposited onto the sintered carbides substrate, b) X-ray energy dispersive plot the area X1 as in a figure a, c) X-ray energy dispersive plot the area X2 as in a figure a*

The results of thickness measurements of the investigated coatings are presented in Table 6 and on the diagram presented in Fig. 26. The thickness of the investigated PVD coatings

obtained on sintered carbides and on sialon tooling ceramics is within the range from 1.3 to 5.0 µm, and the thickness of CVD coatings is from 2.8 to 8.4 µm. In effect of the carried out research it was demonstrated that both PVD and CVD coatings on sintered carbides have higher thickness than the coatings of the same type on the substrate from sialon ceramics. In the case of PVD coatings, this fact is definitely indicative of the possibility of substrate polarization, since the accelerating voltage has the influence on faster growing rate of the coatings than in the case of non-polarized ceramic substrate. With respect to CVD coatings, however, the higher thickness of coatings obtained on the substrate from sintered carbides results from the fact that the carbon in layers Ti(C,N) of both produced CVD coatings is not only from the operating gas but also from the substrate. The coatings (Ti,Al)N and (Al,Cr)N are here an exception since they have higher thickness on the sialon substrate.

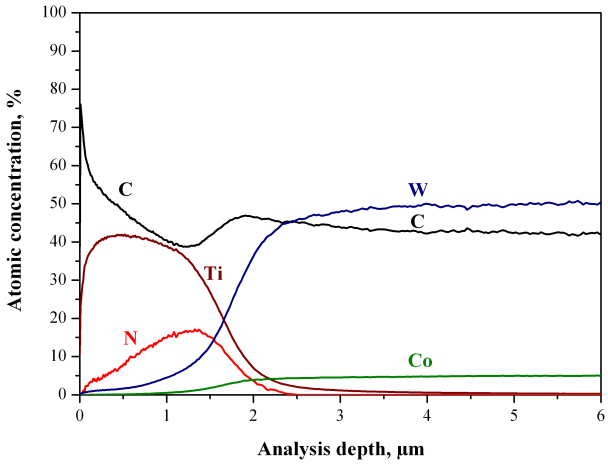

Figure 18. *Changes of constituent concentration of the Ti(C,N) (1) coating and the sintered carbides substrate material*

The research results involving the microhardness of sintered carbides and sialon ceramics without coatings and with the investigated coatings are presented in Table 7 and in Fig. 27. The analysis of statistical significance carried out for the coatings on the substrate from sintered carbides and sialon ceramics shows that there are significant differences between the average values of microhardness, so the zero hypothesis in both cases has been rejected (Table 8). In effect of the statistical significance test, three groups of microhardness have been singled out for each category i.e., for sintered carbides and sialon ceramics without coatings and for those covered by the investigated coatings (Tables 9, 10). The first group of the lowest

microhardness includes non-covered sintered carbides (Table 9) of the microhardness of 1826 HV 0.05, and in the case of sialon ceramics, sialons non-covered and covered with the coating (Al,Cr)N (Table 10) having average microhardness of 2132 HV0.05. And the microhardness of the substrate alone from the sialon ceramics is 2035 HV0.05 (Table 7, Fig. 27).

Table 4. *The depth of absorption X-ray radiation in a research coatings into diffraction analysis by GIXRD technique depending on incidence angle primary beam*

Coating	Sintered carbides substrate		Sialon ceramics substrate	
	α, °	τ, µm	α, °	τ, µm
Ti(B,N)	2	1.13	1	0.56
(Ti,Zr)N	2	1.25	2	1.25
Ti(C,N) (1)	2	1.14	2	1.14
Ti(C,N)+(Ti,Al)N	1	0.89	1	0.89
	2	1.40	2	1.40
	3	2.09	3	2.09
Ti(C,N) (2)	1	0.57	1	0.57
(Al,Ti)N	1	1.16	1	1.16
(Ti,Al)N	2	1.80	2	1.80
(Al,Cr)N	5	2.57	4	2.05
Ti(C,N)+Al_2O_3+TiN	0.5	0.28	0.5	0.28
	2	1.83	2	1.83
	5	5.16	4	4.13
Ti(C,N)+TiN	0.1	0.06	0.5	0.28
	1	0.57	3	1.71
	4	2.28	15	8.47

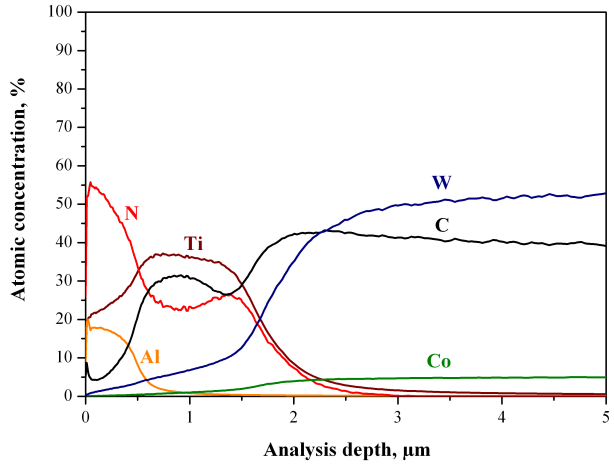

Figure 19. *Changes of constituent concentration of the Ti(C,N)+(Ti,Al)N coating and the sintered carbides substrate material*

The third group containing the coatings of the highest microhardness includes all PVD coatings obtained on the substrate from sintered carbides and the coating (Al,Ti)N obtained on sialon tooling ceramics, having the maximum value of microhardness equal to 3600 HV0.05. The microhardness of coatings obtained on sialon ceramics is within the range from 2230 to 3600 HV0.05, and the microhardness range of coatings on sintered carbides is lower and is within the range from 2315 to 2327 HV0.05.

a)

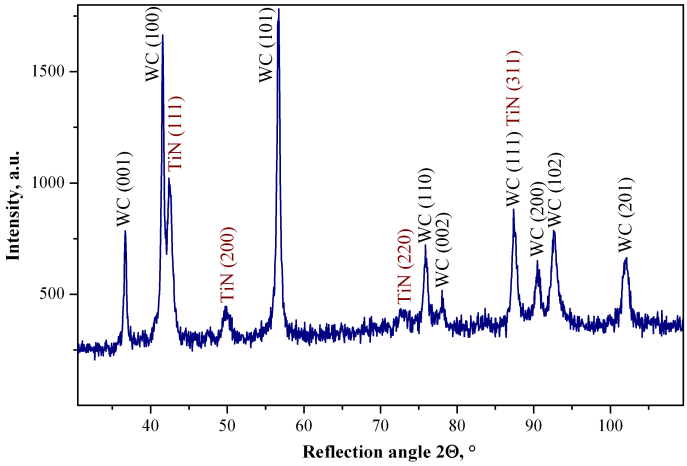

b)

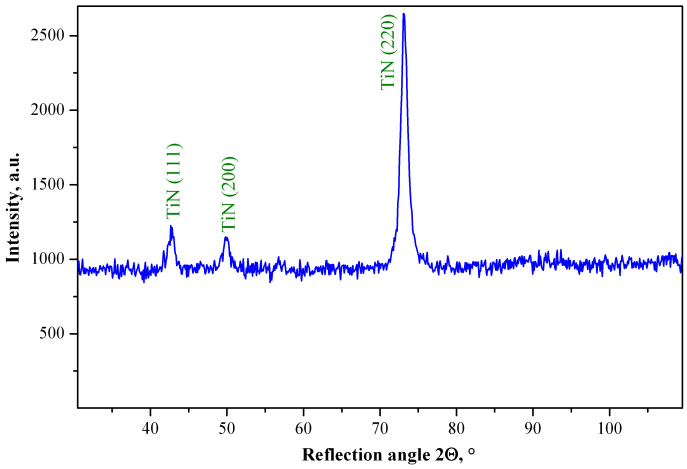

Figure 20. *X-ray diffraction pattern of Ti(B,N) coating deposited on the sintered carbides substrate obtained by: a) Bragg-Brentano method, b) GIXRD method (α=2º)*

a)

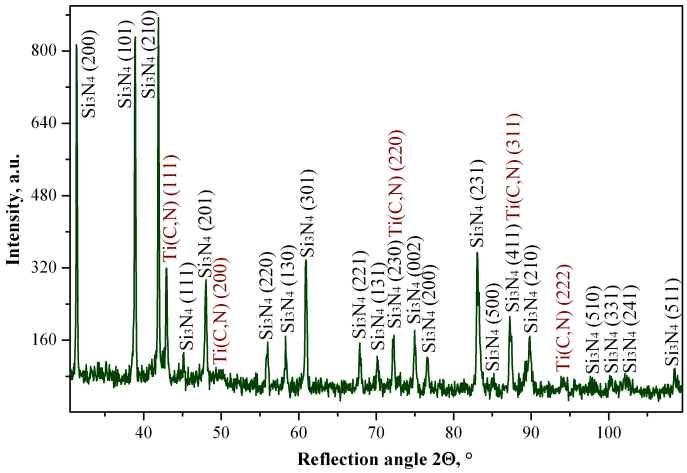

b)

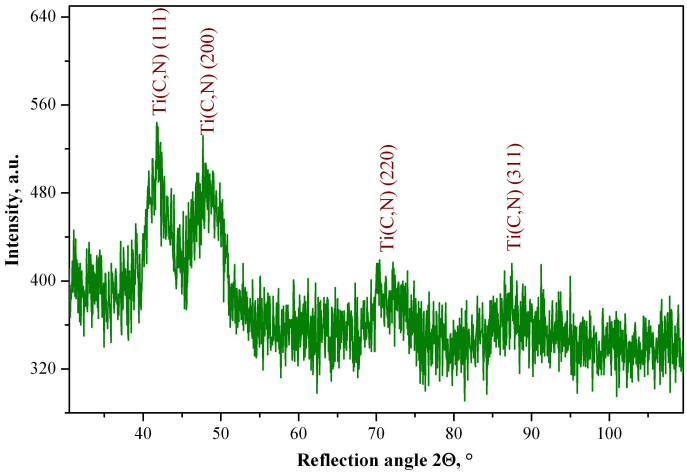

Figure 21. *X-ray diffraction pattern of Ti(C,N) coating deposited on the sialon ceraics substrate obtained by: a) Bragg-Brentano method, b) GIXRD method (α=1º)*

The critical load Lc [N] determined in the scratch test and being the measure of coating adhesion to the substrate considerably depends on the proper selection of coating material (chemical composition, phase composition) (Table 11, Figs. 28-32). This relation is particularly relevant with respect to PVD coatings on the substrate from sialon ceramics. The coatings in which only phases TiN and Ti(C,N) are present have low adhesion to the sialon substrate Lc=13-36 N, and the coatings containing the AlN phase are characterized by very

good adhesion to the substrate Lc=53-112 N. We must remember that sialons belong to covalence ceramics, and in the coatings containing isomorphic phases with titanium nitride TiN there are metallic bonds, which results in low adhesion of these coatings to the substrate of a different bond. In the case of coatings containing AlN phase of the hexagonal lattice there are covalence bonds analogous to the ceramic substrate, which yields good adhesion of these coatings to the substrate.

a)

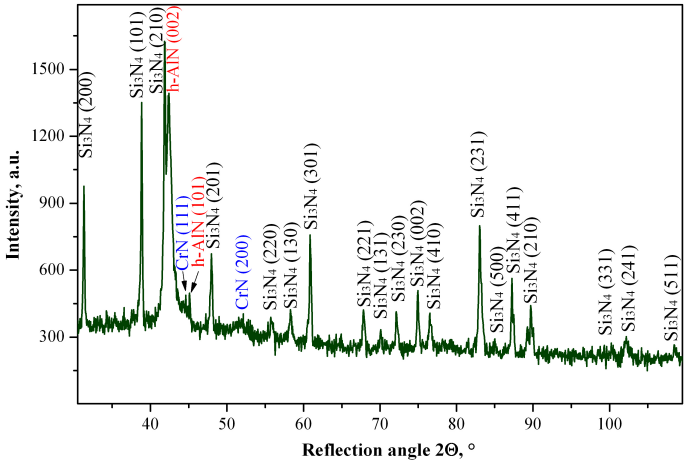

b)

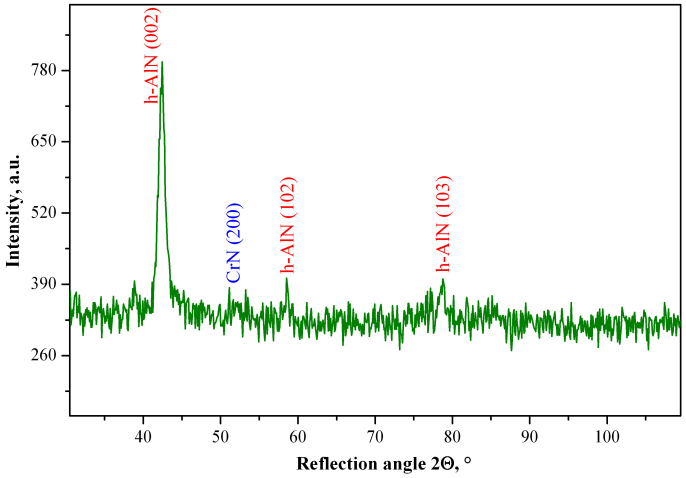

Figure 22. *X-ray diffraction pattern of (Al,Cr)N coating deposited on the sialon ceramics substrate obtained by: a) Bragg-Brentano method, b) GIXRD method (α=4º)*

a)

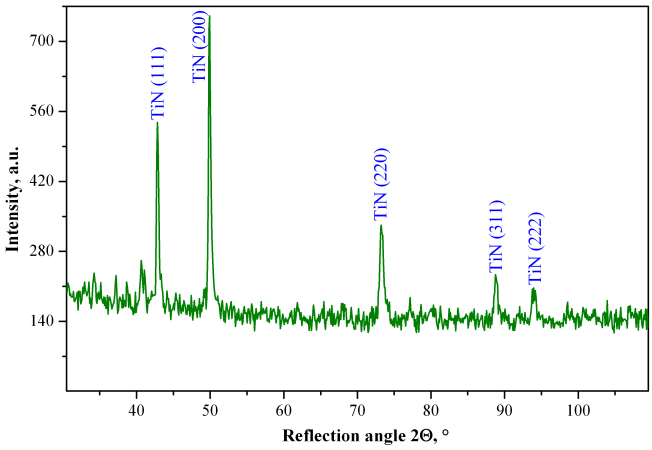
Intensity, a.u.
Reflection angle 2Θ, °
TiN (111)
TiN (200)
TiN (220)
TiN (311)
TiN (222)

b)

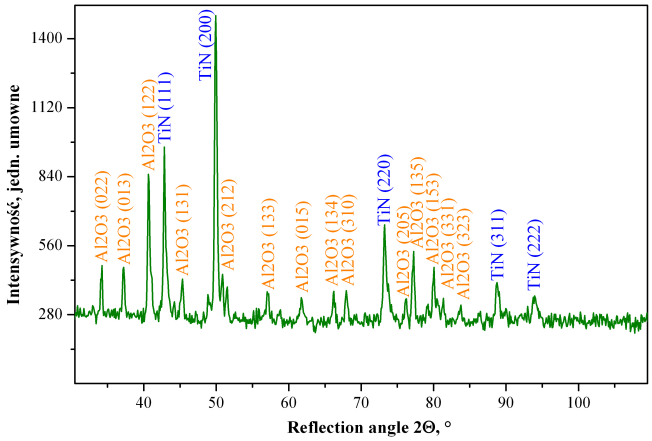
Intensywność, jedn. umowne
Reflection angle 2Θ, °
Al2O3 (022)
Al2O3 (013)
Al2O3 (122)
TiN (111)
Al2O3 (131)
TiN (200)
Al2O3 (212)
Al2O3 (133)
Al2O3 (015)
Al2O3 (134)
Al2O3 (310)
TiN (220)
Al2O3 (205)
Al2O3 (135)
Al2O3 (153)
Al2O3 (331)
Al2O3 (323)
TiN (311)
TiN (222)

c)

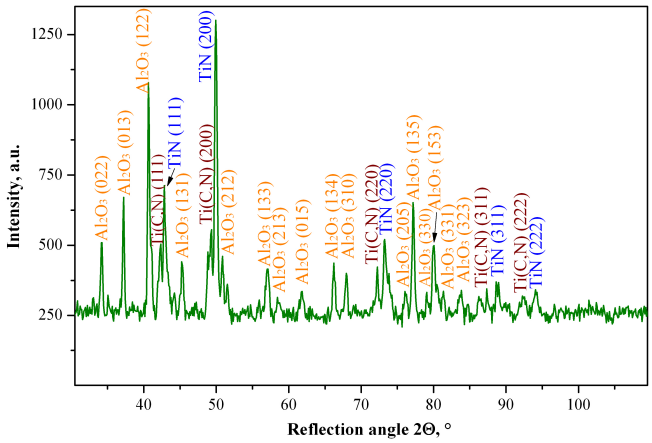
Intensity, a.u.
Reflection angle 2Θ, °
Al2O3 (022)
Al2O3 (013)
Al2O3 (122)
Ti(C,N) (111)
TiN (111)
Al2O3 (131)
Ti(C,N) (200)
TiN (200)
Al2O3 (212)
Al2O3 (133)
Al2O3 (213)
Al2O3 (015)
Al2O3 (134)
Al2O3 (310)
Ti(C,N) (220)
TiN (220)
Al2O3 (205)
Al2O3 (330)
Al2O3 (135)
Al2O3 (331)
Al2O3 (153)
Al2O3 (323)
Ti(C,N) (311)
TiN (311)
Ti(C,N) (222)
TiN (222)

d)

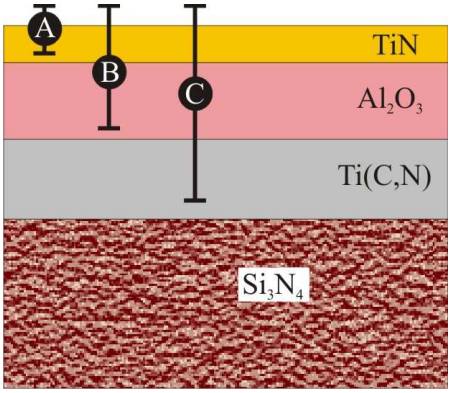

Figure 23. *X-ray diffraction pattern of Ti(C,N)+Al_2O_3+TiN coating deposited on the sialon ceramics substrate obtained by GIXRD method: a) α=0.5°, b) α=2 °, c) α=4°, d) Scheme of packing layers into Ti(C,N)+Al_2O_3+TiN coating, which was deposited on sialon tool ceramic with marking depths of GIXRD phase analysis: A for α=0,5°, B for α=2°, C for α=4°*

It means that the type of interatomic bonds present in the material of the substrate and coating has a great influence on the adhesion of coatings to the substrate. The adhesion of the coating to the substrate from sintered carbides is conditioned among others, apart from adhesion, by a slight diffusive displacement of elements in the contact zone, which is effected by the implantation of high energy ions falling down on the negatively polarized substrates.

Table 5. *Grain size in investigating coatings determined by Scherrer method*

Coating	Grain size, nm	
	Sintered carbides substrate	Sialon ceramics
Ti(B,N)	21	57
(Ti,Zr)N	21.4	13.6
Ti(C,N) (1)	17.7	21.3
Ti(C,N)+(Ti,Al)N	16.5	24
Ti(C,N) (2)	13.5	18.7
(Al,Ti)N	9.8	8.2
(Ti,Al)N	20.9	40
(Al,Cr)N	27.2	16.7
Ti(C,N)+Al_2O_3+TiN	250.7 [1)]	266.5 [1)]
	421 [2)]	324 [2)]
Ti(C,N)+TiN	356 [1)]	332 [1)]
	294.5 [3)]	112 [3)]

[1)] TiN layer; [2)] Al_2O_3 layer; [3)] Ti(C,N) layer

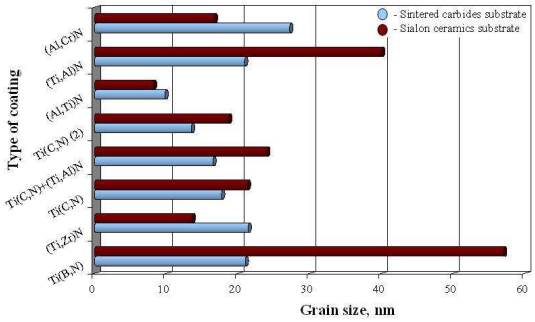

Figure 24. *The comparison of grain size PVD coatings on sintered carbides and sialon ceramics substrates*

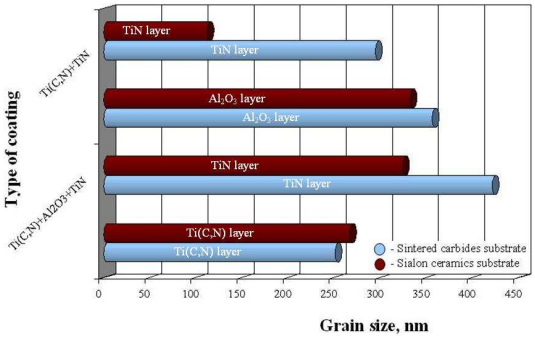

Figure 25. *The comparison of grain size CVD coatings on sintered carbides and sialon ceramics substrates*

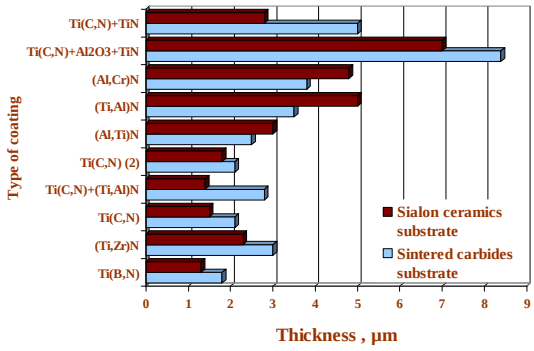

Figure 26. *The comparison of thickness coatings on sintered carbides and sialon ceramics substrates*

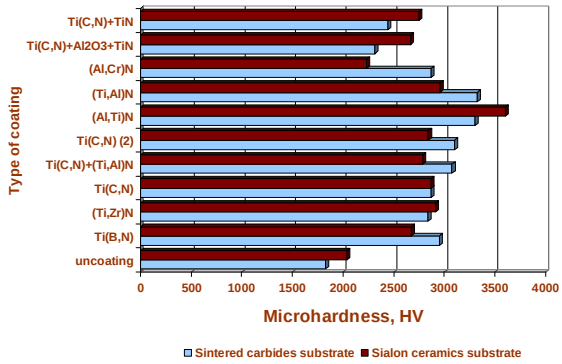

Figure 27. *The comparison of microhardness coatings on sintered carbides and sialon ceramics substrates*

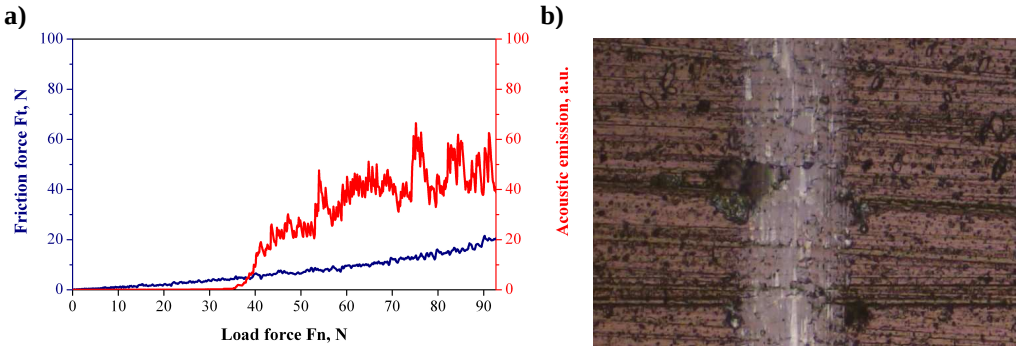

Figure 28. *a) Acoustic emission (AE) and friction force Ft as a function of the load Fn for Ti(C,N)+(Ti,Al)N coating on sintered carbides, b) scratch failure at L_c (opt) = 40 N, mag. 200 x*

Table 6. *Thickness of investigated coatings*

Coating	Thickness, µm	
	Sintered carbides substrate	Sialon ceramics substrate
Ti(B,N)	1.8	1.3
(Ti,Zr)N	3.0	2.3
Ti(C,N) (1)	2.1	1.5
Ti(C,N)+(Ti,Al)N	2.8	1.4
Ti(C,N) (2)	2.1	1.8
(Al,Ti)N	2.5	3.0
(Ti,Al)N	3.5	5.0
(Al,Cr)N	3.8	4.8
Ti(C,N)+Al_2O_3+TiN	8.4	7.0
Ti(C,N)+TiN	5.0	2.8

This has been demonstrated by the research results with the glow discharge optical spectrometer GDOES (Figs. 18 and 19), since, as described in the works [32,42,62], high energy ions falling down on the polarized substrate bring about various phenomena, among others local temperature rise, acceleration of chemisorption, intensification of surface diffusion and that into the substrate. Also a slight ion penetration might occur (about several nm down) as well as partial sputtering of atoms of the deposited coating.

Table 7. *The mean, standard deviation and confidence interval for 1-α=0.95 results of microhardness measurements of coatings deposited on sintered carbides and sialon tool ceramics as well as investigated surface materials*

Coating	Sintered carbides substrate			Sialon ceramics substrate		
	Microhardness, HV	Standard deviation	Confidence	Microhardness, HV	Standard deviation	Confidence
uncoated	1826	27	1804-1848	2035	32	2009-2060
Ti(B,N)	2951	158	2822-3080	2676	357	2386-2966
(Ti,Zr)N	2842	101	2759-2924	2916	393	2596-3235
Ti(C,N) (1)	2871	334	2599-3142	2872	365	2575-3269
Ti(C,N)+(Ti,Al)N	3076	432	2725-3426	2786	105	2700-2871
Ti(C,N) (2)	3101	270	2882-3321	2843	183	2694-2992
(Al,Ti)N	3301	370	3000-3602	3600	314	3345-3856
(Ti,Al)N	3327	494	2925-3729	2961	250	2758-3164
(Al,Cr)N	2867	502	2459-3275	2230	406	1900-2559
Ti(C,N)+Al_2O_3+TiN	2315	221	2135-2494	2669	315	2413-2926
Ti(C,N)+TiN	2443	205	2276-2610	2746	236	2554-2938

Table 8. *The variance analysis for mean microhardness results of coatings deposited on sintered carbides and sialon ceramic as well as investigated surface materials*

Sintered carbides substrate			Sialon ceramics substrate		
F	Value-p	Test F	F	Value-p	Test F
14.06	6.67^{-12}	2.01	11.31	3.34^{-10}	2.01

Table 9. *Results of significance test difference from division onto mean groups from microhardness measurements of coatings deposited on both sintered carbides and investigated substrate as well as results of the variance analysis for particular mean groups*

	Group 1	Group 2	Group 3
Coating	Sintered carbides uncoated	$Ti(C,N)+Al_2O_3+TiN$	Ti(B,N)
			(Ti,Zr)N
			Ti(C,N) (1)
			Ti(C,N)+(Ti,Al)N
		Ti(C,N)+TiN	Ti(C,N) (2)
			(Al,Ti)N
			(Ti,Al)N
			(Al,Cr)N
Average of group HV	1826	2379	3093
Analysis of variance			
F	-	1.89	1.08
Value-p		0.10	0.32
Test F		2.25	4.97

Table 10. *Results of significance test difference from division onto mean groups from microhardness measurements of coatings deposited on both sialon tool ceramics and investigated substrate as well as results of the variance analysis for particular mean groups*

	Group 1	Group 2	Group 3
Coating	Sialon ceramics uncoated	Ti(B,N)	(Al,Ti)N
		(Ti,Zr)N	
		Ti(C,N) (1)	
		Ti(C,N)+(Ti,Al)N	
	(Al,Cr)N	Ti(C,N) (2)	
		(Ti,Al)N	
		$Ti(C,N)+Al_2O_3+TiN$	
		Ti(C,N)+TiN	
Average of group HV	2132	2809	3600
Analysis of variance			
F	1.38	0.82	-
Value-p	0.27	0.57	
Test F	4.97	2.25	

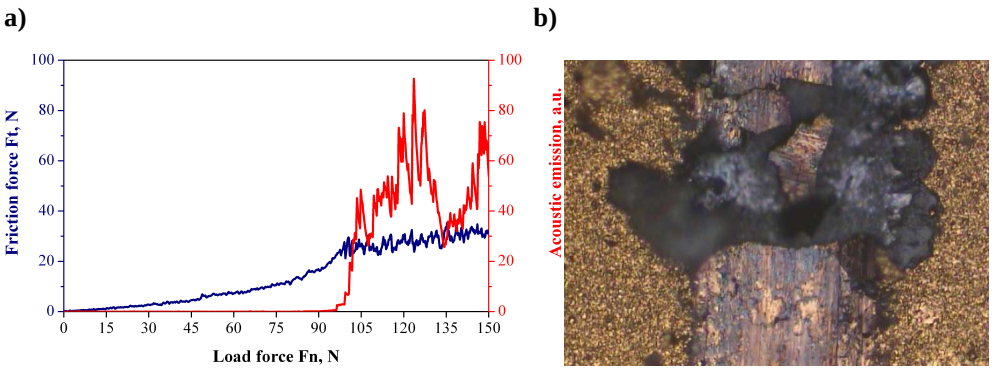

Figure 29. *a) Acoustic emission (AE) and friction force Ft as a function of the load Fn for Ti(C,N)+Al_2O_3+TiN coating on sintered carbides, b) scratch failure at L_c (opt) = 93 N, mag. 200 x*

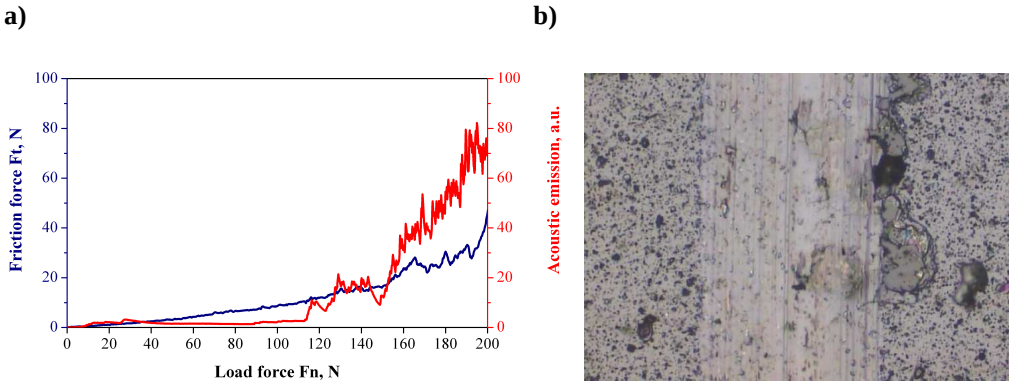

Figure 30. *a) Acoustic emission (AE) and friction force Ft as a function of the load Fn for (Al,Ti)N coating on sialon ceramics, b) scratch failure at L_c (opt) = 112 N, mag. 200 x*

The identification of defects of the coatings which occurred while doing the research on the adhesion with the scratch method was carried out through the observation in the scanning electron microscope and presented in Figs. 33-36. Furthermore, in order to investigate the produced defects more closely in some selected cases, when basing on the materialographic observations alone it was not possible to define if the produced defects penetrate into the substrate, the analysis of chemical composition in microareas was carried out using EDS, and we defined the surface distribution of chemical elements being in the coating and coming from

the substrate (Fig. 36). The research shows that there are four types of dominating damage mechanisms which are accompanied to a lesser degree by other phenomena. The first basic damage mechanism of coatings observed after exceeding the critical load is one-sided and two-sided delamination which principally involves the coatings obtained on the substrates from sintered carbides of the type Ti(B,N), (Ti,Zr)N, Ti(C,N)+(Ti,Al)N, (Al,Ti)N, Ti(C,N)+Al_2O_3+TiN and Ti(C,N)+TiN (Fig. 33), and also the coatings Ti(B,N), Ti(C,N) (1) and Ti(C,N) (2) obtained on sialon ceramics.

a) **b)**

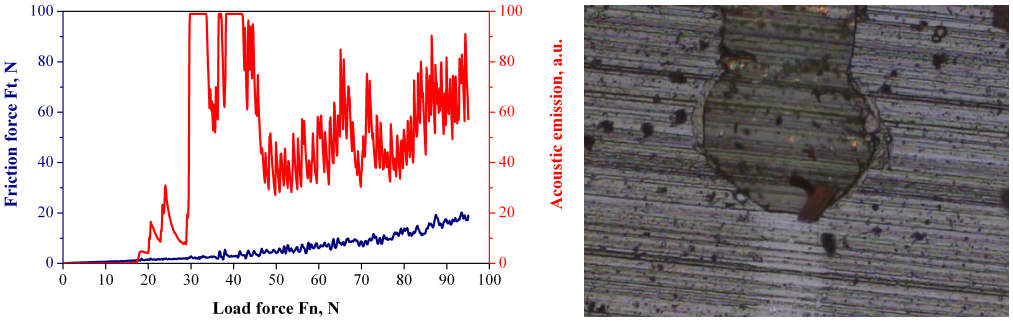

Figure 31. *a) Acoustic emission (AE) and friction force Ft as a function of the load Fn for (Ti,Al)N coating on sialon ceramics, b) scratch failure at L_c (opt) = 21 N, mag. 200 x*

Table 11. *The critical loads L_c of investigated coatings*

Coating	Critical load L_c, N	
	Sintered carbides substrate	Sialon ceramics substrate
Ti(B,N)	34	13
(Ti,Zr)N	40	21
Ti(C,N) (1)	49	25
Ti(C,N)+(Ti,Al)N	39	36
Ti(C,N) (2)	77	26
(Al,Ti)N	100	112
(Ti,Al)N	109	21
(Al,Cr)N	96	53
Ti(C,N)+Al_2O_3+TiN	93	43
Ti(C,N)+TiN	110	72

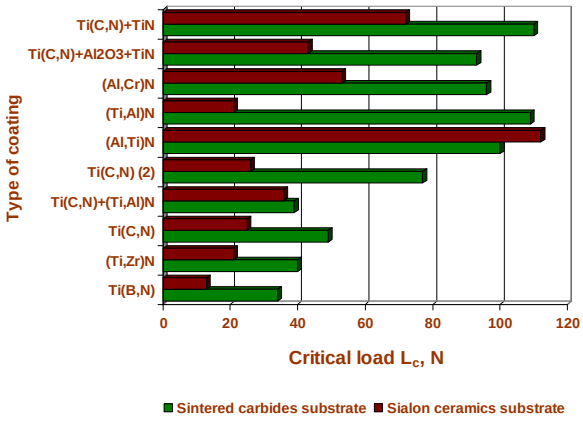

Figure 32. *The comparison of critical load L_c of coatings on sintered carbides and sialon ceramics substrates*

Table 12. *The results of tool life T measurements of investigated inserts*

Coating	Tool life T, min	
	Sintered carbides substrate	Sialon ceramics substrate
uncoated	2	11
Ti(B,N)	15	5
(Ti,Zr)N	13	5.5
Ti(C,N) (1)	13	5
Ti(C,N)+(Ti,Al)N	15	6
Ti(C,N) (2)	53	9
(Al,Ti)N	55	72
(Ti,Al)N	60	9
(Al,Cr)N	45	50
Ti(C,N)+Al_2O_3+TiN	23	3
Ti(C,N)+TiN	27	15

The second dominant damage mechanism is total delamination and it involves coatings of the type Ti(C,N) (1) and Ti(C,N) (2) obtained on the substrate from sintered carbides (Fig. 34). But initially, just after exceeding the critical load the two-sided delamination is taking place which, with increasing load, turns into total delamination. In addition, in all coatings obtained on the substrate from sintered carbides we found inside the scratch the defects effected by tension as well as chipping one- and two-sided along the borders of the scratch. Another damage mechanism found only in the case of coatings obtained on sialon ceramics of the type

(Ti,Zr)N, Ti(C,N)+(Ti,Al)N, (Al,Ti)N and Ti(C,N)+TiN is abrasion which was accompanied by cohesive fractures of the coatings and slight chipping and spalling (Fig. 35). It should be emphasized that in the case of coatings (Al,Ti)N and Ti(C,N)+TiN on the sialon substrate, even with maximum load, which is respectively 200 and 100 N, the coating was not ruptured but there were only a few cohesive defects and slight chipping. The fourth damage mechanism dominating in the coating Ti(C,N)+Al_2O_3+TiN obtained on the sialon ceramics involves vast chipping and spalling which occurred immediately after exceeding the critical load (Fig. 36).

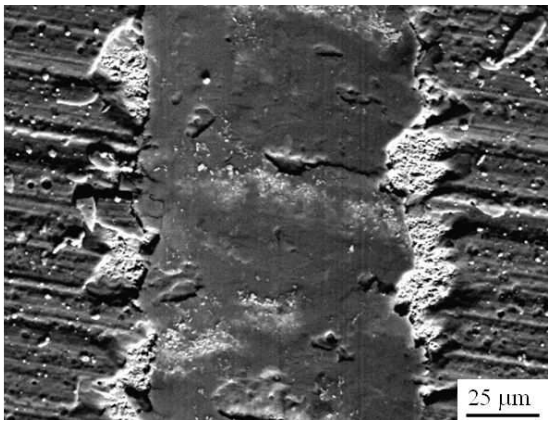

Figure 33. *Characteristic failure obtained by Scratch Test of the (Ti,Zr)N coating deposited on sintered carbides substrate*

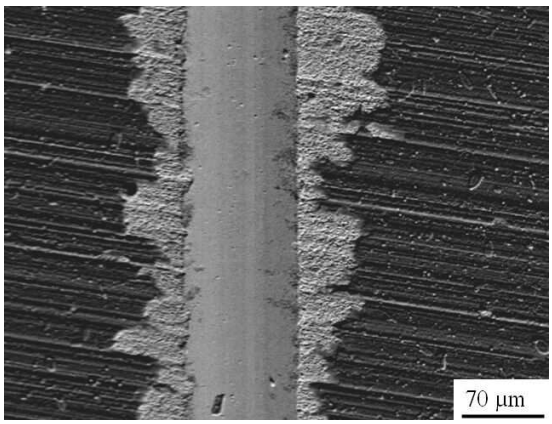

Figure 34. *Characteristic failure obtained by Scratch Test of the Ti(C,N) (1) coating deposited on sintered carbides substrate*

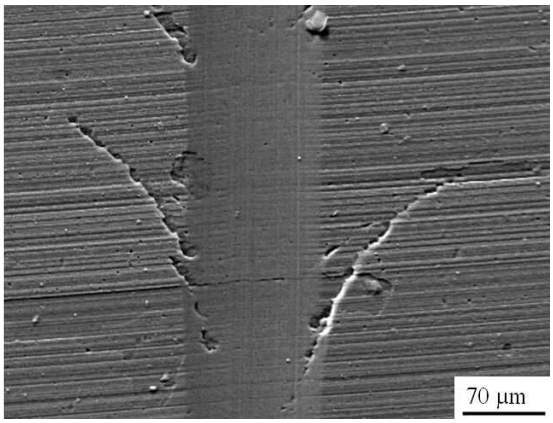

Figure 35. *Characteristic failure obtained by Scratch Test of the (Al,Ti)N coating deposited on sialon ceramics substrate*

The diagram involving the dependence of wear band VB on the tool flank on the machining time T is presented in Fig. 37, and the overall results are presented in Fig. 38 and Table 12. The research has a comparative character and its objective was to produce a durability ranking of coatings. It was found that the highest operating durability T=72 min of the inserts from sialon ceramics was obtained for the cutting edge covered by the (Al,Ti)N coating, and the lowest durability of the cutting edge T=5 min on the same substrate was exhibited by the coatings Ti(B,N) and Ti(C,N) (1).

The durability of the cutting edge from sialon ceramics without the coatings was estimated at T=11 min, which means that the coatings Al,Ti)N, (Al,Cr)N and Ti(C,N)+TiN have the influence on the rise of durability of the sialon cutting edge. In the case of inserts from sintered carbides, the highest influence on the durability of the cutting edge T=60 min has the (Ti,Al)N coating, and slightly lower T=55 and 53min the coatings (Al,Ti)N and Ti(C,N) (2) respectively. With respect to sintered carbides, all coatings increase the durability of the cutting edge since the durability of the non-covered tool is T=2 min, and the durability of the inserts of the lowest cutting ability with the coatings (Ti,Zr)N and Ti(C,N) (1) is T=13. Both in the case of covered sialon ceramics and covered sintered carbides a wide durability range of cutting edges was obtained depending on the type of deposited coating.

In effect of the materialographic observations of the investigated multi-point inserts in the scanning electron microscope it was demonstrated that the tools subjected to machining trials show their wear according to abrasive and adhesive mechanism (Figs. 39, 40).

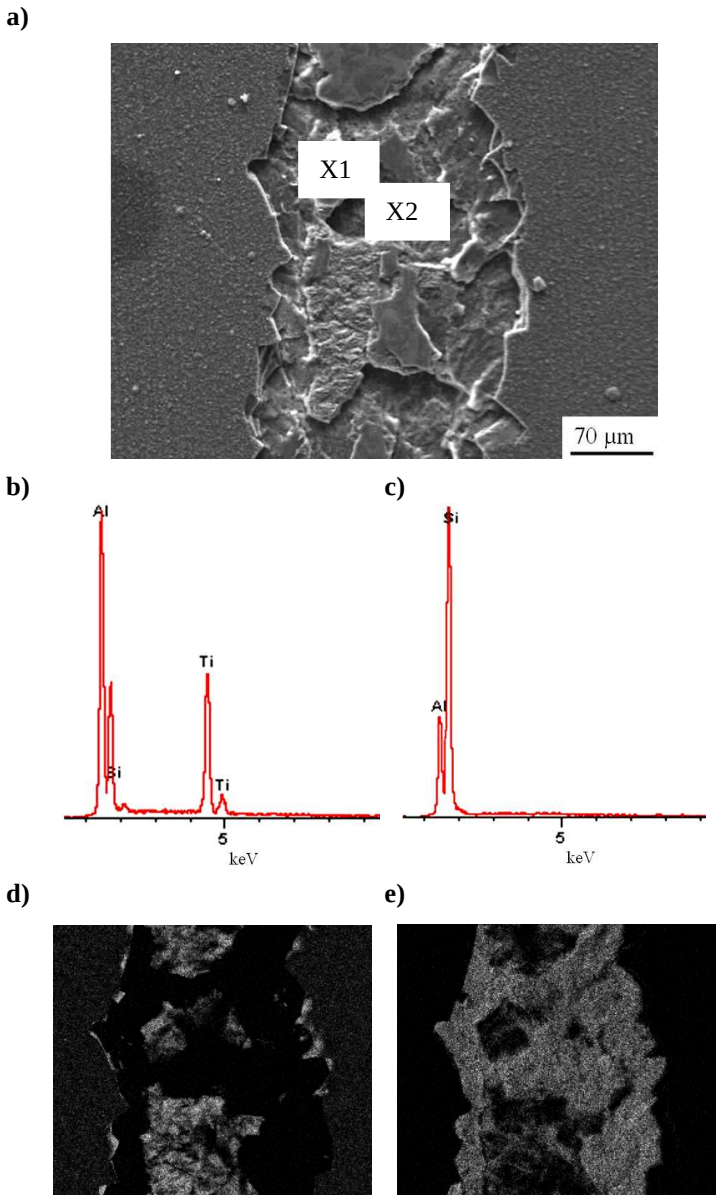

Figure 36. *a) Characteristic failure obtained by Scratch Test of the Ti(C,N)+Al_2O_3+TiN coating deposited on sialon ceramics substrate, b) X-ray energy dispersive plot the area X1 as in a figure a, c) X-ray energy dispersive plot the area X2 as in a figure a. Maps of superficial distribution chemical elements from areas as in a figure a: d) Ti - area with a coating, e) Si - area without a coating (images d and e were reduced)*

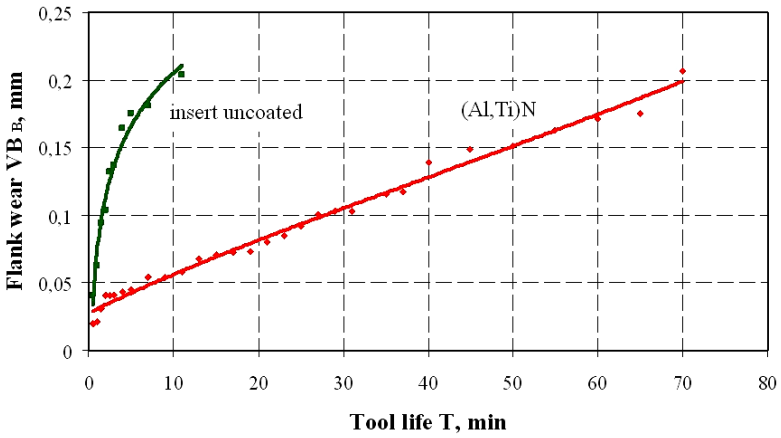

Figure 37. *Dependency graph the width of wear band on the tool flank on machining time T for sialon ceramic with deposited coating (Al,Ti)N*

On the tool flank, in particular on the cutting edges from sintered carbides with and without coatings, we found a build-up of the machined material, which is confirmed by the presence of iron reflexes on EDS graphs from the microareas (Figs. 39 b,c). We also found spalling of the coatings Ti(B,N), (Ti,Zr)N, Ti(C,N) (1), Ti(C,N)+(Ti,Al)N on the ceramic substrate and vast chipping of the coating Ti(C,N) (2) on the same substrate after 9 minutes of machining (Fig. 40).

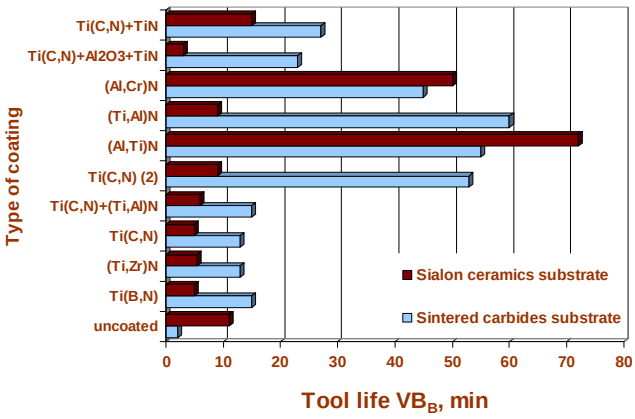

Figure 38. *The comparison of tool life T of investigated inserts*

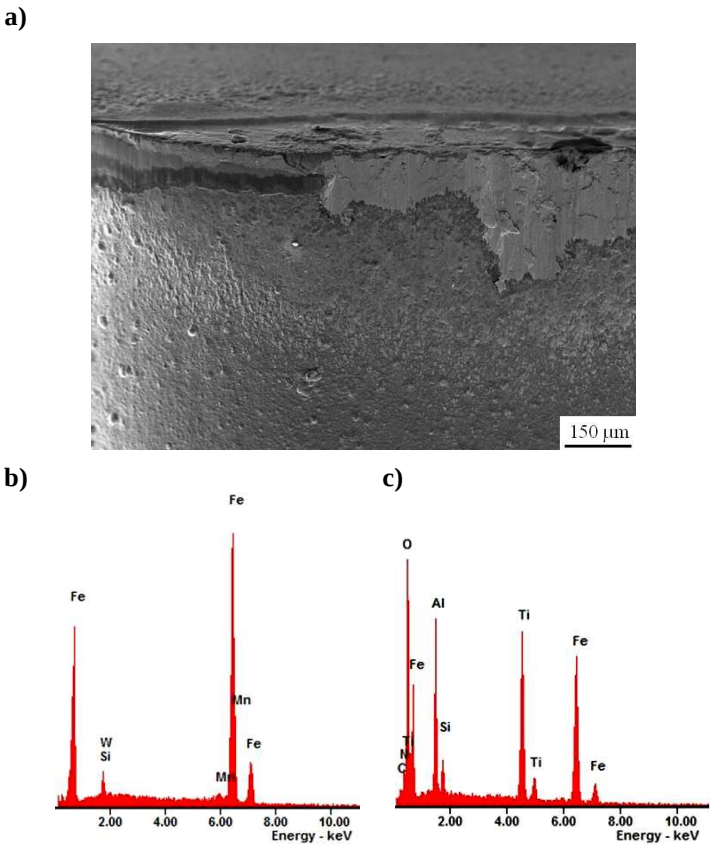

Figure 39. *a) Characteristic wear of tool flank of sintered carbides inserts with Ti(C,N)+Al_2O_3+TiN coating, b) X-ray energy dispersive plot the area X1 as in a figure a, c) X-ray energy dispersive plot the area X2 as in a figure a*

The surface quality of gray cast iron after machining with multi-point inserts without coatings and covered with the investigated coatings was determined on the basis of the measurement of the average deviation of roughness profile Ra of the machined surface (Table 13). The coatings bring about lower value of roughness Ra of the cast iron surface, and hence ensure better quality of the machined surface. The roughness Ra of the cast iron after the machining with cutting edges without coating is 4.55 µm in the case of inserts from sintered carbides and 3.03 µm in the case of sialons. We should emphasize here that the coating (Al,Cr)N leads to the quality deterioration of the gray cast iron surface yet the said differences, as it has been demonstrated by the statistical significance test, are irrelevant. Furthermore, the quality of the surface of gray cast iron after the machining with covered sialons is better than

after the machining with covered sintered carbides, and the average roughness difference is Ra=1.75 µm.

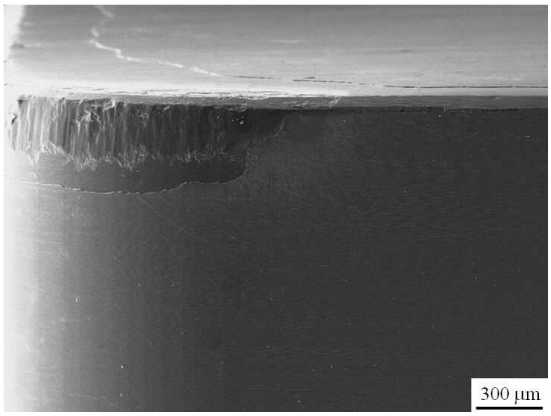

Figure 40. *Characteristic wear of tool flank of sialon tool ceramics inserts with (Ti,Al)N coating*

Table 13. *Roughness of gray cast iron after machining*

Coating	Roughness R_a, µm	
	Sintered carbides substrate	Sialon ceramics substrate
uncoated	4.55	3.03
Ti(B,N)	4.02	2.22
(Ti,Zr)N	3.82	1.96
Ti(C,N) (1)	4.51	2.06
Ti(C,N)+(Ti,Al)N	4.01	2.20
Ti(C,N) (2)	4.16	2.34
(Al,Ti)N	3.86	2.18
(Ti,Al)N	3.50	2.07
(Al,Cr)N	4.89	3.22
Ti(C,N)+Al_2O_3+TiN	3.69	2.76
Ti(C,N)+TiN	4.41	2.09

In the work we applied artificial neural networks to estimate the influence of the properties of the investigated coatings on the durability of cutting edges from sialon ceramics and sintered carbides covered by these coatings. The values of average absolute error, standard deviation and Pearson's correlation factor for the training, validating and testing sets presented in Table 14 bespeak of the fact that the applied artificial neural networks properly reproduce the

modeled relations. It follows from the sensitivity analysis of input data on output data (Table 15) that the durability of the cutting edge is principally influenced by the adhesion of the coatings to the substrate. The change of the critical load being the measure of coating adhesion has the highest influence on the change of cutting edge durability (Figs. 41, 42, 44).

Table 14. *Regression statistics of artificial neural network trained for prediction of PVD and CVD coatings properties deposited onto sialon ceramics*

Network architecture	Regression statistics	Data sets		
		Training Set	Validation Set	Testing Set
MLP3 4:4-6-1:1	Average absolute error	2.57	2.17	2.74
	Standard deviation ratio	0.14	0.10	0.19
	Pearson correlation	0.99	0.99	0.98

Table 15. *Results of sensitivity analysis of input data for output data of artificial neural network trained for prediction of PVD and CVD coatings properties deposited onto sintered carbides*

Data sets	Statistics	Microhardness	Critical load L_c	Grain size	Thickness
Training	Range	4	1	2	3
	Error	2.78	20.30	18.45	5.11
	Ratio	1.33	9.71	8.82	2.44
Validation	Range	4	1	2	3
	Error	3.08	27.12	15.26	4.89
	Ratio	2.49	21.96	12.36	3.96

The other properties such as microhardness, coating thickness and grain size have less significant influence on the changes of durability of the investigated cutting edges (Figs. 41-44). We must emphasize here that from among the other properties the grain size has the highest influence on the change of durability of the investigated cutting edges (Fig. 42), in particular in the case of covered sialon ceramics, yet the durability of the cutting edges is inversely proportional to the grain size. The change of microhardness and the thickness change of the investigated coatings only slightly influence the durability change of the investigated machining cutting edges.

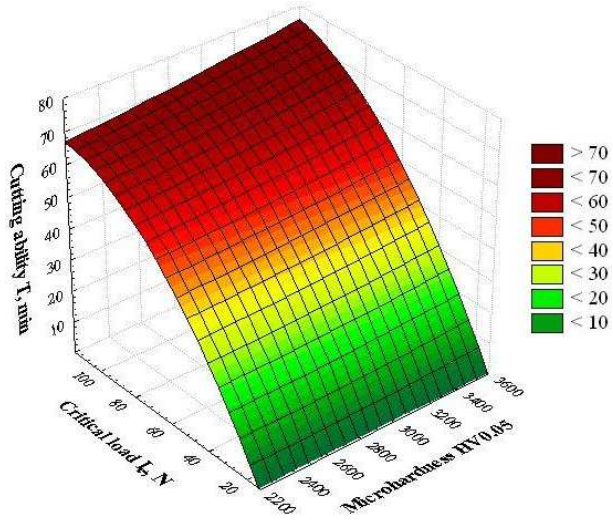

Figure 41. *Evaluation of the PVD and CVD coatings critical load and the microhardness influence of tool life T for sialon ceramics tools coated with PVD and CVD coatings determined by artificial neural networks at a fixed coating thickness 3.0 microns and particle size 8.2 nm*

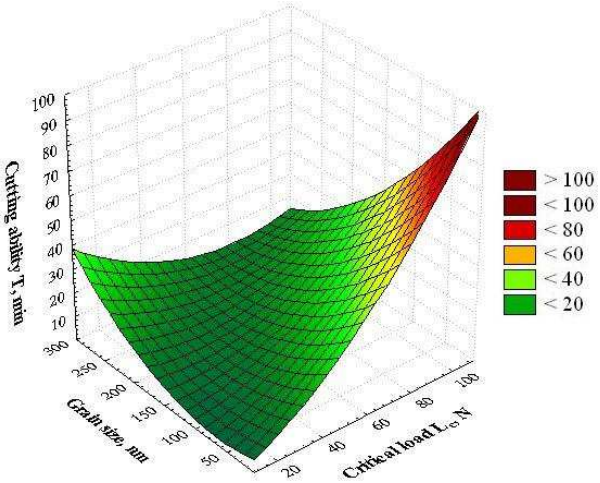

Figure 42. *Evaluation of the PVD and CVD coatings particle size and the critical load influence of tool life T for sialon ceramics tools coated with PVD and CVD coatings determined by artificial neural networks with a fixed thickness of 3.0 microns and coating microhardness 3600 HV0.05*

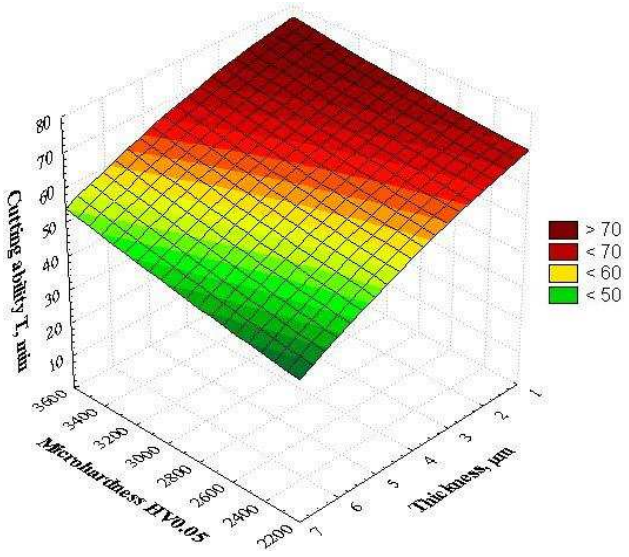

Figure 43. *Evaluation of the PVD and CVD coatings microhardness and the thickness influence of tool life T for sialon ceramics tools coated with PVD and CVD coatings determined by artificial neural networks with a fixed critical load L_c = 105 N and particle size 8.2 nm*

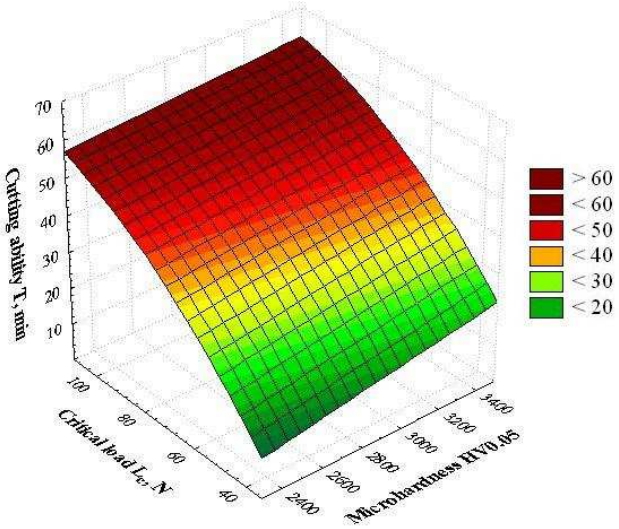

Figure 44. *Evaluation of the PVD and CVD coatings critical load and the microhardness influence of tool life T for sintered carbide tools coated with PVD and CVD coatings determined by artificial neural networks at a fixed coating thickness 2.5 microns and particle size 9.8 nm*

5. Summary

Production technologies and the application of surface layers have a stable position and are regarded as basic knowledge in the field of material engineering. A lot of research centers worldwide working on surface engineering are applying all possible means to fathom and describe the phenomena taking place on the surface of solids. Such a situation instigates scientists to undertake challenging research work aiming to increase the operating durability of surface layers, and, in consequence, the durability of the product [5,6]. The coatings resistant to wear have been successfully applied for around half a century, mainly on machining cutting edges from tooling steel and sintered carbides [7,43,53,81]. What is more, in spite of opinions that the coating of tooling ceramics is aimless due to its sufficiently enough hardness, we can observe an increasing interest in such solutions. A lot of research works [11,12] including also those carried out at the Division of Material Processing Technology, Management and Computer Techniques in Material Science of the Institute of Engineering Materials and Biomaterials of the Silesian University of Technology in Gliwice have been devoted to the problem of coating of tooling materials, including also the coating of tooling ceramics [1,14-29,42,45,52,65,72,73,75,86]. The research studies show that the deposition of thin coatings on the ceramic machining cutting edges is fully grounded, since it has been demonstrated that there is a rise of cutting abilities of ceramic tools covered by the coatings obtained in the PVD and CVD processes. It has been demonstrated that the deposition of coatings on the surface of machining tools such as sintered carbides, tooling cermets, ceramics on the basis of Al_2O_3 and Si_3N_4 contributes among others to a magnificent (around a dozen) rise of the durability of the cutting edge by lowering the wear of cutting edges as compared to the non-covered tools, to the improvement of tribological contact conditions in the contact area tool-machined object and to the protection of the cutting edge against oxidation and excessive heating. These effects directly contribute to the reduction of energy consumption during machining processes, they ensure appropriate technological reliability and reduce standstill incidents of the whole production lines resulting from insufficient durability of the tools.

The designing process of the system coating-cutting edge implies an appropriate selection of coating material in order to reduce or totally eliminate the dominating mechanism of cutting edge wear [55]. As it has been confirmed by numerous research studies, the coating should satisfy various requirements to ensure a suitable protection of the tool during the machining process. Literature studies show that the most important coating properties determining its operating qualities are undoubtedly hardness, adhesion to the substrate and grain size.

Therefore in the paper we present the results of research studies estimating the influence of coating properties on the durability of coated cutting edges.

In order to estimate the relation between the coating properties and operating durability of coated cutting edges we selected the following coatings of the PVD type: Ti(B,N), (Ti,Zr)N, Ti(C,N), Ti(C,N)+(Ti,Al)N, (Al,Ti)N, (Ti,Al)N, (Al,Cr)N and CVD coatings of the type Ti(C,N)+Al_2O_3+TiN and Ti(C,N)+TiN obtained on the substrates from sintered carbides and sialon ceramics. In there investigated coatings we applied solid solutions secondary isomorphic with titanium nitride TiN as well as chromium nitride CrN and aluminum oxide Al_2O_3 in the case of CVD coating.

Basing on the experimental results involving the operating durability we elaborated dependence models between the properties of the coatings and operating durability of the cutting edges covered by the investigated coatings using artificial neural networks. In effect of the carried out simulations it has been demonstrated that the change of coating adhesion to the substrate has most significant influence on the durability of machining cutting edges. Grain size, thickness and microhardness of the obtained coatings have lower influence than adhesion on the durability of cutting edges from sintered carbides and sialon ceramics since the change of these quantities has smaller impact of the operating durability T. However, it has been demonstrated that in congruence with the assumptions the durability of the cutting edge rises with the decreasing grain size, which is confirmed by literature studies [69,91,92,93]. The change of microhardness within the range from 2230 to 3600 HV0.05 has only slight influence on the improvement of cutting edge durability, which is confirmed by 3D images being the results of the simulation with the use of artificial neural networks. The elaborated durability models of the cutting edge can be useful for the prediction of operating properties in view of the knowledge on coating properties, without the necessity to carry out expensive and time consuming cutting ability trials.

Furthermore, in the case of coatings containing AlN phase of the hexagonal lattice, there occur covalence bonds analogous to those in ceramic substrate, which in effect yields good adhesion of these coatings to the substrate. It means that the type of interatomic bonds present in the material of substrate and coating has a great influence on the adhesion of the coatings to the substrate. It can be extremely helpful when selecting the coating material on ceramic cutting edges since the deposition of coatings on cutting edges in PVD processes is difficult due to their dielectric properties, because without the possibility to polarize the substrate during the deposition process it is difficult to obtain coatings which would have good adhesion to ceramic substrates.

Acknowledgements

The paper has been realised in relation to the project POIG.01.01.01-00-023/08 entitled "Foresight of surface properties formation leading technologies of engineering materials and biomaterials" FORSURF, co-founded by the European Union from financial resources of European Regional Development Found and headed by Prof. L.A. Dobrzański.

References

1. M. Adamiak, The structure and properties of TiN and Ti(C,N) coatings deposited in the PVD process on high speed steel. PhD thesis, Silesian University of Technology Library, Gliwice, 1997 (in Polish).
2. M. Arndt, T. Kacsich, Performance of new AlTiN coatings in dry and high speed cutting, Surface and Coatings Technology 163-164 (2003) 674-680.
3. M. Betiuk, T. Borowski, K. Burdyński, The (Ti,Al)N, (Ti,Al)C and (Ti,Al)CN multicompound coatings synthesis in low pressure of DC arc discharge, Engineering Materials 6 (2008) 674-678 (in Polish).
4. T. Burakowski, T. Wierzchoń, Engineering of metal surface, WNT, Warszawa 1995 (in Polish).
5. T. Burakowski, Transformation of superficial layers of areological system, Engineering Materials 6 (2008) 543-547 (in Polish).
6. T. Burakowski, Possibility of areology, Engineering Materials 5 (2006) 890-897 (in Polish).
7. S.I. Cha, S.H. Hong, B.K. Kim, Spark plasma sintering behavior of nanocrystalline WC-10Co cemented carbides powders, Materials Science & Engineering A351 (2003) 31-38.
8. Yin-Yu Chang, Da-Yung Wang, Characterization of nanocrystalline AlTiN coatings synthesized by a cathodic-arc deposition process, Surface and Coatings Technology 201 (2007) 6699-6701.
9. P. Cichosz, Cutting tools, WNT, Warszawa, 2006 (in Polish).
10. F. Čuš, M. Soković, J. Kopač, J. Balič, Model of complex optimization of cutting conditions. Journal of Materials Processing Technology 64 (1997) 41-52.
11. K. Czechowski, I. Pofelska-Filip, P. Szlosek, A. Fedaczyński, J. Kasina, B. Królicka, Chosen properties of hard layers deposited on ceramic material cutting inserts and their influence on the inserts durability, Engineering Materials 5 (2005) 261-264 (in Polish).
12. K. Czechowski, I. Pofelska-Filip, P. Szlosek, B. Królicka, J. Wszołek, Forming the functional properties of cutting inserts of composite oxide-carbide ceramics by nanostructural coatings deposited using the arc PVD method, Engineering Materials 5 (2006) 913-916 (in Polish).

13. D-Y. Wang, C-L. Chang, C-H. Hsu, H-N. Lin, Synthesis of (Ti,Zr)N hard coatings by unbalanced magnetron sputtering, Surface and Coatings Technology 130 (2000) 64-68.
14. L.A. Dobrzański, M. Adamiak, G.E. D'Errico, Relationship between erosion resistance and the phase and chemical composition of PVD coatings deposited onto high-speed steel, Journal of Materials Processing Technology 92-93 (1999) 184-189.
15. L.A. Dobrzański, M. Adamiak, Structure and properties of the TiN and Ti(C,N) coatings deposited in the PVD process on high-speed steels, Journal of Materials Processing Technology 133 (2003) 50-62.
16. L.A. Dobrzański, K. Gołombek, E. Hajduczek, Structure of the nanocrystalline coatings obtained on the CAE process on the sintered tool materials, Journal of Materials Processing Technology 175 (2006) 157-162.
17. L.A. Dobrzański, K. Gołombek, J. Kopač, M. Soković, Effect of depositing the hard surface coatings on properties of the selected cemented carbides and tool cermets, Journal of Materials Processing Technology 157-158 (2004) 304-311.
18. L.A. Dobrzański, K. Gołombek, J. Mikuła, D. Pakuła, Multilayer and gradient PVD coatings on the sintered tool materials, Journal of Achievements in Materials and Manufacturing Engineering 31/2 (2008) 170-190.
19. L.A. Dobrzański, K. Gołombek, Characteristic of nanocrystalline coatings obtained in cathode arc evaporation process onto sintered tool materials, Engineering Materials 3 (2006) 368-371 (in Polish).
20. L.A. Dobrzański, K. Gołombek, Gradient coatings deposited by Cathodic Arc Evaporation: characteristic of structure and properties, Journal of Achievements in Materials and Manufacturing Engineering 14/1-2 (2006) 48-53.
21. L.A. Dobrzański, K. Gołombek, Structure and properties of the cutting tools made from cemented carbides and cermets with the TiN + mono-, gradient- or multi (Ti,Al,Si)N+TiN nanocrystalline coatings, Journal of Materials Processing Technology 164-165 (2005) 805-815.
22. L.A. Dobrzański, J. Mikuła, Structure and properties of PVD and CVD coated Al_2O_3+TiC mixed oxide tool ceramics for dry on high speed cutting processes, Journal of Materials Processing Technology 164-165 (2005) 822-831.
23. L.A. Dobrzański, J. Mikuła, The structure and functional properties of PVD and CVD coated Al_2O_3+ZrO_2 oxide tool ceramics, Journal of Materials Processing Technology 167 (2005) 438-446.
24. L.A. Dobrzański, D. Pakuła, E. Hajduczek, Structure and properties of the multi-component TiAlSiN coatings obtained in the PVD process in the nitride tool ceramics, Journal of Materials Processing Technology 157-158 (2004) 331-340.
25. L.A. Dobrzański, D. Pakuła, A. Křiž, M. Soković, J. Kopač, Tribological properties of the PVD and CVD coatings deposited onto the nitride tool ceramics, Journal of Materials Processing Technology 175 (2006) 179-185.
26. L.A. Dobrzański, M. Polok, M. Adamiak, Structure and properties of PVD coatings on tool steel for nitriding X37CrMoV5-1 to hot work steel, Proceedings of the Third Scientific Conference M^3E'2005, Gliwice–Wisła 2005, 159-166 (in Polish).

27. L.A. Dobrzański, M. Staszuk, J. Konieczny, W. Kwaśny, M. Pawlyta, Structure of TiBN coatings deposited onto cemented carbides and sialon tool ceramics, Archives of Materials Science and Engineering 38/1 (2009) 48-54.
28. L.A. Dobrzański, M. Staszuk, J. Konieczny, J. Lelątko, Structure of gradient coatings deposited by CAE-PVD techniques, Journal of Achievements in Materials and Manufacturing Engineering 24/2 (2007) 55-58.
29. L.A. Dobrzański, M. Staszuk, M. Pawlyta, W. Kwaśny, M. Pancielejko, Characteristics of Ti(C,N) and (Ti,Zr)N gradient PVD coatings deposited onto sintered tool materials, Journal of Achievements in Materials and Manufacturing Engineering 31/2 (2008) 629-634.
30. L.A. Dobrzański, Forming the structure and surface properties of engineering and biomedical materials, Foresight of surface properties formation leading technologies of engineering materials and biomaterials, International OCSCO World Press, Gliwice, 2009. (in Polish)
31. L.A. Dobrzański, The modern tendency into range of development sintered tool materials, Mechanics 1 (1987) 21-31. (in Polish)
32. L.A. Dobrzański, Design and manufacturing functional gradient tool materials - dependence properties on technology and thickness of surface layers with a gradient of both chemical and phase composition manufactured on tool from different applications. Design and manufacturing functional gradient materials, The Polish Academy of Science, Cracow, 2007 (in Polish).
33. S. Dolinšek, J. Kopač, Acoustic emission signals for tool wear identification, Wear 225-229 (1999) 295-303.
34. S. Dolinšek, J. Kopač, Mechanism and types of tool wear; particularities in advanced cutting materials, Journal of Achievements in Materials and Manufacturing Engineering 19/1 (2006) 11-18.
35. Z. Dongli, Y. Dianran, X. Lisong, D. Yanchun, Characterization of nanostructured TiN coatings fabricated by reactive plasma spraying, Surface & Coatings Technology 202 (2008) 1928-1934.
36. L.A. Donohue, J. Cawley, J.S. Brooks, Deposition and characterization of arc-bond sputter Ti_xZr_yN coatings from pure metallic and segmented targets, Surface and Coatings Technology 72 (1995) 128-138.
37. I. Dörfel, W. Österle, I. Urban, E. Bouzy, Microstructural characterization of binary and ternary hard coating systems for wear protection. Part I: PVD coatings, Surface and Coatings Technology 111/2-3 (1999) 199-209.
38. J.L. Endrino, V.H. Derflinger, The influence of alloying elements on the phase stability and mechanical properties of AlCrN coatings, Surface & Coatings Technology 200 (2005) 988-992.
39. G.S. Fox-Rabinovich, J.L. Endrino, B.D. Beake, A.I. Kovalev, S.C. Veldhuis, L. Ning, F. Fontaine, A. Gray, Impact of annealing on microstructure, properties and cutting performance of an AlTiN coating, Surface and Coatings Technology 201 (2006) 3524-3529.
40. C. Gautier, H. Moussaoui, F. Elstner, J. Machet, Comparative study of mechanical and structural properties of CrN films deposited by d.c. magnetron sputtering and vacuum arc evaporation, Surface & Coatings Technology 86-87/1 (1996) 254-262.
41. W. Gissler, P.N. Gibson, Titanium implantation into born nitride films and ion-beam mixing of titanium born nitride multilayers, Ceramics International 22 (1996) 335-340.

42. K. Gołombek: The structure and properties of sintered carbides and cermets tool coated in PVD process by anti-wear coatings. PhD Thesis, Silesian University of Technology Library, Gliwice 2001 (in Polish)
43. J.R. Groza, A. Zavaliangos, Sintering activation by external electrical field, Materials Science & Engineerin A 287 (2000) 171-177.
44. W. Grzesik, Z. Zalisz, S. Król, Tribological behaviour of TiAlN coated carbides in dry sliding tests, Journal of Achievements in Materials and Manufacturing Engineering 17/1-2 (2006) 181-184.
45. H. Hahn, P. Mondal, K.A. Padmanabhan, Nanostructured Materials 9 (1997) 603.
46. S. Hampshire, Silicon nitride ceramics - review of structure, processing and properties. Journal of Achievements in Materials and Manufacturing Engineering 24/1 (2007) 43-50.
47. Y. He, I. Apachitei, J. Jhou, W. Walstock, J. Duszczyk, Effect of prior plasma nitriding applied to a hot-work tool steel on the scratch-resistant properties of PACVD TiBN and TiCN coatings, Surface & Coatings Technology 201 (2006) 2534-2539.
48. P. Holubar, M. Jilek, M. Sima, Nanocomposite nc-TiAlSiN and nc-TiN–BN coatings: their applications on substrates made of cemented carbide and results of cutting tests, Surface and Coatings Technology 120-121 (1999) 184-188.
49. P. Holubar, M. Jilek, M. Sima, Present and possible future applications of superhard nanocomposite coatings, Surface and Coatings Technology 133-134 (2000) 145-151.
50. H. Holzschuh, Deposition Ti-B-N (single and multilayer) and Zr-B-N coatings by chemical vapor deposition techniques on cutting tools, Thin Solid Films 469-470 (2004) 92-98.
51. S. Jonsson, Trita-Mac 506, The Royal Institute of Technology, Div. Physical Mettalurgy, Stockholm, 1992.
52. A. Kloc-Ptaszna: Structure and properties of gradient carbide steel sintered onto groundmass of HS6-5-2 high speed steel. PhD Thesis, Silesian University of Technology Library, Gliwice, 2007 (in Polish).
53. J. Kopač, M. Soković, S. Dolinšek, Tribology of coated tool in conventional and HSC machining, Journal of Materials Processing Technology 118 (2001) 377-384.
54. J. Kopač, Influence of cutting material and coating on tool quality and tool life, Journal of Materials Processing Technology 78 (1998) 95-103.
55. M. Kupczyk, Identification of damage and loss adherence were resistance coatings to edges machineable in adhesion test. Archive of Machine Technology and Automation 21/2 (2001) 231-251 (in Polish).
56. M. Kupczyk, Surface engineering. Wear resistant coatings for cutting edges, Poznań University of Technology Publishing House, Poznań, 2004 (in Polish).
57. T. Kurita, M. Hattori, Development of new-concept desk top size machine tool, International Journal of Machine Tools & Manufacture 45 (2005) 959-965.
58. W. Kwaśny, The structure and properties of coatings obtained in PVD process on sintered high speed steel. PhD Thesis, Silesian University of Technology Library, Gliwice, 2001 (in Polish).

59. T. Leyendecker, O. Lammer, S. Esser, J. Ebberink, The development of the PVD coating TiAlN as a commercial coating for cutting tools, Surface and Coatings Technology 49 (1991) 175-178.
60. Y.H. Lu, Z.F. Zhou, P. Sit, Y.G. Shen, K.Y. Li, Haydn Chen, X-Ray photoelectron spectroscopy characterization of reactively sputtered Ti–B–N thin films, Surface & Coatings Technology 187 (2004) 98-105.
61. K. Lukaszkowicz: Structure and properties of wear resistance and corrosion resistant PVD multilayer coatings. PhD Thesis, Silesian University of Technology Library, Gliwice 2001. (in Polish)
62. A. Michalski, Physical chemistry bases obtaining coatings from gas phase. Outhosue Publishing of Warsaw Technical University Oficyna, Warsaw 2000 (in Polish).
63. A. Michalski, PVD methods applied to deposition both hard and low-fusible material layers on machining tools, Metal science, Heat treatment 79 (1986) 18-23 (in Polish).
64. M. Michalski, D. Siemaszko, Impulsive plasma sintering of WC-12Co nanocrystalline carbides. Engineering materials 3 (2006) 629-631 (in Polish).
65. J. Mikuła, Structure and properties oxides tool ceramic on Al_2O_3 base from PVD and CVD wear resistance coatings. PhD Thesis, Silesian University of Technology Library, Gliwice, 2004 (in Polish).
66. C. Mitterer, P. Losbichler, F. Hofer, P. Warbichler, P.N. Gibson, W. Gissler, Nanocrystalline hard coatings within the quasi-binary system TiN-TiB_2, Vacuum 50 (1998) 313-318.
67. T.P. Mollart, J. Haupt, R. Gilmore, W. Gissler, Tribological behaviour of homogeneous Ti-B-N, Ti-B-N-C and TiN/h-BN/TiB_2 multilayer coatings, Surface and Coatings Technology 86-87 (1996) 231-236.
68. B.A. Movchan, K.Yu Yakovchuk, Graded thermal barrier coatings, deposited by EB-PVD, Surface and Coatings Technology 188-189 (2004) 85-92.
69. J. Musil, Hard and superhard nanocomposite coatings. Surface and Coatings Technology 125 (2000) 322-330.
70. B. Navinšek, P. Panjan, F. Gorenjak, Improvement of hot forging manufacturing with PVD and DUPLEX coatings, Surface and Coatings Technology 137 (2001) 255-264.
71. A.J. Novinrooz, H. Seyedi, M.M. Larijani, Microhardness study of Ti(C,N) films deposited on S-316 by the Hallow Cathode Discharge Gun, Journal of Achievements in Materials and Manufacturing Engineering 14/1-2 (2006) 59-63.
72. D. Pakuła, L.A. Dobrzański, K. Gołombek, M. Pancielejko, A. Kříž, Structure and properties of the Si_3N_4 nitride ceramics with hard wear resistant coatings, Journal of Materials Processing Technology 157-158 (2004) 388-393.
73. D. Pakuła, Structure and properties of PVD and CVD multilayer coatings resistant to abrasion on nitride ceramic tool Si_3N_4. PhD Thesis, Silesian University of Technology Library, Gliwice, 2003 (in Polish).
74. M. Pancielejko, W. Precht, Structure, chemical and phase composition of hard titanium carbon nitride coatings deposited on HS 6-5-2 steel, Journal of Materials Processing Technology 157-158 (2004) 394-298.

75. M. Polok, Structure and properties of PVD coatings deposited onto substrate from X37CrMoV5-1 steel heat treated and plasma nitride. PhD Thesis, Silesian University of Technology Library, Gliwice 2005 (in Polish).
76. W.M. Posadowski, Modern techniques of magnetron atomization, Electronics 4 (2006) 40-43 (in Polish).
77. W. Precht, E. Łunarska, A. Czyżniewski, Corrosion Resistance, Structure and Mechanical Properties of PVD, TiC_xN_{1-x} Coatings. Vacuum 47 (1996) 867-869.
78. W. Precht, Recent advances in hard and superhard anti-wear coating technology, Engineering Materials 3 (2006) 513-515 (in Polish).
79. L. Przybylski, Modern ceramic tool materials. Monograph 276, Technical University of Cracow, Cracow, 2000 (in Polish).
80. A.E. Reiter, V.H. Derflinger, B. Hanselmann, T. Bachmann, B. Sartory, Investigation of the properties of $Al_{1-x}Cr_xN$ coatings prepared by cathodic arc evaporation, Surface & Coatings Technology 200 (2005) 2114-2122.
81. S.H. Risbud, C-H. Shan, Fast consolidation of ceramic powders, Materials Science & Engineering A 204 (1995) 146-151.
82. H. Ronkainen, I. Nieminen, I. Holminen, K. Holmberg, A. Leyland, A. Matthews, B. Matthes, E. Broszeit, Evaluation of some titanium-based ceramic coatings on high speed steel cutting tools, Surface and Coatings Technology 49 (1991) 468-473.
83. D.M. Sanders, Review ion-based coating processes derived from the cathodic arc, The Journal of Vacuum Science and Technology 7/3 (1989) 2339-2345.
84. M. Soković, M. Bahor, On the inter-relationships of some machinability parameters in finish machining with cermet TiN (PVD) coated tools, Journal of Materials Processing Technology 78/1-3 (1998) 163-170.
85. M. Soković, J. Mikuła, L.A. Dobrzański, J. Kopač, L. Koseč, P. Panjan, J. Madejski, A. Piech, Cutting properties of the $Al_2O_3 + SiC_{(w)}$ based tool ceramic reinforced with the PVD and CVD wear resistant coatings, Journal of Materials Processing Technology 164-165 (2005) 924-929.
86. M. Staszuk, The structure and properties of PVD and CVD gradient coatings deposited on sialons and sintered carbides. PhD Thesis, Silesian University of Technology Library, Gliwice, 2009 (in Polish).
87. S. Stolarz, High-melting compounds and phases. Publication of Silesia, Katowice 1974 (in Polish).
88. D.G. Teer, J. Hampshire, V. Fox, V. Bellido-Gonzalez, The tribological properties of MoS_2/metal composite coatings deposited by closed field magnetron sputtering, Surface and Coating Technology 94-95 (1997) 572-577.
89. J.A. Thornton, Journal of Vacuum Science and Technology A 4/6 (1986) 3059-3065.
90. V.V. Uglov, V.M. Anishchik, S.V. Zlotski, G. Abadias, The phase composition and stress development in ternary Ti-Zr-N coatings grown by vacuum arc with combining of plasma flows, Surface & Coatings Technology 200 (2006) 6389-6394.

91. S. Veprek, A.S. Argon, Towards the understanding of mechanical properties of super- and ultrahard nanocomposites, Journal of Vacuum Science and Technology B 20 (2002) 650-664.
92. S. Veprek, S. Reiprich, A concept for the design of novel superhard coatings, Thin Solid Films 268 (1995) 64-71.
93. S. Veprek, New development in superhard coatings: The superhard nanocrystalline-amorphous composites, Thin Solid Films 317 (1998) 449-454.
94. B.G. Wendler, W. Pawlak, Low friction and wear resistant coating systems on Ti6Al4V alloy, Journal of Achievements in Materials and Manufacturing Engineering 26/2 (2008) 207-210.
95. Z. Werner, J. Stanisławski, J. Piekoszewski, E.A. Levashov, W. Szymczyk, New types of multi-component hard coatings deposited by ARC PVD on steel pre-treated by pulsed plasma beams, Vacuum 70 (2003) 263-267.
96. M. Wysiecki, Contemporary Tool Materials, WNT, Warszawa, 1997 (in Polish).

The paper is published also in the Journal of Achievements in Materials and Manufacturing Engineering

Structure and properties of gradient PVD coatings deposited on the sintered tool materials

L.A. Dobrzański*, L.W. Żukowska
Institute of Engineering Materials and Biomaterials, Silesian University of Technology, ul. Konarskiego 18a, 44-100 Gliwice, Poland
* Corresponding author: E-mail address: leszek.dobrzanski@polsl.pl

Abstract

Purpose: *Investigate the structure and properties of sintered tool materials, including cemented carbides, cermets and oxide ceramics deposited with single-layer and gradient coatings (Ti,Al)N and Ti(C,N), and to determine the dependence between the substrate type, coating material or linear variation of chemical composition and the structure and properties of the obtained tool material.*

Design/methodology/approach: *Analysis of the structure (SEM, TEM), analysis of the mechanical and functional properties: surface roughness, microhardness tests, scratch tests, cutting tests. The Ti(C,N) and (Ti,Al)N gradient coating was investigated by XPS and AES method. X-ray qualitative phase analysis and the grazing incidence X-ray diffraction method (GIXRD) was employed to collect the detailed information about phase composition of investigated material's surface layer. Computer simulation of stresses was carried out in ANSYS environment, using the FEM method and the experimental values of stresses were determined basing on the X-ray diffraction patterns.*

Findings: *Results of the investigation the influence of PVD coatings structure (single-layer or gradient) and kind on properties of coated tool materials. Coatings are characterized by dense, compact structure. The coatings were deposited uniformly onto the investigated substrate materials and show a characteristic columnar, fine-graded structure. The coatings deposited onto the investigated substrates are characterised by good adhesion and causes increasing of wear resistance. Gradient coatings are characterized by a linear change of chemical composition in the direction from the substrate to the coating surface. A more advantageous distribution of stresses in gradient coatings than in respective single-layer coatings yields better mechanical properties, and, in particular, the distribution of stresses on the coating surface has the influence on microhardness, and the distribution of stresses in the contact area between the coating and substrate has the influence on the adhesion of coatings.*

Practical implications: *Deposition of hard, thin, gradient coatings on materials surface by PVD method features one of the most intensely developed directions of improvement of the working properties of materials.*

Originality/value: *The grazing incidence X-ray diffraction method (GIXRD) and using the XPS and AES method in the investigated coatings were used to describe the gradient character of the coatings. The computer simulation is based on the finite element method, which allows to better understand the interdependence between parameters of process and choosing optimal solution.*

Keywords: *Materials; Tool materials; Gradient coatings; PVD; Finite Element Method*

Reference to this paper should be given in the following way:

L.A. Dobrzański, L.W. Żukowska, Structure and properties of gradient PVD coatings deposited on the sintered tool materials, in L.A. Dobrzański (ed.) Effect of casting, plastic forming or surface technologies on the structure and properties of the selected engineering materials, Open Access Library, Volume 1, 2011, pp. 187-234.

1. Introduction

The development of material engineering and connected with it application of new structural materials of raised strength properties, improved wear resistance and to high temperature, or to the impact exerted by erosion or corrosion factors is effected by continually rising operating requirements involving the present-day machine design technology [1-10, 31,35,55,60].

In view of the fast development of civilization, continuous production growth and incessant crave to improve the quality of the manufactured products, the requirements involving the applied machining tool materials are becoming progressively higher. Tool materials are facing a considerable challenge to ensure appropriate hardness, wear resistance and very good strength properties. The main groups of tool materials, such as high speed steel, cemented carbides, cermets, tool ceramics and also superhard materials, are being constantly improved, either through the modification of their chemical composition or through the constructional optimization of the tool itself [1,2,40-53,55,56,59].

Equally important is the development of tool materials with respect to the fabrication of thin coatings resistant to wear in PVD and CVD processes. It is of considerable importance, since through the selection of appropriate components, we can obtain a tool material of better

properties. This area of tool material development is a priority nowadays, since it is the main route leading to the acquisition of machining tools of suitable properties [1,54,64,69,62].

The improvement of the functionality properties of the tools and the reduction of ecological hazards can be effected through the application of the technology of hard gradient coatings deposited on the tools in PVD processes, principally by ensuring better conditions of tribological contact in the machining area and by eliminating cutting tool lubricants. The machining process is becoming so common that it is necessary to intensify research studies concerning not only the selection of appropriate material for tools but also the deposition technology of modern coatings resistant to wear to cover the material, primarily such as gradient coatings, and to elaborate them and verify in industrial conditions. The application of physical vapour deposition PVD for the acquisition of gradient coatings of high wear resistance, also in high temperatures, enables to improve the properties of these materials in machining conditions, among others through the reduction of friction factor, rise of microhardness, improvement of tribological contact conditions in the contact area tool-machined item, and also to protect these materials against adhesive or diffusive wear and against oxidation [9,40-42,55-58,63,69].

In the Division of Materials Processing Technology, Management and Computer Techniques in Material Science of the Institute of Engineering Materials and Biomaterials of the Silesian University of Technology research studies have been carried out for several years on various applicability aspects of coatings deposited in the PVD process. The crucial part of the research involves the studies concerning the deposition of thin, wear resistant coatings in the PVD processes on the substrate from high speed steels, both sintered and conventional, of economically selected chemical composition, on cemented carbides and cermets, applied in machining tools and other tools, among others for the processing of polymer materials characterized by high abrasion wear resistance or erosion, as well as the studies on PVD coatings deposited on substrate from oxide [52-55,60], nitride and sialon ceramics with the required resistance to abrasive and operating wear. The carried out investigation studies involve wear resistant PVD coatings deposited on substrates from sintered tool materials having single-, two- several-, and multilayer structures [11-39,48,49,64,65]. A lot is to be expected from gradient coatings being a midway link between the single-layer and multilayer coatings. What makes the gradient coatings exceptional is the possibility to easily regulate the wide spectrum of their functionality properties (from mechanical through anti-corrosion and thermal to decorative ones) by changing the dosage proportions of reactive gases or sputtering intensity of particular shields during PVD processes [5,16,17,31-39,45,46,52,54,57,60,62].

The main objective of the present paper is to investigate the structure and properties of sintered tool materials, including cemented carbides, cermets and oxide ceramics deposited with single-layer and gradient coatings (Ti,Al)N and Ti(C,N), and to determine the dependence between the substrate type, coating material or linear variation of chemical composition and the structure and properties of the obtained tool material.

2. Methodology of research

The research studies were carried out on sintered tool materials, such as cemented carbides, cermets and oxide ceramics, deposited and non-deposited with single-layer and gradient coatings resistant to abrasion of the type (Ti,Al)N and Ti(C,N), using the cathodic arc evaporation method (CAE). The characteristics of the investigated materials are presented in Fig. 1 and Table 1.

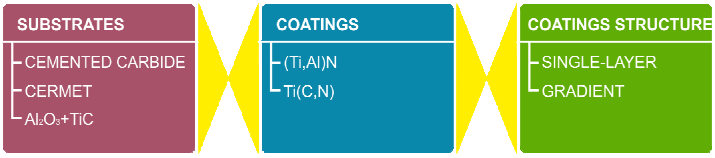

Figure 1. *Characteristics of the investigated materials*

The PVD deposition process of single-layer and gradient coatings of the type (Ti,Al)N and Ti(C,N) was carried out in the Institute of Engineering Materials and Biomaterials of the Silesian University of Technology at Gliwice, on the apparatus DREVA ARC400 of the German Company VTD Vakuumtechnik. The apparatus is equipped with three independent sources of metal vapours.

Before the deposition of coatings, the substrates were prepared for the deposition. The preparation process consisted of two stages. The first stage was carried out outside the operating chamber of the coating apparatus. The multi-point inserts were subjected to chemical cleaning, using washing and rinsing in ultrasonic washers and cascade cleaners, and then they were dried in the stream of hot air. The second preparation stage was carried out in the vacuum chamber of the PVD coating apparatus. That stage consisted in heating the substrate to the temperature of around 400°C with a beam of electrons emitted from the hollow cathode in argon atmosphere with lowered pressure, and then in ionic cleaning using Ar ions with the polarization voltage of the substrate of -300V for 25 minutes.

Table 1. *Characteristics of the investigated materials*

Substrate	Coating	Coating thickness, µm	Roughness, R_a, µm	Micro-hardness, HV	Critical Load, L_c, N	Tool life t, min
Cemented carbide*	uncoated	-	0.13	1755	-	2.5
	(Ti,Al)N	2.2	0.14	2750	52	20.0
	gradient (Ti,Al)N	2.6	0.14	3000	56	25.5
	Ti(C,N)	1.5	0.13	2600	44	5.0
	gradient Ti(C,N)	2.7	0.11	2850	64	5.0
Cermet**	uncoated	-	0.06	1850	-	2.5
	(Ti,Al)N	1.5	0.13	2900	54	19.5
	gradient (Ti,Al)N	3.0	0.12	3150	63	22.0
	Ti(C,N)	1.5	0.12	2950	42	8.0
	gradient Ti(C,N)	2.6	0.11	2950	60	9.5
Al_2O_3+TiC***	uncoated		0.10	2105	-	12.5
	(Ti,Al)N	1.6	0.27	3170	53	21
	gradient (Ti,Al)N	3.2	0.24	3200	65	40
	Ti(C,N)	1.3	0.23	2850	40	15
	gradient Ti(C,N)	2.1	0.21	2950	55	19

***** phase composition: WC, TiC, TaC, Co,
** phase composition: TiCN, WC, TiC, TaC, Co, Ni,
*** phase composition: Al_2O_3, TiC.

For the deposition of coatings, shields of the diameter of 65 mm cooled with water were applied. The shields contained pure Ti and the alloy TiA1 of 50:50% at. The vacuum of 10^{-4} Pa was created in the operating chamber. The coatings were deposited in the atmosphere of inert gas Ar and reactive gases N_2 in order to obtain nitrides, and the mixture of N_2 and C_2H_2 to obtain carbonitride coatings. The gradient concentration change of the chemical composition along the cross-section of the coatings was obtained by changing the dosage proportion of the reactive gases or by changing the intensity of evaporation current of the shield on arc sources.

The surface topography and the structure of the fabricated coatings was investigated at transverse fractures in the scanning electron microscope SUPRA 35 of Zeiss Company, with the accelerating voltage of 10-20 kV and maximum magnification of 60000x. To obtain the images of the structure, the detection of secondary electrons (SE) and back scattered electrons (BSE) was applied. To obtain a brittle fracture of the investigated specimens, notches were cut into their surface with a diamond shield, and then they were broken up after cooling in liquid nitrogen. To improve the conductivity of the investigated material, the specimens were sputtered with carbon using the apparatus JEOL JEE 4B.

The qualitative and quantitative analyses of the chemical composition of the investigated coatings were carried out using the X-ray energy dispersive spectroscopy (EDS), with the application of the spectrometer EDS TRIDENT XM4 of EDAX Company, being a component of the scanning electron microscope Zeiss Supra 35. The research studies were carried out with the accelerating voltage of 20 kV.

The diffraction studies and the observations of thin foil structure were carried out in the transmission electron microscope JEM 3010 UHR of JEOL Company, with the accelerating voltage of 300kV and maximum magnification of 300000x. The diffraction patterns from the transmission electron microscope were being solved using the computer program "ElDyf". Thin foils were made in the longitudinal section, cutting out inserts about 0.5 mm thick from the solid specimens, from which discs of the diameter of 3 mm were cut out, using an ultrasonic erosion machine. Then, such discs were subjected to mechanical rubbing down to the thickness of about 90 µm, and a notch of the depth of around 80 µm was then ground down in the discs. Ultimately, the specimens were subjected to ionic thinning out in the apparatus of Gatan Company.

The changes of chemical concentration of the coating components in the direction perpendicular to its surface, and the concentration changes in the transit zone between the coating and substrate were determined basing on spectroscopic tests: X-ray photoelectron spectroscopy (XPS) and Auger electron spectroscopy (AES). The AES and XPS tests were carried out on the X-ray photoelectron spectrometer of the Physical Electronics Company (PHI 5700/660) whereof diagram is presented in Fig. 2. In this spectrometer the radiation emitted from the anode A1K_α (1486.6 eV) was applied.

The maximum resolution of the spectrometer PHI 5700 applied for the measurements was 0.035 eV. The analysis area from which the electrons are collected is selected using the diaphragm for photoelectrons emitted from the investigated specimen, and the smallest area is defined by a circle of the diameter of 30 µm. Through the application of a pumping system, consisting of the ion and sublimation pumps, we can obtain the pressure of 10^{-7}-10^{-8} Pa, referred to as ultrahigh vacuum UHV. The research carried out with the use of the residual gas analyzer RGA of the mass spectrometer demonstrated that the main components of vacuum in the spectrometer are: CO, H_2, CO_2 (given in the order of the highest partial pressures).

Using the XPS technique [3,6], two types of surface were analyzed: immediately after inserting to the spectrometer and after etching with argon ions. In the second case the beam energy was always 4keV for the preset etching times. The analysis of the surface measured immediately after inserting to the spectrometer showed that there are surface impurities, mainly

oxides and a so called aliphatic carbon (various hydrocarbons, carbon oxides). All locations of photoelectron lines were calibrated against binding energy lines of silver $Ag3d_{5/2}$, gold $Au4f_{7/2}$ and copper $Cu2p_{3/2}$. The pure surface of the investigated gradient coatings was obtained in effect of bombarding the specimen with the beam of ions Ar^+ or Xe^+ of the energy of 4.5keV. The analysis involved the lines of titanium Ti2p and carbon C1s [6,15].

In the case of AES analysis [7], the specimen surface was subjected to etching with argon ions of the energy of 4 keV, and the crater formed on the surface was analyzed by means of linear profile. The analyzed elements were selected in accordance with the preset chemical composition of the investigated coatings. The Auger electrons were recorded with the cylindrical mirror analyzer (CMA). The electrons of the prime beam in the AES PHI660 microscope were emitted from the single crystal LaB_6. The accelerating voltage of the electrons was being changed within the range 3-10 kV. In effect of exposing the solid surface to the illumination of the electrons beam, the emission of Auger electrons, secondary electrons and X-ray radiation is taking place. The depth of the Auger electrons analysis is from 0.4 to 5 nm. These electrons are used for the physicochemical analysis of the composition of the investigated surface, whereas the secondary electrons are used for surface imaging with the application of secondary electron microscopy (SEM).

The analysis of phase composition of the substrates and coatings was carried out using the X-ray diffraction method on the X-ray apparatus X'Pert Pro of Panalytical Company, in the Bragg-Brentano system, applying the filtered radiation of cobalt tube at the voltage of 40 kV and filament current of 30 mA. We accepted the step of 0.05° and calculation time of impulses of 10 seconds. Due to the superposition of the reflexes of substrate and coating material and due to their intensity, hindering the analysis of the obtained results, in order to obtain more precise information from the surface layer of the investigated materials, in our further research we applied the grazing incident X-ray diffraction technique with the application of the parallel beam collimator before the proportional detector.

The thickness of the coatings was tested using the calotest method which consists in the measurement of the characteristic quantities of the crater effected by the wear on the surface of the investigated specimen brought about by a steel ball 20 mm in diameter. The space between the rotating ball and specimen surface was being fed with the suspension of diamond grains of the diameter of 1 μm. The test time was accepted at 120 seconds. The measurement of wear extent was carried through the observations on the illumination metallographic microscope LEICA MEF4A. The thickness of the coating was determined on the basis of the following relation:

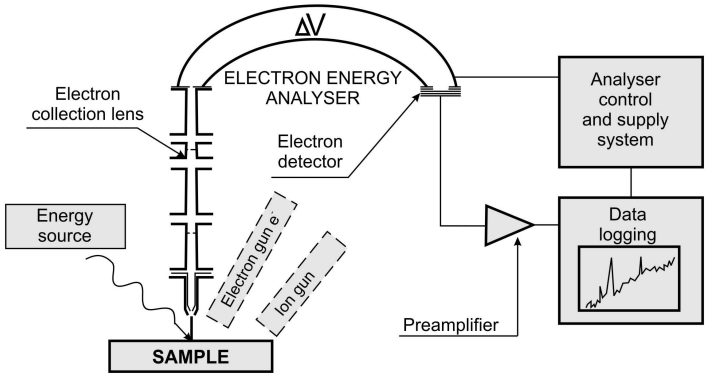

Figure 2. *Schematic diagram of X-Ray Photoelectron Spectroscopy (XPS)*

$$g = \frac{D \cdot (D - d)}{4 \cdot R} \cdot 10^3 \tag{1}$$

where:

g – coating thickness [µm],

D – external diameter of the crater [mm],

d – internal diameter of the crater [mm],

R – ball radius [mm].

In order to obtain average thickness values of the measured coatings, 5 measurements were carried out for each of the investigated specimens. Additionally, to verify the obtained results, the measurements of coating thickness were carried out in the scanning electron microscope at the transverse fractures of the specimens.

The measurements of the surface roughness of the polished specimens without coatings and with deposited coatings were measured in two mutually perpendicular directions on the profilometer Surftec 3+ of Taylor Hobson Company. The accepted measurement length was l=0.8 mm, and measurement accuracy ±0.02 µm. Additionally, to confirm the obtained results, the roughness measurements of specimen surfaces were carried out on the confocal microscope LSM 5 Exciter of Zeiss Company. The parameter Ra was accepted as the quantity describing the surface roughness, in compliance with the Standard PN-EN ISO 4287:1999.

The hardness of the investigated materials was determined using the Vickers method. The hardness of the deposited substrates from sintered tool materials was tested using the Vickers

method with the load of 2.94 N (HV 0.3) in compliance with the Standard PN-EN ISO 6507-1:2007. The tests on microhardness of the deposited coatings were performed on the microhardness meter Future Tech, making use of the Vickers dynamic method. We applied the load of 0.98 N (HV 0.1), enabling, to the highest possible extent, to eliminate the influence of substrate on the obtained results. The measurements were carried out in the mode of periodic loading and unloading, in which the tester loads the indenter with the preset force, maintains the load over some time period and than unloads it. The dynamic hardness is determined from the following equation [11]:

$$DH = \alpha \cdot \frac{P}{D^2} \tag{2}$$

where:
α – a constant allowing for the influence of indenter shape, for Vickers α=3.8584,
P – preset load, mN,
D – imprint depth, µm.

The trial makes it possible to observe the changes of plastic and elastic strain of the investigated material, respectively during the loading and unloading due to a high-precision measurement system which can record the depth of the formed imprint in successive phases of the test. The measurements were carried out making 6 imprints for each of the investigated specimens. An average was determined, as well as standard deviation and confidence interval, assuming the confidence factor at 1-α = 0.95.

The adhesion assessment of the deposited coatings to the investigated sintered tool materials was carried out using the scratch-test on the apparatus REVETST of CSEM Company. The method consists in moving the diamond indenter along the surface at constant speed, with the loading force increasing proportionally with the movement. The tests were carried out for the loading force within the range of 0±100 N, increasing with the speed of (dL/dt)=100N/min along the path of 10 mm.

The critical load Lc at which the coating loses its adhesion was determined basing on the value of acoustic emission (AE) recorded during the measurement and on the observation of scratch lines effected during the scratch-test. The character of the fault was assessed basing on the observations in the scanning electron microscope Zeiss Supra 35 and in the confocal microscope LSM 5 Exciter of Zeiss Company.

The operating properties of the deposited coatings were determined basing on the technological machining trials at room temperature. The tests on cutting ability of the investigated tool materials without coatings and with the deposited coatings were carried out basing on the technological cutting trials without cutting tool lubricants on a universal numerically controlled lathe Gildemeister NEF 320. The cast iron EN-GJL-250 of the hardness of 250 HV was selected as material subjected to machining. For the technological cutting trials, we applied inserts fixed in a universal lathe chuck which ensures the maintenance of geometric parameters of the inserts.

The following parameters were accepted for the cutting ability tests:

- rate of feed f=0.1 mm/rev.,
- turning depth ap=1 mm
- cutting velocity vc=150 m/min.

The durability of the inserts was determined basing on the measurements of wear strip width on the tool flank, measuring the average wear strip width VB after the machining in a definite time interval. The machining trials were being stopped when the VB value exceeded the accepted criterion for after-machining, i.e. VB=0.2 mm. In the case of non-deposited tools, the trial was being carried out until the wear criterion had been reached , and the duration of the trial for the tools with deposited coatings was the same or longer than in the case of non-deposited tools, whereby we can compare the wear strip width VB after the wear criterion has been reached by the non-deposited specimen. The VB measurements were carried out with the application of the illumination microscope Carl Zeiss Jena. The images of tool flank and attack surface of the inserts of different wear degree as well as the topography of the fractured tool with the use of a 3D model were obtained with the application of the scanning electron microscope Zeiss Supra 35 and of the confocal microscope LSM 5 Exciter of Zeiss Company. The analyses of chemical composition in the microareas were carried out using the EDS method. The obtained research results were presented in the form of graphs determining the dependence of wear strip width on the tool flank VB as the function of testing time, assuming the preset conditions of the experiment. Fig. 3 presents the basic tribological faults of the tool material cutting edges, which were then used to assess the wear characteristics of the investigated sintered materials deposited with PVD coatings.

The work presents the application of the finite elements method for the analysis of the distribution of eigen-stresses in the coatings obtained in the PVD process, as dependent on the parameters of the process and the material of the substrate and coating.

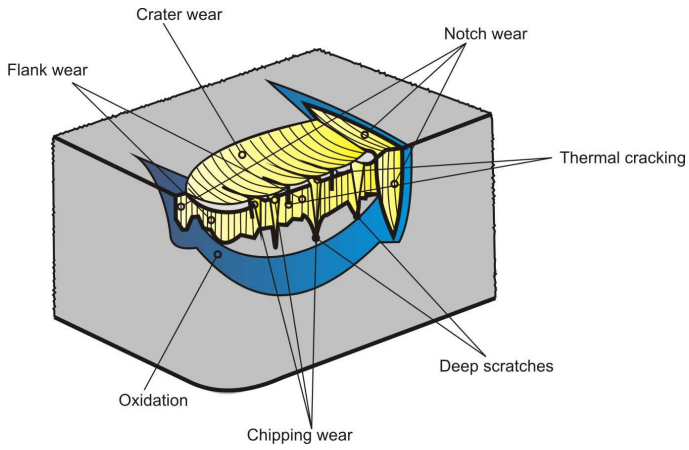

Figure 3. *Tool wear model [1,65]*

The model whereof objective is to determine the eigen-stresses in gradient and single-layer coatings (Ti,Al)N and Ti(C,N) on the substrate from cemented carbides, cermet and oxide tool ceramics, was elaborated using the finite elements method, assuming true dimensions of the specimen. The geometry of the insert with the deposited gradient and single-layer coatings as well as the calculations were carried out using the program ANSYS 12.0. On account of the predicted simulation range, parametric calculation files were elaborated which allowed to perform the analysis in a comprehensive way. We employed the experience involving computer simulation works in material engineering carried out for many years at the Division of Materials Processing Technology, Management and Computer Techniques in Materials Science of the Institute of Engineering Materials and Biomaterials of the Silesian University of Technology [66]. The geometrical model was subjected to discretization with the element of the PLANE 42 type for substrate material and external coating. The element of that type is applied for the modeling of spatial structures with the use of a flat (2-D) element of solids. It can be also applied for the modeling of the structures described by means of axial symmetry. It is a simpler and faster method, by the application of which we can avoid many errors which could have occurred when applying the network on spatial solids. This type of description generates radically smaller MES models as compared to the full 3D description, maintaining the understanding of the general description. The element of PLANE 42 type is defined by four basic nodes and can demonstrate such features as plasticity, creep, swelling, and it also enables the modeling of high bending and tension of the modeled objects. The true model was

subjected to discretization, which is presented in Fig. 4. The calculation model consists of 12816 nodes and 11780 elements. In order to avoid errors in the calculation of eigen-stresses in the coatings, we applied variable quantities of finite elements. In the places where higher gradients of stresses were expected, the network is more condensed than in the areas where the stresses were expected to have values similar to one another. Therefore, in the coatings we applied smaller elements which better reflect the gradients of stresses, and in the substrate material the elements are increasing with the rise of the distance from the coatings.

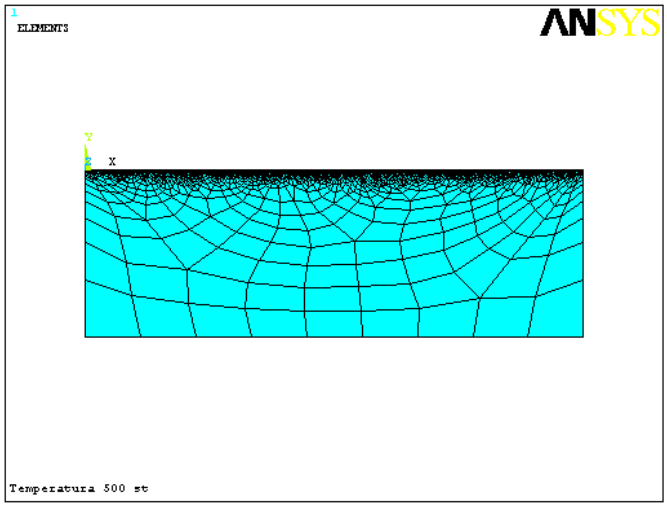

Figure 4. *True model subjected to discretization with deposited gradient and single-layer (Ti,Al)N and Ti(C,N) on different substrates*

Since it was necessary to calculate eigen-stresses in the material of the chemical composition which was changing in the way perpendicular to the surface, the ideographic differentiation of the modeled gradient coatings was carried out into zones corresponding to the areas of similar chemical composition. The model with the spherical division of gradient coating was elaborated in the way ensuring that it was possible to determine the averaged eigen-stresses in the coating areas important in view of the applicability properties and to compare the obtained results with the calculations carried out for homogeneous coatings.

The following boundary conditions were accepted to simulate the eigen-stresses in the gradient single-layer coatings (Ti,Al)N and Ti(C,N) on different substrates:

- the temperature change of the PVD process is reflected by cooling the specimen from 500°C to the ambient temperature of 20°C,
- for the coatings (Ti,Al)N and Ti(C,N) and for the substrate from cemented carbides, cermets and oxide tool ceramics, the material properties were accepted basing on literature data [6] and MatWeb catalogue. The discrepancies in literature data involving the values of physical properties of particular materials result from different acquisition methods, from the differences in the structure and composition of the materials and from errors in the applied measurement method [66],
- the substrate of the investigated specimen is immobilized due to depriving all nodes lying on this axis of all degrees of freedom.

With the temperature drop, from the coating deposition temperature (500°C) to the ambient temperature (20°C), eigen-stresses are generated both in the coating and in the substrate material, connected principally with different thermal expansion of particular materials. The distribution of these stresses is also connected with the geometry of the specimen and with thermal transfer during the cooling process. In effect of non-uniform cooling of the specimen material in the particular areas, the distribution of stresses on the coating surface and their concentration in the corners of the specimen is different.

To verify the results of computer simulation, the values of eigen-stresses in the investigated single-layer and gradient coatings were calculated using the X-ray $\sin^2\psi$ technique.

3. Results

The investigated sintered tool materials are characterized by a well condensed compact structure without pores, and in the case of oxide ceramics Al_2O_3+TiC the topography of the fracture surface bespeaks of high brittleness [24,25], characteristic of oxide ceramic materials (Figs. 5-9).

Basing on the diffraction tests and on the studies involving the structure of thin foils carried out in the transmission electron microscope it was demonstrated that in the investigated substrate materials from cemented carbides and cermets, there are numerous faults of crystalline structure inside the grains of WC and TiC carbides, including dislocations and stacking fault. A part of dislocations is forming low-angle borders dividing the carbide grains into subgrain areas of a small disorientation angle (Figs. 11-12). It was also demonstrated that the average diameter of the wolfram carbide grains is about 1 μm, which places them into the category of fine-grained materials.

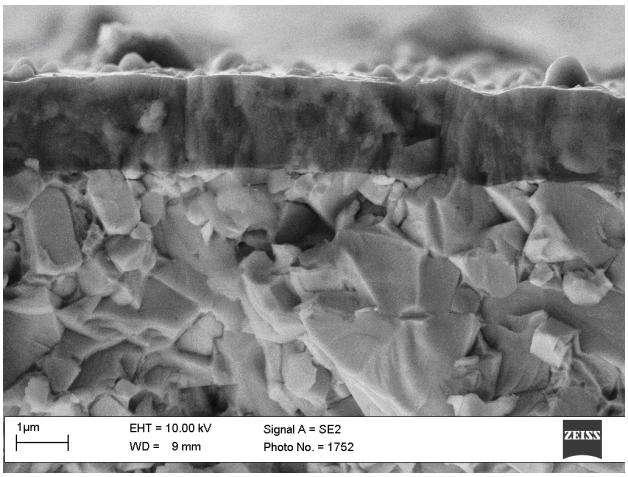

Figure 5. *Fracture surface of the (Ti,Al)N coating deposited onto the cemented carbides substrate*

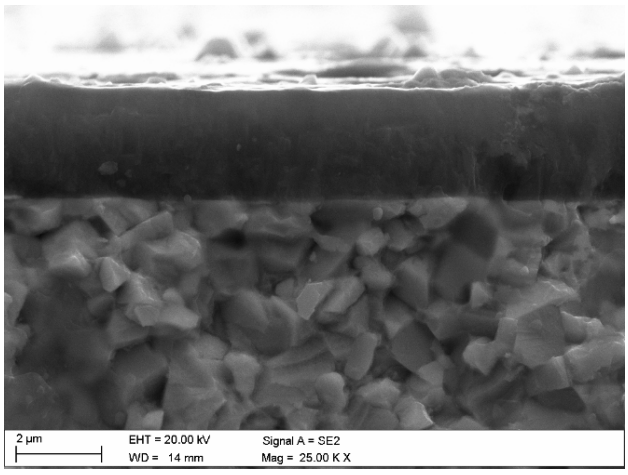

Figure 6. *Fracture surface of the gradient (Ti,Al)N coating deposited onto the cemented carbides substrate*

The results of diffraction tests involving thin foils from the Ti(C,N) coating confirm the occurrence of a phase of the cubic lattice, in compliance with TiN and Ti(C,N). Due to the isomorphism of phases TiN and Ti(C,N) and the similar value of network parameter, it is not possible to differentiate these phases with the electrons diffraction method (Fig. 13). It was also

demonstrated, basing on the tests involving thin foils from the (Ti,Al)N coating that this coating contains principally very fine grains of the crystalline structure corresponding to the phase AlN of the cubic lattice (Fig. 14), and also very few grains of the structure and parameters of AlN phase of the hexagonal lattice. The grains of carbonitrides and of nitrides forming the coating have a very high dislocation density and are very fine – the average grain diameter in the coatings from carbonitrides Ti(C,N) and nitrides (Ti,Al)N does not exceed 0.1 µm.

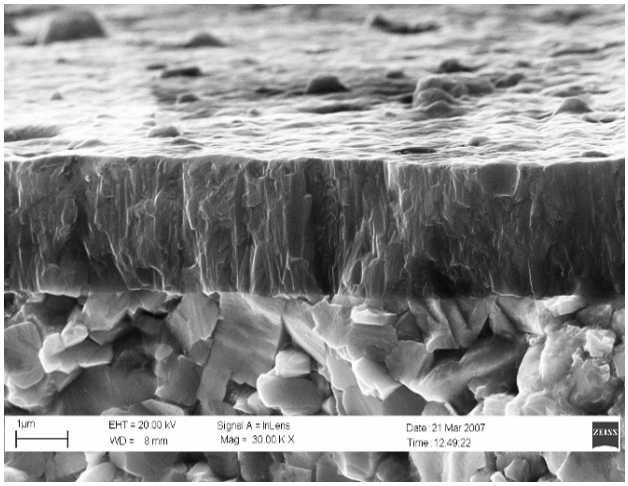

Figure 7. *Fracture surface of the (Ti,Al)N coating deposited onto the cermet substrate*

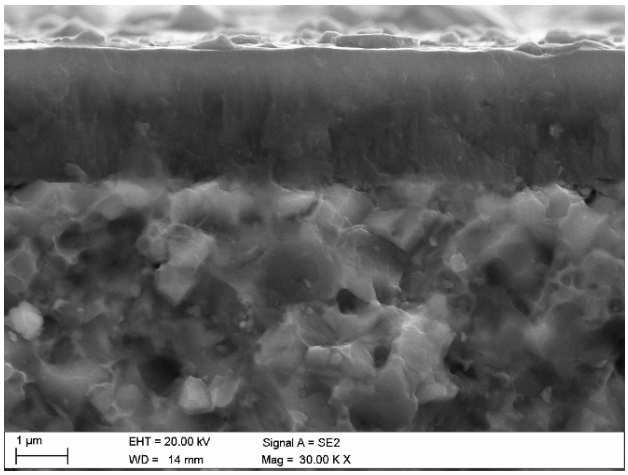

Figure 8. *Fracture surface of the gradient Ti(C,N) coating deposited onto the cermet substrate*

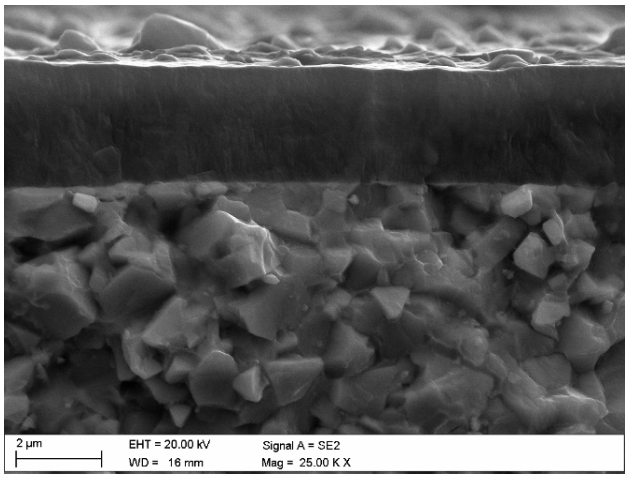

Figure 9. *Fracture surface of the gradient Ti(C,N) coating deposited onto the cemented carbides substrate*

The deposited coatings, both single-layer and gradient ones, have a continuous structure. In the case of gradient coatings, the lines separating particular zones of the coating of the chemical composition different from one another were not determined. It was demonstrated that the coatings are uniformly deposited and are characterized by close adhesion to the substrate, without pores, cracks and discontinuities (Figs. 5-9).

The observations involving the surface morphology of the coatings fabricated in the PVD-CAE process on the substrate from cemented carbides, cermets and oxide ceramics are indicative of high non-homogeneity connected with the occurrence of numerous droplet-shaped microparticles (Fig. 10a). The observed morphological defects brought about during the deposition of the coating are most probably effected by splashing of titanium droplets liberated from the titanium shield onto the substrate surface, which has been confirmed by EDS tests from the microareas (Fig. 10b,c). The droplets observed in SEM assume regular shapes, their size is different and is within the range from the tenths of a micrometer to around a dozen micrometers.

We also observed agglomerates created on the coating surface from several joined microparticles. Furthermore, we observed hollow areas generated in effect of the liberation of titanium microparticles after the termination of the coating deposition process.

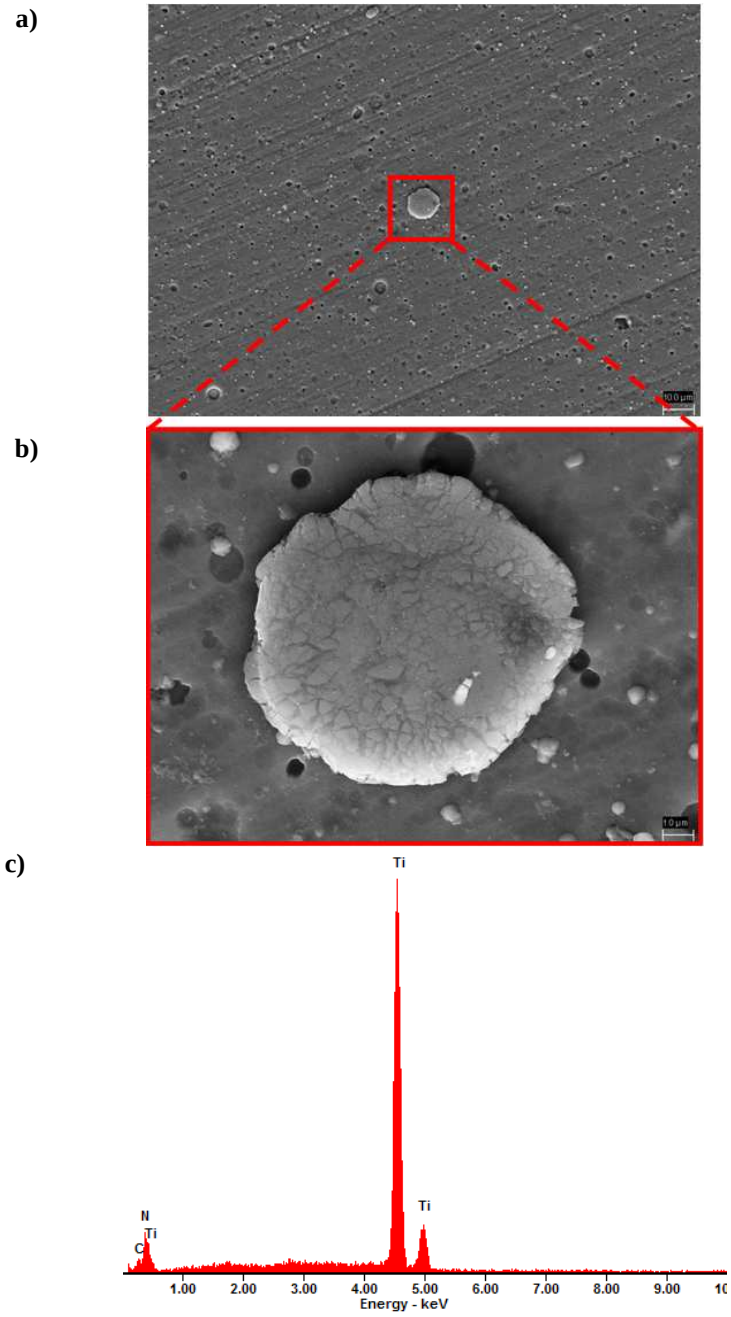

Figure 10. *a,b) Surface topography of the gradient Ti(C,N) coating deposited onto the cermet substrate, c) X-ray energy dispersive plot the area X as in a figure a*

In effect of the carried out research on chemical composition with the use of XPS method, it was demonstrated that the non-etched surface of the coating Ti(C,N) contains small concentration of silicon impurity (around 1% at.) The calculated value of atomic concentration showed that with the fabrication of the coating by means of the PVD method the obtained surface is coated with various adsorbents, mainly carbon oxides and oxygen atoms (Fig. 15). The shape of C1s lines contains at least three components. Two of them are clearly seen at the energy of 284.8 eV and 282.1 eV. The component of the highest intensity, of the energy of 284.8 eV can be ascribed to surface carbon (aliphatic carbon compounds, i.e. hydrocarbons) which does not come from the deposition of Ti(C,N) coating.

The position of lines of lower binding energy of 282.1 eV is typical for carbides. The complex shape of lines observed at the energy of about 288 eV corresponds to carbon oxides adsorbed on the surface of the coating. The intensity of peaks corresponding to surface carbon and carbon oxides is gradually decreasing with the etching time with argon ions. After 20 minutes of etching we can see only one component in the line C1s corresponding to carbides. A similar situation is taking place in the case of titanium lines (Fig. 16). The spectrum of Ti2p lines contains additional components of the doublet. The component of higher binding energy corresponds to titanium atoms in the TiO_2 compound, and the component of lower binding energy corresponds to titanium atoms in the Ti(C,N) coating [60]. After four minutes of etching with argon ions, only one component of the Ti2p doublet is visible. The obtained results for titanium lines and carbon lines demonstrate that the atoms of titanium and carbon are combined with one another in the Ti(C,N) coating in the form of titanium carbide TiC.

In compliance with the accepted assumptions, the deposited Ti(C,N) coating should be characterized by the majority of nitrogen concentration as compared to carbon in the bordering area with the substrate, and by the majority of carbon concentration as compared to nitrogen in the area around the surface. In effect of the analysis of the impurity-free coating surface it was demonstrated that the concentration of the particular components of the coating in the area around the surface is correct (Table 2). A very low atomic concentration of oxygen can be indicative of a low impurity level of the coating with oxygen compounds. Oxygen compounds can be migrating to the inside of the rough coating from residual gases during the PVD process. The obtained ratio of C/N=1.3 is typical for Ti(C,N) coatings. The atomic concentration of carbon with respect to nitrogen atoms in the transit area between the Ti(C,N) coating and substrate should be reversed. But the XPS tests were carried out only to characterize the coating. The investigated specimen was then etched with argon ions for t=50 min, and Fig. 18 presents the depth profile of the chemical composition of the investigated

coating. The oxygen impurity level of the coating is below 2%. The distribution of the particular elements in the investigated coating is maintained at the constant level. The binding energy for the N1s line being 397 eV corresponds to the TiN compound [16].

In effect of etching with argon ions in time t=50 min the depth of the crater did not exceed

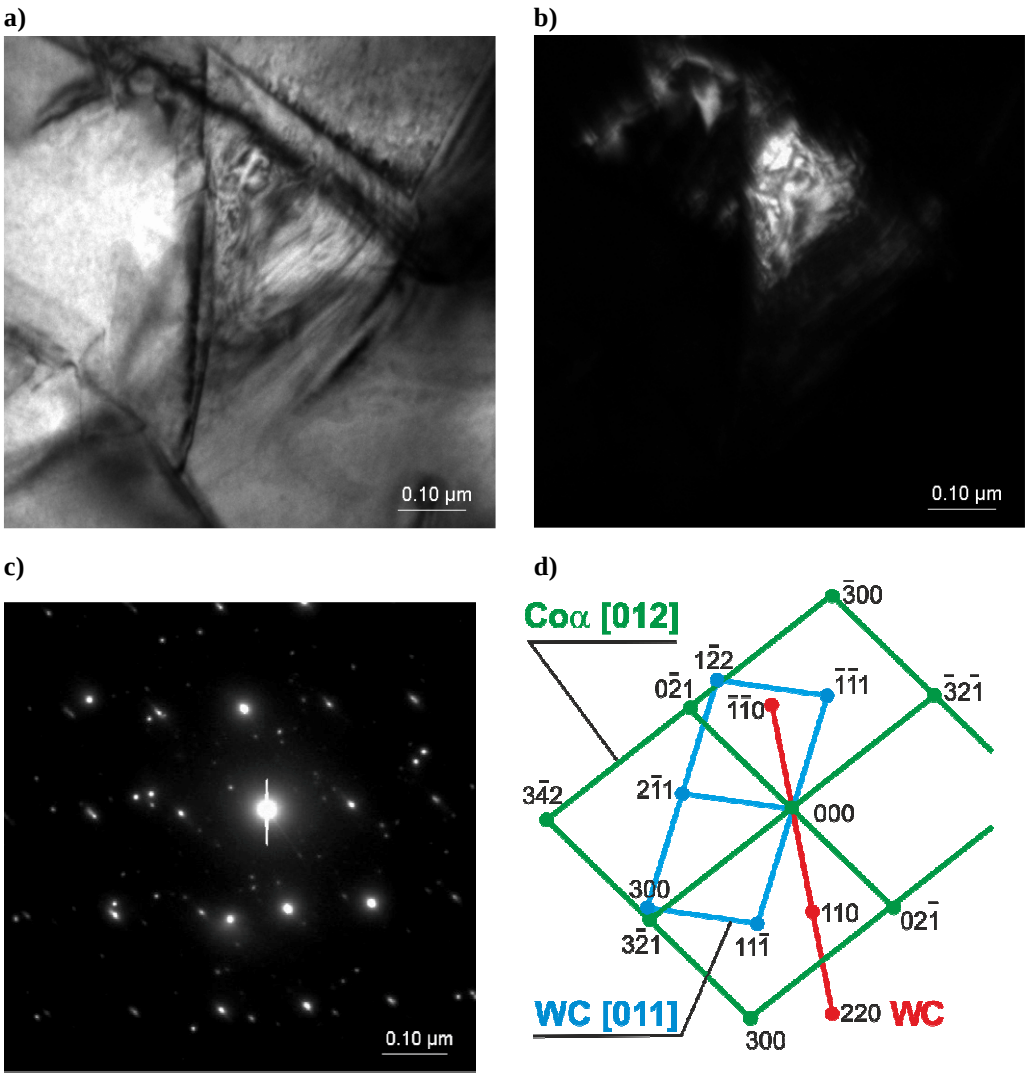

Figure *11.* *Structure of cemented carbides substrate: a) bright field; b) dark field from ($2\bar{1}1$) WC reflex; c) diffraction pattern from area b and d) solution of the diffraction pattern*

the range of area around the surface, and therefore the gradient character of the coating could not be observed. In order to investigate the transit area between the investigated coating and substrate, the etching of the investigated specimen with argon ions to the substrate was carried out.

Basing on the tests involving the chemical composition in the coating area with the AES method, the chemical composition of the coating was confirmed, reflecting the assumptions, and at the bottom of the crater generated in effect of etching we found the elements where of the substrate consists of. The diameter of the crater effected by argon ions bombarding is about 500 micrometers and is dependant on the collimation of the incident ions beam and on the set etching area in the applied ionic area.

The transit area between the Ti(C,N) coating and substrate is presented in Fig. 17a,b with the profile of the created crater. The distribution of particular elements present in the transit area is presented in Fig. 17c. The obtained intensities for all elements were recalculated into atomic concentration. Unfortunately, in the Auger electrons spectrum, the nitrogen line overlaps the titanium line [6,7].

The atomic concentration of wolfram in the substrate is at the level of 4%, and the atomic concentration of nickel is 2%. The width of the transit area in the crater is about 200 micrometers. The change of atomic concentration of the elements in the gradient coating is smooth and not step-wise.

In the case of the gradient (Ti,Al)N coating deposited on the substrate from cemented carbides and cermets, a raised concentration of aluminum, titanium and nitrogen can be observed in the area of external coating, and this concentration is decreasing towards the substrate, which is presented by the linear profile of the investigated specimens with the XPS and AES methods. In the Auger electrons spectrum the nitrogen line overlaps the titanium line, and therefore the analysis of this element with the AES method is not possible. Basing on the produced linear profile, using the XPS and AES techniques, of the (Ti,Al)N coating deposited on the substrates from cemented carbides and cermets, the presence of carbon, wolfram and cobalt in the substrate was determined. The concentration of these elements is gradually decreasing in the transit area, and in the coating itself it is at the level from 0 to 10%.

The tests with the use of X-ray qualitative phase analysis method confirm that the substrate from cemented carbides consists of WC and TiC carbides and cobalt matrix (Fig. 19). In the case of cermet, we determined the presence of carbonitride Ti(C,N), TiC and WC carbides and reflexes from Co and Ni. We also confirmed the presence of phases Al_2O_3 and TiC in the substrate from oxide ceramics. Through the application of the X-ray qualitative phase analysis,

we can confirm that on the substrates from cemented carbides, cermets and oxide ceramics Al_2O_3+TiC, the coatings containing the phases (Ti,Al)N, Ti(C,N) were produced in compliance with the assumptions (Figs. 20-21). On the X-ray diffraction patterns obtained with the use of Bragg-Brentano technique, we also determined the presence of the reflexes from the substrate from cemented carbides, cermet and oxide ceramics Al_2O_3+TiC (Figs. 20-21).

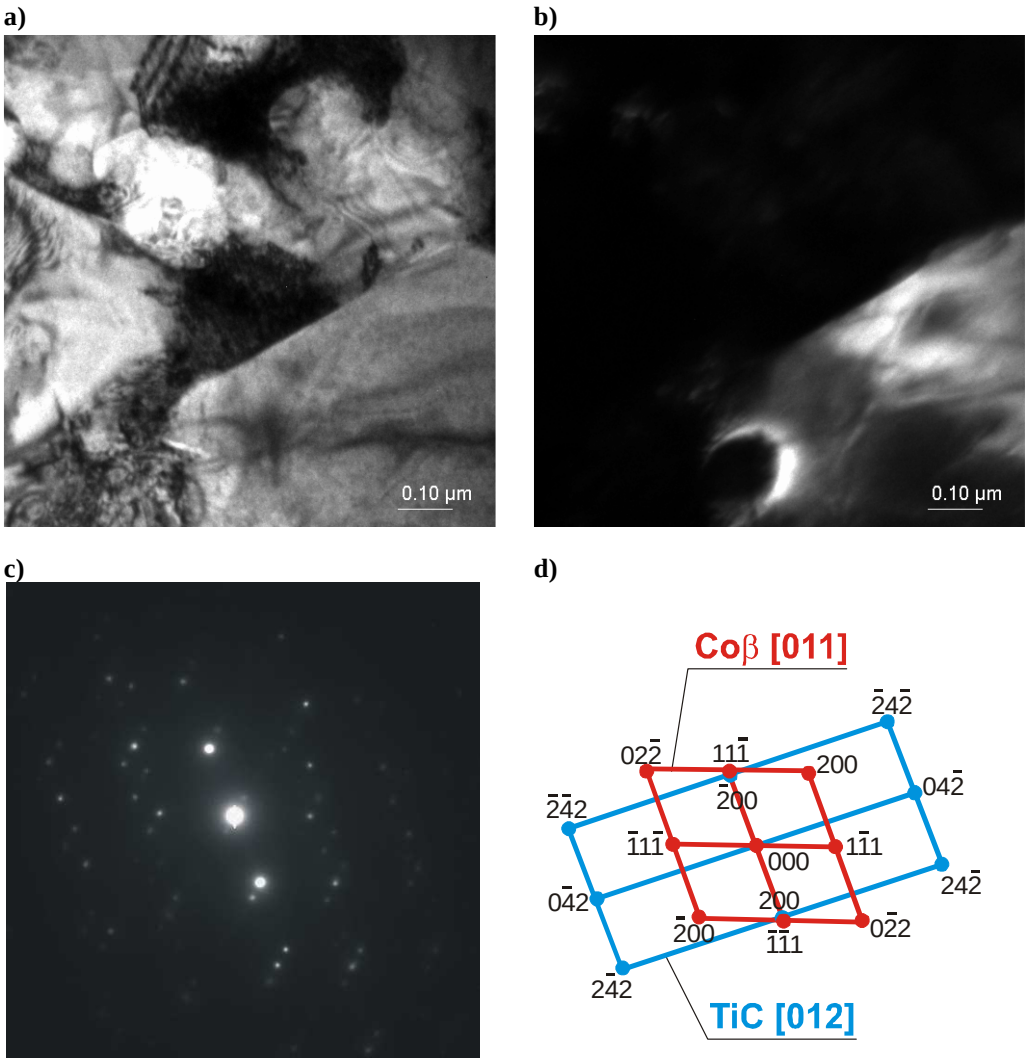

Figure 12. *Structure of cermet substrate: a) bright field; b) dark field from ($\bar{2}00$) TiC i ($11\bar{1}$) Co reflex; c) diffraction pattern from area b and d) solution of the diffraction pattern*

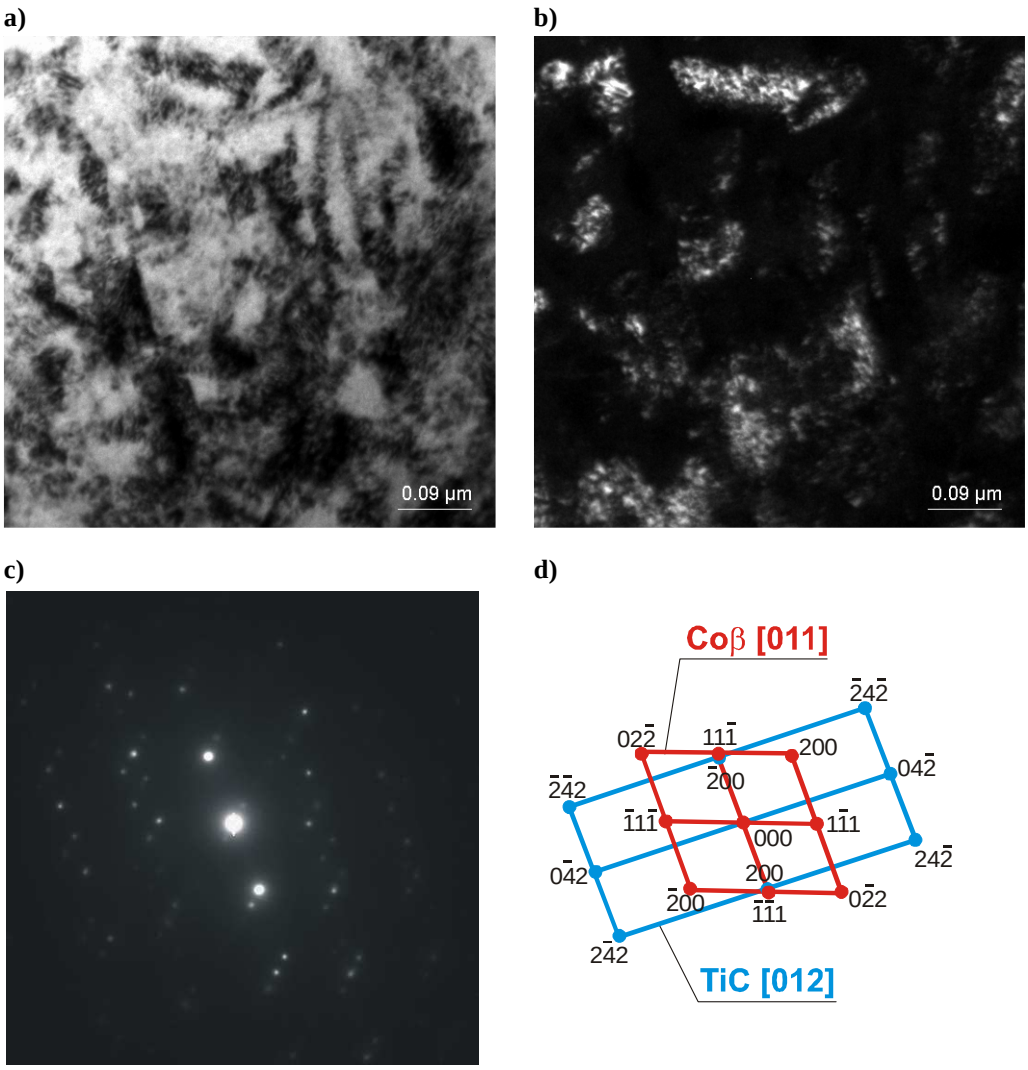

Figure 13. *Structure of Ti(C,N) coating: a) bright field; b) dark field from {111} Ti(C,N) reflex; c) diffraction pattern from area b and d) solution of the diffraction pattern*

Table 2. *Chemical composition of investigated coatings Ti(C,N) on cermet substrates obtained by XPS method*

Element	C	N	O	Ti
Atomic concentration, %	29.9	21.6	4.8	43.7

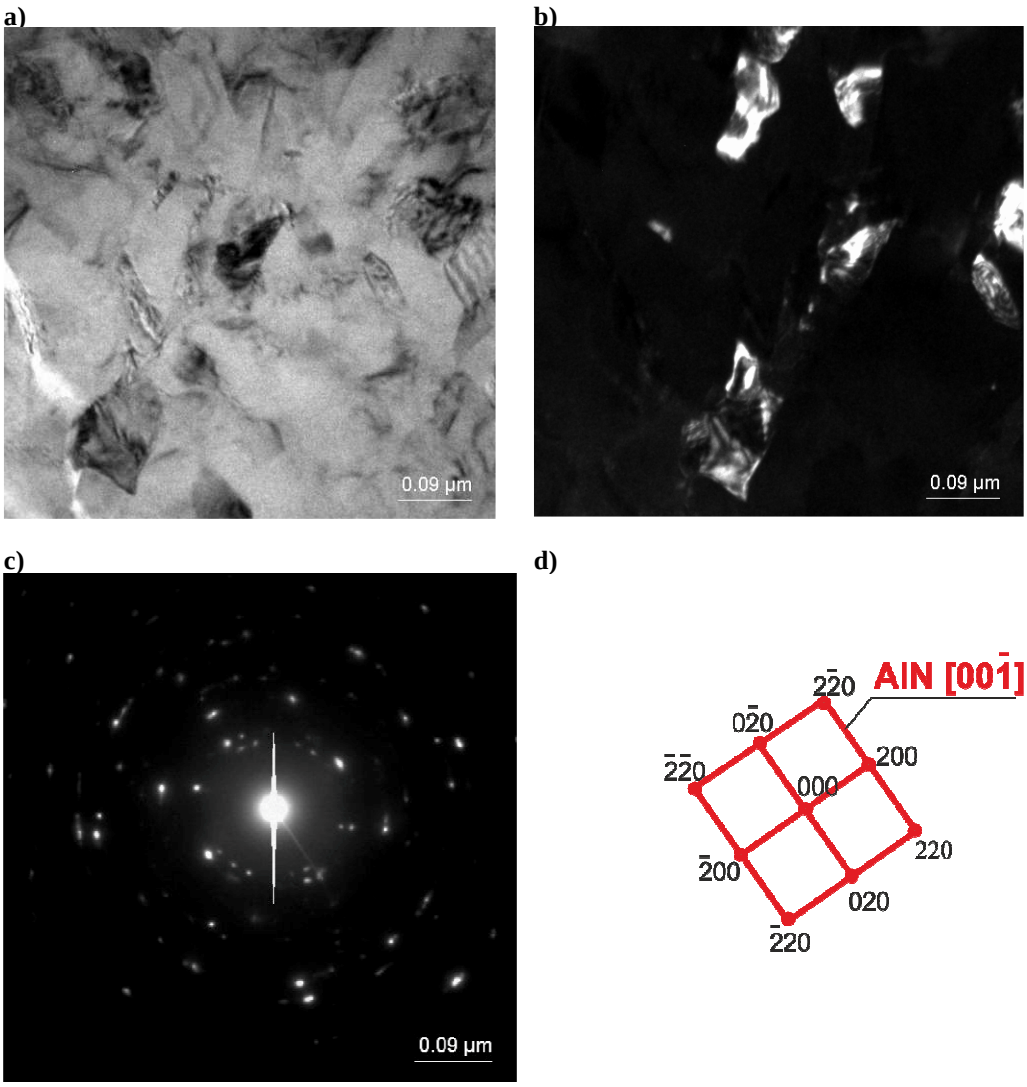

Figure 14. *Structure of (Ti,Al)N coating: a) bright field; b) dark field from ($\bar{2}00$) AlN reflex; c) diffraction pattern from area b and d) solution of the diffraction pattern*

Due to the superposition of the reflexes of the material of substrate and coating and due to their intensity hindering in some cases the analysis of the obtained results, and in order to obtain more precise information from the surface layer of the investigated materials, we applied the SKP or grazing incident X-ray diffraction technique (GIXRD) of the prime X-ray beam (Figs. 22-23).

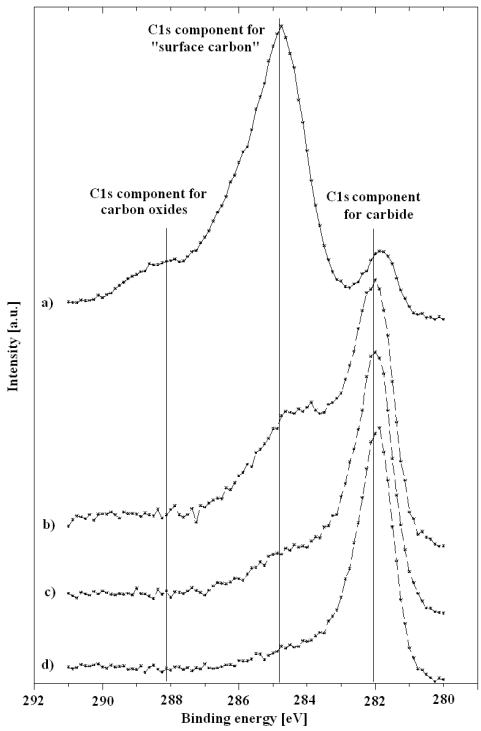

Figure 15. *The shape of C1s lines obtained by XPS method for Ti(C,N) coating: a) "fresh" ex situ surfaces, b) after sputtering Ar^+ ions for t=2 min, c)after sputtering Ar^+ ions for t=4 min, d) after sputtering Ar^+ ions for t=20 min*

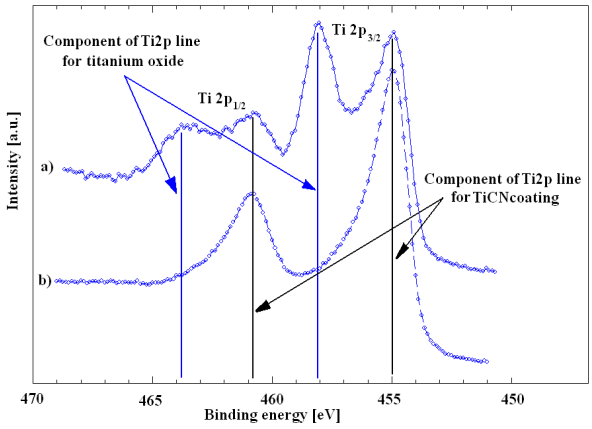

Figure 16. *The shape of Ti2p lines obtained by XPS method for Ti(C,N) coating: a) "fresh" ex situ surfaces, b) after sputtering Ar^+ ions for t=4min*

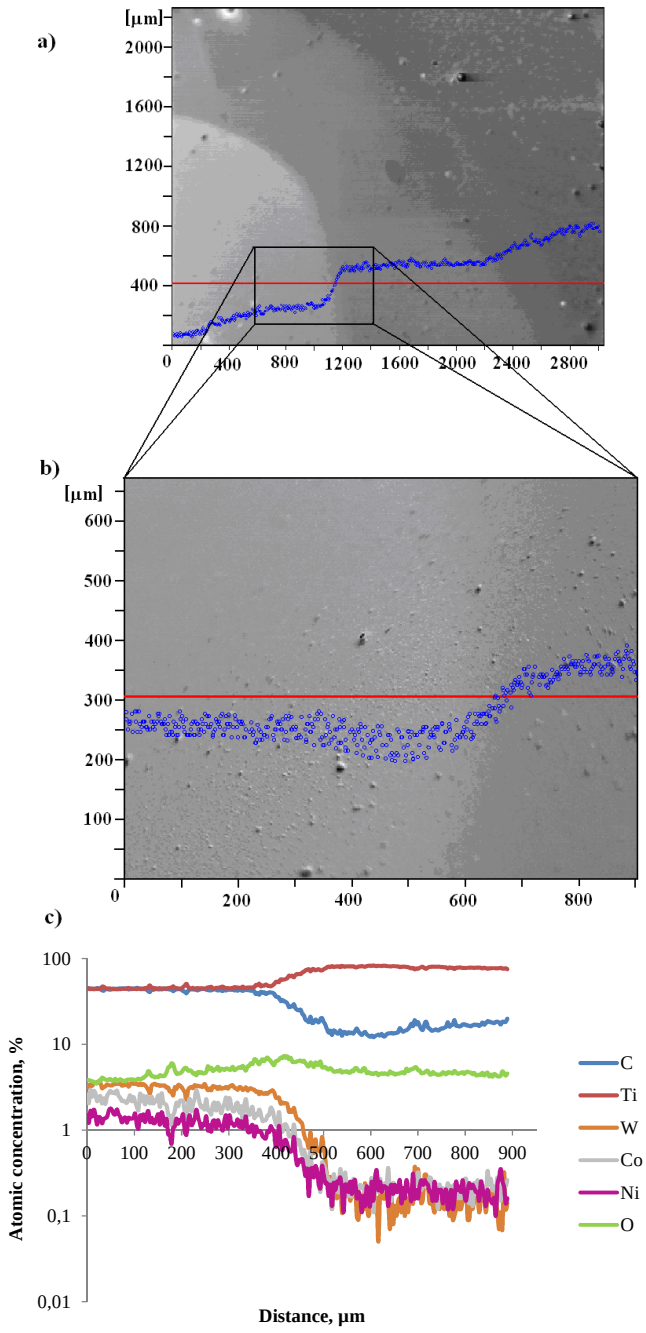

Figure 17. *a,b) SEM picture of transition zone of sputter crater, c) line profile of chemical composition (AES) of gradient Ti(C,N) coating on cermet substrate*

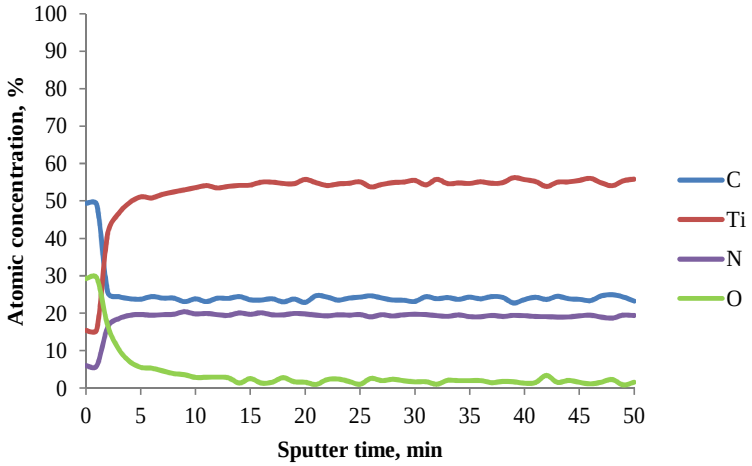

Figure 18. *The distribution of atomic concentration of elements in the surface region of Ti(C,N) coating (XPS)*

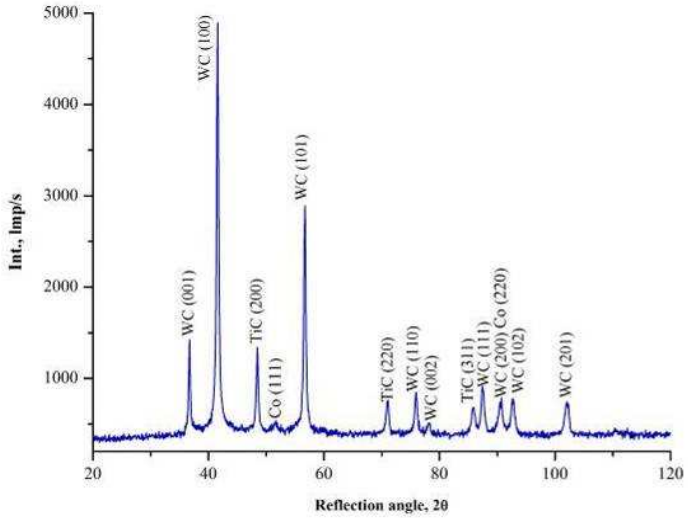

Figure 19. *X-ray phase analysis of the cemented carbides substrate (Bragg-Brentano geometry)*

Basing on the measurement of reflex shift (200) (Fig. 25) in the coating (Ti,Al)N and (111) (Fig. 24) in the coating Ti(C,N) obtained through the grazing incident X-ray diffraction technique (α=1,3, 5, 7) obtained with the use of the proportional detector and the parallel beam

collimator on the side of the bent beam, we determined the network parameters of coatings (Ti,Al)N and Ti(C,N) on the basis of the investigated reflex shift.

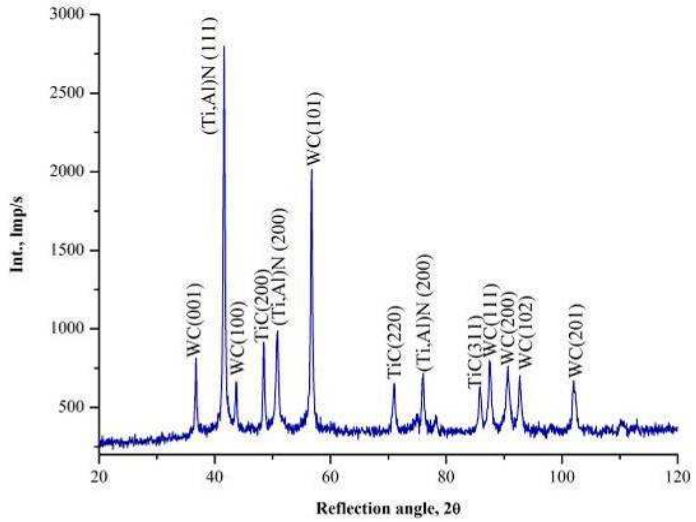

Figure 20. *X-ray phase analysis of the (Ti,Al)N coating (Bragg-Brentano geometry)*

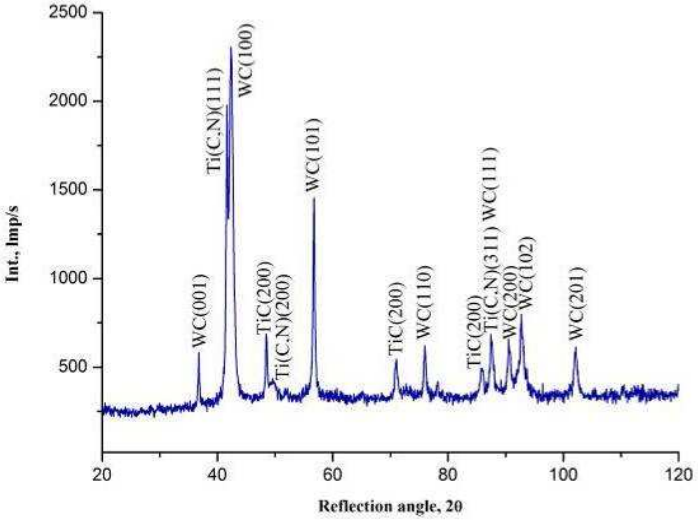

Figure 21. *X-ray phase analysis of the Ti(C,N) coating (Bragg-Brentano geometry)*

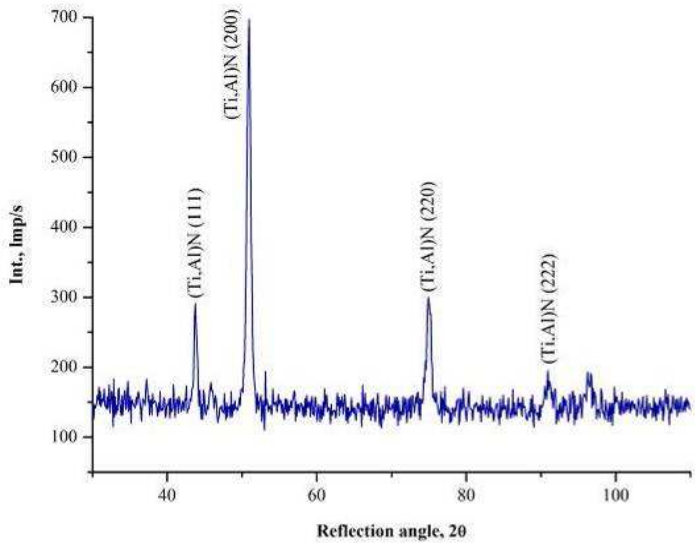

Figure 22. *X-ray phase analysis of the (Ti,Al)N coating (grazing incidence X-ray diffraction GIXRD method), α=1*

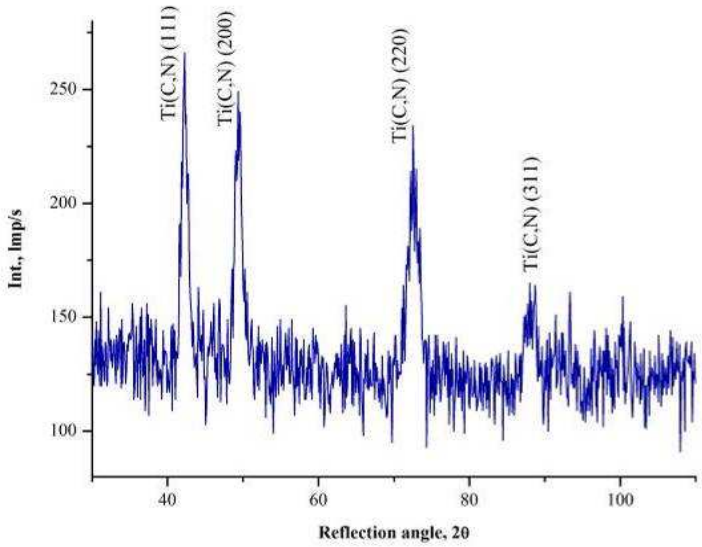

Figure 23. *X-ray phase analysis of the Ti(C,N) coating (grazing incidence X-ray diffraction GIXRD method), α=1*

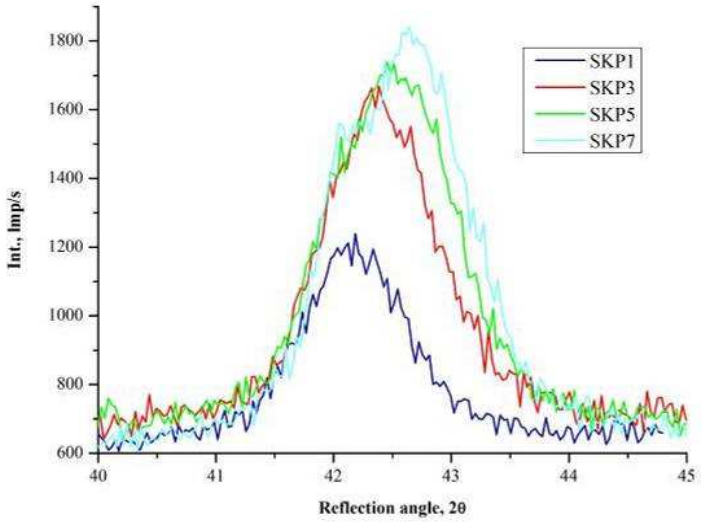

Figure 24. *Change of (111) reflection's position in relation to grazing incidence of the primary beam (Ti(C,N) coating)*

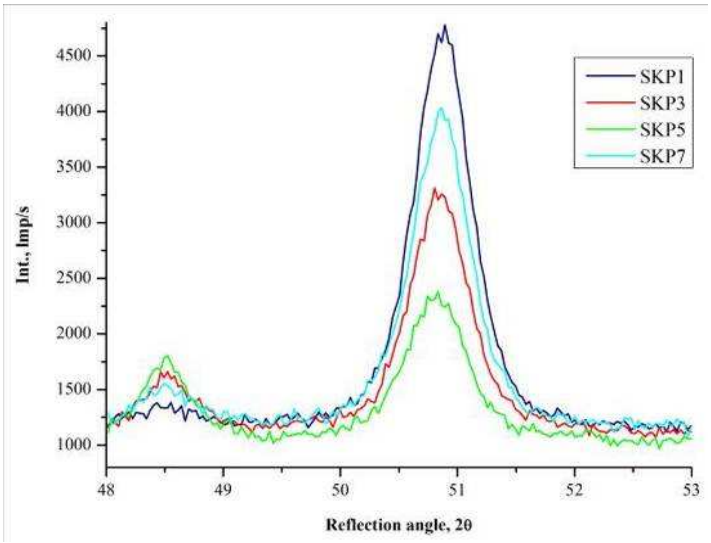

Figure 25. *Change of (200) reflection's position in relation to grazing incidence of the primary beam ((Ti,Al)N coating)*

The experimental results of the X-ray analysis were approximated with the use of a combination of base functions: linear function (adjusting background level) and Voight function (matching the investigated reflexes (Ti,Al)N and Ti(C,N) from the planes (200) and (111). For the determination of base function conditions, the Levenberg-Marquardt algorithm was applied, in which the matching quality was characterized by the function $\chi 2$. The $\chi 2$ function is defined as the sum of the squares of the distance of the experimental results from the values reflected by the determined mathematical model. The parameters of base functions for which the function $\chi 2$ reaches its minimum are indicative of the position of the analyzed reflex on the diffractogram. Basing on the carried out research, in the case of carbonitride coatings, it was determined that the network parameter estimated at the depth of 1µm is close to the one quoted in the JCPDS file (42-1489) to the value corresponding to phase Ti(C,N) richer in carbon. With the rise of the incidence angle of the prime beam, which results in the rise of material volume taking part in the diffraction, the estimated network parameter corresponds to the phase Ti(C,N) richer in nitrogen (42-1488) (Fig. 26). In the case of (Ti,Al)N coating, no considerable changes of network parameter value at the depth of the investigated coating were determined (Fig. 26).

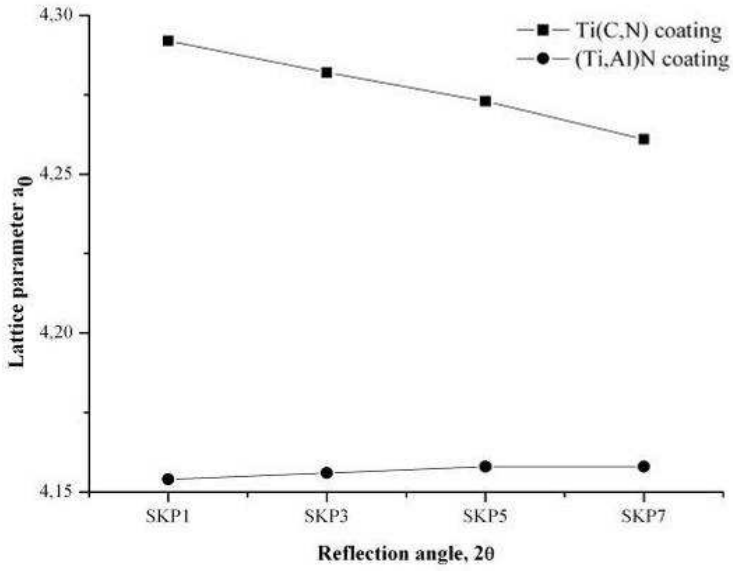

Figure 26. *Comparison of the change of lattice parameter estimated for Ti(C,N) and (Ti,Al)N coating*

The deposition of single-layer and gradient coatings resistant to wear of the type (Ti,Al)N and Ti(C,N) on the investigated sintered tool materials results in the rise of roughness parameter R_a which is within the range from 0.11-0.27µm, and is higher than in the case of material surfaces without coatings (Table 1). The roughness rise of the surfaces of the deposited coatings should be linked to the character of PVD process – physical vapour deposition, which was confirmed by the morphological tests of the surface in the scanning electron microscope (Fig. 10). The roughness of the substrate has the influence on the roughness of the deposited coating and on its structure, as well as on the adhesion of the coating to the substrate (Fig. 27). Too high roughness of the substrate (R_a>0.4) can cause a so called thinning out effect and a generation of coatings of low-compacted structure with numerous surface defects and low adhesion to the substrate. With the application of too smooth substrates (R_a<0.04) we can not ensure a satisfying mechanical anchoring of the increasing coating against the substrate [75,159].

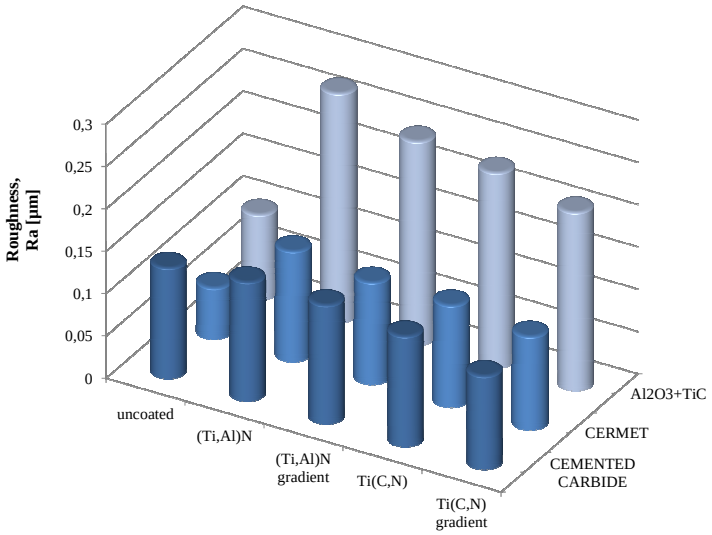

Figure 27. *Comparison of the roughness parameter R_a of the investigated materials*

The deposited PVD coatings are characterized by good adhesion to the substrate within the range L_c=40-65N. In general, the deposition of wear resistant gradient coatings of the type (Ti,Al)N and Ti(C,N) on the investigated sintered tool materials results in a considerable rise of microhardness in the area around the surface (Fig. 28), which, combined with the good

adhesion of the coating to the substrate (Fig. 29) obtained in effect of the application of gradient structure of the coating, yields good functionality properties of these materials, confirmed during machining tests (Table 1).

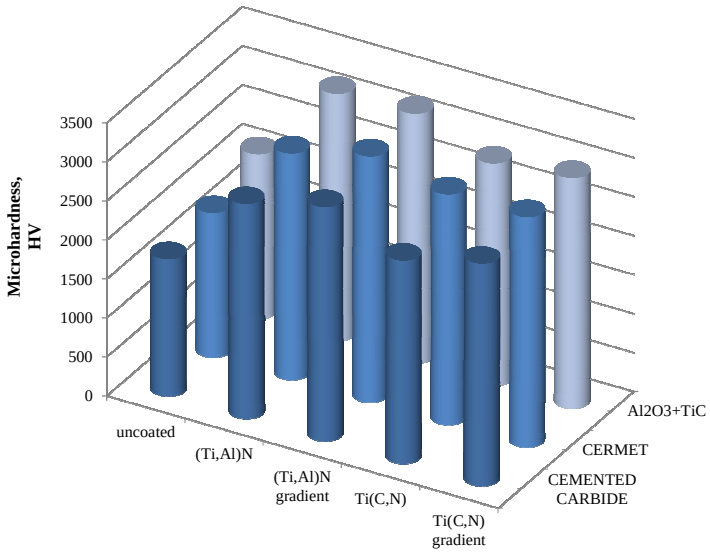

Figure 28. *Comparison of the microhardness of the investigated materials*

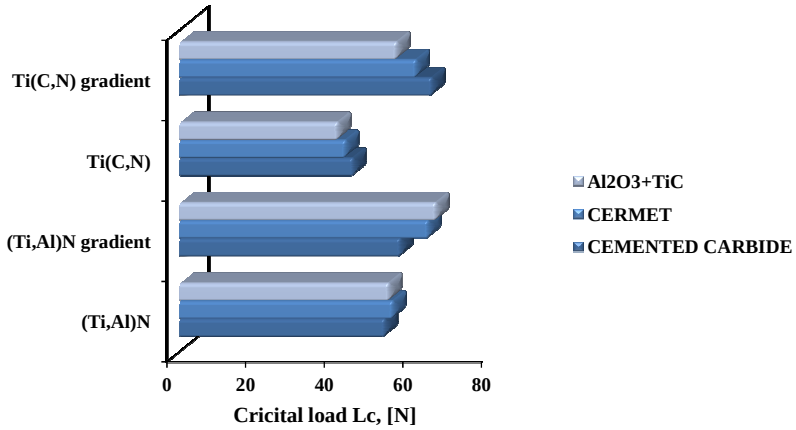

Figure 29. *Comparison of the critical load according to the scratch test of the investigated coating deposited onto cemented carbides, cermets and Al_2O_3 type oxide tool ceramics*

a)

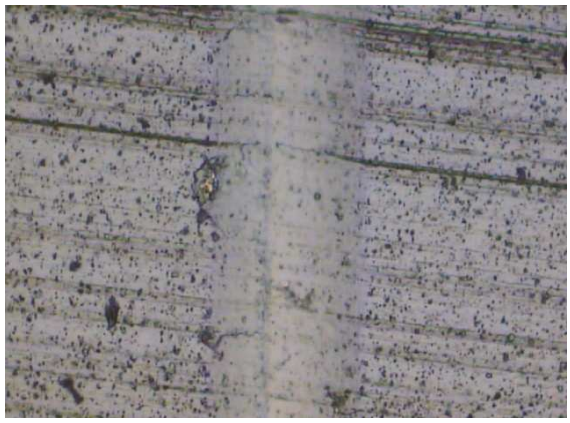

b)

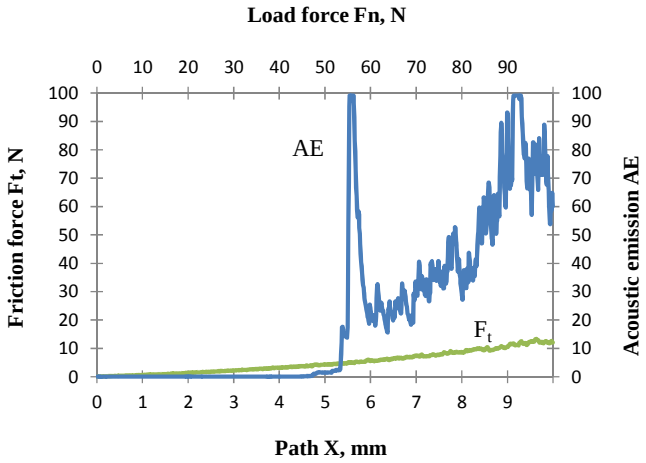

Figure 30. *a) Indenter trace with the optical L_c=45N load (mag. 200x), b) scratch test results of the (Ti,Al)N coating surface deposited on cemented carbides substrate*

The hardness of the substrate material (Table 1, Fig. 28) is 1755 HV for cemented carbides, 1850 HV for cermet and 2105 HV for oxide ceramics. The deposition of the coatings (Ti,Al)N and Ti(C,N) on the investigated sintered tool materials results in a considerable rise of microhardness in the area around the surface within the range of 2600-3200 HV. It was demonstrated that the gradient coatings have higher hardness than the single-layer coatings, independent of the substrate material. Hardness is a property of material dependant on the values of intermetallic bonds, so the hardest materials have covalence bonds, and the rise of the

share of ionic character of the bond is associated with the drop of hardness [11]. Basing on the carried out research it was demonstrated that the hardness of Ti(C,N) coatings, in which the metallic phases TiN and TiC occur, demonstrates lower hardness than (Ti,Al)N coatings in which there are both metallic bonds TiN and covalence bonds AlN. The deposition of the wear resistant coatings on the investigated substrates results in a considerable rise of microhardness of the surface layer, which contributes to lower wear intensity of the cutting edge of machining tools from cemented carbides, cermets and oxide ceramics during the machining process.

a)

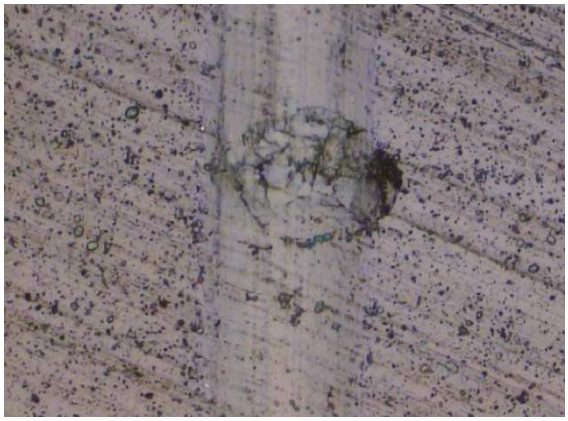

b)

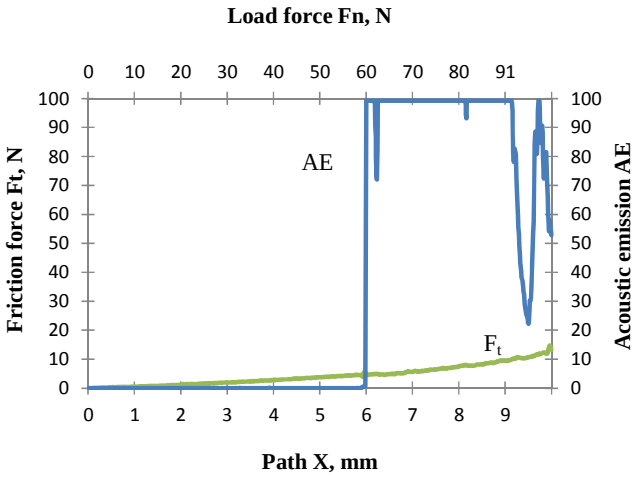

Figure 31. *a) Indenter trace with the optical L_c=59 N load (mag. 200x), b) scratch test results of the gradient Ti(C,N) coating surface deposited on cermet substrate*

In order to check the correlation between the hardness of the investigated materials and the functional properties of the multi-point inserts in the machining tests were carried out, the durability of the inserts was determined on the basis of the measurement of wear width on the flank face after the machining in a definite time interval (Table 1).

The carried out research confirmed that better results are obtained by the tools deposited with (Ti,Al)N coatings, independent of the substrate material. It is connected among others with high microhardness of the coatings and with high wear resistance in raised temperature of the (Ti,Al)N coating. It was also demonstrated that independent of the applied substrate type, higher wear resistance is exhibited by the materials deposited with the gradient coating as compared to the materials deposited with a single-layer coating. It can be related with the reduction of stresses between the coating and substrate in the case of gradient coatings (Table 3), which was also confirmed in the work [54]. Furthermore, it was demonstrated that for the oxide ceramics Al_2O_3+TiC deposited with PVD coatings, the longest durability of cutting edges T=40 min is for the gradient coating (Ti,Al)N and for the single-layer coating (Ti,Al)N T=21 min, as compared to the coatings deposited on cemented carbides and cermets, which can be related with higher hardness of the substrate material (Table 1, Figs. 33-38).

Table 3. *Results of computer simulation of internal stresses in the analysed gradient PVD coatings*

Substrate	Coating	Computer simulation results of internal stress, [MPa]		
		Surface layer	Middle layer	Contact area
Cemented carbide	(Ti,Al)N	-350	-220	130
	Ti(C,N)	-150	160	280
Cermet	(Ti,Al)N	-570	-350	-100
	Ti(C,N)	-300	-50	50
Al_2O_3+TiC	(Ti,Al)N	-380	-250	100
	Ti(C,N)	-170	120	240

The most frequently occurring types of tribological defect indentified in the investigated materials are the mechanical abrasive defects of the flank face, crater formation of the rake face, thermal cracks on the flank face, chipping of the cutting edge (Fig. 39). We also found a build-up of chip fragments of the machined material on the flank face, which is confirmed by the presence of maximums from iron on EDS graphs from the investigated microareas.

The replacement of the single-layer (Ti,Al)N coating with the gradient coating results in a considerable drop of absolute value of eigen-stresses occurring in the material in the contact area between the coating and substrate (Table 3-4), which has a positive influence on the adhesion of gradient coatings to the substrate, which can be one of the main factors yielding better applicability properties such as wear resistance.

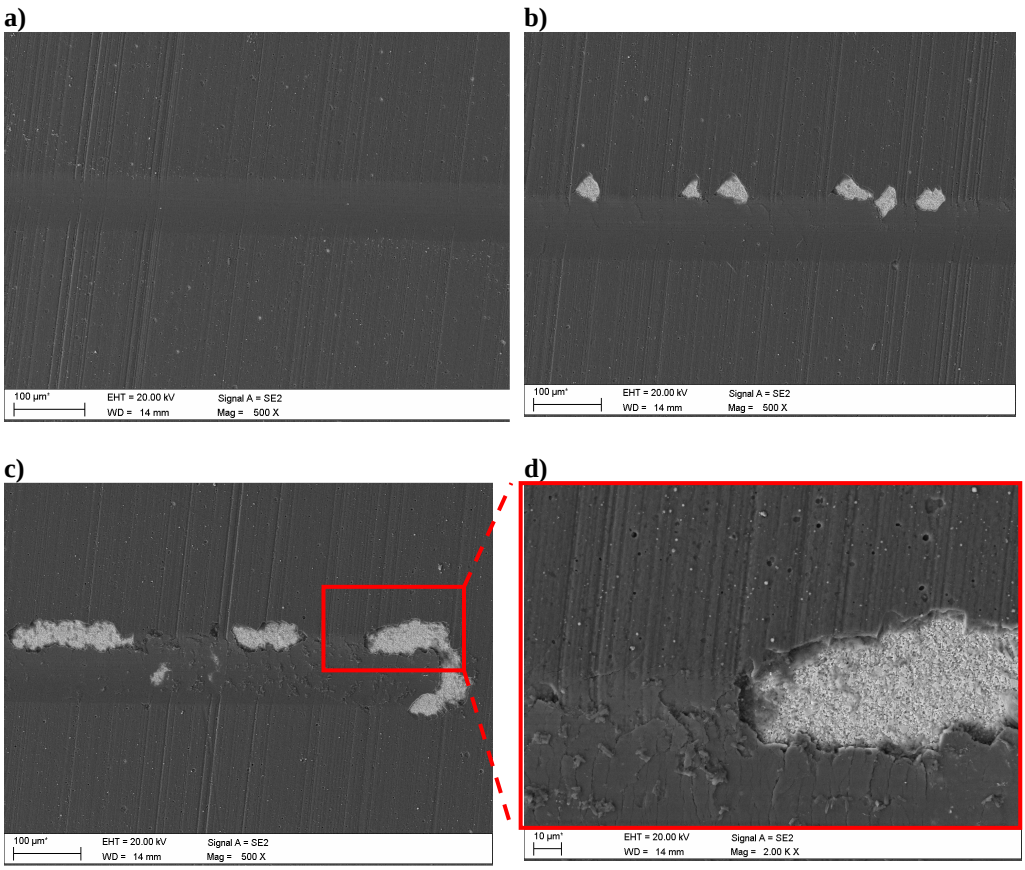

Figure 32. *a,b,c,d) Characteristic failure obtained by scratch test of the (Ti,Al)N coating deposited on cemented carbides substrate*

In the case of Ti(C,N) coatings we can observe the rise of tensile eigen-stresses in the contact area after the replacement of the single-layer coating with the gradient one (Table 3-4). In spite of this, higher adhesion has been demonstrated in the case of gradient Ti(C,N) coatings than in the case of respective single-layer coatings. It can be connected with the character of surface topography and the size of coating grains with respect to the roughness of the substrate, which, combined with the presence of tensile stresses, can result within certain limits in the positive influence of such stresses on the adhesion due to anchoring of the coating in a relevantly developed surface of the substrate [11].

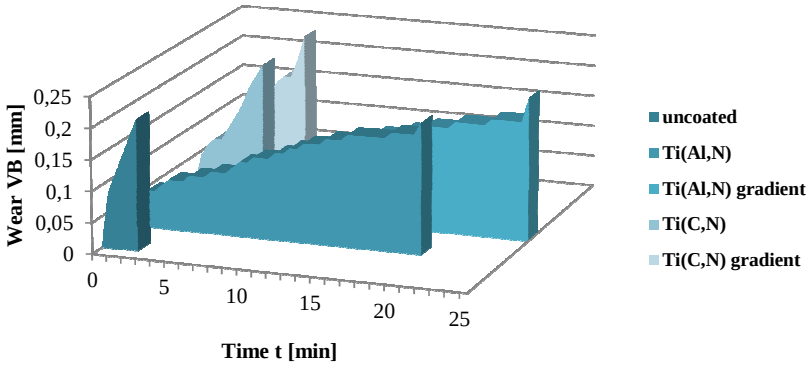

Figure 33. *Comparison of the approximated values of the VB wear of the cemented carbides sample: uncoated and coated with the PVD coatings, depending on machining time*

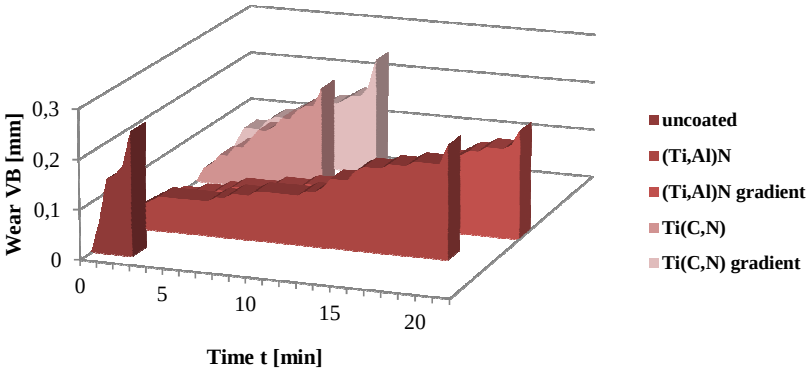

Figure 34. *Comparison of the approximated values of the VB wear of the cermets sample: uncoated and coated with the PVD coatings, depending on machining time*

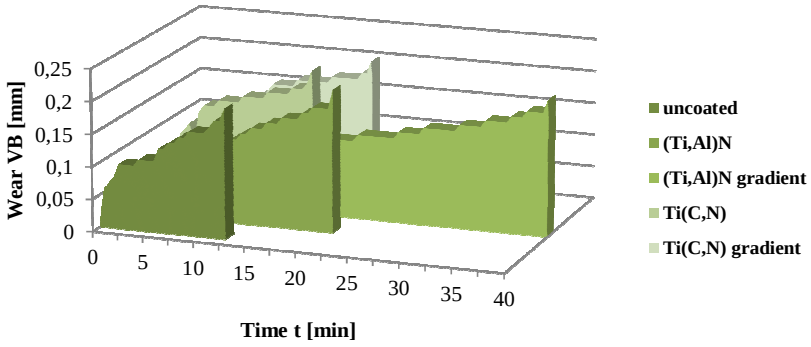

Figure 35. *Comparison of the approximated values of the VB wear of the Al_2O_3+TiC oxide tool ceramics sample: uncoated and coated with the PVD coatings, depending on machining time*

Due to the application of gradient coatings on all investigated substrate materials, we obtained compressive stresses in the surface layer of the coating having a direct contact with the machined material during the operation process (Table 3). In the case of gradient (Ti,Al)N coatings, we can observe a considerable rise of compressive stresses on the coating surface as compared to single-layer coatings (Table 3). In the case of Ti(C,N) coatings we can observe the change in the character of stresses on the coating surface from tensile stresses ,occurring on the surface of single-layer coatings, to compressive stresses occurring on the surface of gradient coatings. The generation of compressive stresses in the surface layer brings about better resistance to cracking, and through the rise of hardness, improves the wear resistance. The generation of compressive stresses in the surface layer can prevent the formation of cracks when the element in the operational conditions is subjected to stresses generated by external forces. Yet, an excessive value of compressive stresses can lead to adhesive wear and can bring about the formation of too high tensile stresses under the coating, lowering the fatigue resistance of the element [61,68]. Volvoda [67] pointed out the relation between the value of stresses and the hardness of the layer of titanium nitrides obtained in effect of magnetron sputtering, demonstrating that with the rise of compressive stresses the hardness of the obtained layer is progressively increasing. Basing on the carried out research, it was demonstrated that the occurrence of compressive stresses on the surface of gradient coatings of the investigated materials has a positive influence on their mechanical properties, in particular on the microhardness (Table 1).

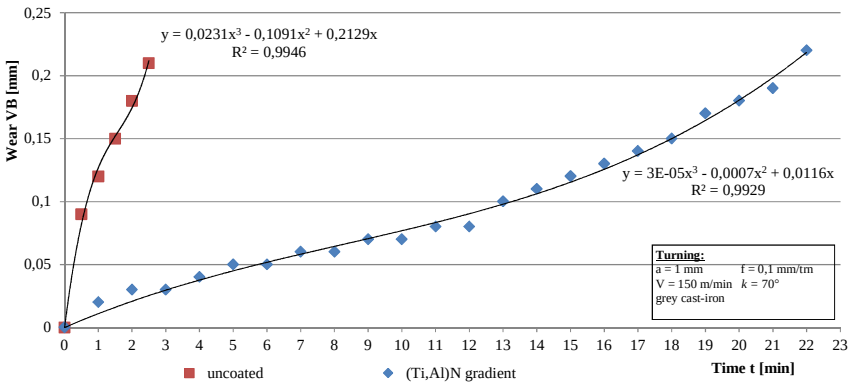

Figure 36. *Comparison of the approximated values of the VB wear of the cermets sample: uncoated and coated with the (Ti,Al)N gradient coating, depending on machining time*

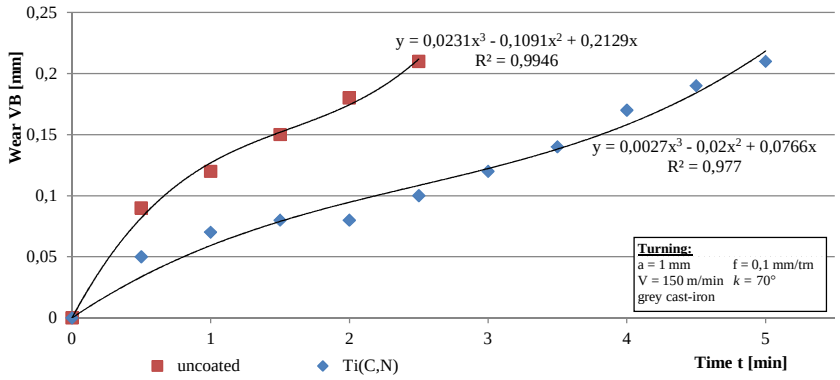

Figure 37. *Comparison of the approximated values of the VB wear of the cemented carbides sample: uncoated and coated with the Ti(C,N) coating, depending on machining time*

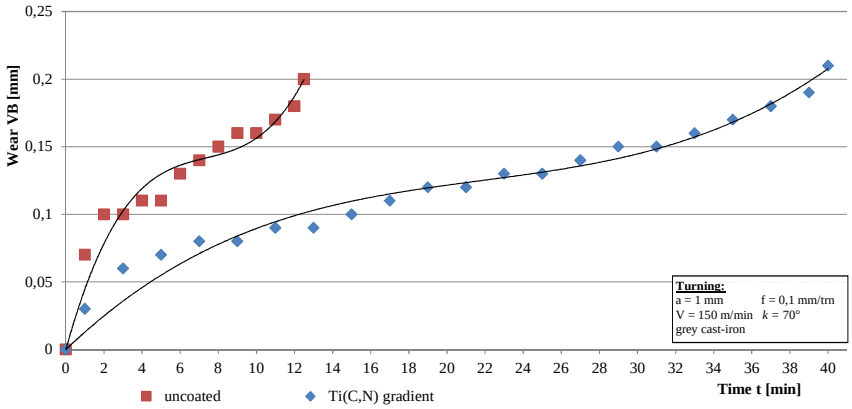

Figure 38. *Comparison of the approximated values of the VB wear of the Al_2O_3+TiC oxide tool ceramics sample: uncoated and coated with the Ti(C,N) gradient coating, depending on machining time*

Table 4. *Results of computer simulation of internal stresses in the analysed single-layer PVD coatings*

Substrate	Coating	Computer simulation results of internal stress, [MPa]
Cemented carbide	(Ti,Al)N	170
	Ti(C,N)	150
Cermet	(Ti,Al)N	-410
	Ti(C,N)	15
Al_2O_3+TiC	(Ti,Al)N	-180
	Ti(C,N)	150

Figure 40 present schematic distribution of stresses in the gradient coating (Ti,Al)N deposited on cemented carbide obtained by computer simulation

To verify the results of computer simulation, the values of eigen-stresses in the investigated single-layer and gradient coatings were calculated using the X-ray $\sin^2\psi$ technique (Table 5).

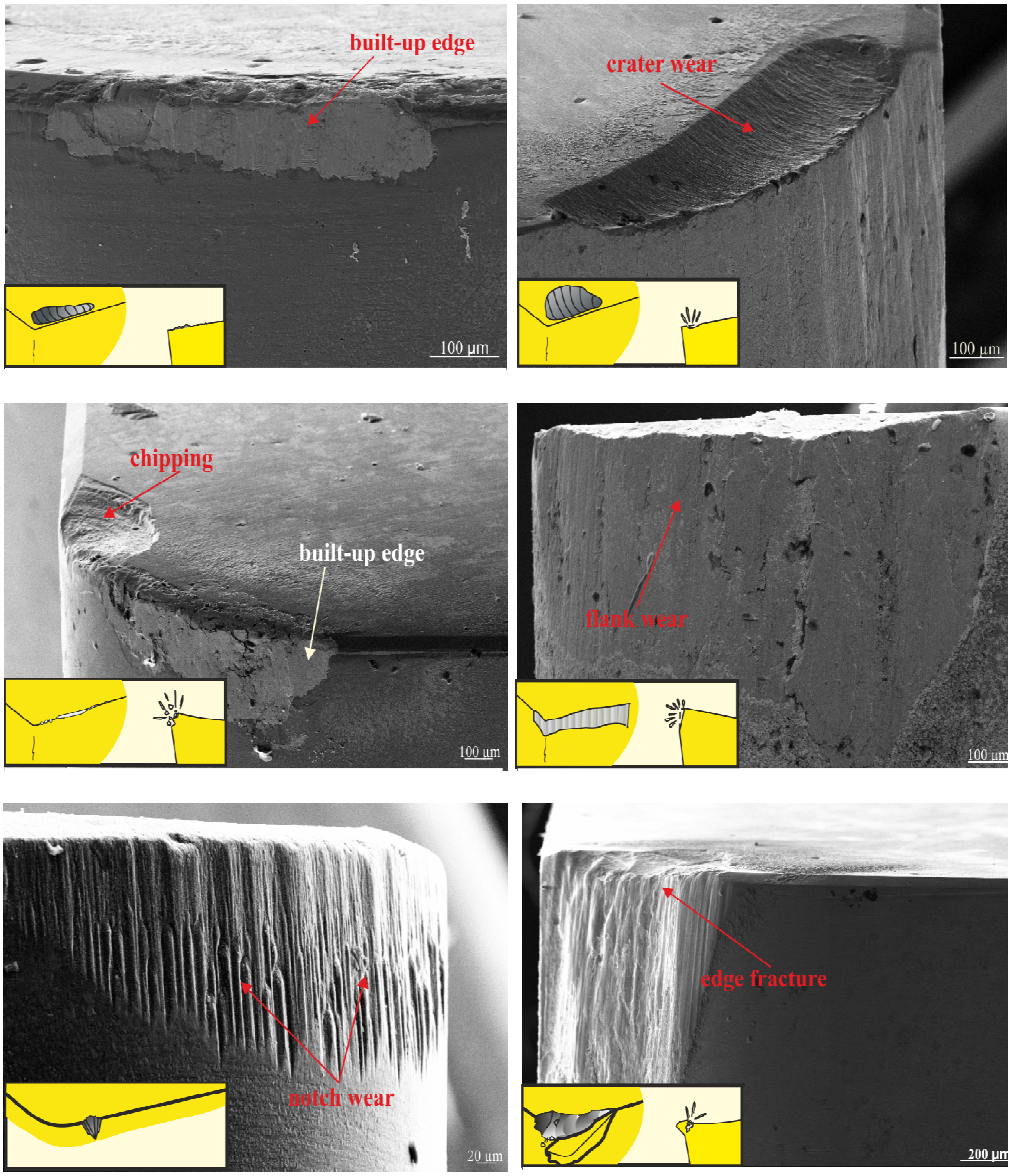

Figure 39. *Classification of character of tool wear of the sintered tool materials uncoated and coated with PVD coatings*

Table 5. *Results of experimental internal stresses using the X-ray $\sin^2\psi$ technique of the analysed PVD coatings*

Substate	Coating	Internal stresses, σ [MPa]
Cemented carbide	(Ti,Al)N	212±42
	(Ti,Al)N gradient	-395±45
	Ti(C,N)	-
	Ti(C,N) gradient	-
Cermet	(Ti,Al)N	-459±49
	(Ti,Al)N gradient	-647±77
	Ti(C,N)	-
	Ti(C,N) gradient	-
Al_2O_3+TiC	(Ti,Al)N	-228±48
	(Ti,Al)N gradient	-456±76
	Ti(C,N)	122±52
	Ti(C,N) gradient	-235±65

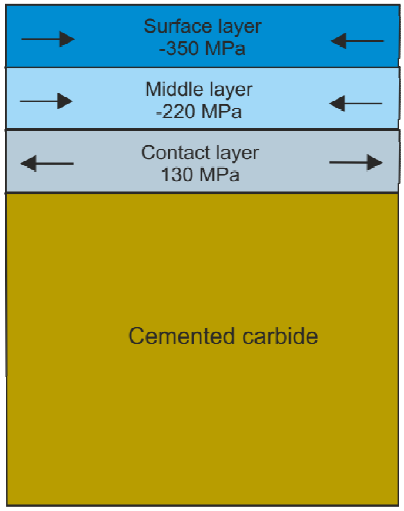

Figure 40. *Schematic distribution of stresses in the gradient coating (Ti,Al)N deposited on cemented carbide obtained by computer simulation*

4. Conclusions

The main objective of the work was to investigate the structure and properties of sintered tool materials, including cemented carbides, cermets and oxide ceramics deposited with single-layer and gradient coatings (Ti,A1)N and Ti(C,N), and to determine the relation between substrate type, coating material and linear variability of the chemical composition of the coating and the structure and properties of the obtained tool material (Fig. 41).

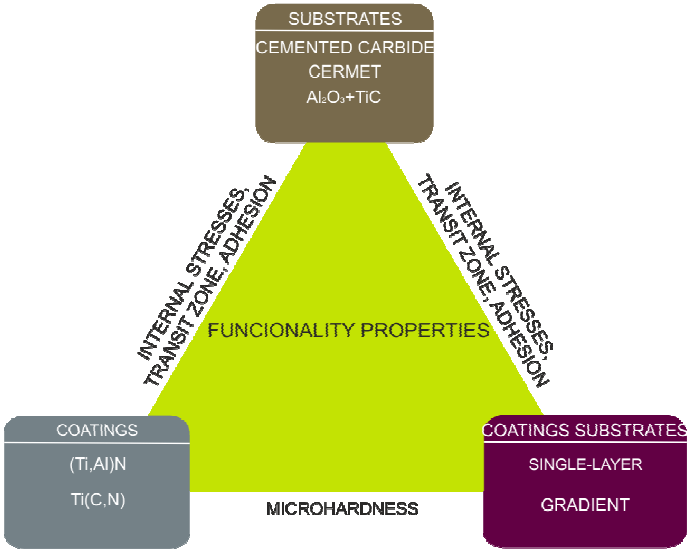

Figure 41. *Schematic diagram of the objective of the work*

Basing on the analysis of the obtained research results the following conclusions can be demonstrated:

1. The fabrication of PVD coatings of the type (Ti,Al)N and Ti(C,N) of the gradient structure and variable concentration of the components on the tools from sintered tool materials results in a considerable rise of applicability properties of tools produced in this way as compared to the tools deposited with a single-layer PVD coating or non-deposited coatings.
2. Gradient coatings are characterized by a linear change of chemical composition in the direction from the substrate to the coating surface. The deposited coatings demonstrate good and uniform adhesion to the substrate material and are characterized by column, fine-grained structure. In the contact area from the surface of the coatings we can observe a rise in the concentration of chemical elements being the components of the substrate, with a simultaneous decrease of the concentration of chemical elements forming these coatings, which can bespeak of the presence of a transit zone between the substrate material and coating.
3. A more advantageous distribution of stresses in gradient coatings than in respective single-layer coatings yields better mechanical properties, and, in particular, the distribution of stresses on the coating surface has the influence on microhardness, and the distribution of

stresses in the contact area between the coating and substrate has the influence on the adhesion of coatings.

4. The wear resistant gradient coatings of the type (Ti,Al)N and Ti(C,N) deposited on the investigated sintered tool materials yield a considerable rise of microhardness in the area around the surface, which, combined with good adhesion of the coating to the substrate obtained in effect of the application of gradient structure of the coating, has the influence on the applicability properties of these materials during machining tests, since the deposition of both single-layer and gradient coatings of the (Ti,Al)N type results in the rise of cutting edge durability as compared to the tools deposited with Ti(C,N) coatings. It is connected with high wear resistance of the (Ti,Al)N coating in raised temperature. It was also demonstrated that independent of the applied substrate type, higher wear resistance is exhibited by the materials deposited with gradient coatings as compared to the materials deposited with single-layer coatings.

Acknowledgements

The paper has been realised in relation to the project POIG.01.01.01-00-023/08 entitled "Foresight of surface properties formation leading technologies of engineering materials and biomaterials" FORSURF, co-founded by the European Union from financial resources of European Regional Development Found and headed by Prof. L.A. Dobrzański.

References

1. M. Antonov, I. Hussainova, F. Sergejev, P. Kulu, A. Gregor, Assessment of gradient and nanogradient PVD coatings behaviour under erosive, abrasive and impact wear conditions, Wear 267 (2009) 898-906.
2. M. Arndt, T. Kacsich, Performance of new AlTiN coatings in dry and high speed cutting, Surface and Coatings Technology 163-164 (2003) 674-680.
3. M.A. Baker, S.J. Greaves, E. Wendler, V. Fox, A comparison of in situ polishing and ion beam sputtering as surface preparation methods for XPS analysis of PVD coatings, Thin Solid Films 377-378 (2000) 473-477.

4. M. Bizjak, A. Zalar, P. Panjan, B. Zorko, B. Pracek, Characterization of iron oxide layers using Auger electron spectroscopy, Applied Surface Science 253 (2007) 3977-3981.
5. Y.Y. Chang, D.Y. Wang, Characterization of nanocrystalline AlTiN coatings synthesized by a cathodic-arc deposition process, Surface and Coatings Technology 201 (2007) 6699-6701.
6. J. R.C.Jr, Chastain, Handbook of X-ray Photoelectron Spectroscopy, Physical Electronics, Inc., 1995.
7. A.R. Chourasia, D.R. Chopra, Auger Electron Spectroscopy, Handbook of analytical chemistry, Prentice Hall, 1997.
8. M. Cłapa, D. Batory, Improving adhesion and wear resistance of carbon coatings using Ti:C gradient layers, Journal of Achievements in Materials and Manufacturing Engineering 20 (2007) 415-418.
9. G.E. D'Errico, R. Calzavarini, B. Vicenzi, Influences of PVD coatings on cermet tool life in continuous and interrupted turning, Journal of Materials Processing Technology 78 (1998) 53-58.
10. A. Demirkiran, E. Avci, Evaluation of functionally gradient coatings produced by plasma-spray technique, Surface and Coatings Technology 116-119 (1999) 292-295.
11. L.A. Dobrzański, Structure and properties of high-speed steels with wear resistant cases or coatings, Journal of Materials Processing Technology 109 (2001) 44-51.
12. K. Dybowski, Ł. Kaczmarek, R. Pietrasik, J. Smolik, Ł. Kołodziejczyk, D. Batory, M. Gzik, M. Stegliński, Influence of chemical heat treatment on the mechanical properties of paper knife-edge die, Journal of Achievements in Materials and Manufacturing Engineering 37/2 (2009) 422-427.
13. W. Kaczorowski, D. Batory, Carbon and titanium based layers for wood-based materials, Journal of Achievements in Materials and Manufacturing Engineering 27/2 (2008) 187-190.
14. B.G. Wndler, W. Pawlak, Low friction and wear resistant coating systems on Ti6Al4V alloy, Journal of Achievements in Materials and Manufacturing Engineering 26/2 (2008) 207-210.
15. M. Richert, A. Mazurkiewicz, J. Smolik, Chromium carbide coatings obtained by the hybrid PVD methods, Journal of Achievements in Materials and Manufacturing Engineering 43/1 (2010) 145-152.
16. L.A. Dobrzański, K. Gołombek, J. Mikuła, D. Pakuła, L.W. Żukowska, Sintered tools materials with multicomponent PVD gradient coating, Journal of Achievements in Materials and Manufacturing Engineering 31 (2008) 15-22.
17. J. Grabarczyk, D. Batory, P Louda, P. Couvrat, I. Kotela, K. Bakowicz-Mitura, Carbon coatings for medical implants, Journal of Achievements in Materials and Manufacturing Engineering 20 (2007) 107-111.
18. Z. Rożek, W. Kaczorowski, D. Lukáš, P. Louda, S. Mitura, Potential applications of nanofiber textile covered by carbon coatings, Journal of Achievements in Materials and Manufacturing Engineering 27/1 (2008) 35-38.
19. R.M. Nowak, S. Jonas, S. Zimowski, K. Tkacz-Śmiech, Amorphous carbon layers on polymeric substrates, Journal of Achievements in Materials and Manufacturing Engineering 25/1 (2007) 23-26.

20. B. Wendler, T. Moskalewicz, I. Progalskiy, W. Pawlak, M. Makówka, K. Włodarczyk, P. Nolbrzak, A. Czyrska-Filemonowicz, A. Rylski, Hard and superhard nanolaminate and nanocomposite coatings for machine elements based on Ti6Al4V alloy, Journal of Achievements in Materials and Manufacturing Engineering 43/1 (2010) 455-462.
21. W. Pawlak, B. Wendler, Multilayer, hybrid PVD coatings on Ti6Al4V titanium alloy, Journal of Achievements in Materials and Manufacturing Engineering 37/2 (2009) 660-667.
22. D. Batory, A. Stanishevsky, W. Kaczorowski, The effect of deposition parameters on the properties of gradient a-C:H/Ti layers, Journal of Achievements in Materials and Manufacturing Engineering 37/2 (2009) 381-386.
23. K. Włodarczyk, M. Makówka, P. Nolbrzak, B. Wendler, Low friction and wear resistant nanocomposite nc-MeC/a-C and nc-MeC/a-C:H coatimgs, Journal of Achievements in Materials and Manufacturing Engineering 37/2 (2009) 364-360.
24. W. Kaczorowski, D. Batory, P. Niedzielski, Application of microwave/radio frequency and radio frequency/magnetron sputtering techniques in polyurethane surface modification, Journal of Achievements in Materials and Manufacturing Engineering 37/2 (2009) 286-291.
25. W. Kwaśny, Predicting properties of PVD and CVD coatings based on fractal quantities describing their surface, Journal of Achievements in Materials and Manufacturing Engineering 37/2 (2009) 125-192.
26. W. Grzesik, Z. Zalisz, S. Król, Tribological behaviour of TiAlN coated carbides in dry sliding tests, Journal of Achievements in Materials and Manufacturing Engineering 17 (2006) 279-282.
27. G. Matula, Influence of binder composition on structure and properties of carbide alloyed composite manufactured with the PIM method, Journal of Achievements in Materials and Manufacturing Engineering 30/2 (2008) 193-196.
28. W. Kwaśny, A modification of the method for determination of the surface fractal dimension and multifractal analysis, Journal of Achievements in Materials and Manufacturing Engineering 33 (2009) 115-125.
29. L.A. Dobrzański, M. Staszuk, J. Konieczny, W. Kwaśny, M. Pawlyta, Structure of TiBN coatings deposited onto cemented carbides and sialon tool ceramics, Archives of Materials Science and Engineering 38/1 (2009) 48-54.
30. L.A. Dobrzański, M. Staszuk, J. Konieczny, J. Lelątko, Structure of gradient coatings deposited by CAE-PVD techniques, Journal of Achievements in Materials and Manufacturing Engineering 24/2 (2007) 55-58.
31. L.A. Dobrzański, L. Wosińska, K. Gołombek, J. Mikuła, Structure of multicomponent and gradient PVD coatings deposited on sintered tool materials, Journal of Achievements in Materials and Manufacturing Engineering 20 (2007) 99-102.
32. L.A. Dobrzański, L.W. Wosińska, J. Mikuła, K. Gołombek, T. Gawarecki, Investigation of hard gradient PVD (Ti,Al,Si)N coating, Journal of Achievements in Materials and Manufacturing Engineering 24 (2007) 59-62.

33. L.A. Dobrzański, L.W. Wosińska, J. Mikuła, K. Gołombek, D. Pakuła, M. Pancielejko, Structure and mechanical properties of gradient PVD coatings, Journal of Materials Processing Technology 201(2008) 310-314.
34. L.A. Dobrzański, L.W. Wosińska, J. Mikuła, K. Gołombek, Multicomponent and gradient PVD coatings deposited on the sintered tool materials, Materials Science 3-4 (157-158) (2007) 627-630.
35. L.A. Dobrzański, L.W. Żukowska, Properties of the multicomponent and gradient PVD coatings, Archives of Materials Science and Engineering 28/10 (2007) 621-624.
36. L.A. Dobrzański, L.W. Żukowska, W. Kwaśny, J. Mikuła, K. Gołombek, Ti(C,N) and (Ti,Al)N hard wear resistant coatings, Journal of Achievements in Materials and Manufacturing Engineering 42/2 (2010) 93-103.
37. L.A. Dobrzański, L.W. Żukowska, J. Mikuła, K. Gołombek, T. Gawarecki, Hard gradient (Ti,Al,Si)N coating deposited on composite tool materials, Archives of Materials Science and Engineering 36/2 (2009) 69-754.
38. L.A. Dobrzański, L.W. Żukowska, J. Mikuła, K. Gołombek, P. Podstawski, Functional properties of the sintered tool materials with (Ti,Al)N coating, Journal of Achievements in Materials and Manufacturing Engineering 36/2 (2009) 134-141.
39. L.A. Dobrzański, L.W. Żukowska, J. Kubacki, K. Gołombek, J. Mikuła, XPS and AES analysis of PVD coatings, Journal of Achievements in Materials and Manufacturing Engineering 32 (2008) 99-102.
40. J. Gu, G. Barber, S. Tung, R.J. Gu, Tool life and wear mechanism of uncoated and coated milling inserts, Wear 225-229 (1999) 273-284.
41. Y.H. Guu, H. Hocheng, Improvement of fatigue life of electrical discharge machined AISI D2 tool steel by TiN coating, Materials Science and Engineering A 318 (2001) 155-162.
42. J. Kopač, Influence of cutting materials and coating on tool quality and tool life, Journal of Materials Processing Technology 78 (1998) 95-103.
43. R. Kosiba, J. Liday, G. Ecke, O. Ambacher, J. Breza, P. Vogrincic, Quantitative Auger electron spectroscopy of SiC, Vacuum 80 (2006) 990-995.
44. J.H. Lee, S.J. Lee, One-step-ahead prediction of flank wear using cutting force, International Journal of Machine Tools and Manufacture 39 (1999) 1747-1760.
45. W. Lengauer, K. Dreyer, Functionally graded hardmetals, Journal of Alloys and Compounds 338 (2002) 194-212.
46. Li Chen, S.Q. Wang, Yong Du, Jia Li, Microstructure and mechanical properties of gradient Ti(C, N) and TiN/Ti(C, N) multilayer PVD coatings, Materials Science and Engineering A 478 (2008) 336-339.
47. C.Y.H. Lim, S.C. Lim, K.S. Lee, Wear of TiC-coated carbide tools in dry turning, Wear 225-229 (1999) 354-367.
48. C.H. Lin, J.G. Duh, J.W. Yeh, Multi-component nitride coatings derived from Ti-Al-Cr-Si-V target in RF magnetron sputter, Surface and Coatings Technology 201 (2007) 6304-6308.

49. T. Liu, C. Dong, S. Wu, K. Tang, J. Wang, J. Jia, TiN, TiN gradient and Ti/TiN multi-layer protective coatings on Uranium, Surface and Coating Technology 201 (2007) 6737-6741.
50. Y.H. Lu, Z.F. Zhou, P. Sit, Y.G. Shen, K.Y. Li, Haydn Chen, X-Ray photoelectron spectroscopy characterization of reactively sputtered Ti-B-N thin films, Surface & Coatings Technology 187 (2004) 98-105.
51. S.J. Skrzypek, W. Ratuszek, A. Bunsch, M. Witkowska, J. Kowalska, M. Goły, K. Chruściel, Crystallographic texture and anisotropy of electrolytic deposited copper coating analysis, Journal of Achievements in Materials and Manufacturing Engineering 43/1 (2010) 264-268.
52. S. Carvalho, E. Ribeiro, L. Rebouta, C. Tavares, J.P. Mendonca, A. Caetano Monteiro, N.J.M. Carvalho, J.Th. M. De Hosson, A. Cavaleiro, Microstructure, mechanical properties and cutting performance of superhard (Ti,SiAl)N nanocomposite films grown by d.c. reactive magnetron sputtering, Surface and Coatings Technology 177-178 (2004) 459-468.
53. R. Manaila, A. Devenyi, D. Biro, L. David, P.B. Barna, A. Kovacs, Multilayer TiAlN coatings with composition gradient, Surface and Coatings Technology, 151-152 (2002) 21-25.
54. G. Matula, Study on steel matrix composites with (Ti,Al)N gradient PVD coatings, Journal of Achievements in Materials and Manufacturing Engineering 34/1 (2009) 79-86.
55. P.H. Mayrhofer, Ch. Mitterer, L. Hultman, H. Clemens, Microstructural design of hard coatings, Progress in Materials Science 51 (2006) 1032-1114.
56. S. Mitura, A. Mitura, P. Niedzielski, P. Couvrat, Nanocrystalline Diamond Coatings, Chaos, Solitons& Fractals 10/12 (1999) 2165-2176.
57. Y. Miyamoto, W.A. Kaysser, B.H. Rabin, A. Kawasaki, R.G. Ford, Funcionally Graded Materials: Design, Processing and Applications, Kulwer Academic Publishers, Boston-Dordrecht-London 1999.
58. S. PalDey, S.C. Deevi, Cathodic arc deposited FeAl coatings: properties and oxidation characteristics, Materials Science and Engineering A355 (2003) 208-215.
59. S. PalDey, S.C. Deevi, Properties of single layer and gradient (Ti,Al)N coatings, Materials Science and Engineering A361 (2003) 1-8.
60. S. PalDey, S.C. Deevi, Single layer and multilayer wear resistant coatings of (Ti,Al)N: a review, Materials Science and Engineering A342 (2003) 59-79.
61. A. Perry, J.A. Sue, P.J. Martin, Practical measurement of the residual stress in coatings, Surface and coatings Technology 81 (1996)17-28.
62. X. Qiao, Y. Hou, Y. Wu, J. Chen, Study on functionally gradient coatings of Ti-Al-N, Surface and Coatings Technology 131 (2000) 462-464.
63. Catalogue, Sandvik-Coromant.
64. D. Rafaja, A. Poklad, V. Klemm, G. Schreiber, D. Heger, M. Sima, M. Dopita, Some consequences of the partial crystallographic coherence between nanocrystalline domains in Ti-Al-N and Ti-Al-Si-N coatings, Thin Solid Films 514 (2006) 240-249.

65. B. Navinsek, P. Panjan, I. Milosev, PVD coatings as an environmentally clean alternative to electroplating and electroless processes, Surface and Coatings Technology 116-119 (1999) 476-487.
66. A. Śliwa, J. Mikuła, K. Gołombek, L.A. Dobrzański, FEM modelling of internal stresses in PVD coated FGM, Journal of Achievements in Materials and Manufacturing Engineering 36/1 (2009) 71-78.
67. V. Volvoda: Structure of thin films of titanium nitride, Journal of Alloys and Compounds 219 (1995) 83-87.
68. U. Welzel, J. Ligot, P. Lamparter, Stress analysis of polycrystalline thin films and surface regions by X-ray diffraction, Applied Crystallography 38 (2005) 1-29.
69. I.Yu. Konyashin, PVD/CVD technology for coating cemented carbides, Surface and Coatings Technology 71 (1995) 277-283.

The paper is published also in the Journal of Achievements in Materials and Manufacturing Engineering

ISSN 2083-5191
ISBN 83-89728-88-5
EAN 9788389728883